USING HIGH RESOLUTION BOREHOLE GEOPHYSICS FOR DNAPL DETECTION AND ENVIRONMENTAL SITE CHARACTERIZATION

A DISSERTATION
SUBMITTED TO THE DEPARTMENT OF GEOPHYSICS
AND THE COMMITTEE ON GRADUATE STUDIES
OF STANFORD UNIVERSITY
IN PARTIAL FULFILLMENT OF THE REQUIREMENTS
FOR THE DEGREE OF
DOCTOR OF PHILOSOPHY

Jonathan B. Ajo-Franklin
January 2005

I certify that I have read this dissertation and that, in my opinion, it is fully adequate in scope and quality as a dissertation for the degree of Doctor of Philosophy.

Jerry M. Harris
(Principal Adviser)

I certify that I have read this dissertation and that, in my opinion, it is fully adequate in scope and quality as a dissertation for the degree of Doctor of Philosophy.

Rosemary Knight

I certify that I have read this dissertation and that, in my opinion, it is fully adequate in scope and quality as a dissertation for the degree of Doctor of Philosophy.

Gary Mavko

I certify that I have read this dissertation and that, in my opinion, it is fully adequate in scope and quality as a dissertation for the degree of Doctor of Philosophy.

Kurt Nihei
(LBNL)

Approved for the University Committee on Graduate Studies.

Abstract

The field-scale detection and spatial delineation of toxic contaminants is a critical problem for environmental scientists charged with protecting our valuable water resources. Dense non-aqueous phase liquids or DNAPLs are a class of contaminants which are difficult to both characterize and remediate using current techniques. A wide variety of geophysical techniques have been proposed for DNAPL detection in the shallow subsurface. However, most methods lack the spatial resolution and sensitivity required for characterization of small DNAPL lenses or pools.

This dissertation investigates the applicability of high-resolution borehole geophysical measurements for the *in situ* detection of DNAPLs. In pursuit of this goal, a series of crosswell seismic and crosswell radar datasets were acquired at a site of known DNAPL contamination, the US DOE Pinellas facility. The combination of an extensive crosswell dataset, a large suite of well logs, and continuous core sampling allowed exploration of the possible petrophysical signatures of DNAPL saturation on both the laboratory and field scale.

To process the Pinellas datasets, a new class of adaptive traveltime tomography algorithms were developed, capable of flexibly accommodating regions of poor ray coverage and highly irregular source/receiver geometries. These techniques, based on greedy mesh refinement, guarantee that the resulting inverse problem fulfills *a priori* model resolution constraints. The method improves on previously developed algorithms through the use of a new refinement heuristic which results in higher quality tomographic meshes. Using this novel approach to traveltime tomography, several multiwell seismic and radar profiles acquired at the Pinellas site were simultaneously inverted to generate high-resolution velocity models. The tomographic imaging results were integrated with logging data to generate a detailed map of the primary lithologic and hydrogeologic units at the site. Although non-aqueous contaminants were not conclusively identified at this facility, several anomalous regions with high radar velocities and high levels of seismic attenuation were detected below the water table; these signatures are consistent with soils partially saturated with either gas or DNAPLs.

The second component of the Pinellas investigation was an extensive laboratory study examining the dielectric and acoustic properties of Pinellas core materials partially saturated with trichloroethylene (TCE), a DNAPL observed in site fluid samples. High frequency dielectric measurements were acquired using the time-domain reflectometry method and a specially designed coaxial cell; these experiments quantified the relationship between TCE saturation and dielectric constant for several soil samples. A series of ultrasonic transmission measurements explored similar relationships between DNAPL levels and P-wave velocity at *in situ* stress conditions. The combined results of these laboratory experiments provide insight into the possible joint seismic/radar signatures of subsurface DNAPLs and partial confirmation of existing effective medium models used to describe such systems.

To Caroline, a partner in all my endeavors.

Acknowledgements

I would like to begin by thanking my advisor, Jerry Harris, for six years of intellectual challenge, patience, and support in times of both excitement and frustration. Back in 1997, when I was still a young computer scientist playing with graph theory, I ran into two former STP researchers (Guan Wang and Jesse Costa) while presenting a poster at SEG. That winter I took a break from attending fall AGU to drive down to Stanford and meet Jerry. With his encouragement, I made the switch to geophysics and by the following June I was in the Mitchell building at the beginning of what has been a delightful, if sometimes intense, 6 years. Jerry has given me tremendous latitude in my research, even when I began to delve into topics which departed from the traditional focus of the group.

This dissertation would have been a very different beast without the help of Jil Geller of Lawrence Berkeley National Laboratory. Jil allowed me to fully participate in the Pinellas project; besides acquiring all of the requisite DOE funding for our field investigation and performing the core-scale seismic measurements (!) discussed in chapter 6, she has been an excellent collaborator and co-author. I greatly benefited from her constructive criticism and sound advice, particularly concerning the nuances of lab measurements on soft sediments.

Ken Williams (LBNL) was instrumental in the acquisition of the Pinellas field dataset, patiently showing me the ropes on LBNLs crosswell acquisition system and answering my frantic 6 am phone calls when equipment failed. Besides working with me in the field, Ken has been a great friend, always ready to discuss topics beyond geophysics including but not limited to fishing, home ownership, and DOE politics. In the words of an anonymous AGU Fall 2004 attendee, “Ken Williams is an inspiration to us all!”. I have also benefited from the knowledge and advice of a host other of friends at LBNL including Seiji Nacagawa, Steve Pride, and Kurt Nihei. John Peterson graciously lent me his traveltime picks while I was resolving problems in my pre-processing codes. Phil Rizzo was a great help during the week he spent at with me at Pinellas hauling antennas and seismic gear.

I owe my reading committee, composed of Jerry, Rosemary Knight, Gary Mavko, and Kurt Nihei, a debt of thanks for both providing feed-back during my graduate career and having persevered through the 300+ pages of this dissertation, “For an environmental thesis you sure killed a lot of trees” (Gary Mavko).

Several institutions provided crucial financial resources for the development of my doctoral research. For three years I was supported under the US EPA’s STAR Fellowship Program which gave me the independence to pursue environmental geophysics. The department generously extended the Chair's Fellowship for Intergroup Research to me during the 2002/2003 academic year. The Shell Foundation has provided auxiliary funding for some of my early resonance experiments and later core analysis work. The acquisition of field data at the Pinellas and Paducah field sites was largely funded through a grant from the Subsurface Contamination Focus Area of the DOE's Environmental Management Program (contract # DE-AC-03-76F0098 : PIs Jil Geller & Ernie Majer).

Our investigation at the Pinellas site would have been impossible without the support of David S. Ingle, the Pinellas DOE Site Manager, and his staff with MACTEC-ERS and later STOLLER-GJO. In particular, I would like to thank technical specialist Bobby Hansen and project manager Joe Daniel for their assistance during our deployments.

My experimental work has migrated through several laboratories and I have profited from exposure to the dedicated "full-time" experimentalists who inhabit them. My most sincere thanks is extended to the Stanford Rock Physics Group for use of lab space, instruments, and the expert experimental advice and enthusiasm of Manika Prasad and Mike Zimmer. Later in my career, I was lent a bench in the environmental geophysics lab and was fortunate to share space with Tracy Bryar. At LBNL, I spent the better part of 9 months running my TCE injection experiments in building 51 at the soil and rock mechanics lab. Many happy hours were spent hanging out with Jil, Seiji, and Kurt.

Despite (or perhaps because of) our small size and diverse areas of expertise, the Wave Physics Lab (formerly the Seismic Tomography Project) has been an exciting research environment; group meetings cycle between modeling, inverse theory, field studies, and lab measurements with applications in both exploration and environmental topics. In particular, Chunling Wu and Jaime Urban have been great friends and labmates, always willing to join me in my primary vice, a mid-afternoon cup of coffee. Jaime was also a key collaborator in developing some of the tomography codes discussed in chapter 8.

Many other friends have contributed to maintaining my sanity over the last 6 years, including but not limited to Hozefa Divan, Jehangir Malegam, Kalindi Dogra, and David Ajo. Although PhD dissertations are perhaps not the most expressive genre of writing, as far as this thesis reflects me, it also reflects the love and support of my family, particularly my mom and dad. But the last words of thanks must go to my love, my wife, Caroline.

Contents

List of Tables

List of Figures

Chapter 1

Introduction

The field-scale detection and spatial delineation of toxic contaminants is a critical problem for environmental scientists charged with protecting our valuable water resources. Many industrial pollutants represent a considerable health threat to humans, with impacts ranging from acute illness to increased risks of cancer and birth defects. To combat toxic contaminants in ground water, the polluting compound must be detected, the source must be characterized, and appropriate remediation/containment actions must be taken. Long-term monitoring complements remediation by providing a measurement of efficacy and an understanding of the current risks associated with using a groundwater resource. The National Research Council (NRC) has singled out noninvasive geophysical techniques as one important area for current and future research in the characterization of contaminated environmental sites [226].

In this dissertation, we investigate the applicability of high-resolution borehole geophysical measurements for the *in situ* detection of dense non-aqueous phase liquids (DNAPLs), a class of contaminants which are difficult to both characterize and remediate using current techniques. As part of this investigation, we acquired a large series of crosswell seismic and radar surveys at a site of known DNAPL contamination, the Pinellas facility, formerly owned and operated by General Electric for the US Department Of Energy (DOE). [1]. We developed a new class of adaptive tomographic algorithms which allowed us to effectively perform traveltime inversion on our multi-well profiles despite the existence of significant gaps in ray coverage. The results of our tomographic imaging process were integrated with logging results to generate a detailed model of site lithology. Although non-aqueous contaminants were not conclusively identified at this facility, we did detect several regions below the water table with high radar velocities and high levels of seismic attenuation, signatures which are consistent with soils partially saturated with either gas or DNAPLs. We also present the results of an extensive laboratory investigation into the dielectric and acoustic properties of Pinellas core

---

[1] The Pinellas geophysics investigation was carried out jointly with Lawrence Berkeley National Laboratory. Jil Geller (LBNL) was the primary investigator for the project (EM-DOE grant #DE-AC-03-76F0098) and Ken Williams (LBNL) provided crucial guidance during the field acquisition process. Phil Rizzo (LBNL), Jaime Urban (Stanford), and Cecil Hoffpauier (LBNL) also assisted in the data acquisition effort. All crosswell seismic and radar equipment were borrowed from LBNL's Geophysical Measurement Facility (GMF).

samples partially saturated with trichloroethylene (TCE) or toluene, two contaminants of concern at our field site. The combined results of these laboratory experiments provide insight into the possible joint seismic/radar signatures of subsurface DNAPLs and partial confirmation of existing effective medium models used to describe such systems. We conclude with a retrospective examination of the role which geophysics might play in future NAPL detection and environmental site characterization efforts.

This first chapter attempts to summarize the physical characteristics and hazards of DNAPLs and the current difficulties related to their detection and removal. We review the geophysical techniques which have previously been applied to the DNAPL detection problem on both the laboratory and field scale. In this overview, we focus on ground penetrating radar and seismic methods, both of which we used as part of our field investigation. We conclude with a brief description of our goals and the structure of this dissertation.

1.1 A Portrait Of The DNAPL problem

Dense Non-Aqueous Phase Liquids or DNAPLs are a family of fluids which includes some of the most common and problematic groundwater contaminants. Chlorinated solvents, including trichloroethylene (TCE), tetrachloroethylene (PCE), and carbon tetrachloride, are the most important sub-class of DNAPLs due to their wide-spread use in the electronics, chemical, dry-cleaning, and metal fabrication industries. Because DNAPLs are denser and often less viscous than water, they easily penetrate deep into the saturated zone and pond at low permeability barriers. As DNAPLs slowly dissolve in the saturated zone, they produce large plumes of contaminated ground water although most of the pollutant mass remains in concentrated pools. The low absolute solubility of most DNAPLs insures that the total pollutant mass mobilizes slowly; some contaminant pools have estimated life-times of several centuries. However, these fluids often have high solubilities relative to EPA toxicity limits making DNAPL plumes long-term groundwater hazards unless properly treated. Table 1.1 provides a brief summary of the solubilities, EPA maximum contamination levels (MCL), and several geophysically relevant physical properties for 7 chlorinated DNAPLs ranked by annual production levels. As can be seen, the aqueous solubilities of the listed DNAPLs are between 4 and 5 orders of magnitude greater than the EPA MCL.

DNAPLs are common groundwater contaminants, present in excess of EPA toxicity levels at thousands of sites in the US [212]. Tetrachloroethylene (PCE), a typical chlorinated DNAPL used in both dry-cleaning and the electronics industry, was found in detectable levels at 43 % of 1070 general use wells in the state of New Jersey [210]. Even relatively small volumes of DNAPL can generate large contaminant plumes; in one well-studied site in San Jose, CA, an estimated 130 L of 1,1,1-Trichloroethane (TCA) served as the source for a 4 km long plume containing approximately 5×10^9 L of groundwater [168]. The Department of Energy (DOE) is responsible for some of the largest DNAPL contaminated sites in the US; five sites, the Hanford nuclear reservation, the Savannah River site, the Oak Ridge reservation, the Rocky Flats facility, and the Idaho National Engineering

Compound	Empirical Formula	Production ($10^6 \frac{kg}{yr}$)	Solubility (in water) ($10^{-6} \frac{kg}{L}$)	EPA MCL ($10^{-6} \frac{kg}{L}$)	ρ (kg/m^3)	V_p (m/s)	κ
1,2-Dichloroethane	$C_2H_4Cl_2$	5871	8690	0.005	1267	1217	10.9
1,1,1-Trichloroethane	$C_2H_3Cl_3$	294	1360	0.2	1338	943	7.2
Carbon Tetrachloride	CCl_4	284	800	0.005	1594	939	2.2
Methylene Chloride	CH_2Cl_2	255	20000	0.005	1326	1089	9.1
Chloroform	$CHCl_3$	191	8000	0.01	1489	1001	4.8
Tetrachloroethylene	C_2Cl_4	184	150	0.005	1623	1059	2.3
Trichloroethylene	C_2HCl_3	75	1100	0.005	1468	1050	3.4
Properties Of Other Common Substances							
Benzene	C_6H_6	-	1780	0.005	879	1326	2.3
Toluene	C_7H_8	-	515	1	866	1323	2.4
Water	H_2O	-	-	-	998	1482	80.1

Table 1.1: Production levels and physical properties for the some common DNAPLs : Production level data (1986) was obtained from Pankow and Cherry [212] while solubility ($\sim 20\ ^oC$) measurements were extracted from Montgomery [185]. Parameters useful for geophysical estimates are also provided and include density (ρ), compressional wave velocity (V_p), and dielectric constant (κ). Unless noted, all values were obtained at $\sim 20\ ^oC$. More detailed tables with all measurement references and temperature dependence information are available in chapter 4. Data on benzene, toluene, and water are provided for the purpose of comparison.

and Environmental Laboratory (INEEL) account for 64 % of DOE clean-up expenditures, estimated to be between 5.6 and 7.2 billion dollars annually [270] [167]. All five have significant DNAPL contamination; the 200 West area of Hanford alone has estimated subsurface DNAPL volumes of upwards of 4×10^6 L, predominantly composed of carbon tetrachloride. Figure 1.1 shows an example of DOE disposal practices circa 1969 at one of INEEL's waste containment sites. DNAPL contamination is certainly not a problem unique to the US. Studies in Germany have documented that PCE is detectable in over 70% of wells downgradient from existing waste sites [141].

Although DNAPLs vary in toxicity, all have both acute and chronic health effects on humans. PCE is a well studied DNAPL useful as an example of the properties characteristic of chlorinated solvents. PCE is acutely toxic at high levels [23], has demonstrated carcinogenic effects in animals and is thought to be a carcinogen for humans [246] [165]. Furthermore, PCE has negative effects on the human reproductive system [83] [229]. Carbon Tetrachloride, another common DNAPL, is a confirmed hepatotoxin [94] [72] [171]. The degradation byproducts of chlorinated solvents are sometimes as toxic as the original compound, as is the case with Vinyl Chloride (VC). VC, which precedes ethene in the reductive dechlorination of PCE [176], is a relatively potent carcinogen [46].

1.1.1 Conceptual Models For Spatial Distribution Of DNAPLs

Since DNAPLs are typically found at depths well below the water-table in regions where direct characterization is difficult, only limited data concerning the spatial distribution of DNAPLs *in situ* are available. Most available information on the architecture of DNAPL pools has been obtained from numerical simulations [149] [150] [151] or controlled mesoscale experiments [152]. Generally,

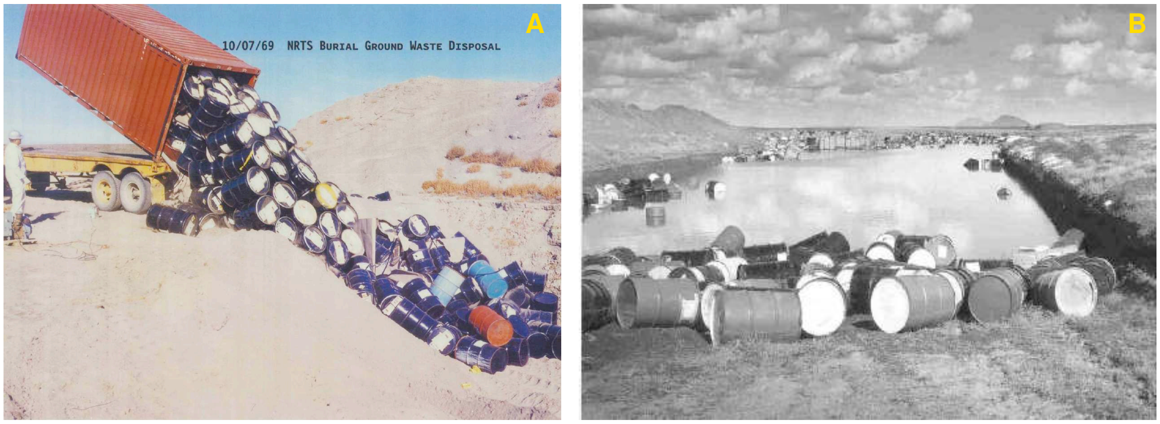

Figure 1.1: DOE disposal practices circa 1969: Panel A shows the dumping of mixed waste into a storage pit at the DOE's INEEL disposal site. Panel B shows a nearby drum pit after spring flooding. Some estimates suggest that up to 50 % of drums deposited at the site ruptured within 10 years.

contaminated sediments can be divided into zones where DNAPLs exist as a continuous phase, which we will refer to as regions of free-product, and zones where DNAPLs only exist in a residual form. Both of these states are distinct from the plume of aqueous contamination which typically extends over a much larger region. The distribution of DNAPLs in the subsurface is controlled by a large number of site factors and is strongly influenced by the spatial heterogeneity of permeability and porosity [160]. Figure 1.2 shows several simple conceptual models useful for understanding DNAPL distribution in the subsurface. Panel A depicts a point source of DNAPL contamination which penetrates the water table and accumulates as a thin high saturation pool directly above the aquitard. Panel B shows a more complicated scenario where the DNAPLs form a complex network of free-product pools in a silty transition region. In some cases, no free-product may exist and the entire DNAPL mass may be in residual form as shown in panel C.

Although the scenarios shown in figure 1.2 give us some basic intuition regarding DNAPL behavior, they are only cartoons and thus cannot provide us with a great deal of insight into what DNAPL saturations and dimensions might be expected in the field. Likewise, it is difficult to capture the strongly coupled physical, chemical, and biological processes of a real contaminant sites using numerical simulations. Recent advances in CPT-based sampling methods offer a new route to obtaining detailed information on the vertical distribution of DNAPLs. Parker et al. [213] uses such a direct-push device to provide an inside look at the architecture of DNAPL source distributions within five contaminated sites located in sandy aquifers. For the two DNAPL spills described by Parker *et al.* most similar to our study area, the free-phase contaminants (TCE and PCE) pooled at permeability transitions, forming layers between 5 and 15 cm in thickness overlain by a thin zone of residual DNAPLs. Peak DNAPL saturations for these pools were on the order of 50% with less than 10% saturation in the residual zones.

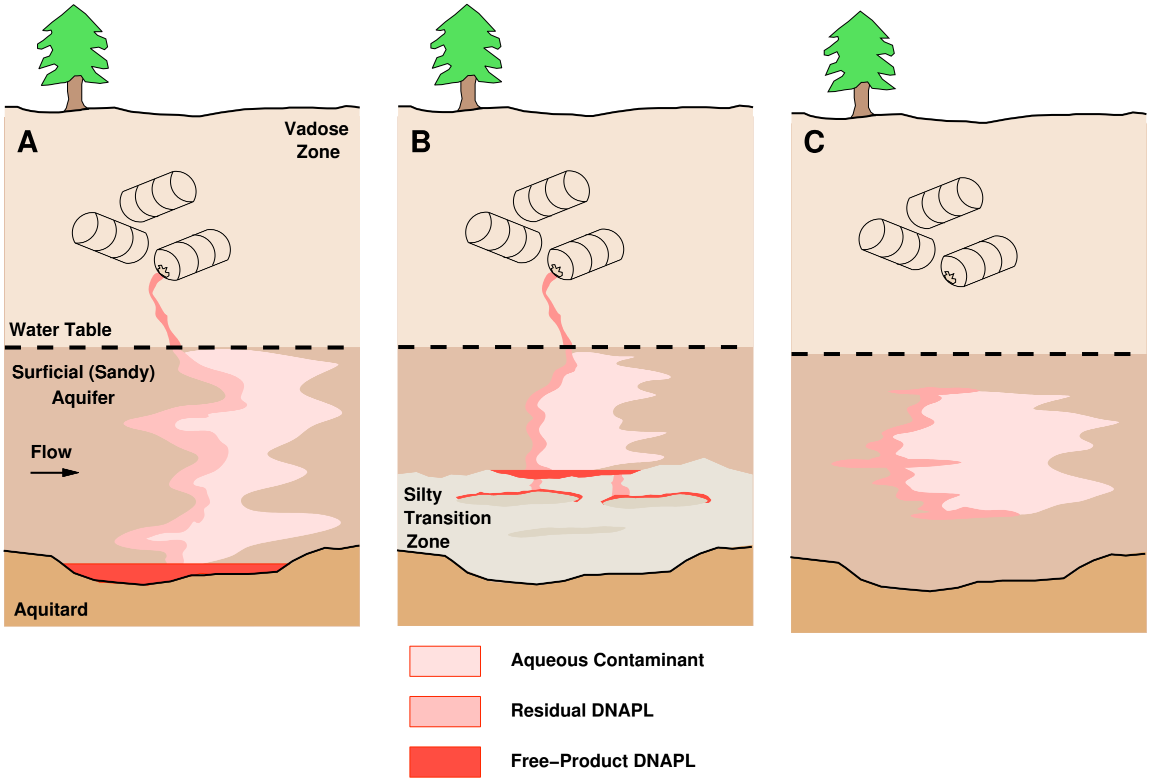

Figure 1.2: Three scenarios for the spatial distribution of subsurface DNAPLs : Panel A shows the traditional “pool” scenario where DNAPLs pass through a permeable upper aquifer and pond at the first significant permeability barrier. Panel B shows distributed free-product within a silty transition zone while panel C shows a contaminated region with only residual DNAPLs remaining.

1.1.2 Current Characterization Techniques : Limitations

While the large plumes of dissolved DNAPLs are easily observable using a variety of chemical analysis techniques, traditional approaches to detecting and characterizing the presence of free-phase DNAPLs in the subsurface often require closely spaced sampling wells for extraction of fluid and soil test materials. Ideally, the location and spatial characterization of the NAPL body would allow a more efficient approach to remediation. Long-term monitoring of these spatial properties allows estimates of remediation success and the public hazard of remaining pollutants. While direct analysis of contaminated water or soil is the only way of confirming the presence of pollutants, the drilling of DNAPL zones is not an efficient technique for characterization and can increase the severity of contamination by providing vertical conduits for contaminant flow. Some of the most promising direct sampling methods for DNAPLs are based on the CPT fluid sampling methods mentioned previously [213] which are both faster and less invasive than a combination of drilling and core analysis. Techniques based on partitioning tracers [88] [279] are another powerful approach to DNAPL characterization which can provide key information on the total NAPL mass *in situ*. The weakness of partitioning interwell tracer tests is their lack of spatial resolution. The perfect detection/characterization method would be able to reliably identify DNAPLs and determine the spatial distribution of free-phase contaminants with a minimum of invasive activity.

1.1.3 Remediation Technologies

DNAPLs are notoriously difficult to remediate using standard pump-and-treat methods [168] [169], making alternative techniques for containment and/or remediation attractive [212]. One established containment method is the placement of a low permeability barrier around the pollutant source region, thus preventing further transport of contaminated water. More experimental "reaction curtain" and gate techniques rely on a biological or chemical process to break down contaminants as they flow through an installed permeable device. Another possible approach is to directly remove the source pool using targeted pumping or *in situ* injection of chemical agents. Injection of pressurized air or steam is sometimes used to volatilize contaminants which are then extracted in gaseous form, a process referred to as air sparging. Water and alcohol flood methods [166] [113], similar in concept to petroleum EOR techniques, are currently being investigated. Some of the most interesting experimental remediation methods rely on anaerobic bacteria that dechlorinate PCE to Ethene, a much less toxic substance [176] [178]. Depending on the bacteria in question, dechlorination may be either energy-producing or a secondary co-metabolic process occurring during methanogenesis [159]. Although naturally existing bacterial communities degrade chlorinated solvents [238] [163] they often proceed at a relatively slow rate motivating research into the addition of key nutrients to enhance this process. The injection of these auxiliary nutrients requires an accurate characterization of the contaminated region since feedstock distribution can depend on subtle variations in permeability. A second approach to bioremediation attempts to change dissolved oxygen levels at depth to allow aerobic bacteria opportunity to degrade solvents [102] [103]. All of the above mentioned remediation techniques can be made more effective and less expensive if accurate knowledge of the size and shape of the contaminant source body as well as the general lithological framework are known. The design of optimal injection wells for enhanced bioremediation activities, the planning of hydraulic barriers, and the efficient use of co-solvents floods are but three aspects of the remediation process which might benefit from accurate geophysical characterization.

In summary, DNAPL contamination is a threat to ground water quality in many parts of the US and the detection, characterization, and remediation of such pollutants is a difficult problem with current techniques. We believe that non-invasive geophysical methods, specifically radar and high-resolution seismic methods might augment current characterization strategies by providing spatially detailed images of subsurface properties, including possible zones of high DNAPL saturation.

1.2 DNAPL Detection Using Geophysics : Previous Experiments

A wide variety of geophysical techniques have been used to assist in shallow environmental investigations. However, most methods lack the spatial resolution and/or sensitivity required for characterization of contaminant lenses or pools ; the largest DNAPL zones reported by Parker *et al.* [213] in sandy aquifers were on the order of 15 cm thick, a relatively thin target by geophysical standards. For a fluid contaminant to be detectable using any sensing technique, the contaminant must have different physical properties than the background saturating fluid, in our case water. As shown in table 1.1, DNAPLs differ from water in several key physical properties [2] which may facilitate remote geophysical detection. Densities for the listed DNAPLs range from 1267 kg/m^3 (1,2-dichloroethane) to 1623 kg/m^3 (tetrachloroethylene). All are effectively non-polar with dielectric constants between 2.2 and 10.9 in contrast to water with a dielectric constant of 80. Of the DNAPLs discussed, all also have P-wave velocities lower than water, with the slowest being carbon tetrachloride ($V_p = 939$ m/s) and the fastest being 1,2-dichloroethane ($V_p = 1217$ m/s). DNAPLs also exhibit lower conductivities than groundwater in most cases; this fluid attribute has motivated several experiments using resistivity methods for detecting and monitoring NAPLs.

In light of these differences, ground penetrating radar and high-resolution borehole seismic methods are two techniques which might possess sufficient resolution and sensitivity to detect DNAPLs *in situ* when appropriate source frequencies and source/receiver geometries are used. When combined, they may also provide enough information to distinguish DNAPL contaminated regions from background variations in soil properties. In the remainder of this section we examine existing data relevant to the acoustic and dielectric signatures of DNAPL contamination on the core, physical model, and field scale. In all three sections we include selected experiments examining LNAPL contamination due to the small number of studies which specifically target DNAPLs. We also briefly mention electrical resistance tomography (ERT), another method suggested for NAPL detection.

---

[2] A comprehensive review of DNAPL properties is available in chapter 4

1.2.1 Laboratory Measurements

Several experimental and theoretical works have examined the impact of NAPL saturation on the bulk electromagnetic and acoustic properties of rocks and soils. However, few experiments have specifically examined the properties of granular materials saturated with dense NAPLs [231] [111] [10]. Because of this gap in the literature, we also include experiments where the effects of LNAPL saturation are considered. LNAPLs, like DNAPLs, have both lower dielectric constants and P-wave velocities than water as can be seen for toluene and benzene in table 1.1. All measurements made to date have shown that the replacement of water with a NAPL fluid phase decreases both bulk dielectric constant and P-wave velocity and increases P-wave attenuation. Generally, bulk dielectric properties have been shown to be more sensitive to DNAPL saturation than seismic properties. More comprehensive literature surveys are available in chapters 5 and 6 for dielectric and acoustic properties respectively.

Between 1986 and 2004, at least seven experiments known to the authors have examined the dielectric properties of granular materials partially saturated with NAPLs, the most relevant of which we will mention now leaving the remainder for the larger literature discussion in chapter 5. Porokhovoi *et al.* [217] made frequency domain dielectric measurements (200 MHz - 1.2 GHz) on synthetic sand/clay mixtures (77/23%) using benzene, heptane, xylene, acetone, and toluene as saturating contaminants. Contaminant fractions of between 1.15% and 13.8% by weight. Their results were difficult to quantitatively interpret in terms of fluid effects due to the limited number of saturation levels examined (3) and the lack of experiments involving clean sand samples. Santamarina and Fam [231] measured the complex dielectric permittivity of soil/pollutant mixtures, using benzene, xylene, toluene, tetrachloroethylene (TCE), trichloroethylene (PCE), and chlorobenzene as organic pollutants. Kaolinite and bentonite clays were used to as the porous background material. Although significant changes in dielectric properties were noted in both clays after injection of TCE, the relationship between complex permittivity and TCE saturation was again difficult to quantitatively determined. Persson and Berndtsson [215] investigated the dielectric properties of synthetic soils partially saturated with sun-flower seed oil (SFSO) using the time domain reflectometry method. They used the Lichtnecker-Roth mixing model with a saturation dependent geometry coefficient to fit their dataset. Fransisca and Rinaldi [99] performed frequency domain dielectric measurements (20 MHz - 1.3 GHz) on silica sand, kaolinite, and loess samples partially saturated with paraffin and lubricant oils. They conclude that both the CRIM and self-similar effective medium models provide adequate prediction of the effects of NAPL saturation on bulk dielectric constants. Ajo-Franklin *et al.* [10] used a coaxial TDR cell to examine the dielectric properties of both synthetic and natural aquifer samples when saturated with mixtures of water and TCE. This experiment, designed to quantify the radar signature of DNAPLs at the Pinellas site, will be discussed in chapter 5.

The acoustic properties of NAPL saturated granular media have not been heavily investigated; however, a small but growing body of experimental results exist for synthetic systems (glass beads), clean sands, and natural aquifer cores at low pressures. All laboratory experiments to date have shown that NAPL saturation reduces P-wave velocity and increases P-wave attenuation at frequencies between 500 and 1000 kHz. Geller and Myer [111] investigated the relationship between NAPL saturation, P-wave velocity, and attenuation using 1,1,2-trichloro-1,2,2-trifluro-ethane (freon 113), n-dodecane, and iso-octane as model contaminants. They made measurements on medium sub-rounded quartz sand samples (212-250 microns) with porosities of 42% at effective pressures of 140 kPa. Measurements examining both NAPL injection into water saturated samples and purely NAPL saturated samples were made using an ultrasonic pulse transmission system operating at central frequency of 500 kHz. Seifert [234] [236] performed a similar set of measurements with a focus on varying fluid viscosity and wetting properties. P-wave velocity and attenuation were measured while saturating with two different grades of silicone oil (10 and 100 cs), castor oil, and n-dodecane. Our investigation (Geller, Ajo-Franklin, and Majer [108]) examined the effects of toluene and trichloroethylene saturation on ultrasonic P-wave velocity and attenuation for a set of natural aquifer samples from the former DOE Pinellas site [112] [11]. Samples with a variety of textures ranging from clean sands to clayey silty sands were tested with porosities ranging from 37% to 46% percent. These experiments will be discussed in more detail in chapter 6.

1.2.2 Mesoscale Experiments

Mesoscale or physical model experiments provide an excellent environment for controlled geophysical measurements a step beyond core-scale investigations. While mesoscale models can seldom capture the complexity present at a field site, they allow the testing of imaging methods in a situation where NAPL source distribution can be directly measured. We will focus on existing radar and seismic experiments although several DNAPL measurements using ERT methods have also been performed [59]. The trends observed in these mesoscale experiments are in agreement with those measured in smaller core scale measurements; both dielectric constant and P-wave velocity were found to decrease with increasing NAPL saturation.

Two mesoscale radar experiments known to the authors have targeted DNAPLs. Johnson and Poeter [132] constructed a 0.31 x 0.42 x 0.82 m (H/W/L) tank and used a 1.5 GHz GSSI SIR-10A to image a descending hydrofluoroether injection over time. DNAPL saturations were confirmed using sequential vertical cores and compared to the results of 1-D waveform inversion. The inversion strategies applied were limited by the S/R geometry since only 2D monostatic surface lines with a single antenna polarization were acquired. Bradford [41] acquired a comprehensive set of radar measurements monitoring the infiltration of a dense mixture of carbon tetrachloride and PCE within a 1.07 x 1.22 m (H/D) cylindrical tank. In this experiment 3D surface GPR data (32 fold) were acquired with two antenna polarizations in addition to borehole transmission and TDR measurements. Although the analysis of these results is not yet complete, the dataset will provide an excellent test of radar AVO/AVA techniques applied to DNAPL detection.

Several other mesoscale radar measurements have examined the related problem of LNAPL monitoring and detection. An interesting physical model experiment using LNAPLs was executed by Lane et al. [157] who measured the reflectivity of a large aperture fracture at 500 MHz during the injection of light hydrocarbons. Kim *et al.* [142] performed another mesoscale LNAPL monitoring experiment using surface reflection GPR to image a controlled 219 L gasoline spill within a cylindrical sand-filled tank. By varying the water table depth and consequently the vertical location of the pooled gasoline, they were able to isolate the radar signature of residual LNAPL saturation. Hagrey [16] acquired surface reflection GPR data (1.5 GHz) over a toluene injection in a quasi-2D rectangular sand tank measuring 0.83 x 0.095 x 0.61 m. He observed both an increases in apparent velocity and amplitude variations once the toluene infiltrated regions of high water saturation. A reduction in radar attenuation was also measured in the toluene contaminated zones and was attributed to the displacement of conductive pore water by the more resistive LNAPL.

Mesoscale experiments investigating the seismic signatures of LNAPL and DNAPL contamination at low pressures have also been performed. A series of physical model (0.61 m tank) experiments were conducted by Kowalsky et. al. [146]. In this experiment, n-dodecane, an LNAPL, was injected into a homogeneous sandpack maintained at a confining pressure of 140 kPa. Acoustic waveforms were acquired using a miniature accelerometer array and bar piezoelectric source operating at a frequency of 60 kHz. The resulting dataset was processed using a 2D straight-ray tomographic algorithm. The velocity decrease due to n-dodecane saturation appeared to be only 2% for the rays of maximum delay. However, amplitude anomalies of up to 65% were observed along high delay paths. A similar experiment performed by Geller *et al.* [109] used the same apparatus operating at 90 kHz to image a lens of n-dodecane pooled at a capillary barrier. They observed reductions in amplitude and an increase in traveltimes for rays traveling through the NAPL zone. Subsequent asymptotic waveform tomography performed by Keers *et al.*[138] revealed peak velocity reductions on the order of 2.5 %.

1.2.3 NAPL Detection And Characterization In The Field

A number of scientists have attempted to use geophysical methods for the characterization and monitoring of NAPLs in the field. These attempts can be divided into four investigation strategies, each requiring differing levels of measurement sophistication and optimism on the part of the investigator.

Direct Detection Direct detection, the process of locating NAPLs *in situ* using remote non-invasive techniques, has been the long-term goal of many in the environmental geophysics community. While offering the greatest possible benefits, this research direction has also presented the greatest technical challenges. The detection problem requires a technique which has high sensitivity to DNAPL saturation, high enough spatial resolution to provide useful guidance for site remediation, and the ability to discriminate between DNAPLs and natural variation in lithology and pore water chemistry. (DNAPLs [3] [250]) (LNAPLs [70] [209] [40] [24] [25])

Characterization If the existence and location of a large DNAPL body is already known, as is the case at several DOE sites, geophysics might be applied to build a more accurate spatial model of the contaminated region. This process of characterization is simpler than direct detection since the goal is to map zones which have been identified *a priori.*

Monitoring In many cases geophysics is most useful in a monitoring capacity, either for mapping the downward progression of DNAPLs or for building combined spatio-temporal models of remediation activities. The problem of discrimination is eliminated since only property perturbations are of interest. (DNAPLs [224] [44] [116] [43] [208] [230] [204]) (LNAPLs [177] [158])

NAPL-oriented Hydrogeophysics This class of techniques does not attempt to directly image NAPLs but focuses on mapping subsurface features relevant to NAPL accumulation and contaminant flow processes. An important goal of this research focus is the effective incorporation of geophysical data into the creation of hydrogeologic models used for predicting multiphase flow and contaminant transport. (DNAPLs [76] [68] [69] [250])

Since the literature documenting field-scale DNAPL detection trials is relatively small, we will again include descriptions of relevant monitoring and characterization experiments as well as measurements conducted on LNAPL sites. As mentioned previously, we focus on GPR and seismic methods, the two techniques used in our field investigations.

Although no field test has demonstrated the direct detection of DNAPLs using GPR, several experiments have successfully monitored controlled injections. The most well known experiments investigating the application of geophysical techniques to imaging DNAPLs were carried out by the Solvents-In-Groundwater program [224], a consortium of industrial and academic institutions led by researchers from the University of Waterloo and the USGS. This group performed a series of controlled DNAPL spills at Canada's Borden Airforce Base which were monitored using a large array of geophysical techniques. Each experiment involved the controlled release of PCE into a section of ground bounded by a containment structure. The two primary cells were 3 x 3 x 3.5 m and 9 x 9 x 3.3 m with PCE injection volumes of 231 and 770 liters respectively. The cells were monitored regularly using radar, Time-Domain Reflectometry (TDR), resistivity and neutron logging. From a monitoring perspective, the reflection radar datasets, were very successful, tracking the migration of the PCE volume through a series of pools at depth [43] [116] [44]. The surface radar datasets were acquired in a 3-D common-offset geometry, at 200 MHz and 500 MHz. The borehole transmission radar (160 MHz) data exhibited some amplitude changes after the PCE injection, due to waveguide effects within thin saturated strata, but could not resolve the spatial characteristics of the spill [208] [230]. Figure 1.3 shows two 200 MHz migrated radar sections collected during the 770 L spill documented by Brewster *et al.* [43]. Panel A is the background profile while panel B is the same profile 984 hours after the controlled PCE release. Several DNAPL pools are visible as radar reflections and some amount of pull-up on the aquitard reflector is visible, indicative of an increase in radar transmission velocities. While the Borden experiments demonstrated the effectiveness of radar in a monitoring capacity, the ambiguity of reflector interpretation suggests that static detection or

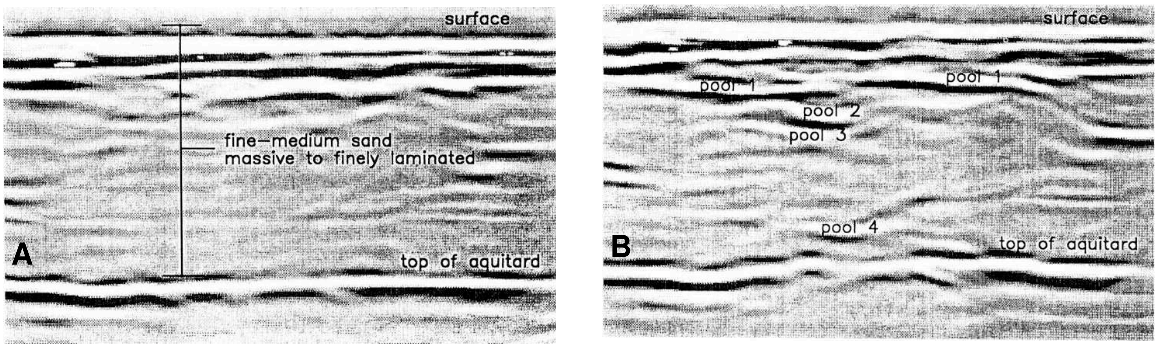

Figure 1.3: Two GPR surface profiles from the Borden Experiment : These profiles are the 200 MHz E5 lines presented in Brewster *et al.* [43]. Panel A is the background radar profile while panel B is the same profile 984 hours after a controlled release of 770 L of PCE. Visible in panel B are several reflectors corresponding to PCE pools at depth. A pull-up in the aquitard reflection is also indicative of PCE saturation in the overlying strata.

characterization of PCE using surface radar would be extremely difficult assuming traditional survey techniques. In terms of the requirements for direct detection discussed previously, GPR proved to have the requisite sensitivity and resolution to image DNAPLs but lacked sufficient discrimination to identify DNAPLs in uncontrolled environments.

A larger number of field trials have targeted LNAPL pools, partially because they often occur at shallower depths more accessible to surface based detection methods. Unfortunately, several factors make the results of LNAPL experiments difficult to apply to DNAPL detection. One difference is the strong biogeophysical signature of LNAPL degradation, typically regions of high conductivity, which overwhelm changes due to the actual LNAPLs [25] [272] [26]. These effects are dominant in the vadose zone where aerobic degradation pathways are operative but seem to be much less significant below the water table. A second factor is the very different contaminant distributions *in situ* with LNAPLs typically pooling above the water table instead of penetrating into the saturated zone and accumulating at permeability barriers. Orlando [209] conducted a 200 MHz surface GPR experiment over a zone with known LNAPL contamination and found that regions where the water-table reflection had high instantaneous amplitude correlated well with hydrocarbon accumulation. Bradford [40] conducted a series of surface GPR lines at Wurtsmith AFB and examined GPR AVO anomalies over a zone of NAPL free-product. Other experiments include radar measurements by Arcone *et al.* [24] over a zone of jet-fuel contamination, resistivity measurements made by Mazzella [177] above a controlled gasoline spill, and GPR experiments carried out by Daniels *et al.* [70] over two sites, both contaminated with diesel fuel.

One promising research direction for the direct detection of NAPLs using surface GPR is the application of amplitude variation with offset (AVO) and amplitude variation with azimuth (AVA) methods, processes which provide more information on the dielectric properties across reflectors. Recent work has examined the theoretical principles of GPR AVO/AVA applied to NAPL detection [133] [29], the field application of GPR AVO to LNAPL contaminated sites [40], a partial reprocessing of the Borden spill dataset incorporating AVO [134], and a controlled mesoscale AVO/AVA experiment examining a PCE/Carbon Tetrachloride pool [41]. However, even with successful AVO/AVA processing, it is unclear whether the DNAPL discrimination problem will be solved since the dielectric information gained by such inversions could still be replicated solely by changes in lithology.

Surface seismic methods have yielded mixed results in the domain of direct detection but have been relatively successful in mapping subsurface features relevant to understanding DNAPL flow, particularly aquitard and bedrock contacts. Temples *et al.* [250] applied AVO processing techniques to a 3D surface dataset acquired at the DOE's Hanford Site (200 West Area) and isolated an anomaly they believe was linked to a large carbon tetrachloride pool. Dana *et al.* [76] [68] [69] have applied high-resolution 3D surface seismic methods to map a subsurface paleochannel within which DNAPLs were thought to accumulate. This experiment, carried out at Hill Air Force Base in Ogden, Utah, used 610 independent single-channel recording systems and a .223 caliber rifle source to acquire 1.8×10^9 traces over a 95 x 37 m zone with a maximum usable frequency of 440 Hz. The ultimate limitation of surface seismic methods seems to be spatial resolution; with central frequencies seldom greater than 400 Hz, we would expect wavelengths in the saturated zone to be between 4 and 7 m, over an order of magnitude larger than the thickest DNAPL pool detected in Parker *et al.*'s investigation [213]. No field experiments to date have attempted to use higher resolution cross-well seismic measurements for the direct imaging of NAPLs although it was considered and rejected by Ellefsen *et al.* [91] based on simple resolution estimates.

Crosswell seismic and crosswell radar transmission methods have the potential for generating quantitative images of V_p and dielectric constant with vertical spatial resolutions on the order of 20 cm in near-surface environments conducive to these measurements, close to that required for the *in situ* detection of DNAPL lenses. Joint crosswell GPR and seismic field experiments at the contaminated TAN site at the Idaho National Engineering Lab [67] [259] and the DOE Hanford reservation [170] have demonstrated resolutions close to these levels. Given the difficulties in uniquely identifying DNAPLs, use of multiple geophysical techniques may offer an alternative approach capable of directly detecting dense contaminants. The combination of both seismic and radar techniques might also provide enough complementary information to identify DNAPLs even in the presence of variations in lithology. Seismic measurements, while less sensitive to DNAPL saturation, could provide secondary information on lithology and partial gas saturation.

Geophysics Applied To Remediation Monitoring

The remediation methods discussed in previous sections might also benefit from geophysical measurements in a monitoring capacity. Air stripping is particularly amenable to seismic imaging due to the large decrease in P-wave velocity induced by partial gas saturation. Elbring [90] used crosswell seismic transmission tomography to monitor gas flow in an air stripping remediation experiment by taking surveys before and after the initial injection period. Direct removal of DNAPLs via pumping results can change both the geometry and maximum saturation levels of contaminants allowing for direct geophysical monitoring of pumping progress [204]. Since many of the substrates used for enhanced bioremediation procedures are physically distinct from water, the remote monitoring of nutrient distribution is another potential area ripe for application of geophysical methods [158]. In addition to monitoring the distribution of nutrients, some methods might also be able to map regions of active biodegradation through the chemical and mineralogical changes generated by bacterial activity [25] [26].

Biogeophysics

Early investigations of NAPL contaminated sites often noted geophysical anomalies which could not be directly linked to the properties of contaminants; In particular, field measurements often indicated that the zones near regions of LNAPL contamination had high conductivities [25], a surprising result considering that the pure NAPL components had conductivities significantly lower than ground water. Further research revealed that many of these anomalous geophysical signatures were caused by biological activity linked to NAPL degradation and resulted in alteration of both pore fluid chemistry and grain surface properties [272] [26]. This area of research, now referred to as biogeophysics, seems to hold potential for both understanding the geophysical signatures of aging contaminant sites and for actively monitoring the progress of bioremediation. In addition to variations in electrical properties, column experiments have observed seismic attenuation signatures generated by biogenic gas production [276] and possibly sulfide precipitation [277].

1.3 Goals And Thesis Structure

In this dissertation, we attempt to evaluate the suitability of high resolution crosswell seismic and radar measurements for the detection of DNAPL contamination *in situ* using a combination of experimental petrophysics and a detailed geophysical investigation of the Pinellas DOE facility's Northeast site. Our analysis can be partitioned into three conceptual units, a description of the site and the primary field experiments (chapter 2 and 3), a comprehensive investigation of the petrophysics of DNAPL saturated sediments (chapters 4, 5, and 6), and an integrated inversion and interpretation of our field datasets using a novel tomographic imaging strategy (chapters 7, 8, and 9).

- Chapter 2 describes the history of the Pinellas DOE facility from its construction in 1956 to the present. We outline the sequence of characterization and remediation activities carried out at the Pinellas Northeast (NE) site and provide a geologic framework for understanding subsurface contamination.

- Chapter 3 details the collaborative field effort with Lawrence Berkeley National Laboratory which yielded the Pinellas geophysical dataset. We provide a chronology for our site investigation activities including well emplacement, coring, and three stages of geophysical measurements. The design and execution of our crosswell seismic and radar surveys are discussed as is the acquisition of several VSP surveys and our suite of well logs. A final analysis of our calibrated gamma logs provides some basic insight into site structure.

- Chapter 4 investigates the physical properties of pure DNAPLs with a focus on physical parameters with relevance to the geophysical detection problem. The density, P-wave velocity, and dielectric constant of theses fluids will be discussed in detail including issues of temperature and pressure dependence. Several simple models describing the properties of contaminant mixtures are developed and applied to datasets existing in the literature. The chapter ends by providing geophysical property estimates for the mixed DNAPL phase collected at Pinellas using sample compositional data.

- Chapter 5 examines the dielectric properties of granular materials partially saturated with DNAPLs. We place radar-based DNAPL detection on a firm petrophysical footing by performing some of the first high frequency dielectric measurements of aquifer sediments partially saturated with TCE. Using the results of our solvent injection experiments, we confirm the applicability of the Bruggeman-Hanai-Sen (BHS) and complex refractive index (CRIM) models for the prediction of the bulk dielectric constant of DNAPL contaminated soils. These models are then applied to the site-specific DNAPL property estimates developed in chapter 4 to yield the likely radar signature of a DNAPL zone at the Pinellas NE site.

- Chapter 6 parallels chapter 5 by examining the acoustic properties of aquifer materials partially saturated with DNAPLs. We present the results of several ultrasonic transmission experiments carried out on the core acquired at the Pinellas NE site and analyze the results in terms of Biot-Gassmann theory. An empirical model for the seismic signature of NAPL saturation is also developed using a property database including all measurements known to the authors. Both models are then applied to the site-specific DNAPL property estimates developed in chapter 4 to yield the likely seismic signature of a DNAPL zone at the Pinellas NE site.

- Chapter 7 combines the dielectric and acoustic models developed in chapters 5 and 6 to estimated the joint radar/seismic signature of DNAPLs at Pinellas. Property cross-plots are used to examine petrophysical non-uniqueness problems in DNAPL identification and P-wave attenuation is added to our joint model to discriminate between partial DNAPL and partial gas saturation. After performing a series of synthetic sensitivity tests we explore some possible approaches to combining seismic and radar datasets and document the barriers to full data fusion.

- Chapter 8 details our development of an adaptive tomographic imaging algorithm designed to flexibly accommodate zones of irregular ray coverage. Our technique, based on greedy mesh refinement, guarantees that the resulting inverse problem will fulfill *a priori* resolution constraints. We improve on previously developed algorithms through the use of a new heuristic point updating scheme which results in higher quality meshes. Our approach is compared to traditional tomographic algorithms using regular meshes and verified on a complex synthetic model. Our final demonstration simultaneously inverts 7 sequential crosswell seismic surveys acquired at the Pinellas NE site.

- Chapter 9 describes the application of the tomographic algorithms developed in chapter 8 to the full Pinellas crosswell dataset, a total of 11 seismic and 7 radar profiles. The crosswell tomograms are qualitatively integrated with logs and interpreted to yield a detailed cross-section of site geology. Several regions of high radar velocity and high seismic attenuation are identified and the dielectric models developed in chapter 5 are applied to provide insight into possible source phenomenon. Although porosity, partial DNAPL saturation, or partial gas saturation could explain the observed dielectric anomalies, combined interpretation of the radar and seismic datasets suggest that a gas mechanism is the most plausible explanation. We then develop a consistent site model based on the gas hypothesis and discuss some possible sources for partial gas saturation at shallow depths including depressurization effects and biogenic methane generation.

- We conclude with a retrospective analysis of the Pinellas experiment and examine possible future roles for geophysics in both DNAPL detection and the more general problem of environmental site characterization.

Chapter 2

The Pinellas DOE Facility History And Hazards

The Pinellas DOE facility was built during the heart of the Cold War (1956-1957) for the purpose of manufacturing neutron generators, a key component in modern nuclear weapons. Located north of St. Petersburg, Florida on the Pinellas peninsula, the Pinellas facility was operated under DOE contract by General Electric from 1956 to 1992. The legacy of DOE activities during this period are several regions of subsurface contamination, the two most significant being the Northeast (NE) site, which contains our geophysical study area, and the 4.5 acre site which is now privately owned. The NE site includes zones with dissolved contaminants and both dense and light NAPL phases. The dominant contaminants at the NE site are toluene, trichloroethylene, and methylene chloride with smaller quantities of cis-1-2-dichloroethylene and a large number of secondary organic compounds. Several phases of site characterization and remediation have been carried out since the first RCRA [1] environmental evaluation in 1987. Current efforts have focused on the use of steam enhanced extraction and thermal stripping techniques for remediation of the NE site NAPL contamination. In this chapter we will provide background information on the Pinellas facility [2] including site history, previous characterization and remediation efforts, and a simple geologic/hydrogeologic framework for understanding possible NAPL contamination scenarios. We will conclude with a discussion of the possible applications of geophysical methods to NAPL detection and lithology characterization at the NE site.

---

[1] RCRA, Resource Conservation and Recovery Act

[2] The historical material presented in this chapter is largely culled from DOE technical reports which may not be easy to obtain. Although references to the appropriate DOE documents are provided, requests for original documents should be sent to the Pinellas Site Manager, David S. Ingle, Pinellas Environmental Restoration Project 7887 Bryan Dairy Road, Suite 195, Largo, Florida 33777, 727-541-8943

2.1 The Pinellas DOE Facility : 1956-2003

The Pinellas DOE facility was constructed during 1956-1957 for the purpose of producing neutron generators and other specialized components for the US nuclear weapon program. The 99 acre site is located on the Pinellas peninsula, 6 miles north of St.Petersburg, Florida and approximately 20 miles west of Tampa. Figure 2.1 shows the location of the greater Tampa/St.Petersburg metro area in panel (A) and the location of the site on the peninsula in panel (B). Figure 2.2 shows the Pinellas facility, dominated by building 100 which housed both the technical and administrative arms of the Pinellas facility. From 1956 to 1992 the Pinellas plant was managed by General Electric's Neutron Device division under contract with the DOE's Albuquerque office. In 1992, GE ended its management role at Pinellas [205] and the DOE re-contracted the plant to Lockheed Martin Specialty Components. Between 1994 and 1997 the Pinellas plant was incrementally closed with capabilities being transferred to other DOE facilities. In 1995, the site was sold to the Pinellas County Industrial Council (PCIC) and transformed into an office park and technology incubator, the Rainey-Young "Science, Technology, and Research" (STAR) center. By 1999, the PCIC had dissolved and the STAR center became the property of the Pinellas County government [7]. After plant closure, all work on neutron generator production was shifted to Sandia National Laboratory [107] with secondary production capabilities transferred to the DOE's Kansas City Plant [2]. As part of the land sales contract, the DOE assumed all responsibility for cleaning up contaminated regions and restoring ground water quality to within federal guidelines. Originally, site expenditures for environmental restoration were predicted to range from 3 to 4.7 million dollars annually for the years 1996-2000 with an estimated life-cycle cost of 45 million dollars [2]. Annual budgets are still within this range, with environmental management allocations for Pinellas during fiscal year 2001 at 3.9 million dollars.

During the Pinellas plant's lifetime, neutron generators, a key component for initiating fission in nuclear devices, was the primary product [3]. Construction of neutron generators requires both exotic materials such as molybdenum, scandium, high purity alumina ceramics, and tritium and specialized manufacturing facilities capable of handling metal plating, ceramic-to-metal bonding, and ultrahigh vacuum fabrication. Secondary components manufactured at Pinellas include radioisotopically powered thermoelectric generators, specialty capacitors, crystal resonators, and other mechanical and electronic components not available through public channels. Such manufacturing tasks involved the production of significant volumes of of both radioactive and non-radioactive waste. We will concern ourselves primarily with organic industrial wastes including chlorinated solvents although other contaminants such as tritium and heavy metals have also been a concern at Pinellas.

Like many DOE sites, waste disposal at Pinellas between 1957 and 1979 were informal and poorly documented activities, often involving the burying of drums or the sinking of contaminated objects in one of several on-site ponds[4]. In 1988, the EPA identified 14 regions at Pinellas with potential

---

[3] Appendix A details the design and use of neutron generators

[4] RCRA investigators documented a case where plant workers disposed of lumber contaminated with tritium and sulfuric acid by attaching buckets of concrete to the boards and sinking them in the site's West Pond.

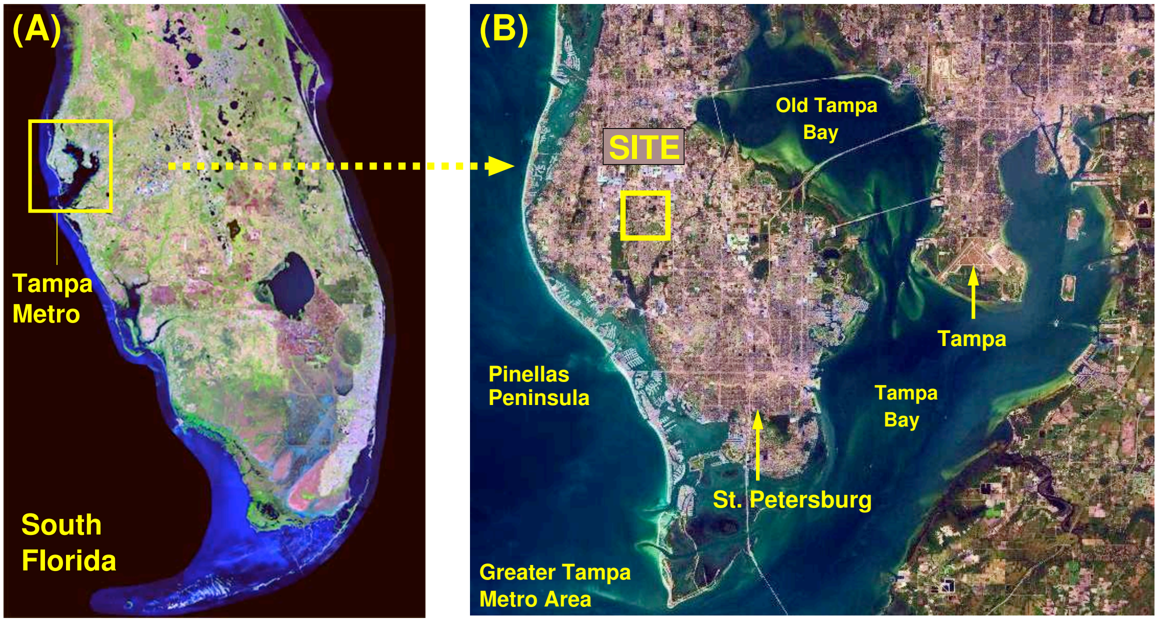

Figure 2.1: Regional and local maps of Pinellas, Florida : Panel (A) shows a satellite image of Florida with an inset for the Tampa/St. Petersburg metro area. Panel (B) shows the metro region with the vicinity of the Pinellas facility marked.

contamination [1], referred to as Solid Waste Management Units (SWMU). Panel A of figure 2.2 shows both these original SWMUs and units added at later phases of the site investigation. We will focus on the Northeast (NE) site which contains the region of our geophysical investigation. While we will make repeated reference to this geophysical study area, a description of how we selected the region and the well locations will be delayed until the following chapter. Figure 2.2 shows the relative location of the NE site within the Pinellas facility while figure 2.3 is a labeled closeup including the geophysical study region. The NE site includes the East Pond and is bounded by Belcher Rd. on the east, parking lots on the south and west, and the Pinellas perimeter fence on the north. Figure 2.3 also shows a panoramic photo of surface condition at the NE site as of 2002, now essentially a level field with a large number of emplaced monitoring and recovery wells. The East Pond was excavated in 1968 within a naturally swampy area and was subsequently deepened in 1972 to expand storage capacity to approximately 3.25 million gallons. Interest in the NE site originated from reports of an undocumented solvent storage and disposal area immediately to the west of what is now the East Pond, last actively used during the early 1970s. Although all drums and waste products were to have been removed by contractors at the time of the pond's construction, three drums containing debris and rebar were found near the pond in 1984. An investigation of the Northeast site was then carried out collaboratively with the USGS [172] consisting of an electromagnetic survey, trenching, soil sampling, and the emplacement of monitoring wells. Some contaminants were detected in sediment samples from the East Pond including insecticides (DDD,DDE), polychlorinated biphenyls (PCB), and several organic coal tar components (eg. anthracene, chrysene, pyrene, benzo(a)pyrene).

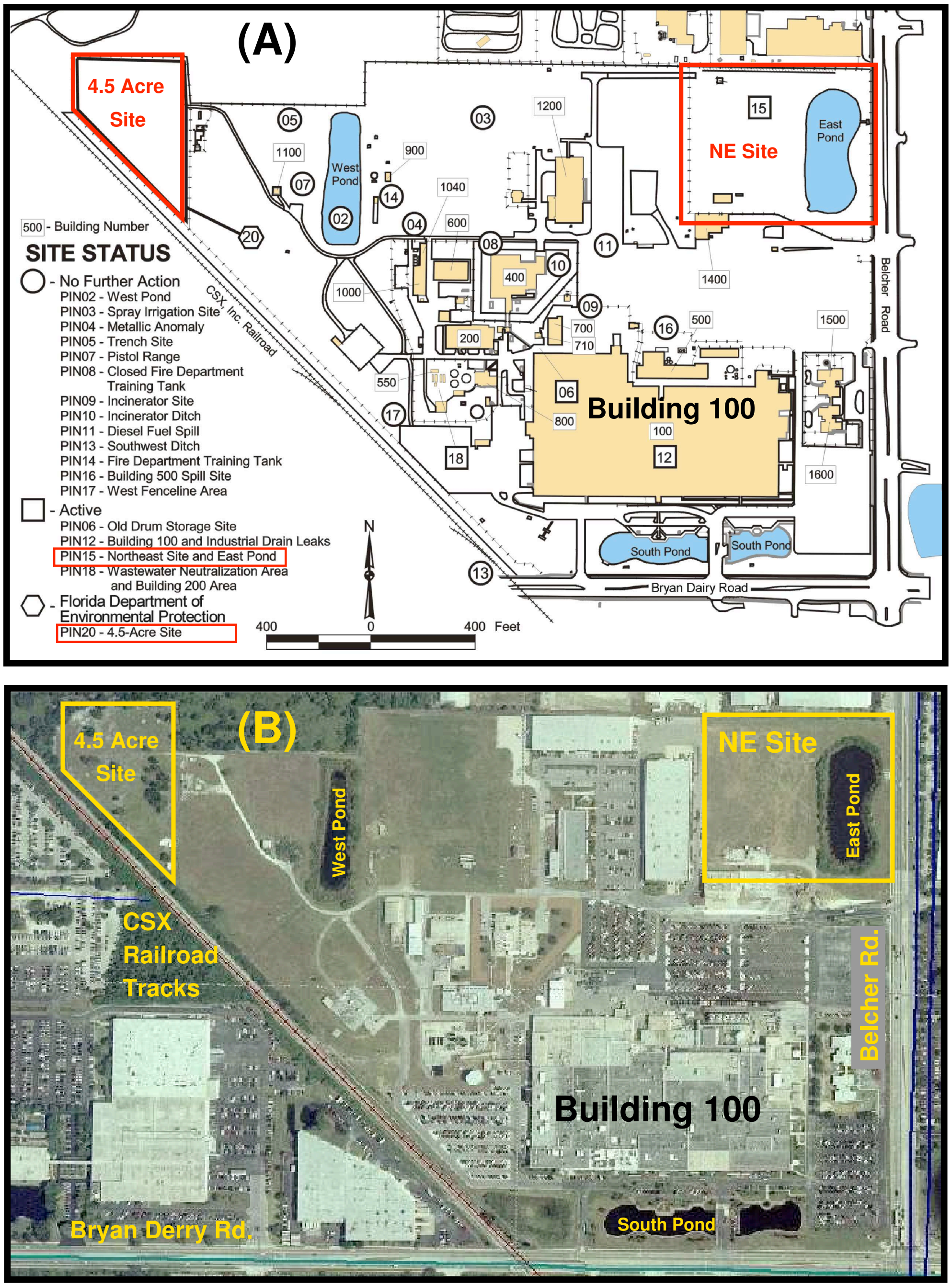

Figure 2.2: Current and historical contaminated regions at the Pinellas facility : Panel A is a map of the solid waster management units (SWMU) delineated during site investigations. Of the active units, the two most relevant are the NE site (location of geophysics study area) and the 4.5 acre site. This map is a modified version of one presented in the DOE 2002 Environmental Restoration Activities white paper [6] Panel B shows an aerial photograph of the facility in the mid 1990's with the NE and 4.5 acre sites highlighted in yellow.

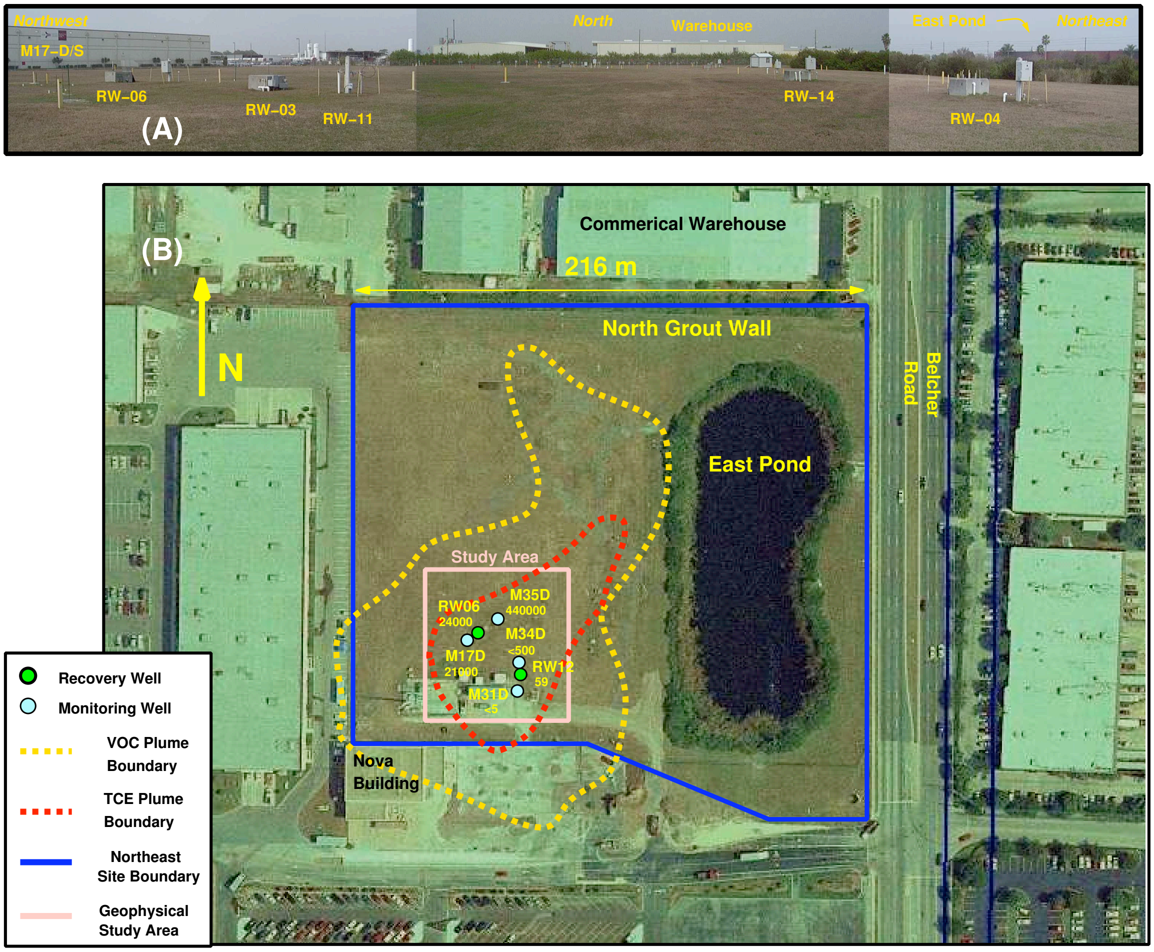

Figure 2.3: NE site aerial and panoramic photography : Panel (A) is a composite of 3 photographs looking north, showing site conditions as of 2002. Panel (B) is a 1 m. resolution aerial photo of the NE site. The geophysical study area, the TCE plume and the combined VOC plume are superimposed in addition to several monitoring and recovery wells. TCE concentrations are shown below their respective well labels in $\mu g/L$.

A second groundwater investigation carried out during the RCRA facility assessment [1] uncovered high levels of several volatile organic compounds (VOCs) at the NE site including methylene chloride, trichloroethylene, dichloroethene, vinyl chloride, and benzene. Figure 2.3 shows the lateral extent of the TCE plume (red) at the NE site as estimated from aqueous contaminant levels. The gold boundary in the same figure delineates the zone where VOCs are detectable above the EPA MCL. Several subsequent remediation programs were implemented including pump-and-treat plume containment, large scale excavation, enhanced anaerobic bioremediation, steam auger treatment, and electro-thermal dynamic stripping, all of which will be discussed in a later section on site remediation projects. A key discovery was made in 1995 when 241 drums containing solvents, resins, and scrap components were excavated from two regions of the site. NAPLs were not observed at the Northeast site until 1998 when inspection of a monitoring well revealed an oily substance coating a sampling device. This evidence prompted a more comprehensive sampling regime in 1999 and 2000 which recovered 6 gallons of NAPLs from well RW-06 and additional samples from well RW-03. Traces of NAPLs were observed in wells 533-15, RW-10, RW-11, M35D, and M17D. Figure 4.5 shows a fluid sample from well RW-06 with distinct light and dense non-aqueous phases. Gas Chromatography/ Mass Spectrometry (GCMS) measurements revealed that the RW06 DNAPL sample was a complex mixture including large amounts of toluene and trichloroethylene with smaller quantities of cis-1-2-dichloroethylene, methylene chloride and PCE. Semi-volatile compounds detected included the pesticide 4,4'-DDD, butyl benzyl phthalate, dimethyl phthalate, and phenol. Considering the proximity of RW-06 to our zone of geophysical investigation, we will examine the components of the RW-06 NAPL sample in greater detail in chapter 4.

In the same time frame, almost 100 soil borings were obtained as part of an effort to map the spatial distribution of NAPLs at the site. Porewater was extracted from selected core samples and analyzed with an on-site GC system to determine dissolved contaminant levels. Using site calibration data and literature relationships linking dissolved concentrations, aqueous solubility, and the presence of free-phase contaminants, the DOE generated a map of likely regions of NAPL contamination [4]. Based on their calculations, any dissolved TCE concentration greater than 20,400 $\mu g/kg$ corresponded to a region with a NAPL phase containing TCE. By this metric, borings SB-42, SB-44, SB-59, SB-62, SB-67, SB-88, and S-108 are all possibly within zones of free-phase TCE contamination. Figure 2.3 shows the recovery and monitoring wells at the NE site near the geophysical study region with more recent (April 2002) dissolved TCE levels. Figure 2.5 shows an enlargement of the geophysical study region with the wells exhibiting visible evidence of NAPL contamination circled in red. Borings with evidence of NAPLs from dissolved contaminant levels are circled in blue.

2.2 Site Geologic/Hydrologic Framework

The hydrologic/lithologic profile at the Pinellas DOE site can be roughly divided into three units, a sandy surficial aquifer, a clayey confining layer referred to as the Hawthorn group, and a deeper limestone unit which forms the upper portion of the Floridian aquifer. Figure 2.6 shows a simplified

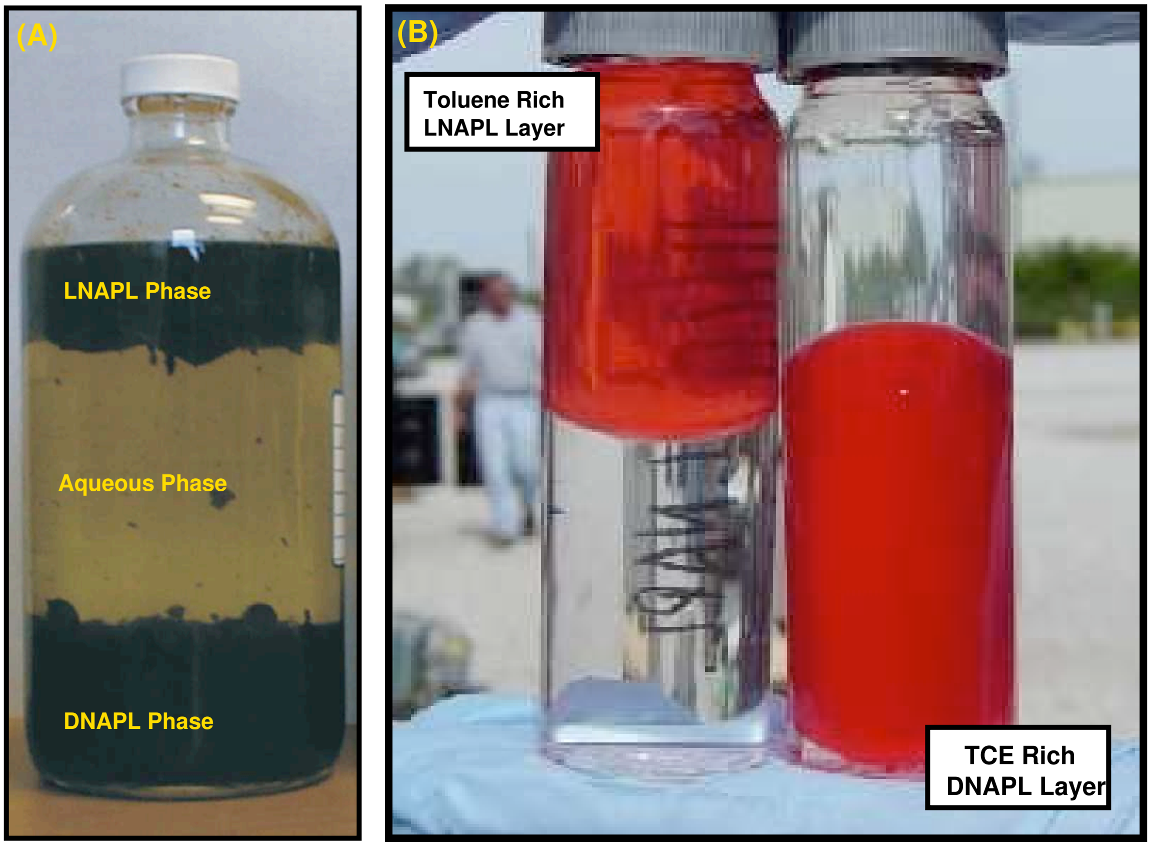

Figure 2.4: NAPL samples from the Pinellas NE site : Panel (A) shows a fluid sample from well RW-06; note the existence of both light and dense phases. Panel (B) shows dyed LNAPL/DNAPL samples from the northern part of the NE site (area A) extracted during remediation. Photograph (B) is from the *NE Site Area A NAPL Remediation Final Report* [9].

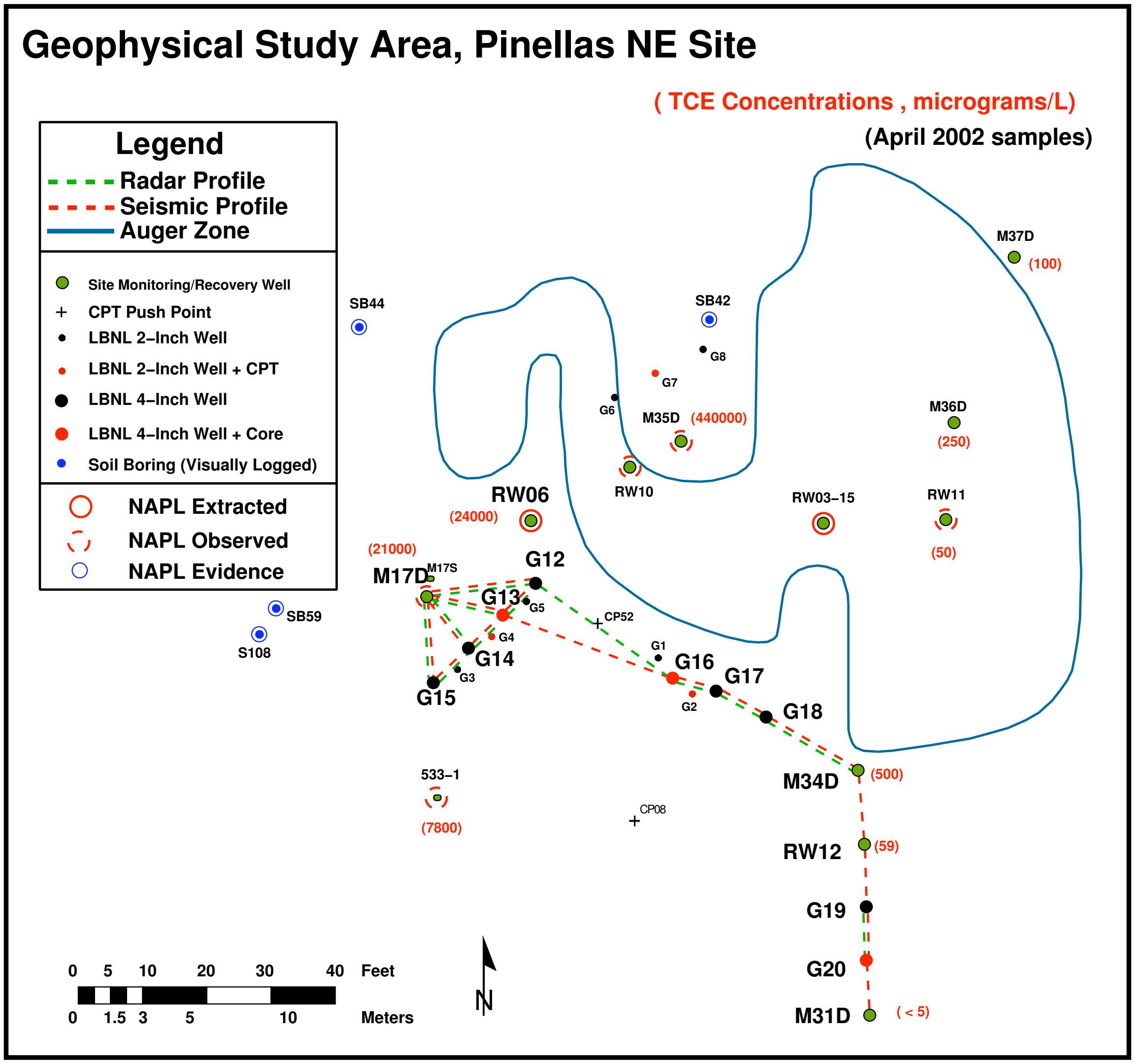

Figure 2.5: Geophysical study area map, Pinellas NE site : Note the dotted lines indicating crosswell profiles (discussed in the chapter 3) and the "camel" shaped region where steam auger remediation was carried out. Red circles around well locations indicated either directly sampled or visually observed NAPL contamination while blue circles are coring locations with NAPLs inferred from aqueous contaminant concentrations. Aqueous TCE concentrations are shown in red ($\mu g/L$).

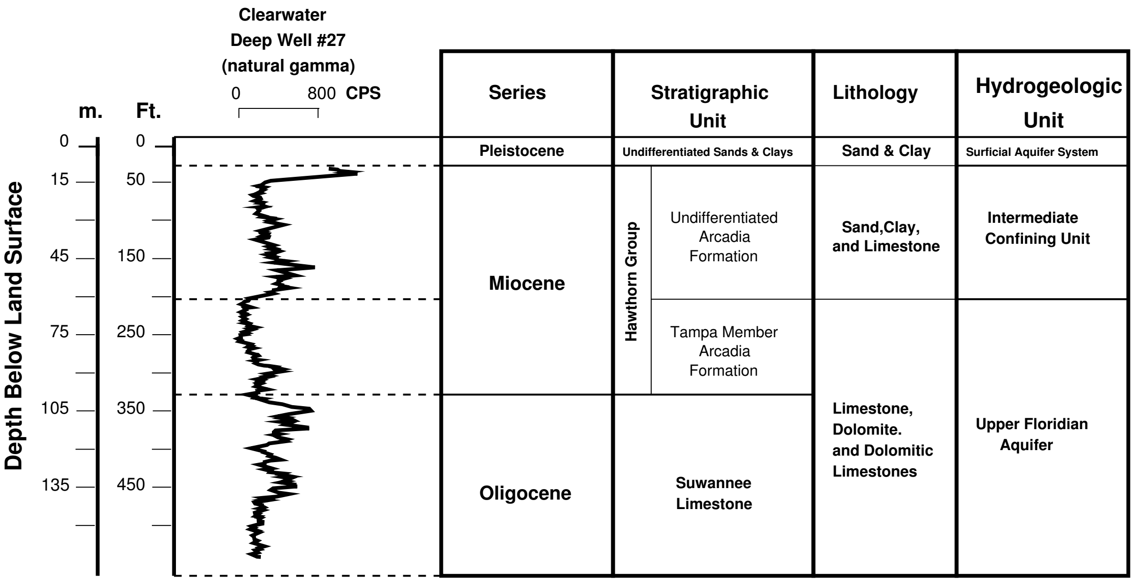

Figure 2.6: Deep stratigraphy/lithology of the Pinellas region : The gamma log on the far left if from a deep monitoring well approximately 4 miles from the Pinellas facility. This figure is a simplified version of the more complete stratigraphic column shown in Broska and Barnette [45]. (CPS = counts per second)

version of the stratigraphic diagram presented by Broska and Barnette [45] accompanied by gamma log data from a deep monitoring well approximately 4 miles from the Pinellas facility. We will again focus on data available for the Northeast site acquired by either the USGS [172] or the DOE [4]; both sources use visual analysis of soil borings and cone-penetrometry data for lithology constraints. A more complete analysis of lithology in the geophysical study region supported by our coring program and well-log suite will be presented in the following chapters.

The top veneer of soil at the Pinellas site is a combination of natural sediments of the Myakka and Wabasso soil units and fill material imported after waste excavation. The average surface elevation in the southern region of the NE site is approximately 5.45 m above sea-level. The water table occurs at an average depth of 2 m although changes due to both pumping and seasonal rainfall variations are common. The surficial aquifer unit is dominated by fine sands with variable amounts of silt and clay, typically not exceeding 10 % by mass. The surficial aquifer unit varies in thickness between 9 and 11 m below ground surface with gradual changes contact depth. Vertical hydraulic conductivities in the surficial aquifer vary with silt and clay content but based on measurements by Fernandez [172] are generally between 2.6×10^{-4} m/s and 3.6×10^{-5} m/s. The termination against the underlying clays of the Hawthorn group is gradational with increases in shell and clay content. Hard phosphate nodules of up to 5 cm in length have also been recovered from test borings in the surficial aquifer. The surficial aquifer is not generally used for the extraction of drinking water but is considered to be a resource with future potential [55] and is already used for irrigation and industrial applications. As of 1985, 132 wells between 4 and 10 cm in diameter were withdrawing water from the surficial aquifer less than 2700 m from the Pinellas plant [172].

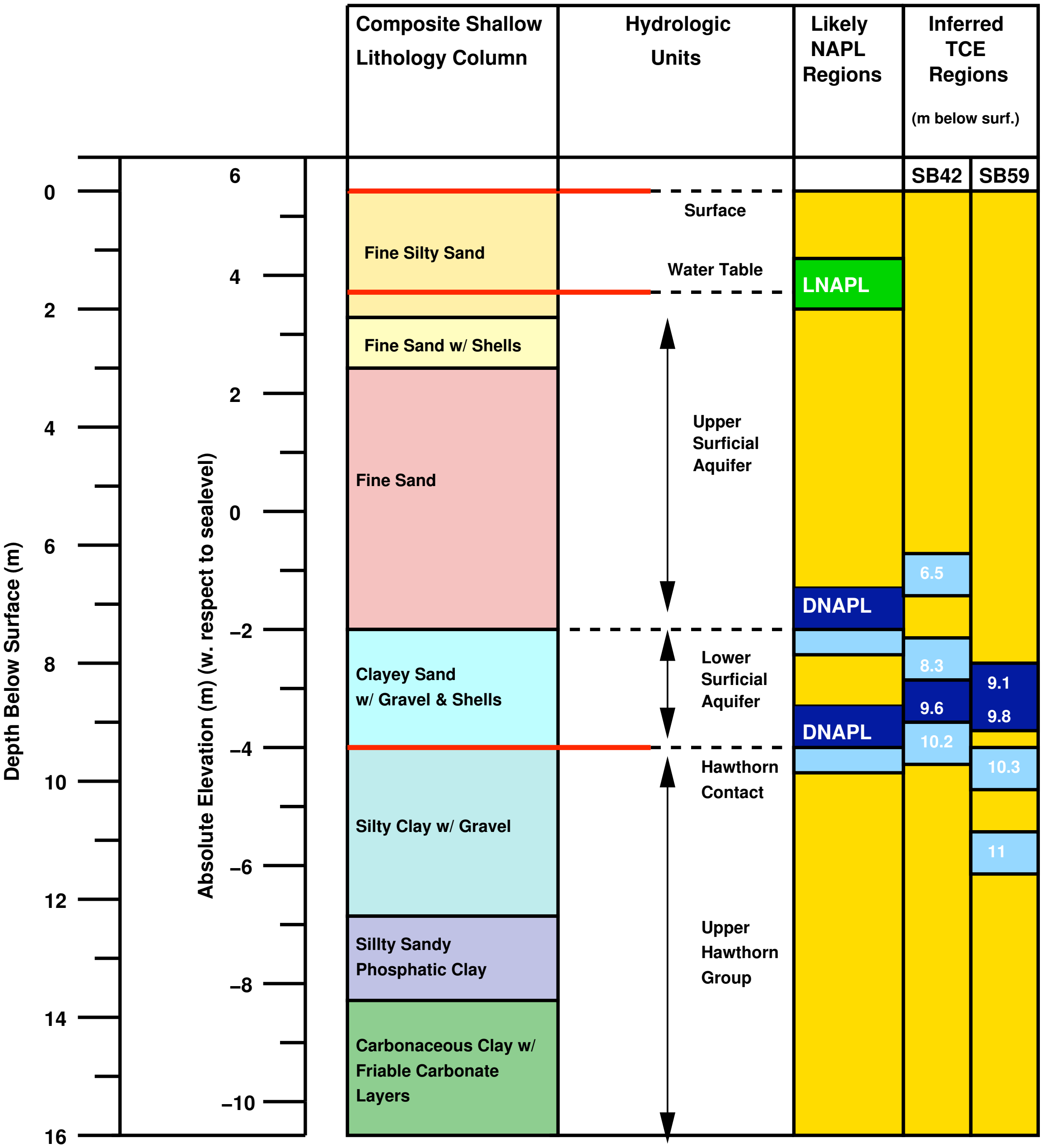

Figure 2.7: Shallow lithology of the Pinellas NE site : Composite lithology information was extracted from visual logs of soil borings [4] and should be considered typical for the site rather than specific to a given location. The column labeled "Likely NAPL Regions" is only based on permeability transitions and should be considered as a rough guide to where detailed characterization efforts might prove most valuable. The column labeled "Inferred TCE Regions" shows the depths of TCE-rich NAPLs as estimated from aqueous TCE levels in DOE documents [4]. Dark blues indicate the regions of highest TCE concentrations.

The upper Hawthorn group forms a confining layer, separating the surficial aquifer from the deeper Floridian aquifer. The Hawthorn group is also lithologically variable, ranging from a green phosphatic silty clay to a mixture of weathered limestone and clay. X-ray diffraction analysis of clay mineralogy from the surficial aquifer and the Hawthorn group show predominantly kaolinite and smectite with trace amounts of chlorite and illite [172]. The upper Hawthorn varies between 18 and 21 m thick at the NE site. The contact between the surficial aquifer and the Hawthorn varies by about 2 m in depth with topographic lows occurring in the southern region of the site [4]. Vertical hydraulic conductivities in the Hawthorn also vary significantly but are generally several orders of magnitude lower than those in the surficial aquifer; of the limited number of existing measurements on the NE site's clay rich materials the average vertical value is approximately 7×10^{-7} m/s.

Figure 2.7 shows a composite shallow lithology column for the southern section of the NE site based on information extracted from visual logs of soil borings. The column should be considered typical for the site rather than specific to a given location. Following the conceptual models of DNAPL distribution discussed in the introduction, we highlight zones where soil permeability changes from higher to lower values, particularly the upper/lower surficial aquifer and Hawthorn transition, as likely accumulation areas. We would expect LNAPLs to be located near the water table with possible vertical distribution due to seasonal variations in water levels. The column labeled "Likely NAPL Regions" is based only on knowledge of these characteristics and should be considered as a rough guide for where detailed characterization efforts might prove most valuable. The column labeled "Inferred TCE Regions" shows the depths of TCE-rich NAPLs as estimated from aqueous TCE levels in DOE documents [4]. Results from DOE analysis of the SB42 and SB59 soil borings suggest that both the Hawthorn contact and the boundary of the upper surficial aquifer may in fact be locations of DNAPL accumulation.

2.3 History Of Site Remediation

In this section we review the long and varied remediation history of the Pinellas site with a focus on the NE region. In addition to summarizing these activities, we attempt to cast each effort in terms indirect information which they provide concerning site status including contaminant fate, hydrogeologic structure, and the natural bacterial community.

2.3.1 Pump-And-Treat

After the Pinellas RCRA investigation discovered significant quantities of dissolved chlorinated contaminants at the NE site in 1990-1991, a pump-and-treat remediation project was initiated, a project which has expanded and remains active to the present day. The early pumping system, conceived of in 1992, consisted of four recovery wells linked to an on-site storage facility. In 1993 modifications were suggested by the DOE and the first system was operational by March of 1994. Modifications in

1996-97 created a new network of seven recovery wells linked to an iron removal pre-treatment system, an air stripper unit for extraction of VOCs (see figure 2.3 for treatment system location), and a second set of on-site storage tanks. A slurry wall was also installed on the north boundary of the site to provide a secondary flow barrier. While the recovery well system has prevented extension of the dissolved plume beyond the boundaries of the site, the low aqueous solubility of the source NAPLs makes a remediation strategy based solely on pumping a long term ($\sim$ 50 years) commitment.

2.3.2 Direct Excavation

In addition to recovery using pumping techniques, early efforts at remediation included large scale direct excavation of site materials [4]. In 1995, approximately 4000 m^2 of the site was excavated to a depth of between 1 and 2 m resulting in the recovery of 241 drums or drum fragments with contents including solvents, solidified resins, and unidentified viscous liquids. During the excavation process, nearly 43 metric tons of hazardous waste and 660 metric tons of non-hazardous waste were removed requiring 500 cubic meters of fill material (mostly sand) to restore the site to a consistent level.

2.3.3 Anaerobic Bioremediation

Stimulated *in situ* anaerobic bioremediation was attempted at the NE site on a pilot scale [126]. During 1997, two 240 ft. horizontal wells were emplaced to provide nutrients in the form of benzoate, lactate, and methanol to naturally occurring bacteria capable of reductively dechlorinating existing DNAPLs. Iodide tracers were also introduced to allow assessment of nutrient distribution in the vicinity of the treatment region. Significant reductions in dissolved dichloroethane, trichloroethylene, and vinyl chloride were observed in co-located monitoring wells. Tracer and nutrient monitoring data suggested that variations in hydraulic conductivity and the associated variations in nutrient transport were the limiting factor for bacterial stimulation. Since the treatment wells were located in the northern portion of the NE site, over 100 m distant from our investigation area in a second contaminant plume, it seems unlikely that the nutrients introduced in the bioremediation pilot project played any role in bacterial activity in the southern DNAPL region. However, this project did demonstrate the biological potential for reductive dechlorination by native bacterial populations present at the site.

2.3.4 Rotary Steam Auger Technique

A technique referred to as rotary steam auger treatment [5] was also used on a pilot scale at the NE site from 1996 to 1997 [125]. This treatment method involves the use of a large crane mounted dual auger bit which vertically tills a column of soil of up to 10 m depth while injecting steam. DNAPLs present are volatilized and captured by a shroud; all captured vapors are then processed by an on-site gas treatment facility. Figure 2.8 shows photographs of both the crane-mounted auger system

---

[5] Deployment and operation of the rotary steam auger system was carried out by *In Situ* Fixation (Chandler, Arizona).

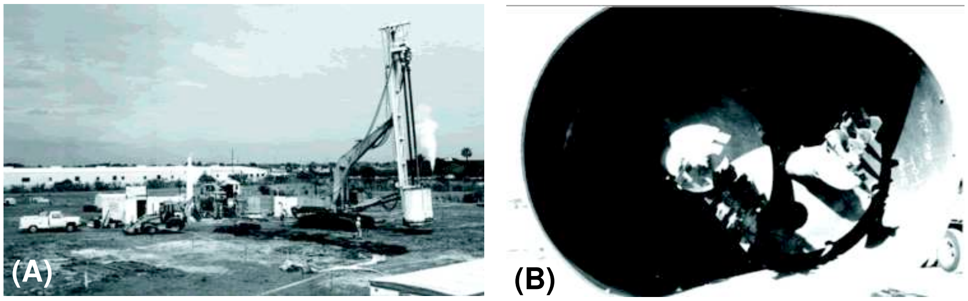

Figure 2.8: Photographs of the rotary steam auger system. Panel A shows the full crane mounted system while Panel B shows a close-up of the dual-auger bit. Both photographs are from the DOE's Cost and Performance report [125].

(panel A) and a close-up of the dual auger bit (panel B) with the attached gas-capture shroud which measures approximately 2 meters wide. The goal of the dual-auger pilot project was to remediate a large portion of the southern DNAPL zone at the NE site through sequential auger operations on a grid of drilling locations. The auger remediation deployment met mixed success; although 550 kg of volatile contaminants were extracted during the pilot project, only 20% of the proposed area was remediated due to load limitations of the CATOX gas treatment system and general equipment failure. Operations staff noted that significantly larger quantities of VOCs were recovered from the western region of the site closest to the geophysics study area.

2.3.5 Biosparging at the 4.5 Acre Site

Although not carried out at the NE site, a large biosparging pilot project [6] was initiated at the nearby 4.5 acre site within the Pinellas facility [8]. The goal of biosparging is to introduce enough oxygen into treated regions of the aquifer to transform conditions from anaerobic to aerobic thereby allowing more efficient biodegradation of contaminants *in situ*. Like the enhanced bioremediation approach described previously, natural bacterial populations are exploited for the dechlorination of subsurface contaminants. Since aerobic conditions were not achieved during the timespan of the project, the biosparging approach was not considered successful in context of the 4.5 acre site. Localization of injected gas in permeable "fast path" regions was one explanation suggested by the contractors since such behavior would prevent gas dissolution in hydraulically less conductive zones. Observations of air bubbling within monitoring wells as far as 200 meters from the injection location confirmed this hypothesis. Similar flow localization may occur at the NE site making these results relevant to our study area.

---

[6] The Biosparging pilot was carried out by Xpert Design and Diagnostic (Stratham, NH) subcontracted through the S.M. Stoller Corporation.

2.3.6 Steam Enhanced Extraction & Electro-Thermal Dynamic Stripping at NE Site, Region A

Between 2002 and 2003 a combination of steam-enhanced extraction (SEE) and electro-thermal dynamic stripping (ET-DSP) applied to region A of the NE Site [9] [124] [248] [135], north of the geophysical study region [7] The ET-DSP/SEE process involves heating the treatment region to near 100 ^oC using a combination of resistive heating and steam injection, thus volatilizing existing contaminants. The resulting contaminants are then recovered either through use of a surface vapor trap or through steam/fluid extraction at depth. To implement the ET-DSP/SEE remediation process, 15 steam injection wells, 28 extraction wells with electrodes within the Hawthorn formation, 21 extraction wells with electrodes in the surficial aquifer, 8 fluid monitoring wells on the perimeter, and 36 temperature monitoring boreholes were drilled, all within a patch approximately 50 × 50 m in dimension. Hydraulic containment was used to prevent migration of contaminated fluids outside the remediation zone. All extracted fluids were processed within an on-site effluent treatment system. Panel (B) of figure 4.5 from the previous section depicts LNAPL and DNAPL samples recovered from the area A treatment system. The ET-DSP/SEE system increased the temperature across the remediation region to at least 84^oC with the majority of the zone from 4 - 10 m below surface maintained at or above 100^oC for at least 6 weeks. The project was considered a success; dissolved contaminant levels decreased by several orders of magnitude, well below project targets, and approximately 1400 kg of VOCs were removed. The project did confirm the existence of a large volume of NAPLs *in situ* but did not provide precise details concerning their spatial configuration.

2.3.7 Current Remediation Strategies

The next stage of remediation at the NE site has targeted the so-called area B which overlaps with our geophysical study area. All wells within that region were abandoned in early 2004 and current plans call for the installation of an ET-DSP/SEE system similar to the one developed for NAPL area A within the 2004/2005 timeframe. Considering the success of the area A remediation project, site managers hope that this next phase will remove enough NAPLs to allow the remnant material to be removed during a short phase of pump-and-treat.

2.4 The Future Of The Pinellas Facility The Role Of Geophysics

Up to the present, both characterization and remediation efforts at the Pinellas facility have been dominated by a brute-force approach; over 200 wells, 100 soil borings, and 80 CPT push-points have been used to build a rudimentary architecture of lithology and contaminant levels at the NE site.

---

[7] The ET-DSP and steam extraction project was carried out by SteamTech Environmental Services (Bakersfield, CA) under contract with S.M. Stoller Corp.

Even with this substantial expenditure of effort, only a coarse model of lateral variations in lithology is available. Knowledge of NAPL location is based upon costly one dimensional sampling and requires careful coring, fluid extraction, and analytical analysis. Even the direct sampling protocol carried out at Pinellas does not yield NAPL saturations; instead aqueous contaminant concentrations are used as a proxy for the presence of NAPLs. The remediation projects have similar characteristics; application of the ET-DSP technique to region A of the NE site required the emplacement of 108 wells of varying dimensions, 36 of which were used only for monitoring temperatures. Geophysical imaging methods might be practically applied at the site on two distinct scales. Surface imaging techniques with sufficient 3D coverage would enable construction of a truly volumetric site lithology model, capable of delineating critical features such as the Hawthorn contact. On a smaller scale, high resolution crosswell and VSP methods could be applied to build accurate property profiles with sub-meter resolution. Such techniques also hold promise for the direct detection of DNAPLs *in situ* and the characterization of DNAPL pools. Fine scale determination of DNAPL location might allow optimization of remediation techniques such as targeted emplacement of steam injection wells thereby increasing the efficiency of existing techniques. The same geophysical methods could also be used for monitoring active remediation efforts, particularly techniques involving temperature changes or the injection of gas (sparging methods). Rather than replacing drilling, geophysics should be considered as a way of extending information traditionally acquired from coring into a second and third dimension, thereby allowing development of site models with a more realistic treatment of temporal and spatial heterogeneity. The next chapter will consider the use of geophysics at Pinellas in more detail and describe the design, execution, and initial results of our field surveys at the Pinellas NE site.

Chapter 3

The Pinellas DOE Facility
A Geophysical Investigation

The goal of our geophysical investigation at the Pinellas facility [1] was to evaluate the suitability of high resolution crosswell seismic and radar measurements for the detection of DNAPL contamination *in situ.* To test this approach we installed a network of geophysical monitoring wells which stretched from a region of the NE site with confirmed DNAPL contamination to a zone which was believed to be free of such fluids. Using these wells we then acquired a series of crosswell surveys to allow examination of changes in seismic and radar properties across this region of the site. We recovered several core sections to allow laboratory investigation of the operative petrophysical relationships (see chapters 4,5, and 6) and secondary measurements including a suite of well logs were acquired to better constrain changes in lithology. In this chapter we will describe both the design and execution of our geophysical field experiments at the Pinellas NE site. We will also examine data quality and provide some initial site lithology models based on our collection of calibrated gamma logs. Laboratory core studies, tomographic processing methods, and the results of our integrated imaging experiment will be described in later chapters.

3.1 Background

As discussed in our introduction, DNAPL contamination is a significant environmental hazard and is a common persistent pollutant at both government and private sector facilities. The goal of our investigation was to evaluate two geophysical methods, crosswell radar and crosswell seismic techniques, which might allow remote detection of DNAPLs *in situ.* Previous mesoscale experiments

---

[1] The Pinellas geophysics investigation was carried out jointly with Lawrence Berkeley National Laboratory. Jil Geller (LBNL) was the primary investigator for the project (EM-DOE grant #DE-AC-03-76F0098) and Ken Williams (LBNL) provided crucial guidance during the field acquisition process. Phil Rizzo (LBNL), Jaime Urban (Stanford), and Cecil Hoffpauier (LBNL) also assisted in the data acquisition effort. All crosswell seismic and radar equipment were borrowed from LBNL's Geophysical Measurement Facility (GMF).

[132] [41] and controlled field-scale experiments [2] carried out in the Borden aquifer [116] [43] have shown that DNAPL bodies can be imaged using time-lapse radar techniques assuming suitable background materials. Both ultrasonic laboratory measurements [111] [236] [108] and mesoscale physical model experiments [109] [146] suggest that DNAPLs may also have a seismic signature. For both seismic and radar measurements, the detectability of DNAPLs hinges on the sensitivity of V_p and dielectric properties to DNAPL saturation; chapters 3,4, and 5 of this text will consider this sensitivity problem from a laboratory perspective.

Equally important to the geophysical detection problem is the maximum level of DNAPL saturation and the geometry of DNAPL pools within the subsurface, a set of parameters which depend on a large variety of contaminant source and site parameters [3]. The DNAPL pool geometries observed in multiphase flow experiments [149] [150] [151] and in controlled field tests [152] suggest that detection of DNAPLs *in situ* requires geophysical techniques with high vertical spatial resolution since DNAPLs seem to often form thin lenticular pools. Parker *et al.* [213] provides a comprehensive review of the architecture of DNAPL source distributions at five contaminated sites located in sandy aquifers. For the two DNAPL spills described by Parker *et al.* most similar to Pinellas, the Connecticut A and B sites, the free-phase contaminants (TCE and PCE) pooled at permeability transitions forming layers between 5 and 15 cm in thickness overlain by a thin zone of residual DNAPLs. Peak DNAPL saturations for these pools were on the order of 50 % with less than 10 % saturation in the residual zones.

Crosswell seismic and crosswell radar transmission methods have the potential for generating quantitative images of V_p and dielectric constant with vertical spatial resolutions on the order of 20 cm in near-surface environments conducive to these measurements. Joint crosswell GPR and seismic field experiments at the contaminated TAN site at the Idaho National Engineering Lab [67] [259] and the DOE Hanford reservation [170] have demonstrated resolutions close to these levels. The combination of both seismic and radar techniques might provide enough complementary information to identify DNAPLs even in the presence of variations in lithology.

As discussed in chapter 2, the presence of DNAPLs at our NE site study region was demonstrated through both NAPL samples extracted from monitoring wells and high aqueous contaminant levels. Since the direct sampling from wells with long screened intervals has no intrinsic vertical resolution, the geometry of DNAPL distribution and peak saturation levels were not known. As will be discussed in later chapters, we expected DNAPLs at the NE site to decrease apparent dielectric constant, decrease P-wave velocity, and possibly increase P-wave attenuation based on our laboratory studies. We anticipated two regions where DNAPL accumulation seemed probable due to permeability contrasts, the boundary between the lower and upper surficial aquifers and the contact between the lower surficial aquifer and the Hawthorn formation. Aqueous contaminant levels measured from depth-segmented soil borings showed peak TCE levels in the vicinity of these regions.

Existing radar observations of DNAPLs in controlled field scale measurements have been in the

---

[2] Chapter 1 provides a literature review of existing geophysical measurements targeting DNAPLs

[3] A complete review of data pertaining to DNAPL pool architecture is provided in chapter 1

time-lapse mode; in the case of monitoring experiments, a reference dataset allows recovery of the DNAPL signature since only fluid distribution is changing with time. When solving the detection problem, a prior image of the site in an uncontaminated state is clearly not available. If the site geology does not have strong lateral variations we might consider using a spatial reference image i.e. compare images of a target region within the site to an image of a nearby zone without contamination.

In our case we decided to acquire a chain of high resolution crosswell surveys extending from a region of the site with known DNAPL contamination to a so-called clean region where aqueous contaminant levels are very low. Figure 3.1 is a map of the geophysical study region with dissolved TCE concentrations marked in red. We chose to start our extended crosswell profile in the vicinity of well M31D[4] (lower right) which has aqueous TCE levels of less than 5 μg/ L indicating that no DNAPLs are present. The survey profile passes through a sequence of wells with sequentially higher TCE concentrations, 59 μg/ L at RW12, 500 μg/ L at M34D, and finally to M17D which has an aqueous TCE concentration of 21000 μg/ L and has produced visible quantities of NAPLs in the past. The top corner of the survey profile (G12) also passes within 3 m of well RW06, the location of the one extracted DNAPL sample for which we have a complete chemical workup. The lower panels in figure 3.1 are photos of the so-called clean and dirty well groups. The lack of chemical sampling data between wells M34D and M17D makes the exact progression of dissolved NAPL levels difficult to determine; this limitation stems from the fact that our G-series wells were not completed (no screening) due to permitting issues. Several smaller more specialized surveys were also acquired including a pseudo-3D survey in the vicinity of M17D and one multioffset co-linear profile (G15-G14,G15-G13) for examination of attenuation phenomenon.

In addition to the seismic and radar imaging experiments, we acquired gamma and conductivity logs for all accessible wells near our geophysical survey profile to provide additional constraints on lithology. A final VSP seismic survey was designed to provide broader lateral coverage and possibly S-wave velocities to better constrain seismic fluid signatures. These geophysical surveys, well emplacement, core collection, and other site investigation activities were carried out in four separate deployments briefly summarized in table 3.1; the following sections will describe each phase of our investigation in detail.

3.2 Well Emplacement And Core Acquisition Techniques and Problems

Two sets of wells were installed as part of our geophysical investigation during the first and second deployments (see table 3.1). PVC was chosen for casing in both cases because of its low cost and compatibility with electromagnetic measurements. Since screened wells required a secondary permit, neither set of wells was completed. Without a screened interval we were not able to obtain fluid

---

[4] For the NE site, the following well abbreviations are used; M = monitoring well, RW = recovery well, G = well emplaced for geophysical measurements. D and S suffixes for monitoring wells indicate screening in the shallow or deep section of the surficial aquifer.

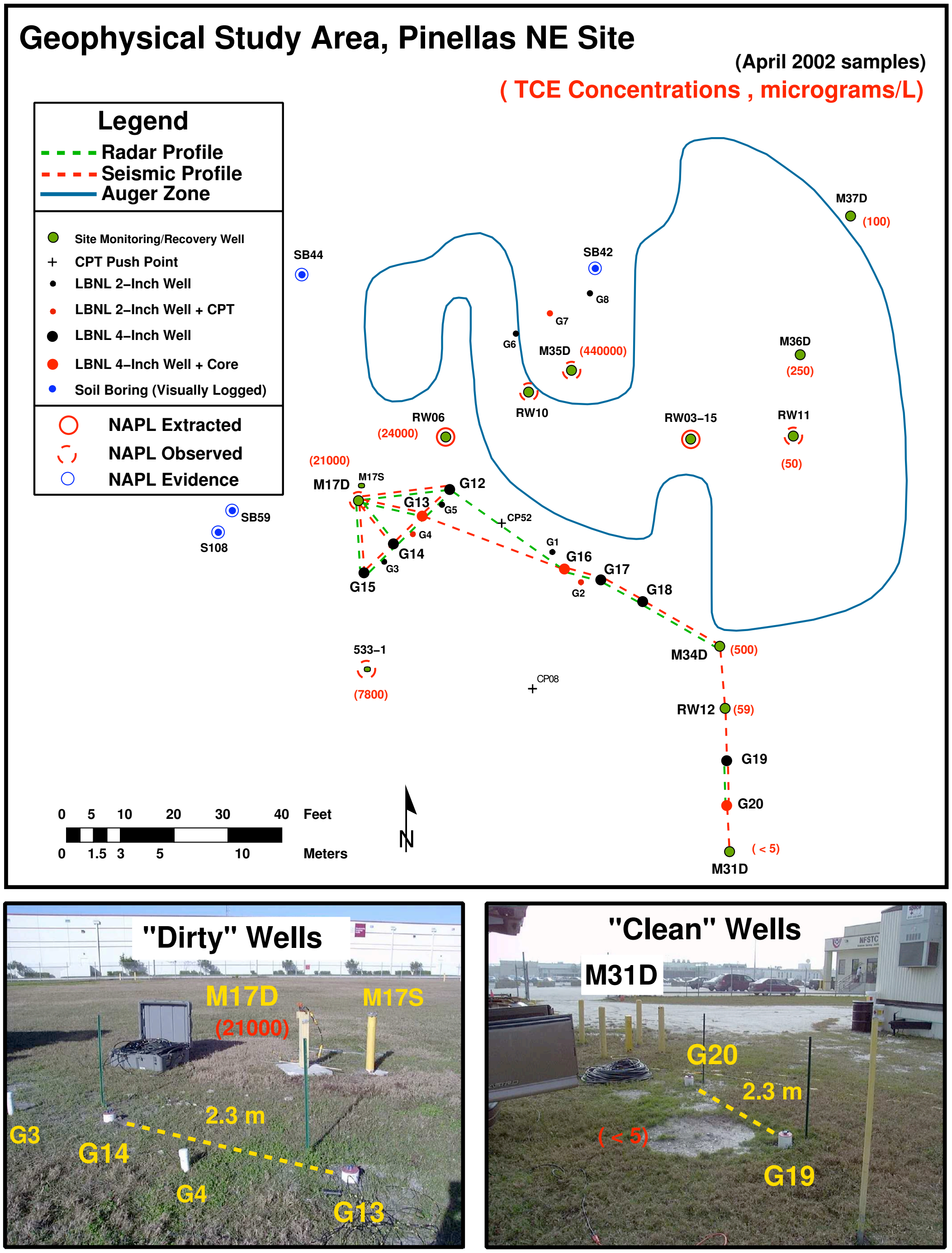

Figure 3.1: Map of the geophysical study area and photographs of key wells : M series wells are site-maintained monitoring wells while RW wells are recovery wells from which water is actively withdrawn. Locations with the S prefix are soil borings and crosses labeled CP are cone penetrometry push points. The G series wells were installed for the purpose of geophysical data acquisition and are not screened. G1-G11 are 2 in. CPT wells while G12-G20 are 4 in. PVC wells. Red numbers are TCE concentrations in micrograms/L as collected during the April 2002 sampling campaign.

Date	**Dep. #**	**Personnel**	**Infrastructure**	**Geophysical**
May 2001	1	K.H.W.(w 1) P.R. (w 1)	2-in CPT wells installed (G1-G11)	3 X-Well Radar 6 X-Well Seismic
Aug. 2001	1a	Century Geophysical H.Marlow Inc.	-	Deviation Logs Well location survey
Nov. 2001	2	C.H. (w 1)	4-in Sonic wells installed (G12-G20)	Core acquisition
Jan/Feb 2002	3	J.B.A-F (w 1+2) K.H.W. (w 1) P.R. (w 2)	-	20 X-Well seismic 11 X-Well radar
Jul/Aug 2002	4	J.B.A-F (w 1+2) K.H.W. (w 1) J.U. (w 2)	-	Gamma logs Conductivity logs Sonic logs VSP seismic

Table 3.1:
Site Deployment Timeline : Abbreviations for survey personnel follow : Jonathan Ajo-Franklin (J.B.A-F), Kenneth H. Williams (K.H.W.), Phil Rizzo (P.R.), Cecil Hoffpauier (C.H.), Jaime Urban (J.U.). Personnel labels followed by weeks in the field i.e. w 1+2 denotes participation in weeks 1 and 2 of a particular deployment. CPT wells installed by Fugro Geosciences while sonic wells were drilled by Boart Longyear Co.

samples for chemical analysis. We had hoped to drill wells into the Hawthorn formation to allow effective imaging of regions at the contact between the Hawthorn and the lower surficial aquifer. However, site administrative personnel were concerned that drilling into the Hawthorn might provide a flow path for migration of existing DNAPLs into deeper regions of the site. Figure 3.2 shows the two target regions corresponding to permeability boundaries where DNAPLs might accumulate. Only target region 1 at the upper/lower surficial aquifer boundary could be effectively imaged within the context of our well geometries.

The first group were 2 in. wells emplaced using a CPT rig (G1-G11) by Fugro Geosciences during May of 2001. After initial quality control on the crosswell data collected in the CPT wells, a deviation problem became apparent when performing angle-velocity analysis [5]. The CPT rig used to emplace the wells did not have an accelerometer system to record tip location so a second firm was contracted to collect gyro-deviation logs for the existing boreholes. Upon deployment, the contractor found that many of the wells were highly deviated, often with a sudden change in direction characteristic of the CPT tip being deflected off of a hard object. Figure 3.3 shows the geometry of the G4-G5 well pair which are typical of the CPT installed boreholes.

A second group of 4 in. wells were installed using a sonic drilling system (G12-G20) by Boart Longyear Co. in November of 2001 during the second deployment. Sonic drilling methods use a vibrating pipe driven by counterweight rotating at 100-150 Hz to smoothly penetrate soils at shallow to moderate depths. Inclusion of a plastic sleeve within the drill pipe allows the recovery of large

---

[5] Chapter 9 details the QC process used to determine the presence of well deviation

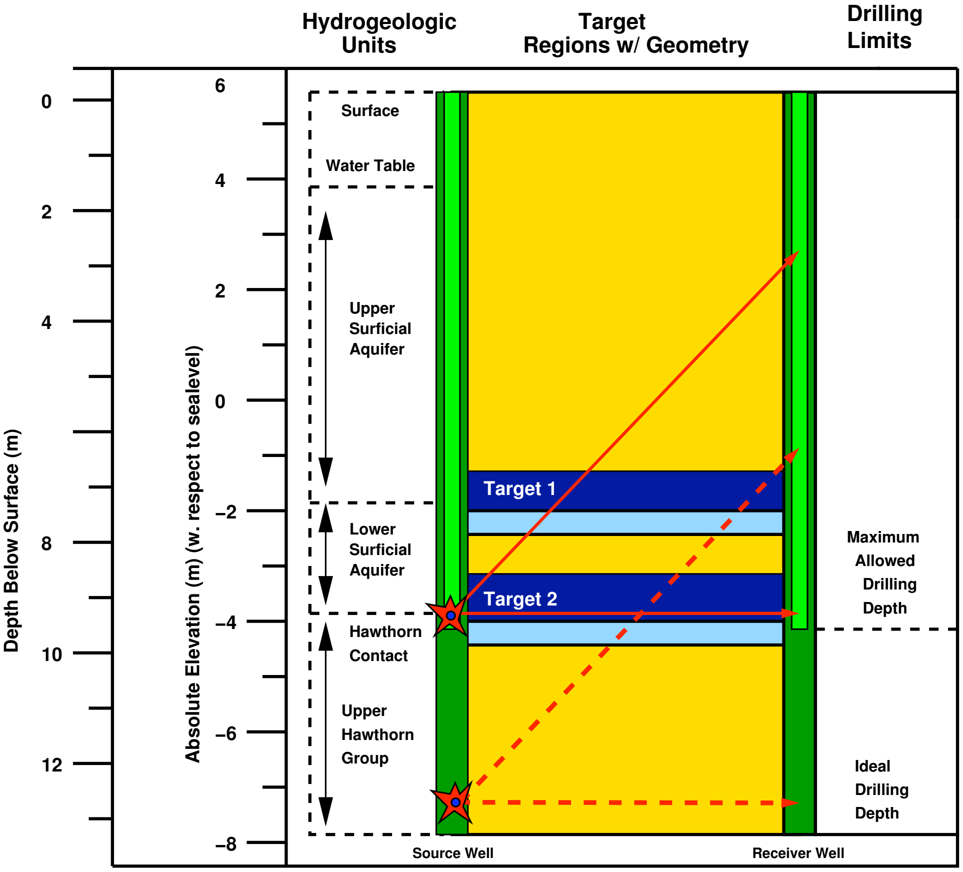

Figure 3.2: Well depth limits and target regions : Limitation in drilling depth prevented sufficient angular coverage of the potential DNAPL zones near the Hawthorn contact (target 2) but the first possible zone of accumulation at the upper/lower surficial aquifer should be well illuminated given our well geometry (target 1).

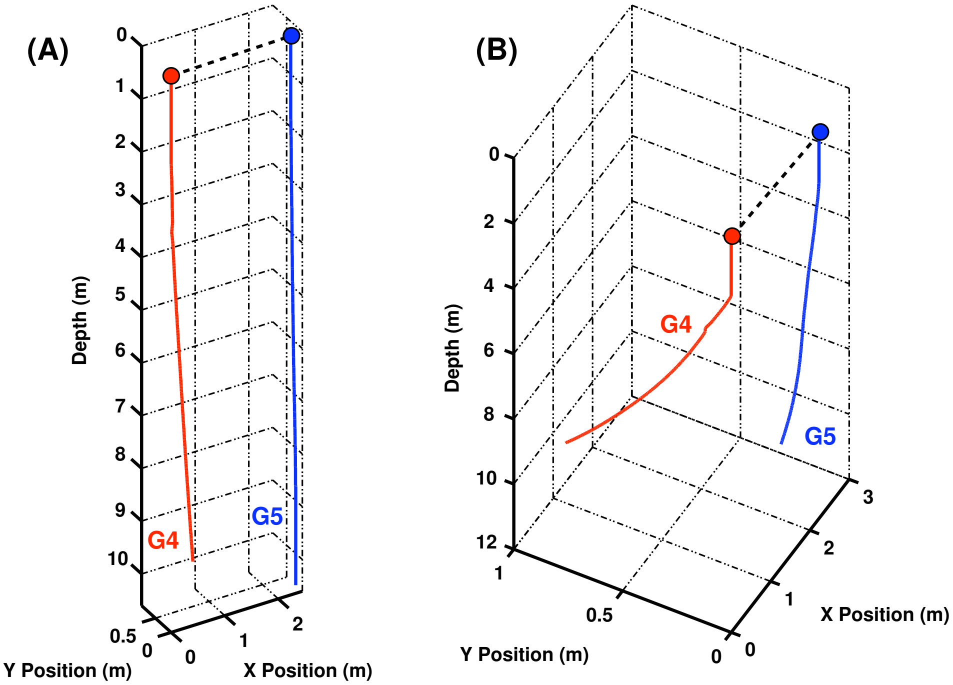

Figure 3.3: An example of strongly deviated CPT wells : Panel (A) is a 1 to 1 aspect ratio 3D plot of CPT wells G4 and G5 showing 1 m change in offset over 10 m of depth. Panel (B) shows the same plot from a different perspective with exaggeration in the X and Y planes : In this case the sharp deviation of G4 is visible.

continuous core sections even in areas with low soil cohesion. While sonic methods are slower and more expensive than CPT push techniques, sonic yields a relatively straight well since the drill pipe can easily shear through cobbles which might deflect a CPT tip. A total of 13 sections of core 4 inches diameter and approximately 5 feet in length were recovered from wells G13, G16, G17, and G20. The sonic system extracted cores within transparent polycarbonate sleeves which enabled a visual evaluation of core integrity. After transport of the cores from Florida to California some fluidization of soil materials was evident. Figure 3.4 shows one zone where materials within the core interior fluidized and moved relative to the exterior annulus, resulting in what appear to be concentric circles of soil with different textures.

Figure 3.5 shows the 4 core sections collected during the emplacement of the G20 well. Included are core photographs, X-Ray CT images of the core cross-section, and sand/silt/clay fraction data acquired from a series of 44 small (∼150 g) sub-samples. Texture analysis of the G20 samples were carried out by the University of Georgia (UGA) Soil Laboratory using the hydrometer method. X-Ray CT measurements were made by Liviu Tomutsa using a modified medical CT scanner (Somaton HiQ). The cores were imaged using a 10 mm slice thickness. The CT measurement yields a map of X-Ray attenuation which is an excellent proxy for density although we did not calibrate the images to an absolute density standard. All cores were similarly scanned for guidance in the selection of sampling locations. Several core sections were chosen for use in our laboratory dielectric and acoustic measurements which will be discussed in later chapters.

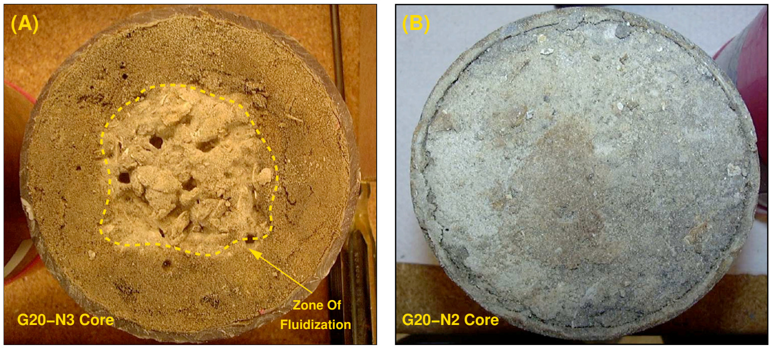

Figure 3.4: Examples of core samples after transport : The left sample (A) has shows the results of fluidization near the center while the right sample (B) is relatively intact.

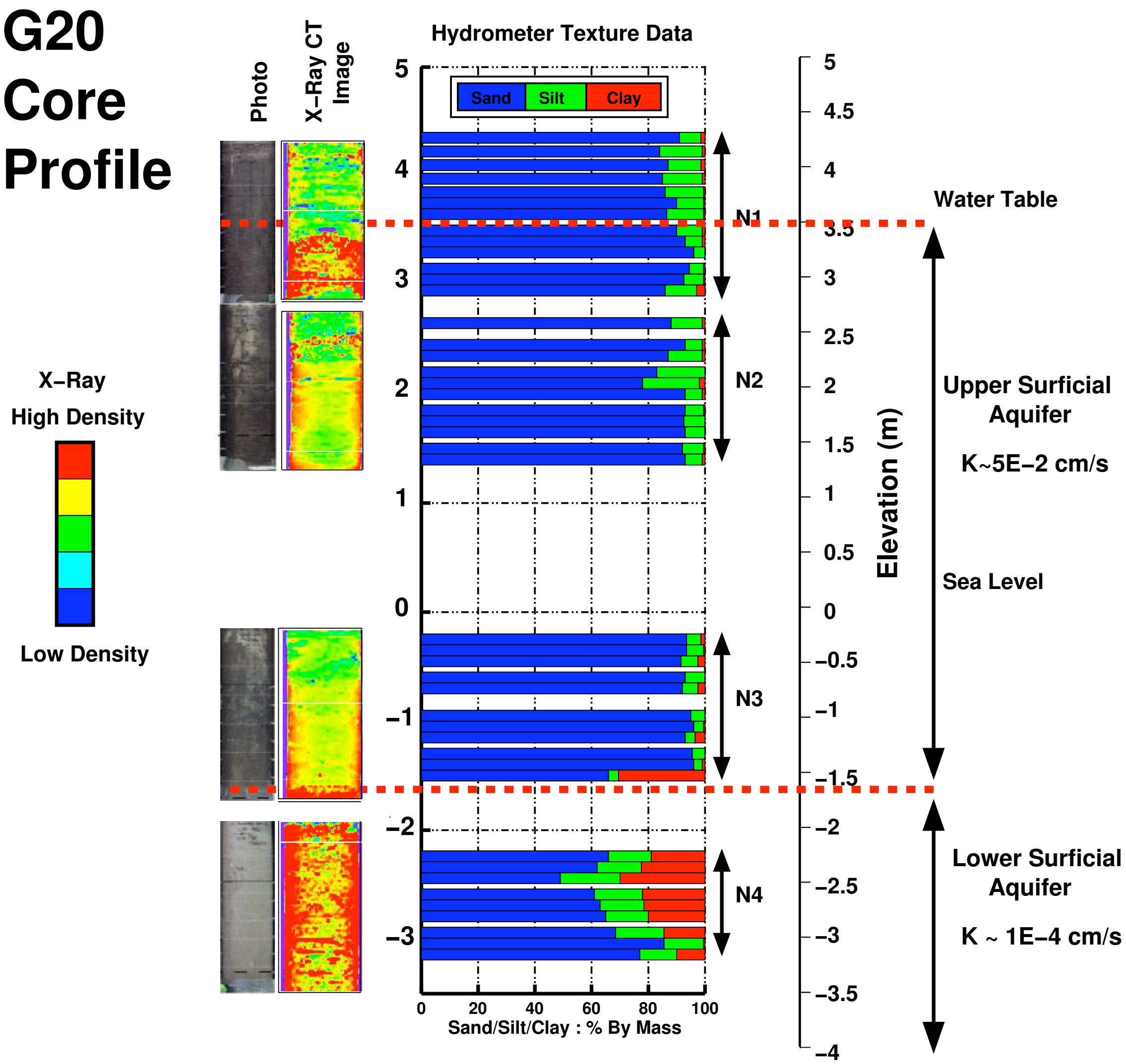

Figure 3.5: Characterization of the G20 core sections : Shown are core photographs, slices of the corresponding X-ray CT images, and texture data obtained from hydrometer experiments. The transition into the lower surficial aquifer (∼ -2 m) is visible in all three columns. Sand/Silt/Clay fractions shown by mass.

3.3 Acquisition Of Well Log Suite

During the first week of the 4th Pinellas deployment (July 22nd - July 26th, 2002) a large suite of logs were acquired to provide independent confirmation of lithology and supporting data for the interpretation of crosswell measurements. Gamma, EM conductivity, and sonic log measurements were made with only the first two providing meaningful results as will be explained in the following sections. All of our log data were collected using a Mt. Sopris MGX-II shallow logging system equipped with a 4MXA-1000 winch. Figure 3.6 shows a typical deployment configuration (panel A), the winch (D), and the various downhole tools (B,C,E). Each logging run was started with the tool at the bottom of the well after which the tool was raised at a constant velocity of 1.8 m/min yielding a depth sampling interval of ~50 samples/m. Each run was recorded in the LAS format and post-processed into flat text files for later analysis. Typically the first run of each tool was repeated to insure consistent instrument response.

3.3.1 Gamma Logs

Natural gamma logs were acquired for 23 wells [6] using the Mt. Sopris 2PGA-1000 tool. The 2PGA-1000 uses a NaI scintillator to measure gamma emissions as a function of depth. These naturally occurring low-level emissions can be correlated with the presence of clay minerals and thus provide an excellent proxy for lithological transitions. While previous CPT measurements gave us some indication of clay rich regions, the lack of reliable site calibration made that dataset somewhat more difficult to interpret. Another consideration was the absence of CPT information co-located with our 4-inch wells and the various secondary monitoring wells used in our imaging experiments. The gamma tool is shown in panel (C) of figure 3.6. Gamma response is recorded in counts per second (CPS), a measure which is dependent upon both detector efficiency and logging rate.

Several simple corrections were applied to the natural gamma logs as part of the processing sequence to allow comparison of profiles from different wells. Since the annulus of water surrounding the scintillation detector attenuates γ emission from the formation, a multiplicative water correction was applied based on the inner borehole diameter. Without this correction, gamma measurements made in 4-inch wells show reduced count rates in comparison to small diameter boreholes. This "water factor" was determined by the manufacturer at a calibrated test site with boreholes varying between 2.25 and 8.5 ID. We applied a second similar correction to account for variations in casing thickness and casing material type. This step is required to compare results from steel cased wells (RW12), which have high γ attenuation coefficients, to the remainder of our measurements acquired in PVC cased wells.

Gamma response is only a proxy for clay content since the actual CPS value is dependent upon a host of secondary factors including detector efficiency and soil density. In most cases, only the location of lithologic transitions are desired from gamma measurements and the raw log can be directly interpreted to determine interface depths. We performed an empirical calibration using

---

[6] G1-G8, G12-G20, M17D, M31D, M34D, RW3, RW6, RW12

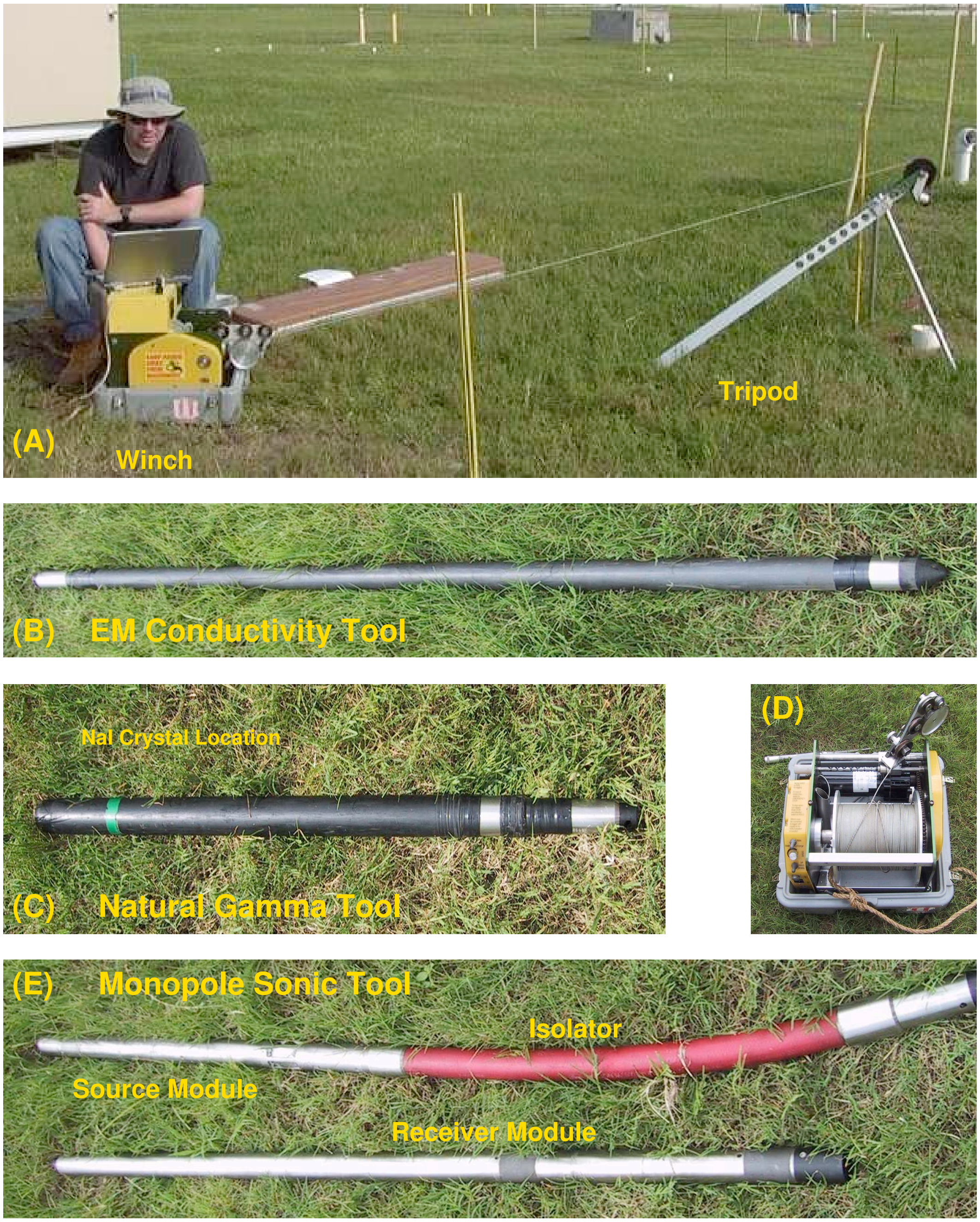

Figure 3.6: Mt. Sopris Logging System : (A) Equipment configuration during logging : winch, acquisition PC, and tripod, (B) EM conductivity tool (Mt. Sopris 2PIA-1000), (C) Natural Gamma Tool (Mt. Sopris 2PGA-1000), (D) Winch system (Mt. Sopris 4MXA-1000), (E) Sonic tool (Mt. Sopris 2SAA(F)-1000)

the extensive texture database recovered from the G20 core set (see figure 3.5) to gain additional insight into variations in clay content. Point-to-point comparison of the texture information to the gamma logs was difficult since the small quantity of soil used in each hydrometer measurement was not necessarily representative of the volume of soil generating a gamma response. Consolidation and fluidization in the core also complicated attempts to establish a clean spatial mapping between the two datasets. We chose to spatially average both clay content and gamma measurements across the length of each core unit generating a single data pair for each of the 4 recovered sections. The resulting measurements were then fit using a linear model and used to convert our gamma log database into a clay fraction model. This calibration has an important caveat, mainly that it assumes that mineralogic clay content as measured by gamma response is equivalent to textural clay content as measured by hydrometer experiments. Exceptions to this assumption can easily occur in situations where some particles which fit the sedimentalogical definition of clay (smaller than 4 microns) are composed of a mineral without significant gamma emissions, such as quartz. Some existing mineralogical data on clay composition from a southern well at the Pinellas facility [172] suggest that they have only a small percentage of quartz but this might not be true across the entire site. Additionally, carbonates tend to be enriched in the radioactive isotope K-40 which introduces an additional source of ambiguity. The textural assumption combined with the problem of representative sample dimensions introduces enough uncertainty into our conversion to treat the resulting clay estimates in only a semi-quantitative manner.

The top panel of figure 3.7 shows the gamma logs for the 11 wells in our M31D-G15 profile converted into clay content. The background colors show a continuous clay content model based on deterministic interpolation of the well log set. The color map is clipped at a clay fraction of 0.1 to make small changes in the surficial aquifer visible. The bottom panel shows a lithology interpretation based on our clay-calibrated gamma log measurements results. Delineation of the upper/lower surficial aquifer contact provides us with a starting point for probable DNAPL pool locations

3.3.2 Conductivity Logs

Inductive EM conductivity logs were acquired for 19 wells (G1-G8,G12-G20,M17D,M34D) using the Mt. Sopris 2PIA-1000 tool, manufactured by Geonics. Conductivity logs could not be recorded for any of the steel-cased wells including the RW series. EM conductivity logging provides a measurement of bulk conductivity as a function of depth. High conductivities are good indicators of clays or briny pore fluids. In addition to providing redundant lithological information, conductivity logs are also useful in constraining zones of high radar attenuation. Conductivity also has the potential of being an indicator of free-phase DNAPLs either through large scale displacement of more conductive pore water (lower observed conductivities) or through the by-products of biological activity which might result in increased total dissolved solids (TDS) and a higher observed conductivity. Literature detailing the tool suggests a lateral depth of investigation of between 10 and 25 cm depending on

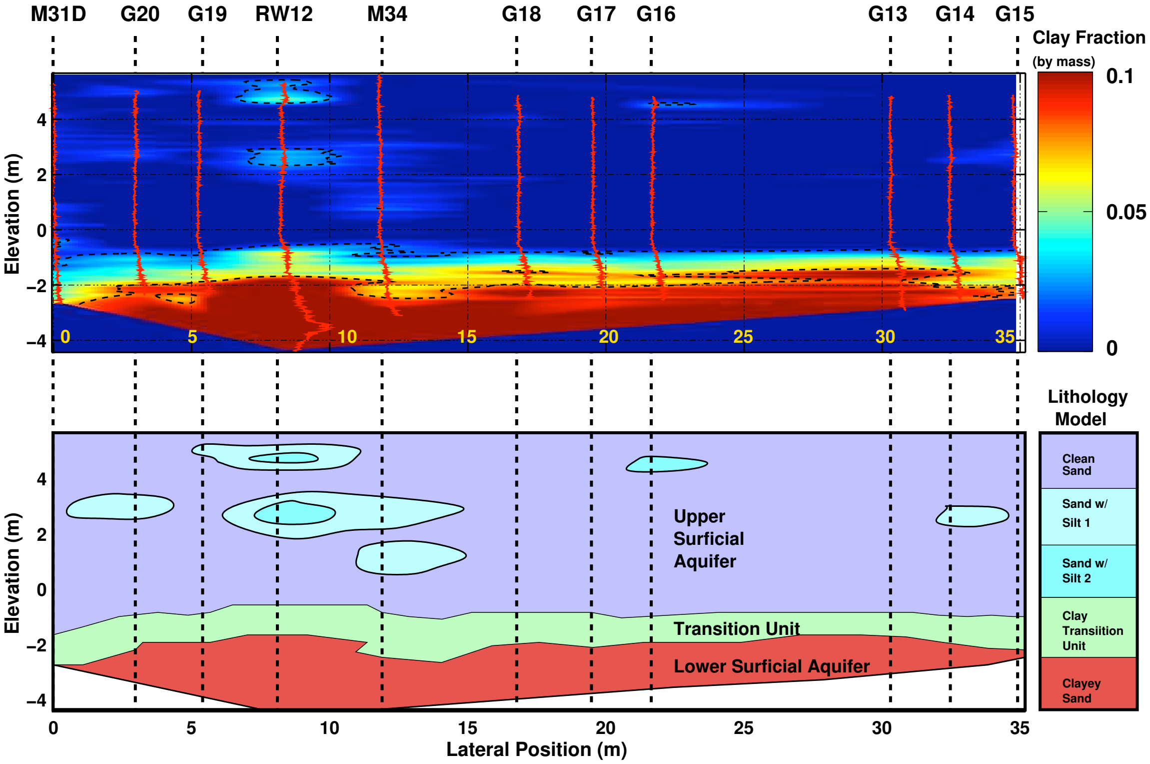

Figure 3.7: Site gamma log/clay content profile from log measurements and geological interpretation : The top panel depicts a site model of clay content based on interpolation of the calibrated gamma logs. The color map is clipped at a clay fraction of 0.1 to make small changes in the surficial aquifer visible. The bottom panel shows a basic interpretation of the clay content map in terms of the contact between the upper and lower surficial aquifers.

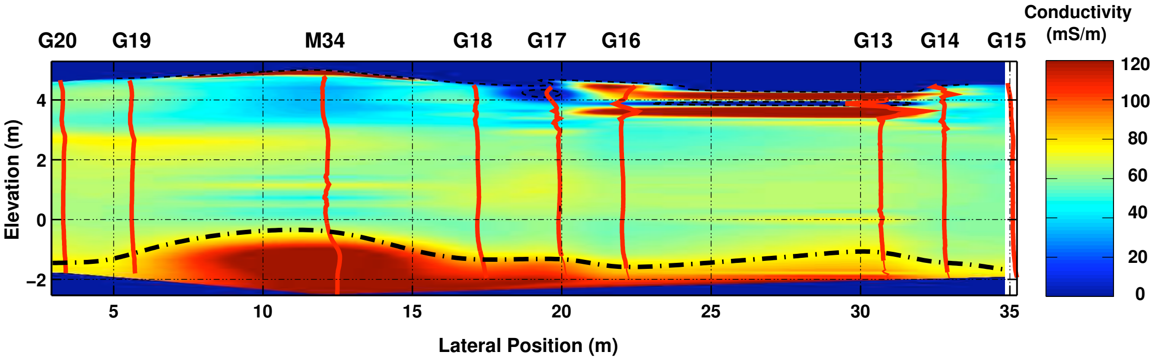

Figure 3.8: Site conductivity profile from log measurements : color map is the result of interpolation of recorded conductivity logs. The scale has been clipped at 0 and 140 mS/m to decrease the visibility of near-surface anomalies due to metallic objects (see text). The inferred upper/lower surficial aquifer transition is shown by the dashed black line.

soil properties and a vertical resolution of approximately 65 cm. All wells were logged at the 0-1000 mS/m sensitivity setting. The tool was warmed to borehole fluid temperature and then calibrated before each run. The conductivity tool is shown in panel (B) of figure 3.6.

Figure 3.8 shows a site-wide profile of conductivity based on the deterministic interpolation of the well log set. Not surprisingly, the upper surficial aquifer was shown to be less conductive than the clay-rich lower surficial aquifer. Several large near-surface anomalies were observed in the conductivity logs (wells G17,G16, and G13) some of which recorded negative values indicative of the presence of metallic objects. The color map in figure 3.8 is clipped to a range of 0 to 140 mS/m to allow viewing of gradients in site conductivity in the presence of the large recorded near-surface values. The inferred upper/lower surficial aquifer transition is shown by the dashed black line.

3.3.3 Sonic Logs

Sonic logs were acquired for 22 different wells using the Mt. Sopris 2SAA(F)-1000 tool. The majority of the wells were logged in a single pass using a single frequency [7] while 6 wells were logged using a multi-pass method [8] to obtain data over 3 different frequency bands (5,10,and 20 kHz). Sonic logging provides a measurement of P-wave and possibly S-wave velocity which can be used as secondary constraints on crosswell seismic tomography at the well bore. As can be seen in panel (E) of figure 3.6, the piezo-electric source module is isolated from the 2 element receiver array by a length of rubber material which damps waves traveling within the tool. Logging runs were attempted with both the rubber isolator shown, and a softer woven kevlar isolator designed for near surface logging. As is clear in the figure, one problem with the tool is its 2.6 m length, considerably longer than many of the features which we wished to log and close to the lateral offset between our wells. We were unable to acquire any usable data from our sonic logging experiments; over the entire site the only visible arrival had a moveout corresponding exactly to water velocity for all depths, below

---

[7] G1-G8,G12,G16,G18,M17D,M31D,M34D,RW3,RW6,RW12

[8] G13-G15,G17,G18,G20

the formation velocity of 1600 to 1800 m/s estimated during our crosswell seismic measurements. We were unable to precisely diagnose the problem but we expect that formation coupling and low exterior velocity were two components. An additional complication was the proprietary file format used by the sonic tool acquisition software which prevented us from performing extensive QC analysis in the field.

3.4 Crosswell Seismic Datasets

During the 1st and 3rd Pinellas deployments a total of 26 short offset crosswell seismic surveys were acquired. The first 6 surveys, shot in the highly deviated 2-inch CPT boreholes were not used because of source/receiver location errors which existed even after incorporation of the deviation logs. We believe that the deviation logs themselves were inaccurate, possibly due to an error in baseline azimuth determination, but we have not been able to confirm this hypothesis. The remaining 20 surveys were shot in the 4-inch sonic wells and existing site monitoring wells with a higher level of success. The surveys spanned the site from the clean region near M31D to the highly contaminated zone near well M17D. The most visible seismic feature was a large zone of high attenuation not visible in the clean region of the site. Figure 3.1 shows the seismic profiles acquired in dashed red lines.

Figure 3.9 shows the LBNL shallow crosswell seismic system used for our acquisition efforts. Panels (A) and (B) show the 2 and 3.5 in. cylindrical piezoelectric transducers that were used as our primary downhole source. When excited with a broadband pulse, the 2 in. source generated a wavelet with a central frequency of between 4 and 6 kHz while the larger source was most efficient at about 3 kHz. The piezo sources were driven by a hybrid tube/solid-state power amplifier. Rectangular pulses with a width of 0.2 ms were generated by a field computer serving as a signal generator and fed to the amplifier. The output of the power amplifier, a fast risetime square wave with an amplitude of between 1.5 and 6.1 kV peak-to-peak, was then used to excite the source. At low excitation levels, an integrated 1U DC Power supply was used to run the amplifier while higher energy levels required a larger external power supply. Panel (D) in figure 3.9 shows the source electronic rack. Both the piezoelectric source and the receiver arrays were fluid coupled.

A broadband 24 channel hydrophone array with integrated downhole preamplifiers was used to receive the generated signal. The hydrophone array had a receiver spacing of 0.5 m; multiple array positions were typically used to obtain closer receiver spacings, typically 0.125 m. Equivalent 0.125 m source spacings were also used. During acquisition the receiver array was kept fixed as the source was raised from the well bottom by hand with depth recorded by visual marks on the source coaxial cable. Data were recorded in SEG-2 format and then converted into SU and DSI formats for processing. A 24 channel Geode seismograph (Geometrics) was used to acquire waveforms with 24 bits of dynamic range. Data was typically recorded for 20 ms at a 20.833 μs sampling rate. A 280 Hz analog low-cut filter and a 60 Hz notch filter were used to remove low frequency noise. Vertical stacking of between 8 and 100 waveforms was used to improve S/N ratio although most surveys used

16 stacks at each shot location.

Figure 3.10 shows a high-quality shot gather from the G19-G20 crosswell profile. In addition to a clean primary arrival, reflections from the water-table and the lower-aquifer transition zone are also visible. Various processing flows were attempted to reveal additional reflections but phase reversals in the first arriving wavelet made removal of the P-wave primary difficult. In areas with good seismic transmission, the observed P-wave first arrival has usable energy up to 6-7 kHz when using the 2 inch piezo source, equivalent to a wavelength of 30 cm in soils with a velocity of 1800 m/s. Although the fluid-coupled sources and receivers are not suited for S-wave generation or detection, some effort was made to detect the S-wave primary. Even in common-angle gathers centered around 45^o from the horizontal, the zone of maximum S-wave energy for a monopole source located in a borehole, no S-wave arrivals were observed.

One of the features most visible within our crosswell datasets is a zone of high seismic attenuation with significant lateral extent. Figure 3.11 shows a panel of true amplitude zero-offset seismic sections extending from well M31D to well G16 with gamma logs plotted for reference. The region of attenuation does not seem to be directly linked to lithology and does not show a strong correlation with any feature visible within the gamma logs. Since figure 3.11 is plotted in true amplitude, some regions which appear to have no signal still possess visible arrivals if the gain is sufficiently increased; this is particularly true for the G19-G20 and G19-RW12 profiles. While we will not consider the cause of this high loss zone in this chapter, the increase in attenuation seems to be partially correlated with increasing levels of dissolved TCE but the lack of fluid samples from the G well series makes further inferences difficult.

3.5 Crosswell Radar Datasets

During the 3rd Pinellas deployment (Jan/Feb. 2002) 11 crosswell radar surveys were acquired with the hope of directly imaging DNAPL bodies, possibly visible as zones of increased radar velocity. Profiles were acquired between all 4 inch G-series wells (G12-G20) and the PVC cased monitoring wells (M17D, M34D) but could not be recorded from either of the steel cased wells (M31D, RW12). Figure 3.1 shows the collected radar profiles as dashed green lines.

Our crosswell surveys were acquired using a Pulse-Ekko 100 borehole radar unit (Sensors & Software). Figure 3.12 shows the components of the Pulse-Ekko system. The downhole antennas (A) are connected to the transmitter and receiver units using high grade coaxial cable. The source and receiver units are housed in Farraday cages to decrease electrical interference and are connected to the console unit via a fiber-optic link. The entire system is controlled using a field PC. Centralizers (C) were used to insure that the antenna did not drift within the borehole, a significant source of error for short offset surveys. The 200 MHz antenna pair were used for the majority of the surveys acquired. Records of 200 nS length were acquired at a 0.4 nS sample rate. Vertical stacking of 16 waveforms was used to improve S/N. Datasets were acquired in Sensor & Software's DT format and were converted to SU and DSI formats for later processing. To eliminate zero-time errors, several

Figure 3.9: LBNL Crosswell Seismic System : (A) 2 in.piezoelectric sources, (B) 3.5 in. piezoelectric source, (C) 24 channel hydrophone array, (D) Source electronics rack and recording system.

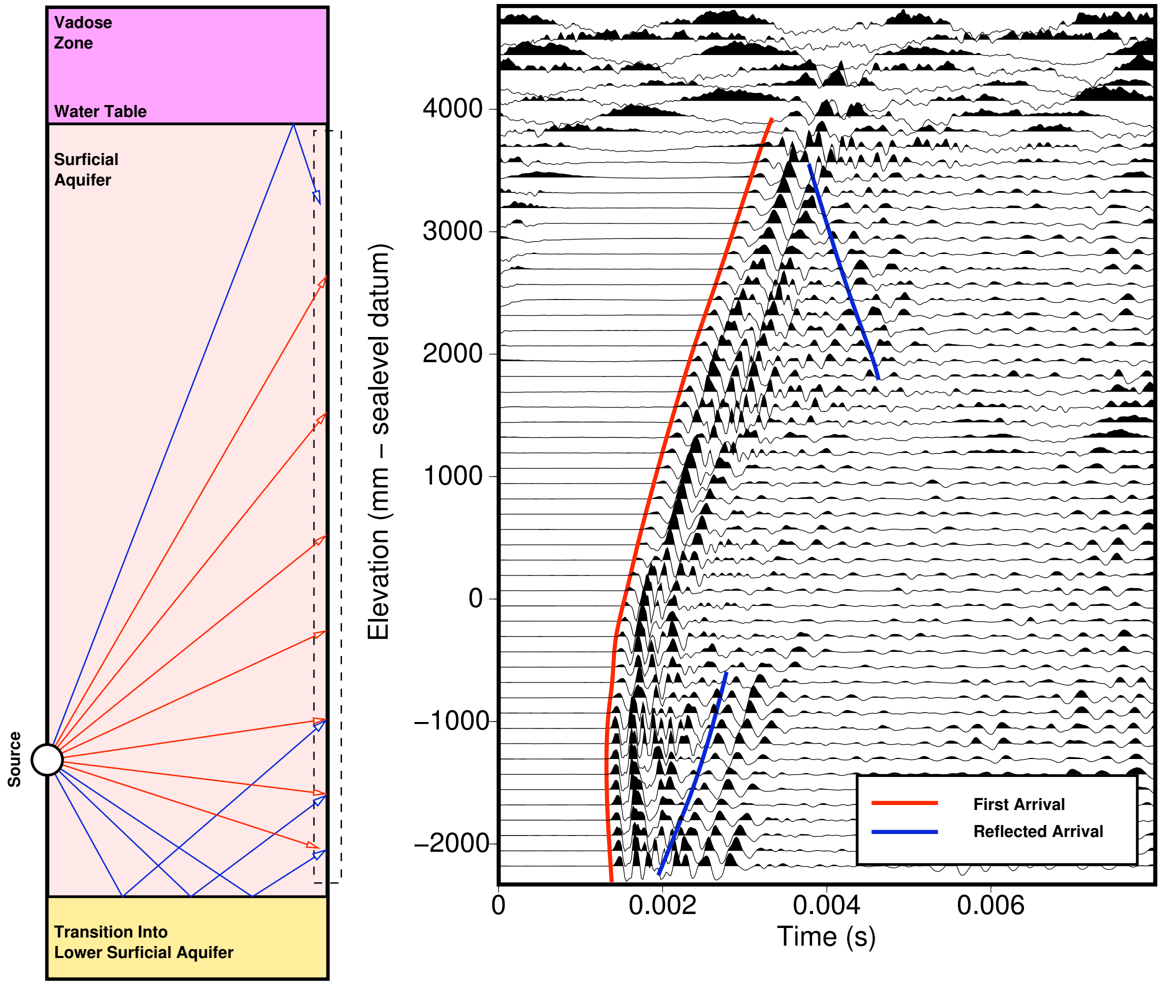

Figure 3.10: Example shot gather from the G19-G20 crosswell seismic profile : A clean primary arrival is visible in addition to reflections from the water-table and the transition into the lower surficial aquifer.

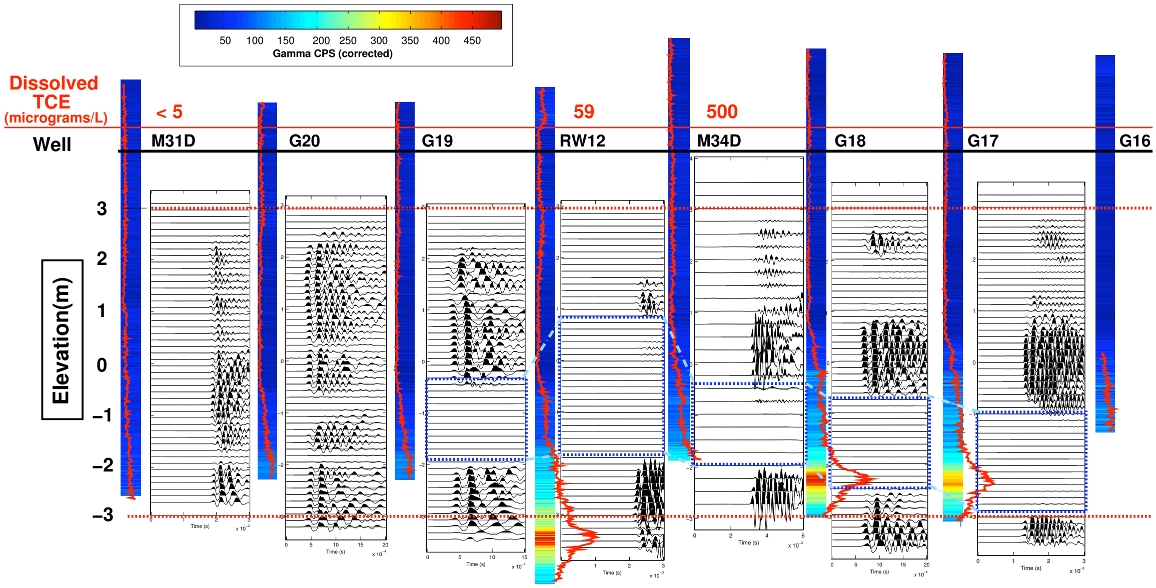

Figure 3.11: ZOFF (Zero Offset) profiles of the seismic attenuation zone : Shown are zero offset gathers for the well pairs between M31D and G16 with no energy balancing or AGC (true amplitudes). Gamma logs are included for comparison.

calibration traces were acquired before each crosswell survey. With the antennas held at a fixed distance apart in air, a medium with a known homogeneous dielectric constant, a zero-time offset was calculated for use in the subsequent profile. A source/receiver depth increment of 0.125 m was used during acquisition of our radar datasets to allow both sufficient spatial sampling and easy comparison with the similarly acquired seismic profiles. Because of the length of the radar antennas (1 m), the maximum sensor depth for our radar surveys was typically 1/2 m shallower than for the equivalent seismic profile.

Despite the use of the 200 MHz antenna set, the first-arriving wavelet in the recorded data generally had a central frequency of approximately 80 MHz indicating some degree of attenuation or problems with antenna coupling. We were not able to acquire crosswell data at long offsets due to signal loss. The G16-G12 and G18-M34D profiles in particular could not be acquired even with the use of our 100 MHz antenna pair and 256 vertical stacks at each S/R location. Figure 3.13 shows a typical set of shot gathers; this particular set was acquired as part of the G19-G20 profile with 200 MHz antenna. As can be seen from the shot gathers, very few features were visible in the recorded wavefield besides the first arrival with reflections being conspicuously absent. Also visible in figure 3.13 is the limited angular aperture of radiated EM energy. We recorded data up to the maximum allowable angle within a given geometry but typically only picked arrivals out to $\pm 50^o$ from the horizontal. From an imaging perspective this restricted aperture reduces the lateral resolving power of our crosswell radar datasets. Several general features were visible in the radar data even in raw form. Figure 3.14 shows a 200 MHz zero-offset radar profile from the G19-G20 well-pair in both true amplitude and with trace energy balancing. High apparent radar velocities above 3 m demarcate the beginning of the vadose zone while waveforms collected in the lower surficial aquifer exhibits

Figure 3.12: Crosswell Radar System : The Pulse-Ekko 100 borehole GPR system, (A) 200 MHz antennas with borehole centralizers, (B) transmitter unit with Farraday cage, (C) close-up of borehole centralizer, (D) control equipment

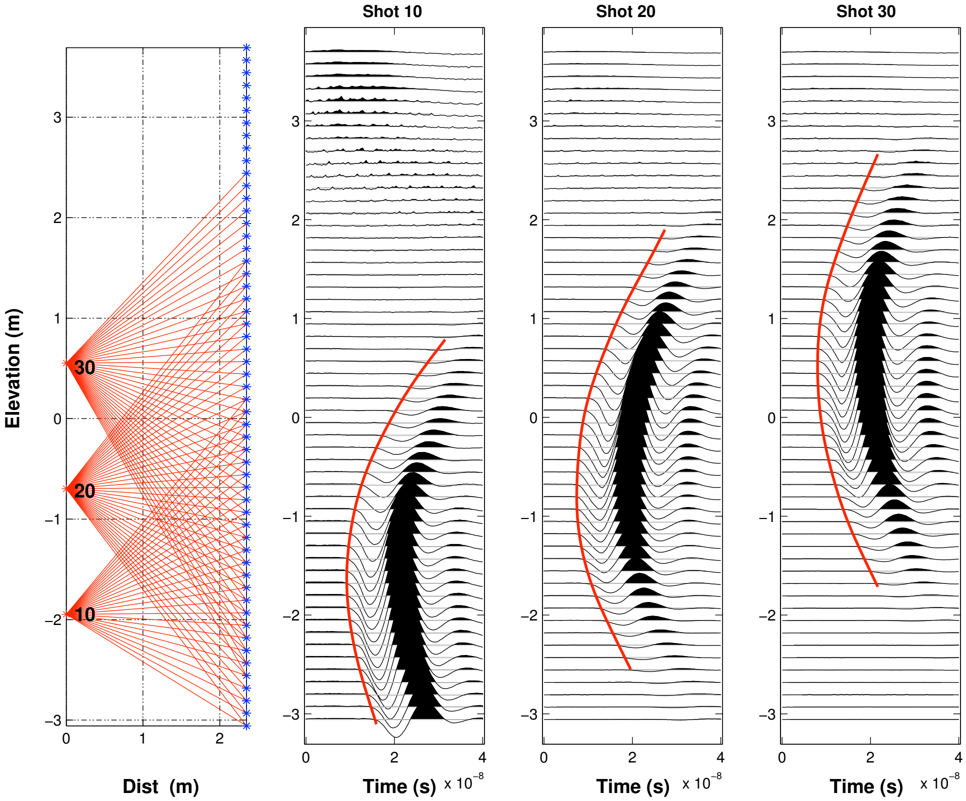

Figure 3.13: Sample radar shot gathers from G19-G20 (200 MHz antenna) : the leftmost panel shows straight raypaths for the three gathers in true spatial coordinates. First arrival picks for the three gathers are marked in red.

lower apparent velocities and amplitudes than the cleaner sands above.

3.6 VSP Seismic Datasets

During the 4th (July/August 2002) Pinellas deployment, a series of Vertical Seismic Profiling (VSP) experiments were undertaken with the goal of providing V_p, V_s, and possibly seismic Q information in both clean and contaminated regions of the NE site at lower frequencies and with larger lateral extent than previous seismic crosswell measurements. For P-wave velocity estimation purposes, the 24 channel hydrophone array described previously was equipped with a tube-wave suppressor and used to record several high-resolution datasets (up to 20 shot offsets and 52 receiver levels). A second series of short offset VSP experiments using a locking 3-component geophone were planned to provide high quality shear wave data.

Seven hydrophone VSP surveys were collected with receivers sequentially deployed in G12, G14, G17, G18, G19, and G20. Figure 3.15 shows the equipment used for the VSP measurements with an emphasis on the 3-component tool; an image of the hydrophone array and the 24 channel Geometrics seismograph were included in figure 3.9. To reduce tube-wave activity in the receiver well we constructed a simple suppressor consisting of pipe insulation (closed-cell foam) which was placed

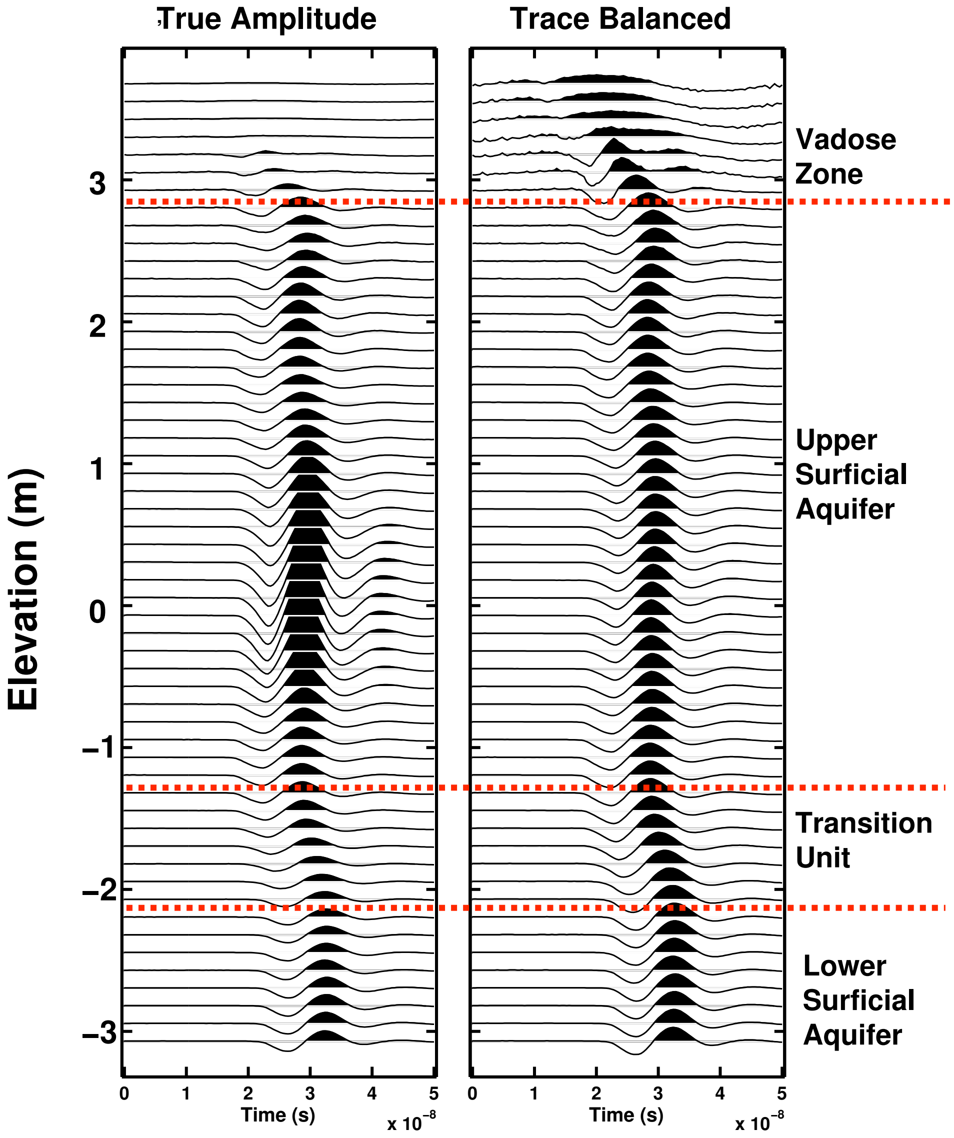

Figure 3.14: Zero offset radar gather for G19-G20 well pair : the transition into the vadose zone and the upper and lower surficial aquifer units are visible even in the in the raw section

between each hydrophone pair, similar to the scheme described by Milligan *et al.* [183]. The source sledge hammer, shown in panel (C), was swung against a steel plate. Before each shot, the steel plate was seated in the soil to reduce changes in source signature during compaction. Vertical stacking of between 4 and 8 swings were typically used to improve S/N ratio. Attempts to generate shear waves by using horizontal hammer strokes against a weighted concrete block were unsuccessful. Recording was triggered by a reed-switch mounted on the hammer shaft. Data were typically acquired out to 0.1 s at a 20.833 μs sampling rate with 200 Hz analog lowcut and 60 Hz notch filters. Although the hydrophone array had a receiver spacing of 0.5 m, multiple array positions were typically used to obtain receiver spacings of either 0.125 or 0.25 m. Data were acquired in SEG-2 format and then converted into SU and DSI formats for processing.

The surveys were collected in a format similar to the crosswell datasets where multiple shots were executed followed by a change in the depth of the receiver array. To reduce operator fatigue, the individual swinging the sledge-hammer was usually replaced after each move of the hydrophone array which unfortunately resulted in inconsistent source signatures between sub-gathers. Figure 3.16 shows this inconsistency in one of our integrated common shot gathers. As can be seen, the wavelet and aspects of the static offset vary with subgather due to differences in swing and triggering.

Figure 3.17 shows a full hydrophone VSP survey with 52 receiver levels spaced at 1/8 m. and 8 surface shot locations spaced at roughly 1 m. Although first breaks were easily picked, the central frequency of the first arriving wavelet was typically between 400 and 600 Hz, a full order of magnitude lower than our crosswell surveys. Since the average velocity in the surficial aquifer below the water table is about 1800 m/s, these frequencies are equivalent to wavelengths on the order of 3.5 m, which is greater than the mean thickness of the lower surficial aquifer. No prominent reflections or S-wave arrivals were visible although hints of a possible reflection off the Hawthorn boundary were seen in some gathers.

Two surveys were collected using an OYO locking single-level 3-component tool. Figure 3.15 shows the 3-component tool (A), the lever arms used for locking the tool (C), and the electronics associated with engaging the locking mechanism (D). The most significant problem encountered during our 3-component surveys was the failure of the locking mechanism. The Oyo 3-component borehole tool was qualitatively tested before deployment but the lever-arm assembly was unable to effectively lock the tool in our relatively small 4 in. observation wells, rendering the collected 3C data worthless. Since the deployment of the arms is driven by a DC motor/worm gear system, at low arm angles the motor lacks the torque required to lock the tool. At higher angles the arms have sufficient mechanical advantage to securely couple the tool to the borehole.

In conclusion, the combination of source signature problems, low frequency content, and locking problems with the 3-component made our VSP survey project less successful than our crosswell seismic experiments.

Figure 3.15: VSP Seismic System : single level locking 3-component downhole receiver (A), sledgehammer source (B), lever locking mechanism on the 3-component tool (C), (D) VSP surface control setup

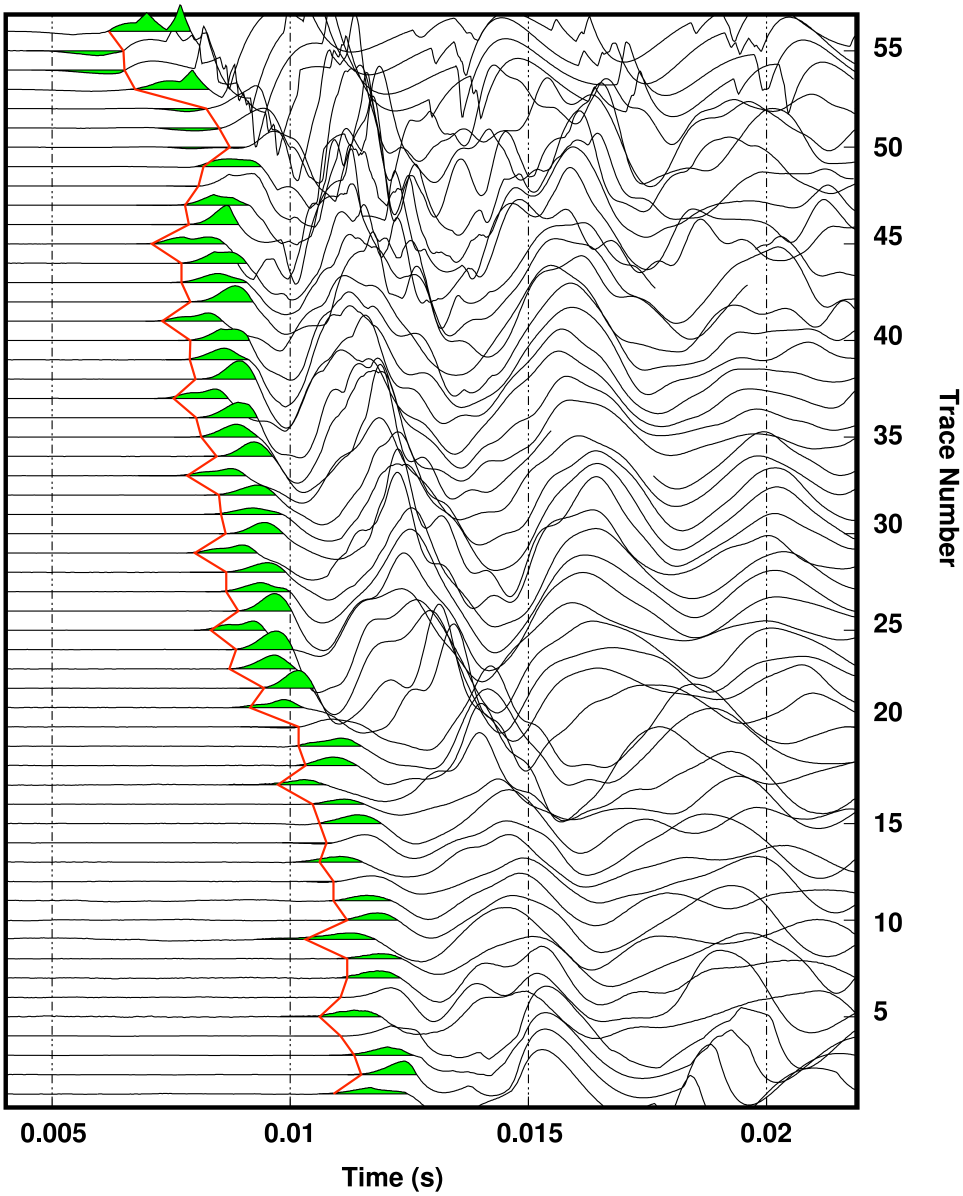

Figure 3.16: Source signature variations in a VSP gather : Oscillation in first break location correspond to shot sub-gathers with different hammer operators.(VSP survey 9, well G18, shot 1)

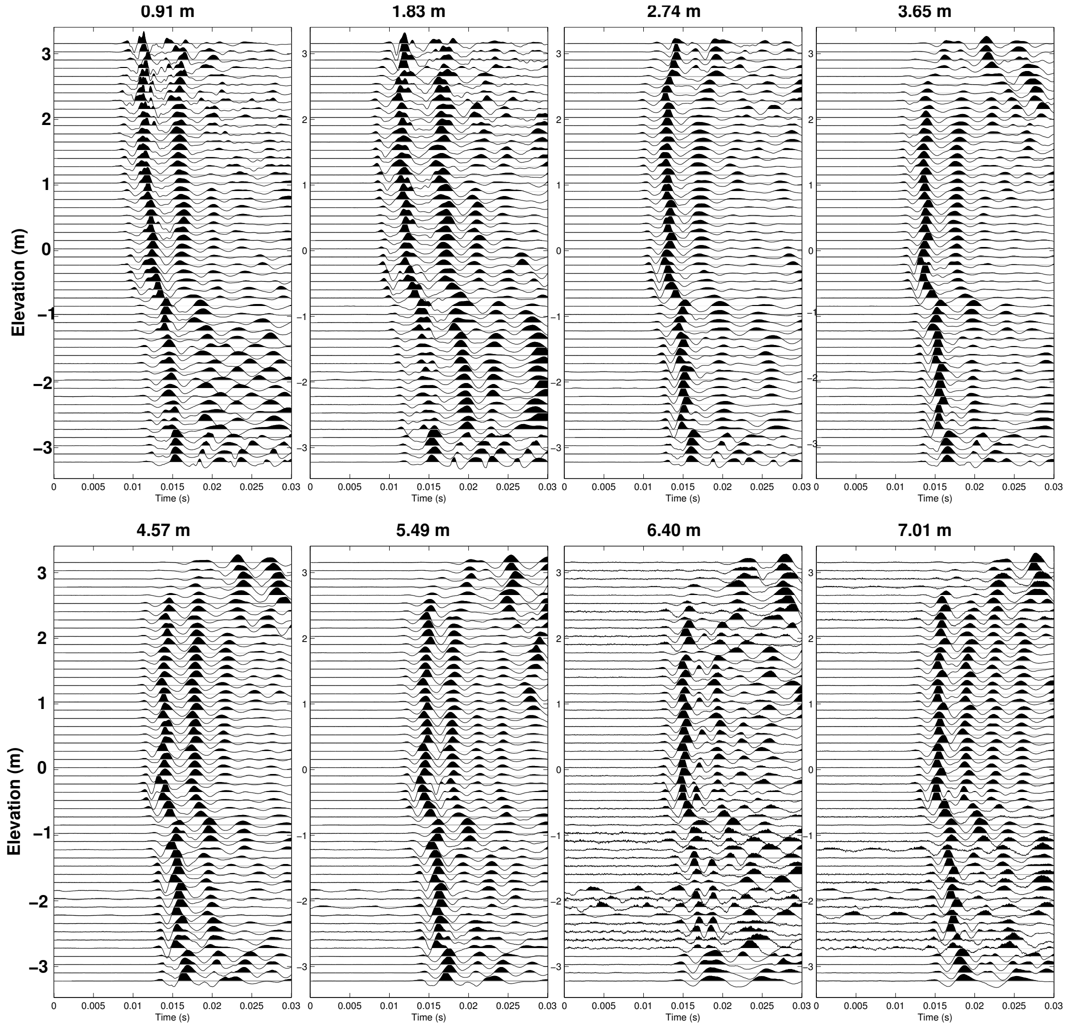

Figure 3.17: Offset gathers for G18 VSP survey 9 : A complete hydrophone VSP survey with the array deployed in well G18 and 8 surface shot locations with offsets between 0.91 and 7.01 m in a line oriented towards well RW-12.

3.7 Conclusions and Lessons Learned

As we have described in the previous sections, a variety of issues were encountered during our field efforts. In the hope of preventing future difficulties we have prepared a set of warnings and pointers for the design of future borehole experiments in near-surface environmental sites.

Take restrictions into account before selecting an experimental site At the Pinellas site there were significant restrictions on well emplacement both in terms of maximum depth and completion. When considering imaging targets, well placement, and chemical sampling strategy, insure that the site can accommodate your needs or that the experiment can be modified to fit within existing site restrictions.

Be wary of well deviation Significant well deviation can greatly complicate the processing of borehole tomographic data. When given the option, choose drilling techniques which are less susceptible to unintentional deviations. If push methods are used for well installation, insure that they are equipped to record tip location to high accuracy for later inclusion in your processing flow. Traditional gyro-deviation tools are often poorly suited for CPT wells due to their lengths (> 2 m).

Be smart about handling cores Think carefully about how to handle recovered cores within the context of your required measurements. Never transport unconsolidated cores horizontally due to the possibility of soil fluidization. If spatial distribution of pore fluids is an important aspect of your measurement, subsection the core in the field and collect fluid samples before transport. Label every core shipped with information concerning well, orientation, and original depth.

Sonic logging is difficult in soft sediments Sonic logs are generally difficult to acquire in soft sediments. Do not expect spectacular results, particularly in the top 20 m. Consider tool length when planning your logging experiment since longer tools (> 2.5 m) may not be particularly useful in shallow wells. Insure that the logging acquisition program can save waveform files to a publicly known format and not a proprietary one requiring secondary software.

Gamma logs are quick and handy Gamma logs, while not the most quantitative measurement for near-surface geophysics, are extraordinarily useful. They are very fast to acquire, have excellent depth resolution, and are sensitive to important variations in lithology related to clay content. A days worth of gamma logging can provide a quick way of building a preliminary site lithology model in cases where wells already exist.

Use care with non-repeatable seismic sources When acquiring sledge-hammer seismic data, carefully consider the source signature as a function of operator and location. If two operators have different "swings", insure that surveys are collected consistently to prevent later processing headaches. Consider the use of a more repeatable surface source such as an accelerated weight drop system.

Consider the effects of small boreholes on tools Borehole tools that perform well in typical oil-field scenarios are often poorly suited for near-surface acquisition. Test your tools before deployment to insure reasonable performance in 2 and 4 inch wells. In the case of downhole seismic measurements, locking force is a crucial consideration and may be dependent on borehole dimensions.

During the Pinellas geophysics investigation we succeeded in acquiring a substantial dataset consisting of high resolution crosswell seismic and radar data and a suite of well logs for constraining site lithology. When combined, our 20 crosswell seismic profiles covered a 40 x 7 m vertical plane of the site which is substantial considering the estimated 40 cm wavelength [9] of the acquired seismic data. Few experiments mentioned in the literature achieve this combination of spatial extent and high resolving power. Similarly the combined acquisition of both crosswell seismic and radar data with compatible scales and geometries is unusual and provides an excellent opportunity for integrated data interpretation. In the following chapters we will apply modern tomographic algorithms to our site dataset in an attempt to identify features associated with DNAPL contamination and develop a more complete model of site lithology.

---

[9] The 40 cm wavelength is the result of $\lambda = v/f$ using a 4 kHz central frequency (a conservative estimate) and a P-wave velocity of $\sim$ 1600 m/s.

Chapter 4

The Geophysical Properties Of Pure DNAPLs And DNAPL Mixtures

For a DNAPL to be detectable using any remote sensing technique, the contaminant must have different physical properties than the background saturating fluid which it displaces. In the saturated zone, fluids with geophysical characteristics distinct from water have the most potential for remote detection. Estimates of DNAPL properties are a required component of both forward modeling studies and quantitative interpretation of imaging results. In general, DNAPLs have a higher density, a lower acoustic wave velocity, and a lower dielectric constant than water.

In this chapter we provide a survey of the geophysical properties of the most common DNAPLs and a short investigation of applicable effective fluid models for understanding homogeneous contaminant mixtures. More importantly, we will provide an estimate for the typical properties of the DNAPL phase encountered at Pinellas through use of mixture models and compositional data obtained from contaminants recovered at the site. The DNAPL phase recovered closest to the geophysical survey profile was composed primarily of trichloroethylene, toluene, and a heavy oil. The extracted DNAPL had an experimentally measured density of 1030 kg/m^3. Our best estimate of the properties of this contaminant phase at Pinellas suggests a dielectric constant of ~ 2.7 and an acoustic velocity of ~ 1340 m/s. A DNAPL target with similar properties would generally have a good radar signature at high contaminant saturations but a significantly smaller seismic response.

4.1 DNAPLs Defined : Basic Properties

As explained in previous chapters, Dense Non-Aqueous Phase Liquids or DNAPLs are a family of fluids which includes some of the most problematic industrial contaminants such as the chlorinated solvents trichloroethylene (TCE) and tetrachloroethylene (PCE). In this section we present a short literature survey of acoustic velocity, density, and dielectric constant measurements for an important subset of commonly encountered dense chlorinated contaminants. Viscosity and surface tension data are included to allow exploration of contaminant signatures within the context of poroelastic or contact theory models. When possible we provide the results of multiple laboratory measurements and document the temperature, pressure, and frequency dependence of the examined properties. Preference is given to results from recent papers over handbook values due to the difficulty in determining the conditions and experimental apparatus used for the latter class of data.

4.2 Basic Chemical, Regulatory, And Toxicological Properties

Table 4.1 lists the most commonly used chlorinated solvents ranked by annual production [212] with tabulated values for solubility, EPA maximum allowable contaminant levels (MCLs), and basic chemical information. Benzene and toluene, two common light NAPL contaminants, and water are included for reference. Because DNAPLs are denser and often less viscous than water (see Table 4.2), they easily penetrate deep into the saturated zone and pond at low permeability barriers [152]. As DNAPLs slowly dissolve in the saturated zone, they produce large plumes of contaminated ground water although most of the pollutant mass remains in concentrated pools. The low absolute solubility of most DNAPLs insures that the total pollutant mass mobilizes slowly; some contaminant pools have estimated life-times of several centuries. However, these fluids often have high solubilities relative to EPA toxicity limits making DNAPL plumes long-term groundwater hazards unless properly treated. Most chlorinated solvents have aqueous solubilities 4 to 5 orders of magnitude greater than the EPA's maximum allowable contaminant level (MCL) (see Table 4.1). Chlorinated solvents also typically have high vapor pressures and low boiling points, properties which facilitate volatilization in the vadose zone.

Although chlorinated solvents vary in toxicity, all have both acute and chronic health effects on humans. PCE is a well studied DNAPL useful as an example of the properties characteristic of chlorinated solvents. PCE is acutely toxic at high levels [23], has demonstrated carcinogenic effects in animals and is thought to be a carcinogen for humans [246] [165]. Furthermore, PCE has negative effects on the human reproductive system [83] [229]. Carbon tetrachloride, another common DNAPL, is a confirmed hepatotoxin [94] [72] [171]. The degradation byproducts of chlorinated solvents are sometimes as toxic as the original compound, as is the case with vinyl chloride (VC).VC, which precedes ethene in the reductive dechlorination of PCE [176], is a relatively potent carcinogen [46].

4.3 The Geophysical Properties Of Chlorinated Solvents: A Survey

Table 4.2 presents the results of a collection of several acoustic and dielectric measurements on common dense chlorinated solvents. The first eight chemicals are ranked by total U.S. production in 1986 in millions of kilograms [212]. Letters following each measurement denote the appropriate reference and experimental conditions found in Table 4.6. For the purpose of comparison we also present data on other common organic substances (toluene and benzene) and water.

Tables 4.3, 4.4, and 4.5 document a smaller subset of experiments which provide insight into the temperature dependence of density, acoustic velocity, and dielectric constant for the same fluids. Measurement sets were individually fit using linear models and the resulting coefficients are included.

Table 4.6 provides the reference codes and information on the condition under which each measurement was performed if an experimental description was available. In addition to fluid temperature, we also provide the frequency of both the acoustic and dielectric measurements.

4.3.1 Acoustic Properties

The most basic parameters for understanding the seismic response of a fluid are density (ρ) and compressional wave velocity (V_p). Within the geophysics community, little attention has been paid to the acoustic properties of DNAPLs; the most studied fluids besides water are the light hydrocarbons present in petroleum mixtures [269]. The existing database of acoustic velocity values for chlorinated solvents are found almost entirely within the physical chemistry and chemical engineering literature; most of the papers cited measure pure solvent velocities as end-members of binary and ternary mixture experiments. The majority of the measurements use interferometric methods at ultrasonic frequencies, typically between 1 and 3 MHz. Freyer *et al.* [101] describe an early interferometric instrument operating at 0.4 MHz. A smaller number of experiments use time domain techniques; Pellam and Galt [214] use a pulsed reflection measurement apparatus to make both velocity and attenuation measurements at 15 MHz. Eggers and Kaatze [89] provide an excellent review of ultrasonic measurement techniques for liquids, including both CW and pulse methods.

For the chlorinated solvents examined, the ultrasonic velocities ranged between 906 and 1177 m/s, considerably slower than the speed of sound in pure water, $\approx$ 1500 m/s. The densities were higher than that of water, with 1,2-dichloroethane being the lightest at 1238 kg/m^3 and PCE the densest at 1606 kg/m^3. Table 4.2 includes dynamic bulk moduli calculated from the most recent and consistent combination of velocity and density data using $K = \rho V_p^2$. Table 4.2 also includes fluid viscosity to allow easy calculation of the poroelastic properties of solvent saturated soils.

Tables 4.3 and 4.4 detail the temperature dependence of density and acoustic velocity for the same solvents. For each fluid, multiple measurements were fit using a linear relation of the form,

$$P(T) = A + BT, \tag{4.1}$$

where A and B are fitting coefficients, P is the property being investigated, and T is temperature in ^oC. To the best of our knowledge, the V_p and ρ values for the solvents listed have a linear temperature dependence in the range of 5 to 50 ^oC; however, some caution should be applied in cases where the listed property models are based upon a small number of data points. For all of the DNAPLs discussed in this paper, V_p and ρ decrease with increasing temperature. For the density fits, B, the gradient of ρ with respect to T, were between -1.649 and -4.3 kg/(m^3 ^{o} C) for the chlorinated solvents. B values for V_p were between -3.3 and -4.75 m/(s ^{o} C). Interestingly, the B coefficient for water displays the opposite sign with V_p increasing with temperature. Column 2 of Tables 4.3 and 4.4 are extrapolations of the linear models to 20 ^{o} C to allow easy comparison between fluids. Column 5 of Tables 4.3 and 4.4 specify the range of temperatures for which property values were available with the number of measurements used for the fit specified in brackets.

Acoustic velocity and density were observed to increase with increasing pressure for all of the solvents for which data were available; see the excellent review by Oakley *et al.* [206] [207] and the early experimental paper by Swanson [247] for pressure data on chloroform and carbon tetrachloride. Bobik [36] measured pressure dependent velocity changes in benzene on the order of 4.76 m/(s MPa) between 0 and 20 MPa at 17 ^oC, a low enough gradient to allow neglecting pressure effects on V_p in near-surface environments. Pure fluid attenuation measurements (see [214], [122] and others) are not tabulated here but are typically very small in comparison to the intrinsic attenuation of near-surface materials, particularly between the quasistatic state and 10 MHz where few molecular relaxation mechanisms occur. Direct measurements of velocity dispersion in pure liquids are relatively rare, particularly for low frequencies, but existing data suggest that the frequency dependence of acoustic velocity in pure chlorinated solvents is insignificant below 50 MHz. Andreae [21] provides velocity dispersion data from a variety of sources for methylene chloride between 7.54 and 209 MHz at 25 ^oC. Over the decade from 7.54 to 70 MHz he observed a change in velocity of only 5 m/s. More significant velocity changes occur in methylene chloride near a relaxation peak at approximately 480 MHz [22]. Cartensen [52] measured acoustic velocity dispersion between 0.3 and 10 MHz in water, a natural oil (LNAPL), and condensed milk at 32 ^oC. For both the water and oil samples less than 1 m/s variation in acoustic velocity occurred over the decade from 1 to 10 MHz.

4.3.2 Dielectric Properties

One of the most essential parameters for understanding the electromagnetic (EM) signature of a fluid is the relative dielectric permittivity or dielectric constant. While we begin with a very general formulation for such properties described by Knight [143], we will quickly adopt a simplified notation geared towards high frequency measurements.

In the most general case, the total frequency-dependent dielectric permittivity, ϵ_T, can be expressed as,

$$\epsilon_T(\omega) = \left[\epsilon'(\omega) + \frac{\sigma''(\omega)}{\omega}\right] - i \left[\epsilon''(\omega) + \frac{\sigma'(\omega)}{\omega}\right], \tag{4.2}$$

where ϵ' and ϵ'' correspond to dielectric polarization and energy losses due to polarization effects, σ' and σ'' denote ohmic conduction and losses due to Faradaic diffusion respectively, and ω is angular frequency. For convenience we will drop the functional notation for ϵ and σ components; their frequency dependence is implicit in the following formulas unless otherwise noted. In the high-frequency case we can assume that $\sigma''/\omega \approx 0$ and that σ' is dominated by the DC component, σ_{dc}, simplifying equation 4.2 to,

$$\epsilon_T(\omega) = \epsilon' - i\left[\epsilon'' + \frac{\sigma_{dc}}{\omega}\right]. \tag{4.3}$$

The term *dielectric constant* is used to refer to ϵ values normalized by the permittivity of free space, ϵ_o. We use κ^* to denote the total complex frequency dependent dielectric constant which, in the high frequency case, can be expressed as,

$$\kappa^* = \kappa' - i\left(\kappa'' + \frac{\sigma_{dc}}{\omega\epsilon_o}\right) \tag{4.4}$$

In cases with low conductivity, high measurement frequencies, and a small κ'' loss term, the second term in the RHS of equation 4.4 is negligible and $\kappa^* \sim \kappa'$. The values reported in the experimental papers referred to in this chapter are for κ', although several provide auxilliary data for κ''. At low frequencies, dielectric properties are typically measured using capacitance bridges [264] while resonant cavities [115] [20] and network analyzers [147] are used in the MHz and GHz range.

All DNAPLs are effectively non-polar with dielectric constants at room temperature ranging from 2.24 for carbon tetrachloride to 10.95 for 1-2,dichloroethane. Displacement of water, a polar fluid with a dielectric constant of 80.1 at 20 ^oC, is believed to be largely responsible for generating the radar signatures observed in laboratory [215] [99] [10], mesoscale [132] [41], and controlled field scale monitoring experiments [224] [44] [116] [43]. Table 4.5 summarizes the sensitivity of dielectric constant to variations in temperature. All of the solvents examined exhibit decreasing dielectric constants as a function of increasing temperature. Available temperature data were fit to the same linear model as equation 6.20, with the B coefficient again indicating the gradient of dielectric constant with respect to temperature. The value of B is relatively small for the chlorinated solvents (-0.002 to -0.05) in comparison to that of water (-0.346). Dielectric constants were observed to be weakly dependent on pressure. Mopsik [186] measured the pressure dependence of carbon tetrachloride's dielectric properties; fitting a linear model to his data at 25 ^oC yields a gradient of 0.0016 per MPa, a value small enough to be negligible in near-surface scenarios. For pure chlorinated solvents, no significant variation in κ' occurs between 10 kHz and 1 GHz. Von Hippel [264] presents frequency dependent dielectric values for tetrachloroethylene and carbon tetrachloride; in both cases κ' is constant between 100 Hz and 3 GHz.

Compound	**Empirical Formula**	**Mol. Weight** ($\frac{g}{mol}$)	**Annual Prod.** ($10^6 \frac{kg}{yr}$) [212]	**Solubility** (in water) ($10^{-6} \frac{kg}{L}$) [185]	**EPA MCL** ($10^{-6} \frac{kg}{L}$)	**Vapor Pressure** (Torr@20C) [185]	**Boiling Point** (C) [185]
1,2-Dichloroethane	$C_2H_4Cl_2$	98.96	5871	8690	0.005	64	83.5
1,1,1-Trichloroethane	$C_2H_3Cl_3$	133.40	294	1360	0.2	90	74.1
Carbon Tetrachloride	CCl_4	153.82	284	800	0.005	90	76.5
Methylene Chloride	CH_2Cl_2	84.93	255	20000	0.005	348	40.2
Chloroform	$CHCl_3$	119.38	191	8000	0.01	160	61.7
Tetrachloroethylene	C_2Cl_4	165.83	184	150	0.005	14.2	121.2
Trichloroethylene	C_2HCl_3	131.39	75	1100	0.005	57.8	87.2
Properties Of Other Common Substances							
Benzene	C_6H_6	78.11	-	1780	0.005	76	80.1
Toluene	C_7H_8	92.14	-	515	1	22	110.6
Water	H_2O	18.02	-	-	-	17.5	100

Table 4.1: Production levels and physical properties for the most common chlorinated solvents. Data on benzene, toluene, and water are provided for the purpose of comparison

4.4 The Properties Of Contaminant Mixtures

While the properties of pure DNAPLs are well understood, the contaminants found at most environmental sites are complex mixtures containing both the original substances and the products generated by weathering and biodegradation. Often, existing documentation of the waste disposal process are vague enough to lack utility in the prediction of DNAPL properties; in many sites both the volume and original components of the contaminant are unknown. Sampling and chemical analysis of DNAPLs from monitoring wells can provide clues as to the geophysical properties of the contaminants *in situ*. In the ideal case, comprehensive lab scale geophysical measurements would be made on extracted DNAPL samples to establish the properties of the contaminant before acquisition of field data. In practice, many sites do not have DNAPL samples for analysis (hence the need for detection) and even in cases where samples do exist they are often destructively analyzed for information on chemical fractions and are not available for geophysical measurements. We will first consider the case where an estimate of the chemical components of the contaminant phase and their relative fractions are available, obtained from either sampling information or prior knowledge of disposal history at the site. Even without detailed information on fractions, we can often bound the properties of the composite considering a selection of likely NAPLs.

Given the components present in a contaminant phase, we can use effective fluid models to estimate the acoustic and dielectric properties of the mixture. Additionally, separate phases can also be averaged in the same manner to yield a single effective fluid for every point in the subsurface. In this section, we will provide several potential models for estimating the characteristics of fluid mixtures. We will also attempt to delineate the situations where these models are likely to fail, thus requiring laboratory confirmation of mixture properties.

Before embarking on a detailed discussion of effective fluid models, a distinction should be drawn

Compound	**Density** ρ $(\frac{kg}{m^3})$	**P-Wave Velocity** V_p $(\frac{m}{s})$	**Bulk Modulus** K $(10^9\ Pa)$	**Dielectric Constant** κ	**Absolute Viscosity** [180] η $(10^{-3}\ Pa \cdot s)$	**Surface Tension** [180] T_s $(10^{-3}\ \frac{N}{m})$
1,2-Dichloroethane	1238 (a)	1173 (a)	1.703		0.887	35.3
		1177 (b)		10.08 (b)	$[15^{o}C]$	
	1238 (d)	1174 (d)		10.95 (c)		
1,1,1-Trichloroethane	1321 (e)	943 (e)	1.175	7.252 (f)	0.903	28.28
	1329 (a)	942 (a)		7.52 (g)	$[15^{o}C]$	
Carbon Tetrachloride	1584 (i)	918 (i)	1.335	2.240 (f)	0.965	29.49
	1594 (h)	935 (h)		2.241 (j)	$[20^{o}C]$	
		906 (k)		2.213 (k)		
Methylene Chloride	1336 (l)	1093 (l)	1.596	9.14 (j)	0.449	30.41
	1316 (i)	1052 (b)		8.62 (b)	$[15^{o}C]$	
		1053 (m)		8.72 (m)		
Chloroform	1489 (h)	1003 (h)	1.498	4.84 (j)	0.596	29.91
	1476 (i)	985 (i)			$[15^{o}C]$	
		968 (m)		4.66 (m)		
Tetrachloroethylene	1606 (a)	1027 (a)	1.694	2.29 (b)	1.932	32.86
	1606 (d)	1030 (d)		2.28 (o)	$[15^{o}C]$	
Trichloroethylene	1451 (t)	1015 (t)	1.495	3.335 (t)	0.566	29.5
	1451 (q)	1014 (q)		3.409 (r)	$[20^{o}C]$	
				3.42 (s)		
Properties Of Other Common Substances						
Benzene	866 (u)	1276 (u)	1.410	2.253 (v)	0.6028	28.9
	879 (h)	1324 (h)			$[25^{o}C]$	
		1276 (k)		2.268 (k)		
Toluene	866 (h)	1328 (h)	1.527		0.552	30.90
	862 (z)			2.381 (z)	$[20^{o}C]$	
		1283 (k)		2.365 (k)		
Water	998 (z2)	1482 (z2)	2.192	78.36 (z3)	1	72

Table 4.2: Geophysical properties of common chlorinated solvents. Letters refer to experiments detailed in Table 4.6. Temperatures and measurement frequencies for density, acoustic, and dielectric measurements are also included in Table 4.6. Bulk moduli are calculated from tabulated velocity and density data ($K = \rho V_p^2$). Note the temperature sub-headers for viscosity values

Compound	**Density**				
	@ 20^o C (kg/m^3)	**A** (kg/m^3)	**B** ($kg/(m^3\ ^oC)$)	Range [pnts] (^oC)	Reference
1,2-Dichloroethane	1267.1	1353.1	-4.302	25-30 [2]	[194] (ac)
1,1,1-Trichloroethane	1338.4	1372.4	-1.698	16-40 [2]	[164] (ad)
Carbon Tetrachloride	1594.1	1632.7	-1.929	0-50 [6]	[101] (h)
Methylene Chloride	1325.7	1363.9	-1.910	25-35 [3]	[17] (i)
Chloroform	1488.6	1526.7	-1.908	0-50 [6]	[101] (h)
Tetrachloroethylene	1622.8	1655.8	-1.649	30-40 [2]	[261](n)
Trichlorethylene	1468.1	1520.3	-1.950	30-50 [3]	[221] (ae)
Benzene	879	900.4	-1.072	10-50 [5]	[101] (h)
Toluene	866	884.6	-0.940	0-50 [6]	[101] (h)
Water	998.2	1001.9	-0.2	0-30 [4]	[71] (z2)

Table 4.3: The temperature dependence of density. **A** and **B** are fitting coefficients for the linear models. All curves were interpolated/extrapolated to 20 ^oC for comparison (column 2). Range column indicates the range of temperatures used for the linear fit and the number of measurement points.

Compound	**Acoustic Velocity**				
	@ 20^o C (m/s)	**A** (m/s)	**B** ($m/(s^oC)$)	Range [pnts] (^oC)	Reference
1,2-Dichloroethane	1217	1297	-4.0	30-40 [2]	[199] (b)
1,1,1-Trichloroethane	-	-	-	-	-
Carbon Tetrachloride	938.6	1004	-3.27	0-50 [6]	[101] (h)
Methylene Chloride	1089	1163	-3.7	20-30 [2]	[199] (b)
Chloroform	1001.4	1070	-3.44	0-50 [6]	[101] (h)
Tetrachloroethylene	1059	1125	-3.3	30-40 [2]	[199] (b)
Trichlorethylene	1050	1120	-3.5	30-40 [2]	[199] (b)
Benzene	1325.9	1421	-4.75	10-50 [5]	[101] (h)
Toluene	1322.7	1414	-4.29	0-50 [6]	[101] (h)
Water	1482.3	1407	3.55	0-30 [4]	[71](z2)

Table 4.4: The temperature dependence of acoustic velocity. **A** and **B** are fitting coefficients for the linear models. All curves were interpolated/extrapolated to 20 ^oC for comparison (column 2). Range column indicates the range of temperatures used for the linear fit and the number of measurement points.

Compound	Dielectric Constant				
	@ 20^o C	**A**	**B** $(1/^oC)$	Range [pnts] (^oC)	Reference
1,2-Dichloroethane	10.95	11.977	-0.0506	10-45 [8]	[61] (c)
1,1,1-Trichloroethane	7.242	7.962	-0.0360	5-20 [4]	[162] (f)
Carbon Tetrachloride	2.240	2.281	-0.0020	3-22 [14]	[162] (f)
Methylene Chloride	9.140	10.014	-0.0433	0-40 [5]	[188] (j)
Chloroform	4.841	5.212	-0.0185	0-50 [6]	[188] (j)
Tetrachloroethylene	2.297	2.365	-0.0034	25-30 [2]	[198] (o)
Trichloroethylene	3.409	3.525	-0.0062	16-30 [3]	[252] [253] (r) [197] (k)
Benzene	2.284	2.312	-0.0014	14-50 [5]	[13] (ab)
Toluene	2.38	2.420	-0.0020	15-35 [3]	[191] (af)
Water	80.10	87.164	-0.3465	5-55 [10]	[20] (ag) [79] (g)

Table 4.5: The temperature dependence of dielectric constant. **A** and **B** are fitting coefficients for the linear models. Note that κ is dimensionless. All curves were interpolated/extrapolated to 20 ^oC for comparison (column 2). Range column indicates the range of temperatures used for the linear fit and the number of measurement points.

between homogeneous mixtures, composed of miscible fluids, and heterogeneous mixtures which include multiple phases. We adopt the definition of homogeneous mixtures used in the physical chemistry and chemical engineering communities in order to maintain consistency with the experimental papers discussed. In this context, homogeneous refers to mixing occuring on the molecular scale i.e. a combination of miscible fluids. In common geophysical parlance, the term homogeneous requires specification of an effective scale length over which the system can be viewed as uniform. The effective fluid models discussed below will typically be valid only in cases of *ideal* mixing, situations where there is marginal distortion of molecular packing due to interaction between the two chemical species. When interaction does occur, density, bulk modulus, and dielectric constant can change in unexpected ways as a result of some preferential repacking. Hydrogen bonds between the two types of molecules might be formed, adding an additional attractive force. In physical chemistry, mixtures of this type are referred to as *non-ideal* [27]. In the same nomenclature, *excess properties* are used to describe the difference between ideal and non-ideal physical characteristics. In this section, the bulk of the data presented will be from experiments investigating the properties of homogeneous mixtures of organic compounds. These results are most relevant to predicting the properties of the composite DNAPL phases present at the Pinellas site. However, the same models may have some utility in describing the effective properties of multiphase mixtures; this case will be discussed in more detail in the following chapters.

4.4.1 Effective Fluid Models : Acoustic

The Reuss model predicts the effective bulk modulus of a fluid mixture by assuming that all fluid components experience the same stress (the *isostress* assumption) [173] [233]. If K_{fl} is the effective bulk modulus of the fluid mixture, K_i is the bulk modulus of each fluid component, and f_i is the

Code	**Reference**	**Cite**	**Temp.** (C)	**EM Freq.** ($10^6 hz.$)	**Aco. Freq.** ($10^6 hz.$)
a	Krishnaiah (1996)	[148]	30	-	2
b	Nath and Saini (1990)	[199]	30 [30:40,2]	1.8	2
c	Corradini et.al. (1996)	[61]	20 [-10:80,17]	2	-
d	Kumari et.al. (2002)	[153]	30	-	4
e	Sekhar et.al. (2001)	[237]	30	-	4
f	Van Loon et.al. (1967)	[162]	19.8 [-25:20,10]	0.1	-
g	Lange's Handbook (1992)	[79]	20	*	-
h	Freyer et.al. (1929)	[101]	20 [0:50,6]	-	0.414
i	Aminabhavi et.al. (1998)	[17]	25 [25:35,3]	-	0.004
j	Morgan and Lowry (1930)	[188]	20 [-30:70,11]	0.1	-
k	Nath and Dubey (1980)	[197]	30 [30:40,2]	1.8	2
l	Lagemann et.al. (1948)	[155]	20	-	0.5
m	Nath and Tevari (1992)	[201]	30 [20:30,2]	1.8	2
n	Venkatesulu et.al. (1997)	[261]	30 [30:40,2]	-	-
o	Nath and Narain (1982)	[198]	25 [25:35,2]	1.8	-
p	Nath and Dixit (1984)	[196]	25 [25:35,2]	-	2
q	Iloukhani et.al. (1999)	[130]	30		1
r	Timmermans et.al. (1955)	[253]	20	0.5	-
s	Walden and Werner (1924)	[266]	16	36 (*)	-
t	Nath (1995)	[195]	30	1.8	3
u	Weissler (1949)	[271]	30	-	3
v	Sastry et.al. (1999)	[232]	35	3	-
w	Pellam and Galt (1946)	[214]	21.8 [7.5:21.8,2]	-	15
x	Nath and Singh (1986)	[200]	30 [30:40,2]	-	2
y	Ritzoulis et.al. (1986)	[225]	25 [15:25,3]	2	-
z	Mopsik (1969)	[186]	25 [-50:25,4]	*	-
z2	D'Arrigo and Paparelli (1987)	[71]	20 [-40:30,8]	-	10
z3	Al-Azzawi et.al. (1990)	[15]	20 [25:55,4]	1	-
ab	Akhadov (1980)	[13]	[14:50.3,5]	*	-
ac	Mussari et.al. (2000)	[194]	[25:30,2]	-	-
ad	Lorenzi et.al. (1996)	[164]	[16:40,2]	-	-
ae	Prasad et.al. (2002)	[221]	[30:50,3]	-	-
af	Moumouzias et.al. (1997)	[191]	[15:35,3]	2	-
ag	Anderson et.al. (2000)	[20]	[5:55,10]	25-250	-

Table 4.6: Reference codes and experimental conditions. Where measurements at multiple temperatures are available, the [C:D,N] notation denotes N measurements ranging from temperature C to temperature D. The first number in the temperature column corresponds to the measurements conditions for the experimental values in Table 4.2. References where measurement frequency were unclear or not specified are marked with a *.

appropriate volumetric fraction, the Reuss model can be written as,

$$K_{fl} = \left(\sum_{i=1}^{n} \frac{f_i}{K_i} \right)^{-1} \tag{4.5}$$

To estimate fluid velocity, a model of mixture density must also be assumed. A simple weighted average of the densities is used in cases where non-ideal mixing effects are absent,

$$\rho_{fl} = \sum_{i=1}^{n} f_i \rho_i \tag{4.6}$$

Combining the two models allows calculation of the velocity of a fluid mixture,

$$V = \sqrt{\frac{K_{fl}}{\rho_{fl}}} = \sqrt{\frac{\left(\sum_{i=1}^{n} \frac{f_i}{K_i} \right)^{-1}}{\sum_{i=1}^{n} f_i \rho_i}} \tag{4.7}$$

Velocity predictions from the Reuss model should be valid when mixing occurs at a scale significantly smaller than the wavelength of the acoustic signal, as is certainly the case for homogeneous mixtures. Since the Reuss effective fluid model has been extensively used to predict the properties of reservoir rocks saturated with inhomogeneous water/oil and water/gas mixtures [82] we will delay discussion of the validity of multiphase effective fluid property estimates until the chapter on the acoustic properties of water/DNAPL/soil composites.

A quick examination of several previous ultrasonic measurements of homogeneous binary liquid mixtures reveals a range of possible behavior. Nath and his colleagues [197] [198] [201] [195] have closely studied the acoustic properties of trichloroethylene (TCE) when mixed with related chlorinated solvents and other organic compounds. As a first example, we will consider the ultrasonic velocities of TCE/toluene mixtures, measured by Nath and Dubey [197]; this mixture class is particularly relevant to contamination at the NE Pinellas site where Toluene and TCE are the two most prevalent NAPL components. The TCE/toluene binary mixing experiment was performed at both 30 and 40 ^oC using a 2 MHz acoustic interferometer. We consider only the low (30 ^oC) temperature data. Figure 4.1 shows the mixture velocity with changing volumetric TCE fraction [1]. Plotted next to the measurements is the expected Reuss velocity (equation 4.7) assuming ideal mixing and no excess density effects.

The pure toluene velocity agrees well with values available elsewhere in the literature [101]. The maximum and average differences between measured and Reuss velocities are 1.542 % and 0.875 % respectively. Looking only at this experiment, the Reuss model appears to work well with mixtures of organic liquids. The existence of small deviations from ideal properties is taken to be indicative of some intermolecular re-configuration. These deviations can probably be ignored for estimating the response of a field-scale seismic experiments where sensitivity to fluid velocity variations on the order of 1% is seldom achieved. One should note that both TCE and toluene are non-polar molecules

---

[1] Nath and Dubey [197] and many other researchers report binary mixture properties in terms of molar fractions which require conversion to volume fractions before application of traditional mixing laws.

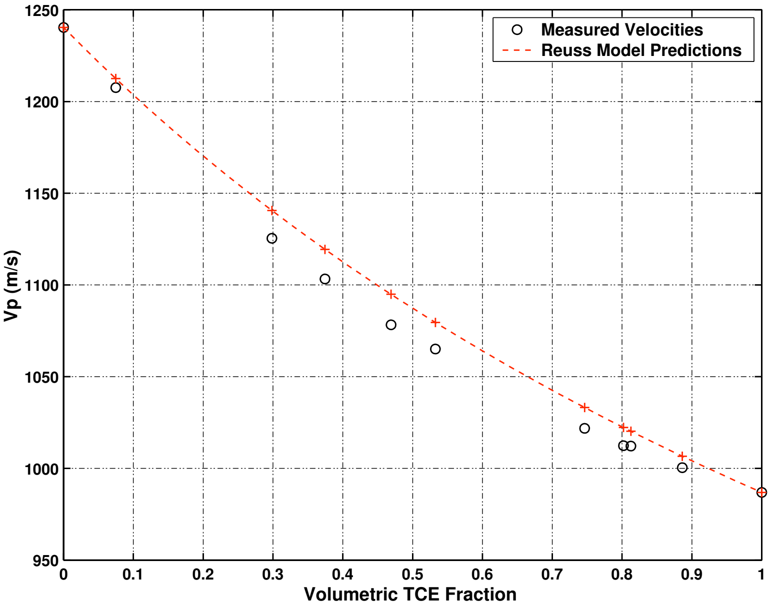

Figure 4.1: Measured V_p vs Reuss predictions for TCE/Toluene mixtures. Data from Nath and Dubey [197].

with dielectric constants of 3.337 and 2.365 respectively. In such cases, London Dispersion forces will be the dominant contributor to long-range intermolecular behavior.

The results of later experiments by Nath on TCE/pyridine systems [195] are similar. Pyridine (C_5H_5N) is an organic liquid with a molecular weight of 79.1 g/mol, a density of 972.84 kg/m^3, and a V_p of 1399 m/s [195]. We plot the data from the measurement performed at 30 Celsius using a 3 MHz interferometer with an estimated accuracy of 1 m/s (see Figure 4.2). In this case, the deviation from the Reuss model is very small ; the maximum and average differences between measured and Reuss velocities are 0.20 % and 0.08 % respectively.

In the previous cases the mixed fluids were non-polar or weakly polar. The most common solvent in the earth however is water, a highly polar molecule with a dielectric constant of approximately 80.1 at room temperature. D'Arrigo and Paparelli examined the acoustic and excess density properties of water/ethanol mixtures [71]. Ethanol (C_2H_5OH) is a polar fluid fully miscible in water with a density of 789 kg/m^3, a molecular weight of 46.07 g/mol, and a V_p of 1182 m/s at 20 ^oC. Figure 4.3 is a plot of one water/ethanol experiment performed at 20 ^oC using a 10 MHz thermostatted phase comparison apparatus. Large deviations from Reuss velocity exist at volumetric ethanol fractions of only 5 % where a 13.6 % departure from the iso-stress estimate is apparent (229 m/s). Averaging across all mixture fractions, an 5.5 % deviation from Reuss velocity exists (87 m/s). The same paper also provides excess density measurements which show a peak difference of 30 kg/m^3 from simple density estimates based on arithmetic means.

The unusual behavior of water mixtures is not fully understood but complex water-solute and water-water hydrogen bonding is probably the basic cause. One useful conceptual model views changes in non-ideal water mixture properties as fluctuations in the number of water molecules

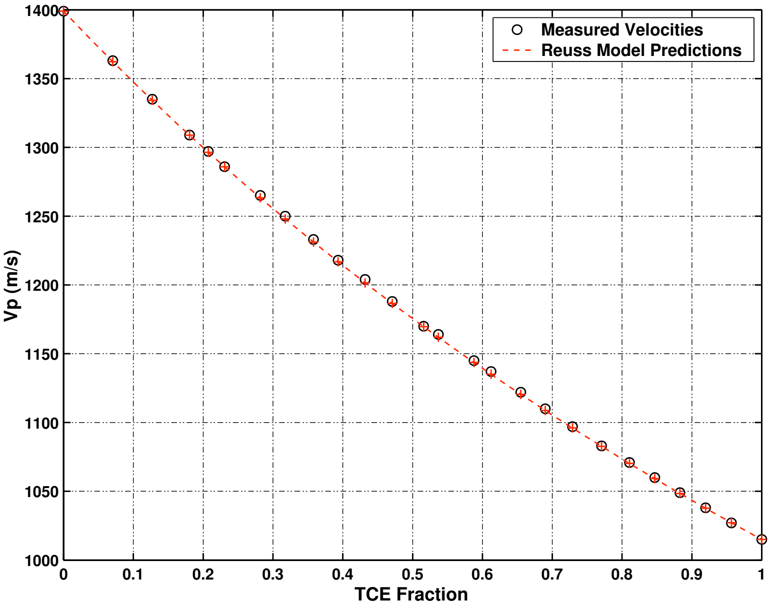

Figure 4.2: Measured V_p vs Reuss predictions for TCE/Pyridine mixtures. Data from Nath [195].

which are locally H-bonded to solute molecules and to each other. Solute molecules might form the core of stiffer water-solute subunits or promote development of ordered water structures nearby, sometimes referred to as a solvation or hydration shell. D'Arrigo and Paparelli [71] hypothesize that ethanol molecules fill “cages” of water molecules to produce a stiffer intermolecular system. Unfortunately, a full review of water micro-structure theories is beyond the scope of this work.

From this short preliminary review of existing measurements two conclusions can be drawn. First, homogeneous mixtures of non-polar or weakly polar liquids, while exhibiting small deviations from ideal behavior, can be modeled using Reuss effective fluid theory when high accuracy is not required. A second tentative conclusion is that the Reuss model is not suitable for describing miscible systems that include water or other polar solvents. In these cases, laboratory calibration of fluid mixture velocities and densities is probably required.

4.4.2 Effective Fluid Models : Dielectric

Many of the same questions concerning ideal mixing behavior apply to contaminant dielectric properties. While the dielectric behavior of water/DNAPL/soil composites will depend on the distribution of the various phases, we limit our discussion of effective dielectric properties to homogeneous mixtures of DNAPLs and save discussion of multiphase issues for chapter 5. We consider the Complex Refractive Index Model (CRIM) and arithmetic and harmonic volumetric means for estimating fluid mixture properties.

The Complex Refractive Index Model (CRIM) [227] [92] provides a useful form for estimation of the effective dielectric properties of multiphase materials. The model is only strictly valid for one dimensional layered composites in the ray theoretic limit, although in practice CRIM is often

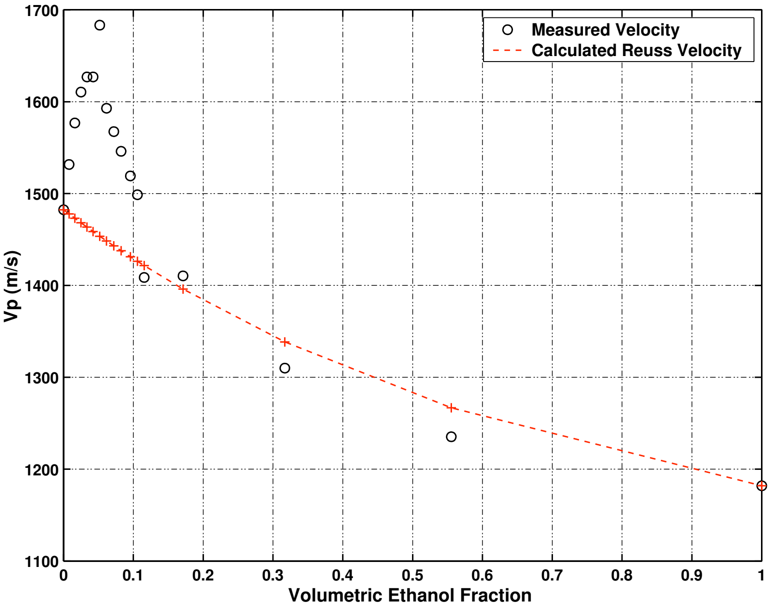

Figure 4.3: Measured V_p vs Reuss predictions for Water/Ethanol mixtures. Data from D'arrigo and Paparelli [71] recorded at 20 ^oC and 10 MHz

effective at modeling the properties of more complex composites. CRIM can be considered as a special instance of the more general Lichtnecker-Rother mixing equations with a fixed γ exponent of $\frac{1}{2}$ [173] [118]. The effective dielectric constant, κ_{eff} can be written in terms of the volumetric fractions f_i and dielectric values κ_i of the constitutive phases,

$$\kappa_{CRIM} = \left[\sum_{i=1}^{N} f_i\sqrt{\kappa_i}\right]^2 \tag{4.8}$$

Nath and Dubey [197] and Nath and Saini [199] use a simple arithmetic average to estimate the dielectric properties of TCE/toluene and TCE/methyl ethyl ketone mixtures respectively. They assume that any deviation from such an average is evidence of non-ideal mixing behavior. We will consider such an arithmetic mean (Equation 4.9) and the harmonic mean (Equation 4.10) as alternative ad-hoc mixing laws,

$$\kappa_A = \sum_{i=1}^{N} f_i\kappa_i \tag{4.9}$$

$$\kappa_H = \left[\sum_{i=1}^{N} \frac{f_i}{\kappa_i}\right]^{-1} \tag{4.10}$$

Figure 4.4 shows the dielectric properties of TCE/toluene mixtures at 30 ^oC as measured at 1.8 MHz [197]. The CRIM model generates a reasonable fit with maximum and mean relative deviations from the experimental data of 2% and 0.2% respectively.

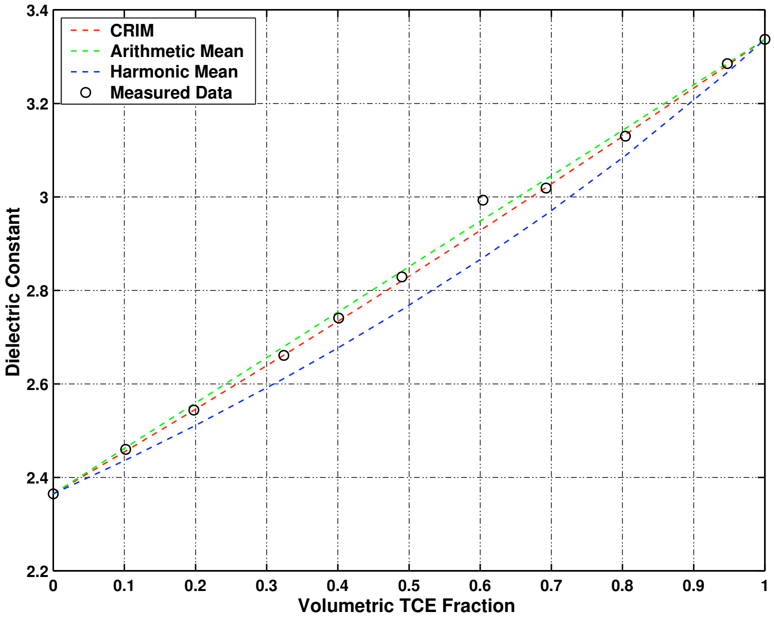

Figure 4.4: Measured κ vs mixing law predictions for TCE/toluene mixtures. Data from Nath and Dubey 1980 [197]. Comparison of CRIM 4.8, arithmetic 4.9 and harmonic 4.10 averages.

Similar results were obtained from examining measurements of carbon tetrachloride and 1,1,1-trichloroethane mixtures [162] as well as carbon tetrachloride and methylene chloride mixtures [188]. From these existing datasets we can conclude that the CRIM model is usually a reasonable approximation for the dielectric constants of homogeneous mixtures of non-polar and weakly polar fluids.

4.5 Understanding DNAPLs At Pinellas

To conclude this chapter, we will apply the pure fluid database and effective fluid models discussed in the previous sections and attempt to generate the properties of an idealized DNAPL characteristic of the Pinellas NE site. The composition of a given DNAPL phase *in situ* can vary across a contaminated site due to differences in the contaminant source and the distribution of secondary solutes; the fluid we construct should be thought of as a best guess for the average properties of the dense contaminants at Pinellas. The alternative is to assume the existence of a single pure DNAPL phase such as TCE. Since we have some chemical sampling and bulk fluid property measurements available to constrain the mixture, the creation of a composite DNAPL seems reasonable.

InformaWe adopt the definition of homogeneous mixtures used in the physical chemistry and chemical engineering communities. In this case, homogeneous refers to mixing occuring on the molecular scale i.e. a combination of miscible fluids. In geophysics, the term homogeneous requires specification of an effective scale length over whiichtion concerning the composition of DNAPLs at Pinellas comes from direct well sampling, fluids extracted from soil samples, and fluids recovered from remediation procedures. During October of 2000, DOE personnel extracted a mixture of light and dense NAPLs from recovery wells RW03, RW06, and DRW05. Visual observations of NAPLs were made at wells RW10, RW11, 0533, M17D, and M35D but no samples were recovered. Figure 4.5 shows a fluid sample from well RW06 with distinct light and dense non-aqueous phases. The DNAPL sample recovered from RW06 is the closest to our region of investigation and will provide the primary constraints for the model fluid.

Figure 4.6 shows the relative location of the wells with recovered NAPLs with respect to the crosswell imaging profiles.

The DNAPL phase [2] recovered from RW06 was analyzed by a DOE subcontractor using gas chromatography and mass spectrometry (GCMS) according to EPA methods 8260 and 8100. Bulk density and boiling point distributions were also measured on samples from the same fluid phase. The density measurements revealed that the DNAPL samples from RW06 and RW03 were only marginally denser than water with values of 1030 kg/m^3 and 1010 kg/m^3 respectively. Assuming that these measurements are correct, this implies that the DNAPL phase must consist of a homogeneous mixture including both light and dense components. GCMS results revealed that the RW06 sample was a complex mixture including large amounts of toluene and trichloroethylene with smaller quantities of cis-1-2-dichloroethylene, methylene chloride and PCE. Semi-volatile compounds detected pesticide 4,4'-DDD, butyl benzyl phthalate, dimethyl phthalate, and phenol. Secondary GCMS measurements characterized the RW06 sample's consistency as approximately 27 % heavy oil and 0.6 % dense chlorinated solvents by volume with the remaining fraction unaccounted for. Commentary from the analytical laboratory suggested that the GC signature of the oil fraction was consistent with used 10W-30 motor oil or a similar compound. Since 10W-30 oils are relatively light (880 kg/m^3) and no significant amounts of dense non-chlorinated substances were detected, either the bulk density value or the GC derived compositional information is incorrect.

Since bulk density is generally a simple measurement to make in comparison to quantitative GCMS, we assume that the density values are correct and treat the sample as a mixture of a volatile organic component and heavy oil with the ratio between the two determined by the measured density. The volatile organic solvent fraction is assumed to have the same relative composition as that determined by GCMS. The density constraint on contaminant volume fractions can be posed using a simple volume weighted mean,

$$\left(\frac{V_v}{V_v + V_o}\right)\rho_v + \left(\frac{V_o}{V_v + V_o}\right)\rho_p \;=\; \rho_t, \tag{4.11}$$

where V_v and V_o are the volumes of the volatile and oil fractions, ρ_v and ρ_o are the corresponding fluid densities, and ρ_t is the density of the mixture. Solving equation 4.11, for the volume ratio of the oil and volatile components yields

$$\frac{\rho_v - \rho_t}{\rho_t - \rho_o} = \frac{V_o}{V_v}. \tag{4.12}$$

---

[2] At this point we should note that the DNAPL samples collected were, in fact, single phases and not heterogeneous mixtures of DNAPL components. No density partitioning was visually observed in the DNAPL component and the different constituent chemicals, as determined by GCMS, are fully miscible.

Compound	**% By Mass**	**% By Volume**	**Bulk Density** (kg/m^3)
cis-1,2-Dichloroethylene	0.9	0.85	1284
Methylene Chloride	7.9	6.96	1317
Tetrachloroethylene (PCE)	1.4	0.74	1615
Toluene	37.9	50.68	862
Trichloroethylene (TCE)	52.1	40.77	1472

Table 4.7: Composition Of The Volatile Fraction of the RW06 DNAPL sample as determined by GCMS

Figure 4.7 provides the mass and volume fractions of the primary volatile organic components of the RW06 DNAPL sample as determined by GCMS. The resulting density value, ρ_v, is 1151 kg/m^3.

We use the properties of Havoline 10W-30 motor oil for the oil phase. Kajfez *et al.* [136] determine the dielectric constant of both clean and dirty 10W-30 oil at 10 GHz using a resonant cavity method. Both fluids had a relative permittivity of 2.2 although the dirty oil had a significantly higher loss tangent. Unpublished measurements compiled by A. Selfridge of Specialty Engineering indicate that a generic SAE30 motor oil has a density (ρ_o) of approximately 880 kg/m^3 and an acoustic velocity of 1700 m/s. The use of this V_p value introduces some uncertainty due to small differences between the SAE30 and 10W-30 oil blends.

Since ρ_t, the bulk density of the recovered DNAPL at RW06, was experimentally measured to be 1030 kg/m^3 we can now use Equation [4.12] to calculate the oil and volatile organic fractions of the sample. The result is a mixture of 55.5 % volatiles and 45.5 % heavy oil. Using an *in situ* temperature [3] of 25 ^oC we can estimate the properties of the DNAPL phase using the mixing laws outlined in the previous section. From these calculations we estimate that the DNAPL phase has a dielectric constant of 2.7 and an acoustic velocity of 1341 m/s in addition to the measured density of 1030 kg/m^3. The velocity value has a larger uncertainty due to the lack of velocity measurements on 10W-30 oil blends and the differences between the clean and weathered oil properties *in situ*. Based on the property contrasts between this characteristic DNAPL and water (V_p = 1482 m/s, ρ = 998 kg/m^3, κ = 80.1), we might expect that a DNAPL target with similar properties would generally have a good radar signature at high contaminant saturations but a significantly smaller seismic response. The theoretical and experimental exploration of this hypothesis is the topic of the next two chapters.

---

[3] A minor factor to consider is the fluid temperature *in situ*. Measurements from Pinellas monitoring wells have shown groundwater temperature to be depth dependent with higher temperatures (up to +30 ^oC) at shallow depths. Temperatures also exhibits annual variations of approximately 2 ^oC. We used data from quarterly monitoring results from both shallow and deep wells at M17, M31, and M34 monitoring locations to generate an average groundwater temperature of 24.6 ^oC [7] which we will use in subsequent calculations of fluid properties. As mentioned in the previous sections of this chapter, fluid pressures up to 1 MPa have a negligible effects on bulk fluid properties; consequently we will neglect pressure effects in the following estimates.

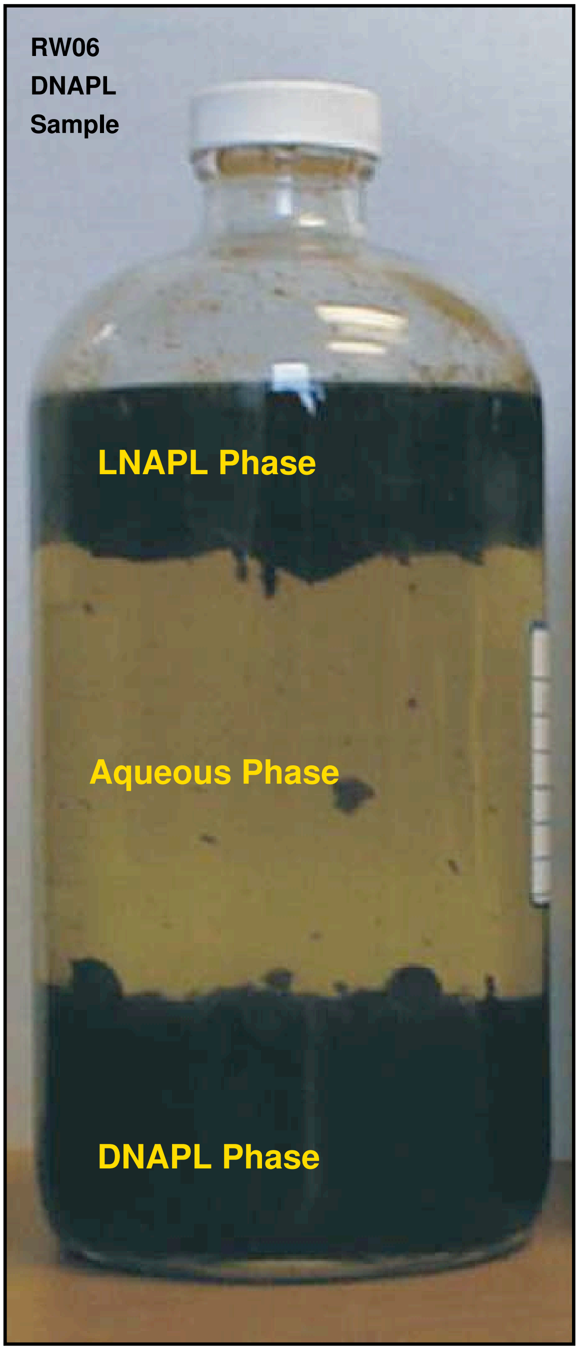

Figure 4.5: Photograph of the 3 phase sample extracted from well RW06

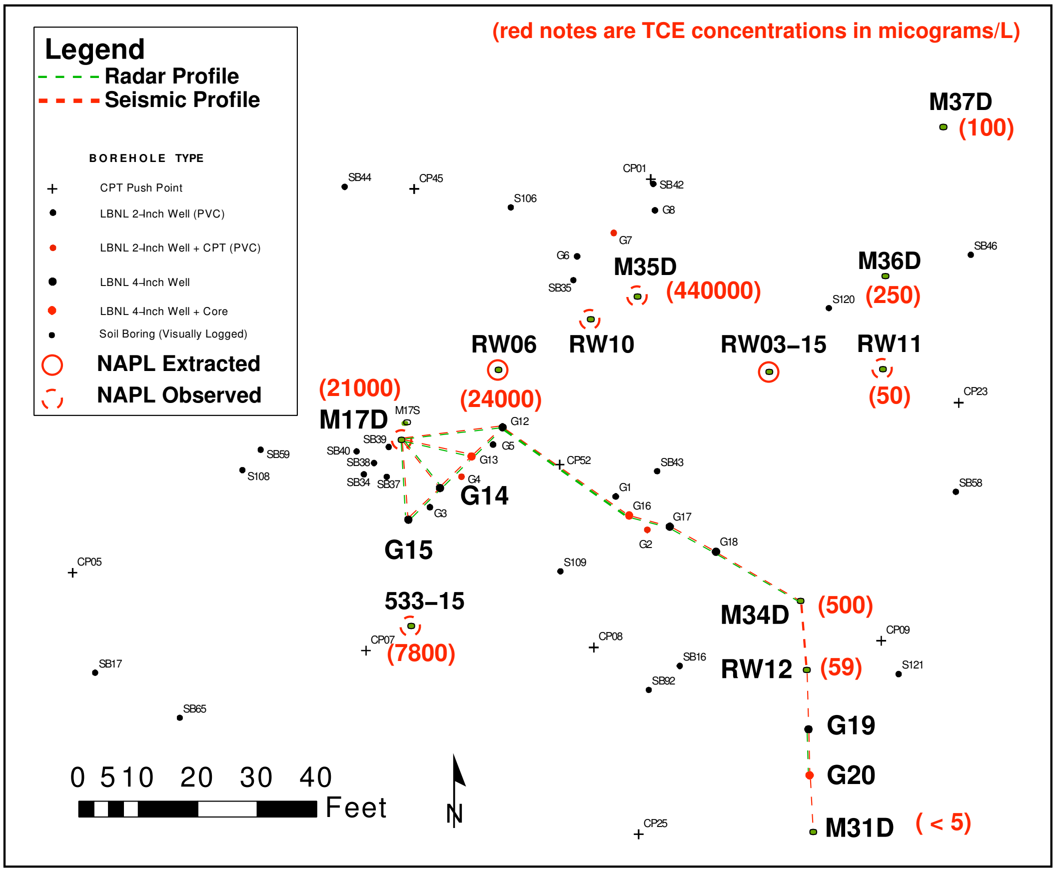

Figure 4.6: Section of the Pinellas NE site-map depicting NAPL recovery locations and aqueous phase TCE concentrations. Red numbers are aqueous phase TCE concentrations in micrograms/L as collected in the April 2002 sampling campaign.

Chapter 5

The Dielectric Properties Of DNAPL Saturated Granular Media

Ground penetrating radar (GPR) is the only geophysical technique which has been used successfully on the field-scale for the monitoring of DNAPLs *in situ*, albeit in the context of a carefully controlled experimental site. During the controlled field-scale experiments carried out by the Solvents-In-Groundwater program [224] near Borden Air Force Base, Ontario, changes in radar reflectivity and transmission characteristics were observed during the injection of tetrachloroethylene (PCE) into a sandy aquifer. From a monitoring perspective, the reflection radar datasets were very successful, tracking the migration of the PCE volume through a series of pools to depths of up to 3 m [43] [44]. The most significant components missing from the Borden experiment were appropriate core-scale calibration experiments to quantify the dielectric signature of PCE saturation in soil.

The goal of this chapter is to place radar-based DNAPL detection on firm petrophysical footing by developing an experimental and theoretical framework for understanding the dielectric properties sediments partially saturated with free-phase contaminants in the laboratory. We will present the results of five new laboratory experiments investigating the dielectric properties of Pinellas sediment samples partially saturated with trichloroethylene (TCE), a common dense non-aqueous phase contaminant. We performed broadband dielectric measurements using a time domain reflectometry (TDR) system coupled to a solvent-compatible coaxial transmission line. Two synthetic samples and three natural aquifer samples from the Pinellas site were fully saturated with water and then slowly flooded with TCE. The resulting dielectric measurements show good agreement with the semi-empirical complex refractive index model (CRIM) and the self-similar Bruggeman-Hanai-Sen (BHS) effective medium model [239]. The use of these models allows us to provide a reasonable prediction of the radar reflectivities and transmission velocities expected in field surveys targeting pools of similar non-aqueous contaminants. Based on our best estimate of soil properties at the Pinellas site and the characteristics of the extracted DNAPL phase we predict that high radar velocity is a likely geophysical signature of free-phase contamination at Pinellas. At physically reasonable DNAPL saturations on the order of 40 % we expect a increase in radar velocity of between 26 and 36 % with respect to the water saturated state with variations depending on matrix porosity. However, the non-uniqueness introduced by variations in matrix properties or by the introduction of small amounts of gas prevents a unique inversion for DNAPL saturation using only radar velocity information.

5.1 Dielectric Properties And Radar Signatures

Although most DNAPLs have physical properties distinct from water, the detection of such fluids strongly depends on the characteristics of the porous matrix. The porosity of the matrix obviously limits bulk contaminant content. Below the water table, wetting behavior can also limit peak contaminant saturation. Both of these factors limit the possible radar and seismic signatures of contaminated sands. An important fact to note is that most soils have a dielectric constant between 4 and 8 [202] [264] [140] close to that of TCE (3.35 [195]) and other organic solvents. Consequently, the radar signature of DNAPLs is largely dependent on the displacement of water and not on the contaminant itself. Although field radar measurements do not directly measure the spatially varying dielectric constant, they can obtain information on the apparent radar velocity and reflectivity.

Before continuing with our discussion of DNAPL signatures, we will clarify the measurement terminology and the relationship between dielectric properties and related observables. While we begin with a very general formulation for such properties described by Knight [143], we will quickly adopt the simplified notation used within the TDR community, similar to the form described by Topp *et. al* [255]; this formalism is geared specifically towards high frequency measurements.

In the most general case, the total frequency-dependent dielectric permittivity, ϵ_T, can be expressed as,

$$\epsilon_T(\omega) \;=\; \left[\epsilon'(\omega) \;+\; \frac{\sigma''(\omega)}{\omega}\right] \;-\; i\;\left[\epsilon''(\omega) \;+\; \frac{\sigma'(\omega)}{\omega}\right], \tag{5.1}$$

where ϵ' and ϵ'' correspond to dielectric polarization and energy losses due to polarization effects, σ' and σ'' denote ohmic conduction and losses due to Faradaic diffusion respectively, and ω is angular frequency. For convenience we will drop the functional notation for ϵ and σ components; their frequency dependence is implicit in the following formulas unless otherwise noted. In the high-frequency case we can assume that $\sigma''/\omega \;\approx\; 0$ and that σ' is dominated by the DC component, σ_{dc}, simplifying equation 5.1 to,

$$\epsilon_T(\omega) \;=\; \epsilon' \;-\; i\;\left[\epsilon'' \;+\; \frac{\sigma_{dc}}{\omega}\right]. \tag{5.2}$$

The term *dielectric constant* is used to refer to ϵ values normalized by the permittivity of free space, ϵ_o. Following Topp *et al.* [255] we will use κ^* to denote the total complex frequency dependent dielectric constant which, in the high frequency case, can be expressed as,

$$\kappa^* = \kappa' - i\left(\kappa'' + \frac{\sigma_{dc}}{\omega\epsilon_o}\right) \tag{5.3}$$

Our one departure from the traditional notation used in the TDR community is our choice of a negative sign convention for the imaginary component of κ^*. In cases with low conductivity, high measurement frequencies, and a small κ'' loss term, the second term in the RHS of equation 5.3 is negligible and $\kappa^* \sim \kappa'$.

Our experimental system does not measure κ components directly but rather captures the velocity at which a broad-band electromagnetic pulse propagates through a sample. The frequency dependent phase velocity of EM wave propagation (V_{EM}) through a homogeneous, non-magnetic medium can be expressed as,

$$V_{EM} = \frac{c}{\sqrt{\kappa' \frac{1+\sqrt{1+\tan^2\delta}}{2}}} \tag{5.4}$$

where c is the velocity of light in a vacuum and δ is the loss tangent, defined as,

$$\tan\delta = \frac{\kappa'' + \frac{\sigma_{dc}}{\omega\epsilon_o}}{\kappa'} \tag{5.5}$$

If $\kappa^* \sim \kappa'$ as mentioned previously, V_{EM} can be written in a highly simplified form as,

$$V_{EM} \approx \frac{c}{\sqrt{\kappa'}}. \tag{5.6}$$

Equation 5.6 is often used for the interpretation of TDR and GPR data [255] [60].

For the range of frequencies used in subsurface radar, the dependence of κ' on f is weak and $\kappa'' << \kappa'$ [73]. The assumption of frequency independence is only a reasonable approximation in the frequency range above Maxwell-Wegner polarization effects and below the molecular relaxation peaks for polar fluids (f < 5 GHz). Small amounts of clay can also introduce significant EM dispersion; in clay-rich soils a more detailed examination of V_{EM} as a function of frequency is required. In the case of our own laboratory experiments we assume σ_{dc} to also be negligible because of the low clay content in our samples and the use of DI water as the primary saturating fluid.

Transmission radar geometries are often used for direct tomographic reconstructions of V_{EM} as a function of space. Surface GPR reflection surveys are sensitive to variations in radar reflectivity which, for normal incidence angles, TE mode wave propagation, and two non-magnetic layers, can be written as

$$R_{EM} = \frac{\sqrt{\kappa_1} - \sqrt{\kappa_2}}{\sqrt{\kappa_1} + \sqrt{\kappa_2}} \tag{5.7}$$

where κ_1 and κ_2 are the dielectric constants of the top and bottom layers [73]. Both crosswell and surface methods have the potential to detect DNAPLs in ideal circumstances. Although the direct detection of DNAPLs is non-trivial, time-lapse measurements are significantly simpler since interpretation ambiguities due to lithologic changes are eliminated.

5.2 Previous Core Scale Investigations

Several experimental and theoretical works have examined the impact of fluids besides water on bulk electromagnetic properties of rocks and soils. However, only one known experiment has examined the dielectric properties of DNAPL saturated granular materials [231] and none have investigated the properties of clean sands partially saturated with DNAPLs. Because of this gap in the literature, we also include experiments where the effects of LNAPL saturation are considered. Experiments using clay or sand/clay mixtures as the porous matrix are difficult to interpret due to the presence of both volumetric and complicated interfacial effects relating to bound fluids on clay platelets. Regardless of these difficulties, all measurements made to date have shown that the replacement of water with a non-polar or weakly polar fluid phase decreases the bulk dielectric constant of the porous composite.

Sen *et al.* [239] performed a series of experiments measuring the dielectric constant of fused glass bead packs fully saturated with either water, methanol ($\kappa = 30$), or air at a variety of porosities. The authors used a TM mode resonance cavity to make dielectric measurements at approximately 1.1 GHz. The resulting values fit Sen's self-similar effective medium model. This experiment, while not examining NAPLs or partial saturation, provided an excellent demonstration of the effects of fluid dielectric constant on bulk properties.

Kutrubes [154] made a series of frequency domain measurements examining the dielectric properties of sand and montmorilonite saturated with benzene and methanol. Kutrubes focused on measurement technique and unfortunately could not provide the dependence of dielectric constant on contaminant saturations.

Porokhovoi *et al.* [217] used a Rhode & Schwartz ZPV-Z5 S-parameter test set to make frequency domain dielectric measurements (200 MHz - 1.2 GHz) on synthetic sand/clay mixtures (77/23%) using benzene, heptane, xylene, acetone, and toluene as saturating contaminants. The resulting experiments consider contaminant fractions of between 1.15% and 13.8% by weight. Their results are difficult to interpret in terms of fluid effects due to the limited number of saturation levels examined (3) and the lack of experiments involving clean sand samples.

Santamarina and Fam [231] measured the complex dielectric permittivity of soil/pollutant mixtures, using benzene, xylene, toluene, tetrachloroethylene (PCE), trichloroethylene (TCE), and chlorobenzene as organic pollutants. Kaolinite and bentonite clays were used to as the porous matrix. Measurements were made between 0.2 and 1.3 GHz using an HP-8752A network analyzer and an HP-85070A dielectric probe. Although significant changes in dielectric properties were noted in both clays after injection of TCE, the relationship between complex permittivity and TCE saturation was not quantitatively determined.

Kaya and Fang [137] measured the dielectric constant and conductivity of bentonite and kaolinite saturated with methanol, anilene, and different brine solutions at 13 MHz using an HP 4192A LF impedance analyzer. Their results were difficult to interpret due to unexpected soil flocculation effects.

Persson and Berndtsson [215] investigated the dielectric properties of synthetic soils partially saturated with sun-flower seed oil (SFSO) using the time domain reflectometry method. Their measurements were performed using a three-prong TDR probe and a Tektronix 1502C cable tester to measure the dielectric constants of homogenized sand/water/NAPL mixtures. They used the Lichtnecker-Roth mixing model with a saturation dependent geometry coefficient to fit their dataset.

Fransisca and Rinaldi [99] performed frequency domain dielectric measurements on silica sand, kaolinite, and loess samples partially saturated with paraffin and lubricant oils. Measurements were made using an HP 8752A network analyzer and an HP 85070A dielectric probe at frequencies between 20 MHz and 1.3 GHz. They conclude that both the CRIM and self-similar effective medium models provide adequate prediction of the effects of NAPL saturation on bulk dielectric constants.

Ajo-Franklin *et al.* [10] used a coaxial TDR cell to examine the dielectric properties of both synthetic and natural aquifer samples when saturated with mixtures of water and TCE. This experiment, designed to quantify the radar signature of DNAPLs at the Pinellas site, will be discussed in detail in the following sections.

5.3 Dielectric Measurements On Synthetic Samples and Natural Aquifer Cores From The Pinellas Site

A prerequisite for either reliably modeling the signature of DNAPLs in the field or performing quantitative inversions for DNAPL saturation is a basic understanding of the operative rock physics. Predicting the possible radar characteristics of DNAPL pools *in situ* requires both general theoretical models linking contaminant saturation to soil dielectric properties and site-specific confirmation of these relationships. Both of these requirements can be fulfilled through careful use of core-scale laboratory measurements.

In this section we present the results of five new laboratory experiments investigating the dielectric properties of both synthetic samples and sediment cores from the Pinellas NE site partially saturated with trichloroethylene (TCE). TCE is the dominant dense contaminant at Pinellas and is a common groundwater hazard at many DOE and DOD facilities. TCE is a colorless fluid with a density of 1451 kg/m^3, a dielectric constant of 3.35 [195], and a viscosity of 0.56×10^{-3} Poise [180]. TCE has a relatively low aqueous solubility (1100 μ g/L [185]) but is also tightly regulated by the EPA with a maximum allowable concentration of 0.005 μ g/L in drinking water. Broadband dielectric measurements were performed using a time domain reflectometry (TDR) system coupled to a solvent-compatible coaxial transmission line. Two synthetic samples and three natural aquifer samples from the Pinellas were fully saturated with water and then subjected to an axial TCE injection until breakthrough was observed. The resulting dielectric measurements show good agreement with the semi-empirical complex refractive index model (CRIM) and the self-similar

Bruggeman-Hanai-Sen (BHS) effective medium model [239] allowing a reasonable prediction of the radar reflectivities and transmission velocities expected in field surveys targeting pools of similar non-aqueous contaminants.

5.3.1 Measurement Methodology

Techniques for the measurement of changes in soil dielectric properties due to fluid saturation have been extensively developed in the vadose zone science community. Time Domain Reflectometry (TDR) was first used for the assessment of cable integrity and spectroscopic measurements on fluids [95] and was later adopted for water content measurements [255] [256]. The TDR method measures the 2-way reflection traveltime for a broadband EM pulse propagating within a sample-filled transmission line of known length. The reflection traveltimes are then converted into estimates of V_{EM} and κ using the transmission line length and a time calibration parameter extracted from measurements on two materials with known dielectric properties. Coaxial probes have uniform averaging properties in the direction of transmission but the sensitivity in lateral cross-sections is spatially variable due to the non-uniform electric field.

Figure 5.1 depicts a typical TDR waveform at two different time scales. A step EM pulse is generated by the TDR unit. This pulse then propagates along a coaxial feed line until encountering the cell containing the sample. The impedance mismatch at the cable/cell interface generates a reflection, shown in the lower panel of figure 5.1. A second reflection is generated when the pulse reaches the far end of the coaxial sample cell. Assuming that the low loss assumption holds (see equation 5.6) as discussed previously, the effective dielectric constant of the sample can be expressed in terms of the time difference between these two reflections (Δt_s), the electrical length of the sample (L), and the velocity of light (c) as

$$\kappa = \left[\frac{c\Delta t_s}{2L}\right]^2. \tag{5.8}$$

The process of picking reflections to determine Δt_s and the calibration steps for obtaining L will be discussed in later sections.

5.3.2 A System For Dielectric Measurements On DNAPL Saturated Materials

We designed and constructed a TDR system for acquiring dielectric data on soils partially saturated with organic solvents. The primary components of our apparatus were a solvent-proof coaxial transmission line, the requisite pumps and flow hardware for water and contaminant injection, and electronics for TDR waveform acquisition. We used off-the-shelf equipment for all components besides the coaxial cell which required a customized design.

The coaxial cell was inspired by a similar system described in [255]. TCE's high reactivity with common plastics necessitated careful construction of a chemically compatible coaxial transmission

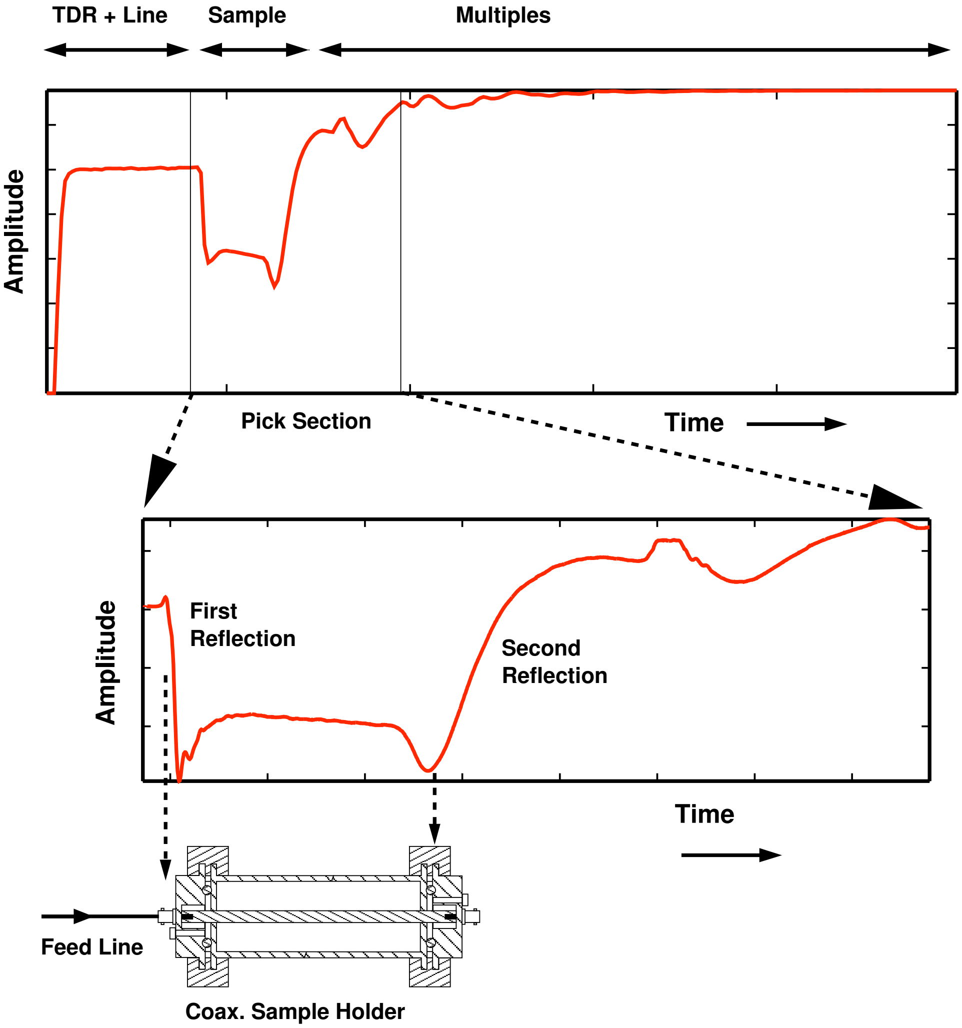

Figure 5.1: Characteristics of a sample TDR trace : Top panel depicts the entire acquired trace while the bottom panel shows the zone used for analysis of the sample.

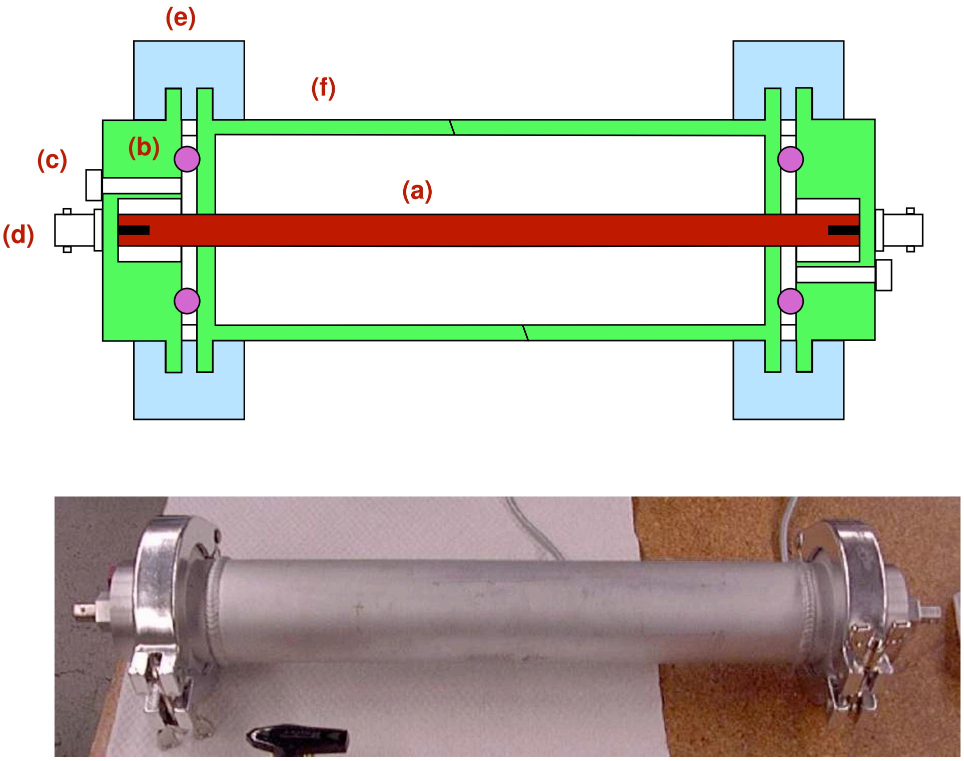

Figure 5.2: Schematic/Photographs of the solvent-compatible coaxial transmission line used in the TCE flood experiments. (a) center conductor, (b) aluminum end-cap, (c) PEEK injection port, (d) BNC connector, (e) seal clamp, (f) aluminum cell casing. (Schematic not to scale)

line for the solvent injection measurements. The cell, shown in Figure 5.2, was 33 cm long with a diameter of 4.76 cm and an inner conductor width of 0.64 cm . Flow ports were machined into the aluminum endcaps and poly-ether-ether-ketone (PEEK) fittings. PEEK fittings [1] were chosen for solvent resistance, low electrical conductivity, and superior wear characteristics. Endcap seals were maintained using Viton O-rings. Figure 5.3 shows all of the primary system components including the fluid injection pumps.

The water saturation stage of each experiment was handled using an ISCO precision syringe pump (f) with a 500 mL capacity operating in constant flow rate mode. TCE injections were performed using a Harvard 33 precision syringe pump and a 100 mL steel syringe (e). All flow lines were teflon with brass intermediate valves and steel Swagelok fittings for pump-side connections.

The TDR measurements were acquired using a Tektronix 1502C cable tester interfaced to a lab PC using the University Of Utah's WinTDR package. Spectral analysis of the reflected arrival from one of our calibration traces indicated approximately 800 MHz of usable bandwidth, somewhat less than the manufacturer specification (1.3 GHz) for the 1502C due to cable and connector losses. A series of scripts were developed to import waveforms acquired through WinTDR into MATLAB for postprocessing, picking, and amplitude analysis.

---

[1] PEEK is commonly used for high performance liquid chromatography (HPLC) flow components and has a chemical compatibility profile similar to Teflon but has a significantly higher hardness making it more suitable for parts requiring threading. We obtained PEEK components from Upchurch Scientific.

Figure 5.3: Primary Components of the TDR System : (a) Lab computer used for data acquisition, (b) Tektronix 1502B TDR, (c) Coaxial sample holder used for dielectric measurements, (d) Close up of coaxial end-cap showing BNC connector and PEEK flow port, (e) Harvard precision syringe pump used for TCE injection, (f) ISCO precision pump used for water saturation process

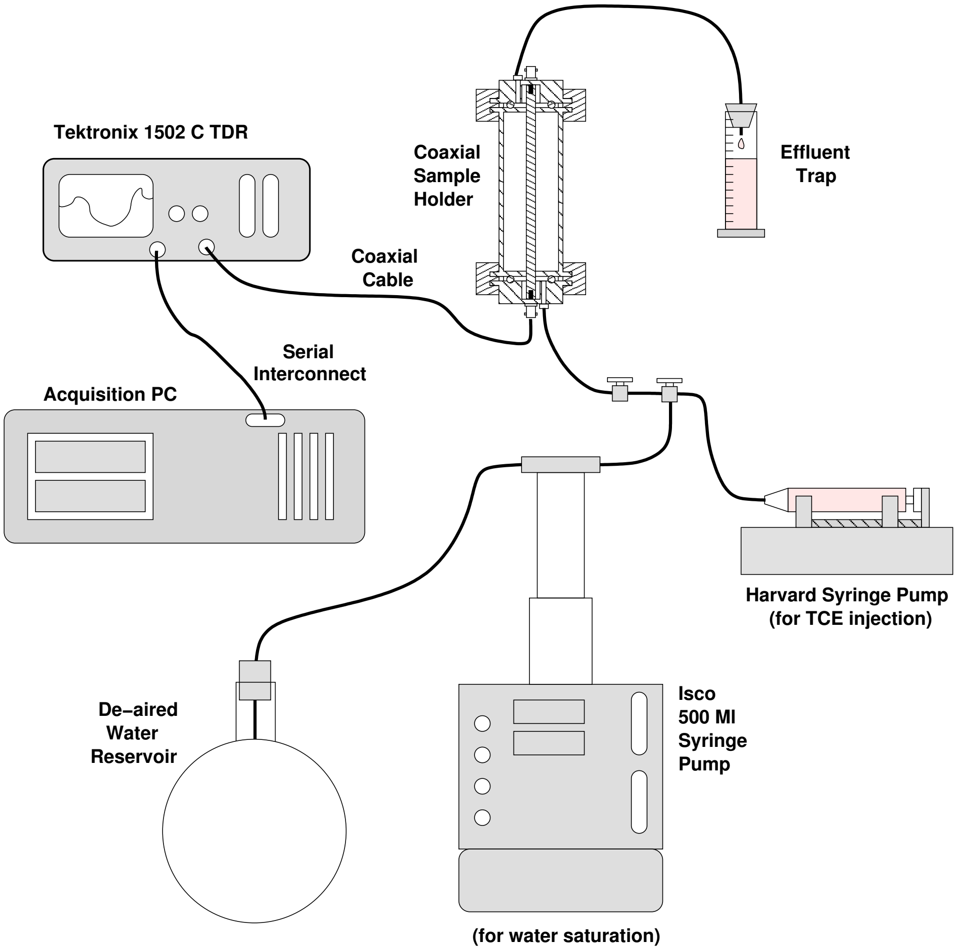

Figure 5.4: Schematic of TDR system : see previous photograph set

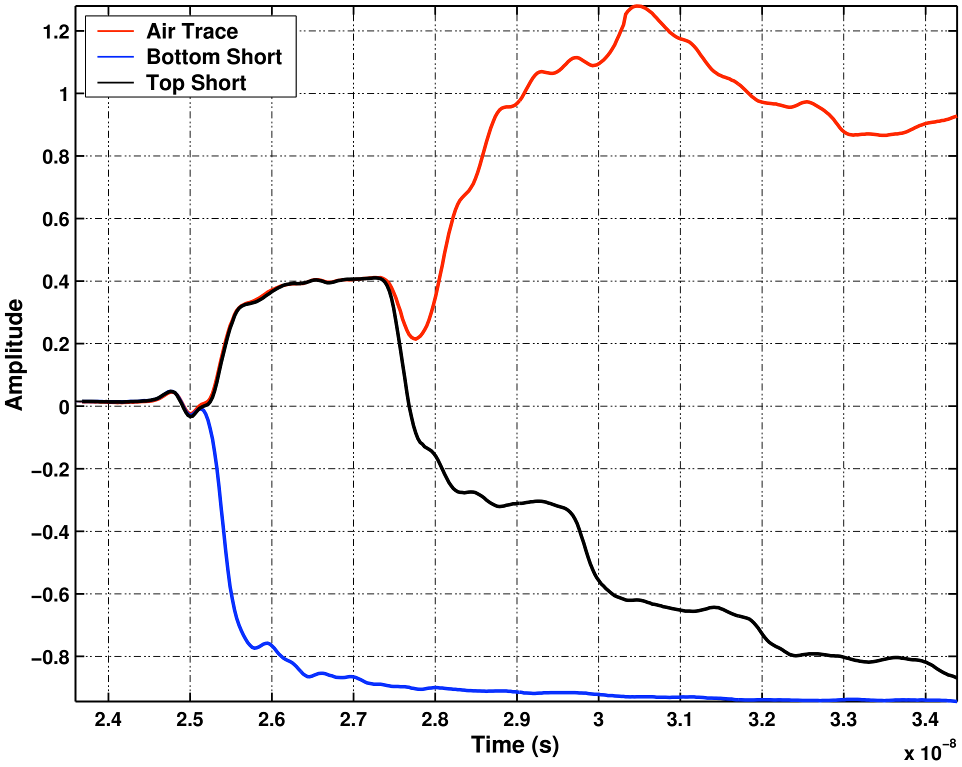

Figure 5.5: Determining the TDR reflection locations using the short circuit method [60]. The blue line corresponds to a short at the bottom end of the coaxial cavity while the black line is a short at the top. A trace collected on the unmodified cavity is shown in red.

5.3.3 Calibration and Processing Schemes For The Coaxial Cell

Before we acquired any data on porous samples, we performed a careful characterization of our system's response including calibration of the coaxial cell and development of a reflection picking scheme. The sample holder's top and bottom reflections were identified by shorting both ends of the coaxial cylinder as suggested in Chan and Knight [60] and shown in figure 5.5.

After the first and second reflections were correctly identified for our coaxial cavity, we picked waveforms manually using a modification of the two-tangent method. Figure 5.6 shows a schematic of the picking process. The first reflection was chosen to be the absolute maximum of the trace in a user defined window, in figure 5.6 the window is between (a1) and (a2) and the maximum is at (b). The second reflection (d) was determined by finding the intersection of the tangents of the trace within the sample (c1) and the rising limb of the reflection (c2). We manually chose the locations of the points for which the tangents were calculated. The tangents were not estimated from a single pair of points but by fitting a line to all values within a specified temporal window centered on the chosen locations. This fitting process reduces the sensitivity of slope estimates, and therefore the final reflection pick, to noise within the TDR trace.

The maximum method used for determination of the first reflection position does not represent the true beginning of the sample but does provide a stable location on the waveform invariant

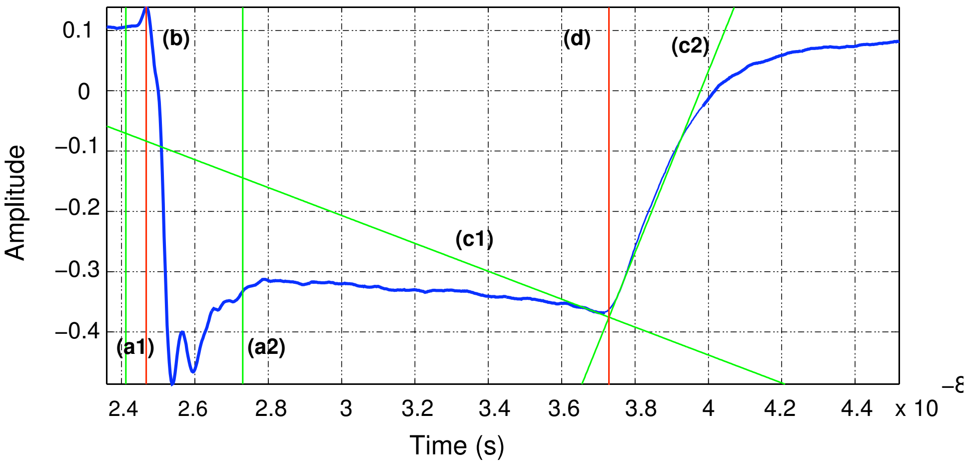

Figure 5.6: Diagram illustrating the process used for picking TDR traces : (a) Window used for selecting first reflection, (b) Chosen 1st reflection, (c) Tangent used for second reflection pick, (d) Chosen 2nd reflection. The TDR trace shown is for the coaxial cavity filled with DI water.

between measurements. We use the method of Heimovaara [123] to obtain both the effective length of the sample holder (L) and a time constant (Δt_o) which includes the static offset in the choice of first reflection location. If Δt_s is the total reflection time, equation 5.8 can be modified to include time offset,

$$\Delta t_s = \Delta t_o + \frac{2L\sqrt{\kappa}}{c}. \tag{5.9}$$

If we have two consistent time measurements available for fluids with known κ we can solve equation 5.9 for both Δt_o and L. The resulting calibration parameters can then be used for subsequent measurements of materials with unknown κ values since L and Δt_o do not change. If t_{s1} and t_{s2} are time measurements for two materials with known dielectric constants κ_1 and κ_2 then the explicit solution of equation 5.9 can be written as

$$L = \frac{c(\Delta t_{s2} - \Delta t_{s1})}{2(\sqrt{\kappa_1} - \sqrt{\kappa_2})} \tag{5.10}$$

$$\Delta t_o = \Delta t_{s1} - \kappa_1 \frac{\Delta t_{s2} - \Delta t_{s1}}{\sqrt{\kappa_1} - \sqrt{\kappa_2}}. \tag{5.11}$$

Our TDR system's response was calibrated using distilled DI water at 17 ^oC and air as the reference fluids. Figure 5.7 depicts TDR traces from several samples including air, water, and glass beads with different levels water and TCE saturations.

5.3.4 Experimental Procedure

Five samples were chosen for investigation of the dielectric signature of TCE saturation. Two synthetic samples, a clean sand and glass beads, were selected for their well-defined microstructure

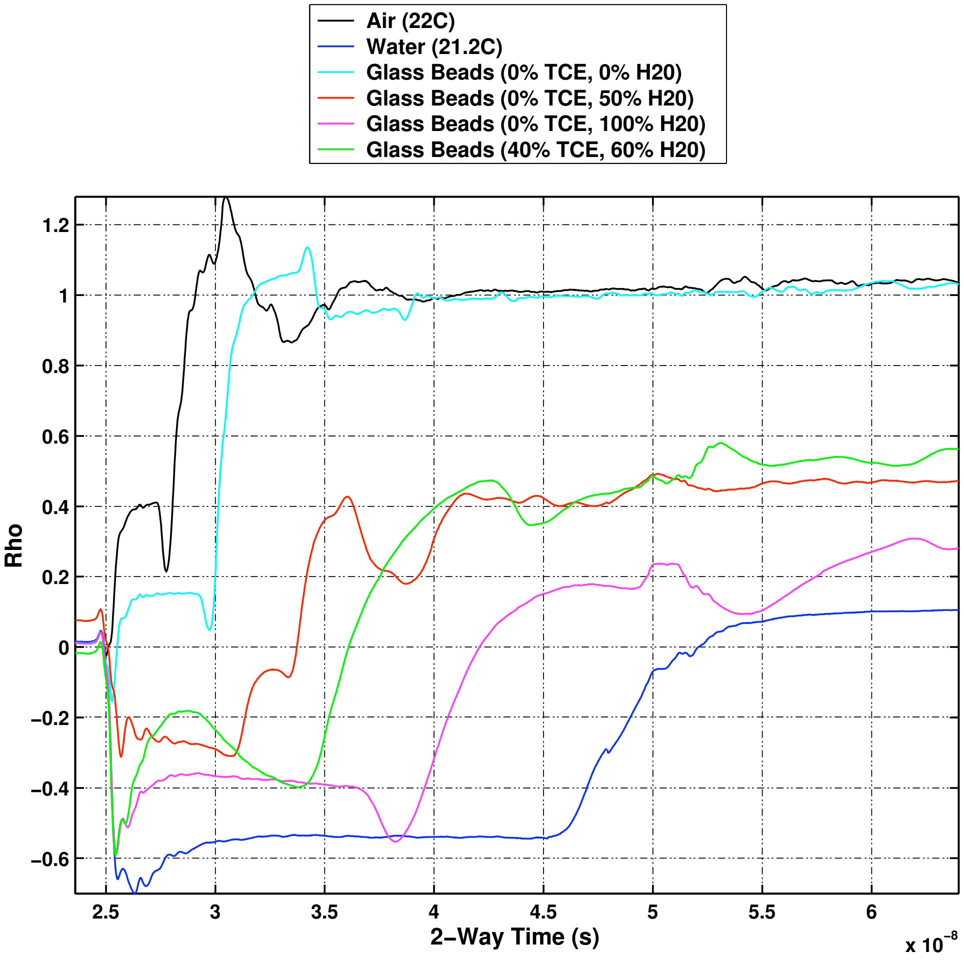

Figure 5.7: Examples of TDR traces acquired using the coaxial cavity: The black and dark blue traces were similar to those used for the calibration process

Table 5.1: Summary of Sample Characteristics

Sample	Porosity	Sand/Silt/Clay Mass Fraction	Mean Grain Diameter (μ m)	Maximum TCE Saturation (%)
Synthetic Granular Samples				
Glass Beads	0.40	100/0/0	275	52.8
Clean Quartz Sand	0.38	100/0/0	181	53.6
Natural Aquifer Samples				
G20-N2-110-125	0.41	94/4/2	223	25.3
G20-N3-55-70	0.44	91/8/1	267	31.0
G20-N3-125-141	0.39	93/6/1	243	17.4

and grain properties. Three natural soils obtained from the Pinellas core collection were included to provide calibration information for our crosswell radar investigation. Figure 5.8 shows the spatial distribution of the G20 samples used for the dielectric measurements.

The natural aquifer samples were acquired in 4 in. diameter sleeves using a rotary sonic drilling system. The samples were initially wet sieved to remove shell and rock fragments larger than 1.5 mm. This step was included to prevent large fragments from generating excess void space in the packing process and interfering with emplacement of the center conducting rod. The resulting materials were oven dried for two days at 70 ^oC before being mixed and sequentially transferred to the sample holder. Samples were packed in an initially dry state by slowly saltating the material into the coaxial cell followed by tamping. This sample preparation procedure clearly disrupts the natural soil fabric. Earlier attempts to use intact soil samples failed due to the long narrow shape of the TDR cavity; no reasonable method was found for cutting stable subcores with the appropriate dimensions.

Table 5.1 summarizes basic sample properties including porosity, sand/silt/clay mass fraction, and maximum TCE saturation before breakthrough. All three natural aquifer samples were sands with small amounts of silt and trace clay. The first synthetic sample was composed of glass beads (250-300 microns) and the second was a clean sub-angular quartz sand (150-212 microns).

After packing and mass measurements, the samples were slowly saturated (1 mL/min) at a fluid pressure of approximately 200 KPa with de-aired DI water which had been previously equilibrated with glass beads. Three to four pore volumes of de-aired water were slowly passed through the sample after initial saturation to evacuate most of the remaining trapped air. Previous control experiments on similar soils indicated that this protocol typically leaves between 1% and 2.5% residual gas. TCE, dyed red (Oil Red O Dye, Sigma Aldrich) for visibility, was then injected at low fluid pressure (0.25 mL/min, $\sim$ 50 KPa). Effluent mass was monitored to estimate the total injected TCE volume. TDR measurements were made at the initially water-saturated state and at 5 or 10 mL increments during the TCE injection process. TCE was injected until solvent breakthrough was observed in the effluent stream. Auxiliary sample properties measured include dry bulk density, grain density, sand/silt/clay mass fractions, and the mean grain diameter for the sand fraction.

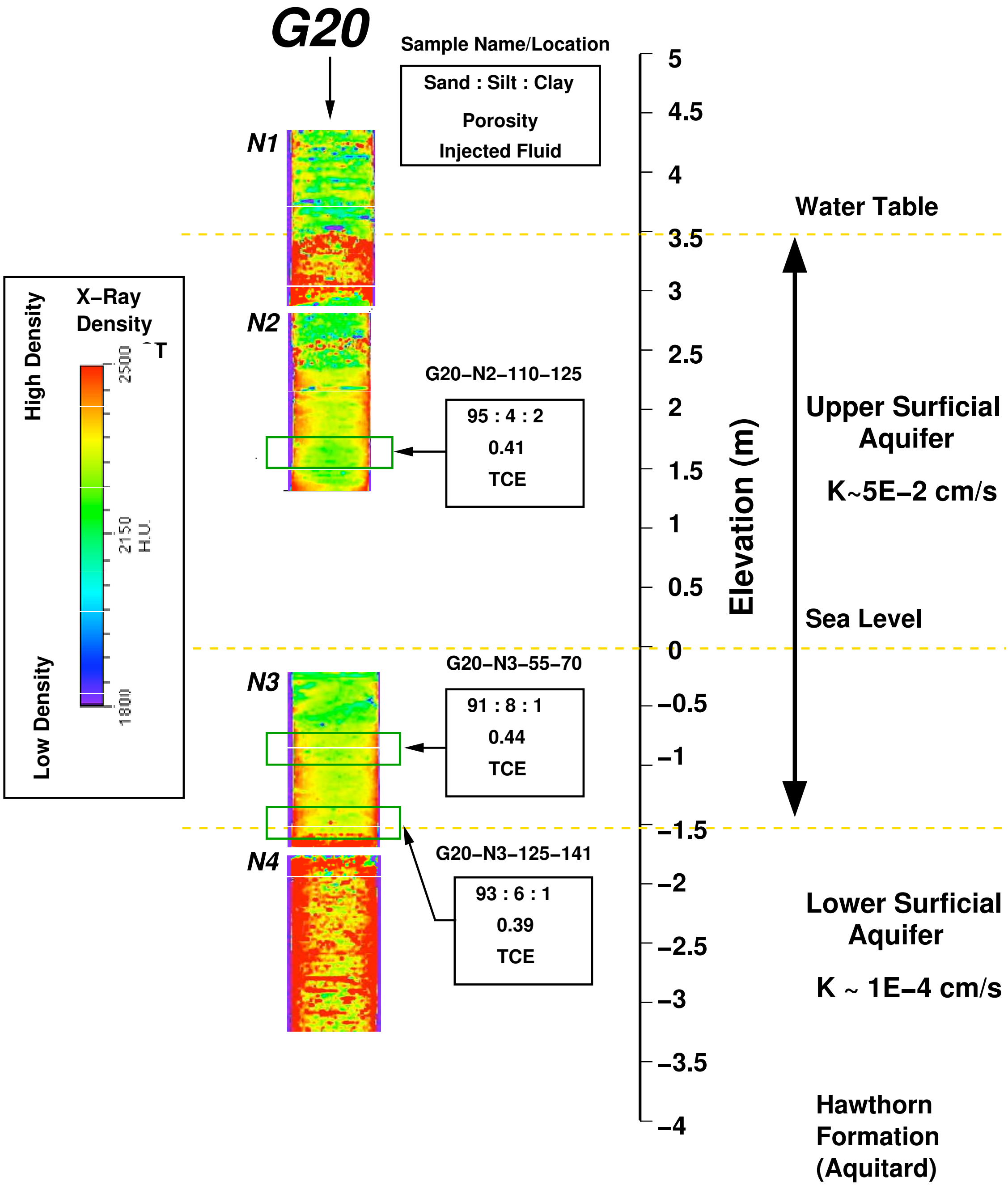

Figure 5.8: Vertical spatial distribution of Pinellas core samples used for dielectric measurements : Core color maps are generated from X-ray CT imagery. Green boxes superimposed indicate the location of samples taken for injection experiments. Labels show the sand/silt/clay content by mass and porosity of each sample in addition to fluid type used in the injection experiment.

Porosity Estimation

Sample porosities were estimated from dry bulk density and mean grain density measurements. For a fully saturated sample, bulk density (ρ_b) can be expressed in terms of grain density (ρ_{gr}), fluid density (ρ_{fl}), and porosity (ϕ) as,

$$\rho_b \; = \; \rho_{gr}\,(1-\phi) + \rho_{fl}\,\phi. \tag{5.12}$$

In our experiment, the samples were initially fully air saturated since the sample materials were oven-dried before being packed into the coaxial cell. For the air saturated case, ρ_{fl} is effectively zero and equation 5.12 can be solved for ϕ,

$$\phi \; = \; 1 \; - \; \frac{\rho_b}{\rho_{gr}}. \tag{5.13}$$

ρ_b is simply the total sample mass (M_{ts}) divided by the total sample (V_{ts}) volume. Since the sample is packed into the coaxial cell, the sample volume is the interior cell volume. The total sample mass was obtained from micro-balance measurements on the cell before and after loading. ρ_{gr}, the mean grain density, was obtained using the pycnometer method. A small powdered subsample of soil material was initially oven-dried and weighed. The dried material was placed in a pycnometer filled with de-aired DI water allowing measurement of the subsample volume; ρ_{gr} was calculated using the grain mass and grain volume values.

Several sources of error exist in the porosity estimation procedure. In particular, grain volume measurements made using the pycnometer method are sometimes inaccurate due to bubbles entrained during addition of the powdered subsample to the DI water. Grain volume measurements can also be distorted by the presence of swelling clays, however previous X-ray diffraction measurements suggest that the small clay fraction present in our samples is dominated by kaolinite which does not demonstrate swelling behavior.

Since all of the measurements described above were made on the samples before the beginning of the injection procedure, NAPL saturation levels (S_n) during the experiments could be directly calculated from sample void space ($\phi\, V_{ts}$) and the volume of injected NAPL (V_n),

$$S_n \; = \; \frac{V_n}{\phi\, V_{ts}}. \tag{5.14}$$

As can be seen from equation 5.14, uncertainty in both sample porosity and injected NAPL volume propagate into estimates of NAPL saturation.

5.4 Experimental Results

Figures 5.10 and 5.11 show dielectric properties as a function of TCE saturation for the synthetic and natural soils samples respectively. Dielectric measurements correlated well with porosity and TCE saturation. In all cases, measured dielectric constant decreased with increasing TCE saturation. A comparison between samples at a fixed TCE saturation shows the dielectric constant decreases with decreasing porosity. The horizontal error bars in the data plots are generated from the 1 mL uncertainty in injected TCE volume and 2% uncertainty in sample porosity. The vertical error bars are calculated from a rough estimate of the uncertainty in picking the reflected arrival. Both synthetic samples exhibited higher peak TCE saturations, probably due to their relatively open pore structures.

Destructive excavation of the samples after TCE injection revealed preferred flow paths within the sample, visible as red zones within the soil fabric. In all cases the TCE distribution was concentrated in the lower half of the sample. Preferred flow paths were more apparent in the natural soil samples, probably due to larger variations in permeability generated during the packing process [2]. Preferred flow zones along the center conductor were not visible during sample excavation but higher TCE saturations along the exterior of the sample were observed. Ideally, the full three-dimensional distribution of TCE within the sample could be obtained from 3D dual-energy X-Ray CT measurements during the injection experiment. We did not have access to such a monitoring system and were unable to precisely characterize the TCE distribution. This presents some difficulties in the interpretation of the dielectric measurements since different TCE distributions might break the theoretical assumptions of a given predictive model. Figure 5.9 schematically depicts three possible flow scenarios. Panel (a) shows a plug flow scenario where a uniform DNAPL front advances across the sample during saturation. Panel (b) depicts a patchy fluid distribution with might be characterized by a set of characteristic length scales. Panel (c) shows a hybrid flow scenario where the injected TCE starts as a uniform front but transitions into a patchy distribution when a significant high permeability path is encountered. Given the observed higher saturations near the injection port and the fabric related localization of TCE in the upper portion of the sample, scenario (c) seems to be the most likely configuration for our experiment. Since the true fluid distribution was not accessible to us, explicit inclusion of complicated flow geometries within our theoretical analysis did not seem justified.

Some researchers have advocated making measurements on samples where the fluids are homogenized within the soil to generate a uniform distribution of contaminants. We decided against this approach for several reasons. Since only a single contaminant saturation is measured for each soil sample in the homogenization approach, this method is vulnerable to inconsistent packing of materials *i.e.* porosity can easily vary between samples of the same soil type. Secondly, the homogenization approach requires a large volume of both contaminants and soil; since we were actually using TCE instead of a nontoxic proxy, minimizing the generation of waste was a high priority. Our natural soil samples were also volume limited since only a small amount of material was available at any given

---

[2] Even in samples specifically prepared to be homogeneous, local fluctuations in structure sometimes occur due to self-organization of the granular materials during sample fabrication. Vega-Ruiz [260] observed that the process of pouring granular material into a container generated sufficient local structure to introduce measurable P-wave anisotropy. The combination of pouring and saltation might produce a slightly less ordered system but one with sufficient local structure to generate variations in permeability.

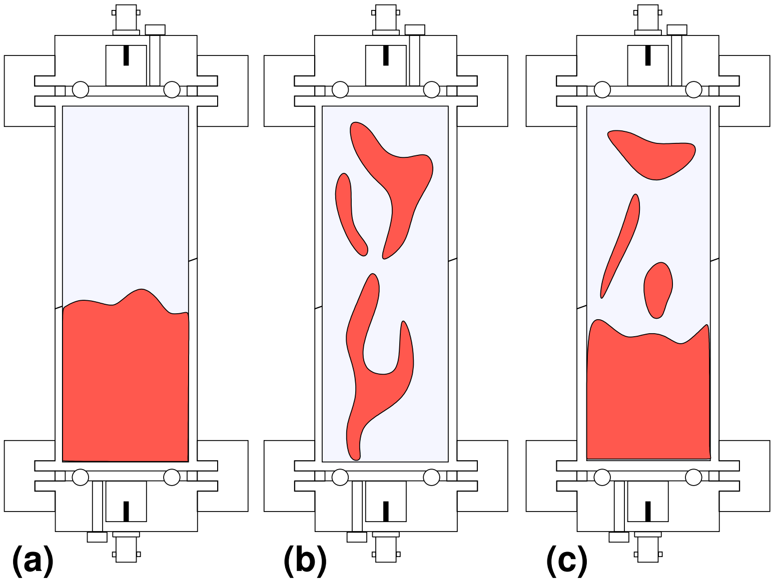

Figure 5.9: Three possible distributions of TCE within the soil sample : (a) Plug flow, a homogeneous flood front, (b) Patchy, (c) Plug flow with a transition into a patchy distribution

depth. Thirdly, the homogenization approach is not a good model for contaminant distribution in the subsurface where we would expect localization on multiple length scales. A final problem is that TCE, being denser and less viscous than water can redistribute itself within the sample, even after thorough manual mixing.

5.5 Theoretical Analysis

To move beyond qualitative statements linking fluid saturation to bulk properties requires a theoretical model linking information on phase properties and geometries to the characteristics of the multiphase composite. In the case of dielectric properties, a variety of empirical, semi-empirical, and physically derived models exist for describing these relationships for composite granular materials. In this section, we examine several of these models in the context of our experimental data. In particular, we compare the efficacy of the semi-empirical Lichtnechter-Roth/CRIM models, the non-self-consistent model of Maxwell and Garnett (MG), a symmetric self-consistent model (SC), and the self-similar effective medium model due to Bruggeman, Hanai, and Sen (BHS) [239].

Only a few existing papers have explicitly dealt with the dielectric signatures of DNAPL saturation; we mention these studies before embarking on a more detailed examination of both the applicable theories and our experimental data. Endres and Redman [93] investigate the consequences of using a modified differential effective medium theory to model the dielectric effects of saturating soils and rocks with various contaminants. Sneddon *et al.* [243] use the BHS model with a [(grain + water) + DNAPL] mixing sequence as part of a one-dimensional inversion scheme for DNAPL saturation. Carcione and Seriani [50] develop a novel, yet complicated, symmetric formulation of

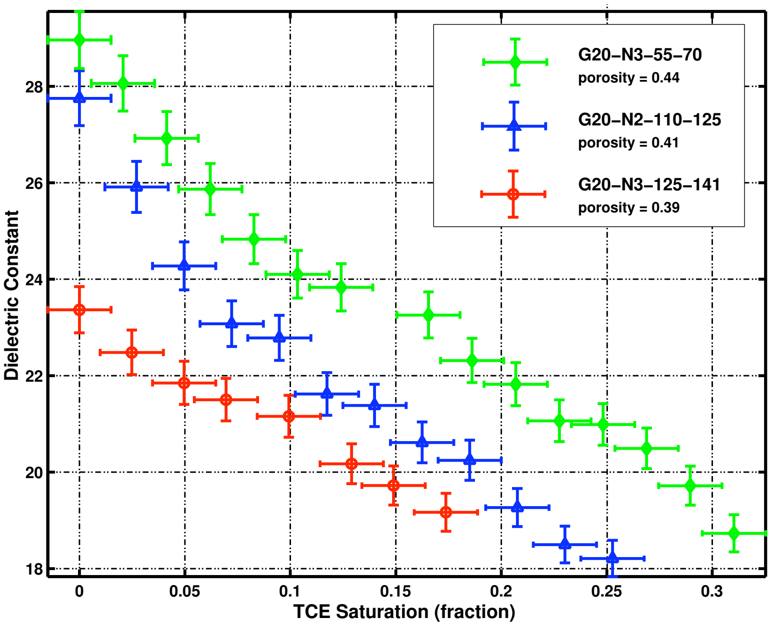

Figure 5.10: Dielectric constant as a function of TCE saturation : natural soil samples

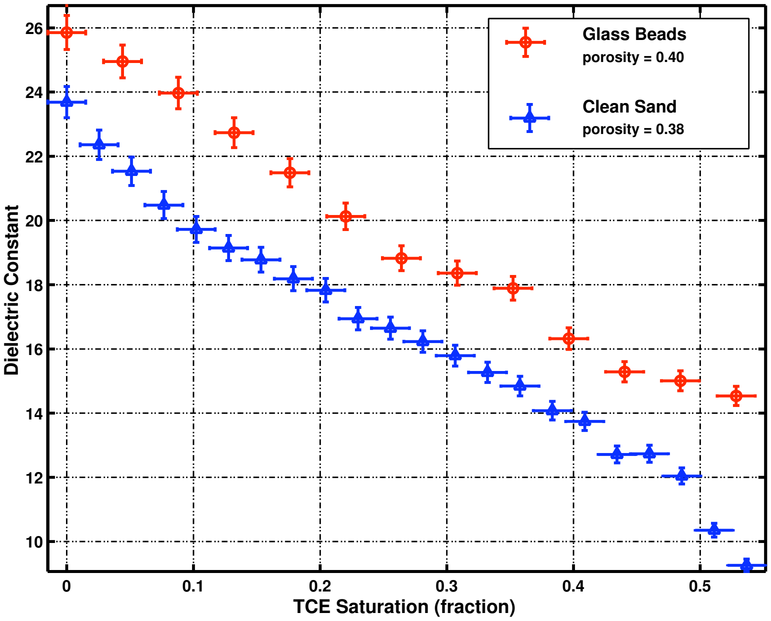

Figure 5.11: Dielectric constant as a function of TCE saturation : synthetic soil samples

the BHS model for predicting the electromagnetic properties of hydrocarbon spills Carcione *et al.* [51] models the electromagnetic properties of NAPL saturated materials using the BHS model with a [grain + (water + DNAPL)] mixing sequence as part of a joint acoustic/electromagnetic model of contaminant signatures. A defining aspect of these previous papers is that none of them compare the models described to any experimental datasets. Carcione and Seriani [50] claim to provide an experimental comparison but closer investigation revealed that they mistakenly fit their model to another author's [116] theoretical predictions.

With the exception of the semi-empirical models, all the techniques we will discuss fall within a class of solutions usually termed effective medium (EFM) models. The goal of all such methods is the calculation of some bulk property of a composite material, in this case the effective dielectric constant (κ_{eff}), from information on the fractions, geometries, and properties of i constituent phases. Effective medium models share the limitation that property heterogeneities must be considerably smaller than the probing wavelength. Since DNAPL localization probably existed at multiple length scales within our injection experiments, this assumption is probably broken but we will neglect this difference in our analysis.

The Maxwell-Garnett, self-consistent, and BHS effective medium models can be developed using the theory of perturbations. We follow the derivations from Sen *et al.* [239] which begin with an assumed mean dielectric constant, κ_o, which is then perturbed on a small scale. Although we will not derive the EFM formulas directly from the perturbation analysis, most of the models we consider can be viewed as special cases of the more general form,

$$\kappa = \kappa_o \left(1 + 2\sum_{i=1}^{N} f_i \frac{\kappa_i - \kappa_o}{\kappa_i + 2\kappa_o}\right)\left(1 - \sum_{i=1}^{N} f_i \frac{\kappa_i - \kappa_o}{\kappa_i + 2\kappa_o}\right)^{-1} \tag{5.15}$$

where f_i and κ_i are the volume fractions and dielectric constants of the component material phases. Before equation 5.15 can be evaluated, some choice must be made as to the value of κ_o; the effective medium models we will consider each make different assumptions in this respect.

The following modeling examples require baseline estimates of the dielectric properties of the relevant material phases. Literature values for grain dielectric properties were used for all model curves which we will discuss. For the synthetic samples, grain dielectric values were estimated to be 6.3 (Soda-Silica Glass, [264]) and 4.27 (Quartz, [140]). The natural samples were assumed to be predominantly quartz with small amounts of feldspar (6.03 [202]) and calcium carbonate (7.8 [140]) yielding an approximate grain dielectric constant of 5. For fluid properties we used dielectric constants of 80 and 3.35 [197] for water [3] and TCE respectively. Measured sample porosities and saturation values provided the necessary volumetric constraints.

---

[3] Numerical experiments were carried out to determine the relative importance of including the imaginary component of κ for water in our modeling examples; results indicated that imaginary dielectric values between 0 and 10 had negligible impact on the calculated real κ curves. Sen *et al.* [239] measured the imaginary component of κ for DI distilled water to be 4.5 at 1.1 GHz, the top end of the TDR band. Santamarina and Fam [231] performed similar measurements at frequencies from 0.3 to 1.3 GHz and found the imaginary component to vary between 0.5 to 5.2.

5.5.1 Semi-Empirical Models

Semi-empirical mixing models are typically simple volumetric averages which only have physical meaning in a very limited and often inapplicable context. The fact that they represent material averages makes them intrinsically more "physical" than true empirical models such as the polynomial equations relating water content to dielectric constant developed by Topp [255]. The Lichtnecker-Rother (LR) equation [118] [173] is a commonly used member of this family of models and can be written as,

$$\kappa_{eff} = \left[\sum_{i=1}^{N} f_i \kappa_i^s \right]^{1/s} \tag{5.16}$$

where s is a geometric fitting parameter and f_i and κ_i are the volume fractions and dielectric constants of the component material phases. Typically, a dataset is fit using s as a free parameter although the physical meaning of the resulting s-value is unclear except in a limited number of cases.

When $s = 1$, equation 5.16 reduces to the weighted mean of the dielectric constants of the component phases. The resulting formula is physically valid in the case of a layered medium with an electric field applied perpendicular to the layer orientation. In contrast, $s = -1$ corresponds a harmonic mean, valid in the case where the applied field is parallel to the layer orientation.

When s is equal to $1/2$, equation 5.16 becomes the Complex Refractive Index Model (CRIM) [100] [227] which provides perhaps one of the simplest form for estimation of the effective dielectric properties of multiphase materials. CRIM is only strictly valid for one dimensional layered composites in the ray theoretic limit. In practice, CRIM is relatively effective at modeling the properties of more complex materials. CRIM is the electromagnetic analogue of Wyllie's time-average formula used in seismic analysis. Following equation 5.16, the general form of CRIM is

$$\kappa_{eff} = \left[\sum_{i=1}^{N} f_i \sqrt{\kappa_i} \right]^2 . \tag{5.17}$$

For the special case of a three phase mineral/water/NAPL mixture, the CRIM formula reduces to

$$\kappa_{eff} = \left[\phi \left(S_w \sqrt{\kappa_w} + S_n \sqrt{\kappa_n} \right) + (1 - \phi) \sqrt{\kappa_g} \right]^2 \tag{5.18}$$

where ϕ is the porosity of the solid matrix, S_w is the water saturation, S_n is the NAPL saturation, and κ_n, κ_w, κ_g are respectively the NAPL, water, and grain dielectric constants.

Figures 5.12 and 5.13 show the results of fitting the Lichtnecker-Rother equation to our experimental datasets. The CRIM model results are shown in dotted lines and do not include any fitting parameters. CRIM provided a reasonable fit for most of the dataset with minor departures at high and low water saturations. CRIM systematically underpredicted dielectric values for the G20-N3-55-70 sample and for both synthetic samples. Some deviations from CRIM are expected since the

TCE distribution in the samples was not a uniform layer. Fitting the data using the Lichtnecker-Rother equation yielded optimal s values between 0.486 and 0.605, relatively close to the value of 0.5 assumed by CRIM. Both synthetic samples had high values of s in comparison to the aquifer samples suggesting some difference in flow geometry due to their higher permeability. However, the overall quality of the theoretical fits suggest that bulk dielectric properties are not highly sensitive to the geometry of TCE distribution within a given sample and are instead largely determined by the volume fractions of the constituent materials. CRIM seems to possess both a theoretical simplicity and a high predictive value which makes it a useful building block for both forward modeling and inversion schemes.

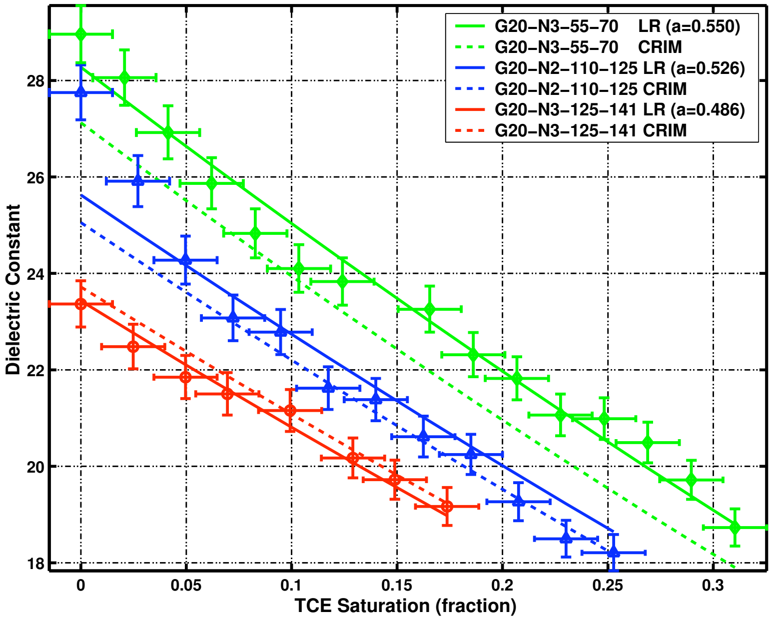

Figure 5.12: CRIM and Lichtnecker-Rother fits for the natural aquifer samples

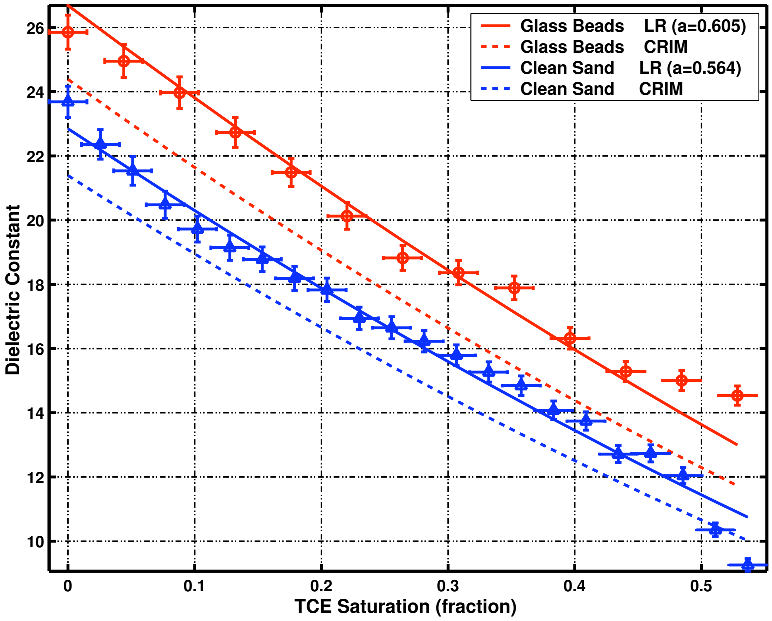

Figure 5.13: CRIM and Lichtnecker-Rother fits for the synthetic samples

5.5.2 The Maxwell-Garnett Model

The Maxwell-Garnett (MG) model, also known as the Clausius-Mossotti formula or the Lorentz-Lorentz equation, is a non-self-consistent effective medium theory applicable to one or more dielectric phases embedded in a homogeneous matrix. This model, in the form discussed here, is limited to a dilute dispersion of spheres but extensions also exist for unaligned ellipsoidal inclusions [32]. The formula is not symmetric with respect to the choice of host material *i.e.* exchanging the host properties with those of the inclusions does not yield the same dielectric constant estimate.

The two phase form of the Maxwell-Garnett model can be written as

$$\frac{\kappa_{eff} - \kappa_1}{\kappa_{eff} + 2\kappa_1} \;=\; (1 - f_1)\frac{\kappa_m - \kappa_1}{\kappa_m + 2\kappa_1} \tag{5.19}$$

where κ_{eff} is the effective dielectric constant of the composite, κ_m is the dielectric constant of the matrix material, κ_1 is the dielectric constant of the inclusion phase, and f_1 is the volume fraction of inclusions. The MG model can be derived from equation 5.15 with the assumption that $\kappa_o \;=\; \kappa_1$. The same equation can be solved for κ_e explicitly,

$$\kappa_{eff} \;=\; \kappa_m + 3f_1\kappa_m \left[\frac{\kappa_1 - \kappa_m}{\kappa_1 + 2\kappa_m - f_1(\kappa_1 - \kappa_m)}\right]. \tag{5.20}$$

The dielectric properties of composite materials with more than two phases can be estimated either through sequential application of equation 5.20 or through use of a form due to Berryman [32],

$$\kappa_{eff} = \left(\sum_{I=1}^{N} f_i \,\frac{1}{\kappa_i + 2\kappa_m}\right)^{-1} \;-\; 2\kappa_m \tag{5.21}$$

where f_i and k_i are the volume fraction and the dielectric constant of the ith phase respectively. Figures 5.15 and 5.16 show the experimental data plotted with the Maxwell-Garnett predictions for two different mixing orders. The solid (upper) lines correspond to assuming that water is the background material with solid grains and contaminant fluids treated as inclusions. The dashed (lower) lines show model evaluations which use the grain material as the homogeneous background and treat both fluid phases as inclusions. Figure 5.14 depicts the geometry of these two mixing sequences.

While neither mixing order approximates the experimental data well, the curves which treat water as the background material are significantly closer to our observations for both the natural aquifer and synthetic samples. The failure of the Maxwell-Garnett model is not surprising due to both the high concentration of inclusions and the large contrasts between the inclusion and matrix materials.

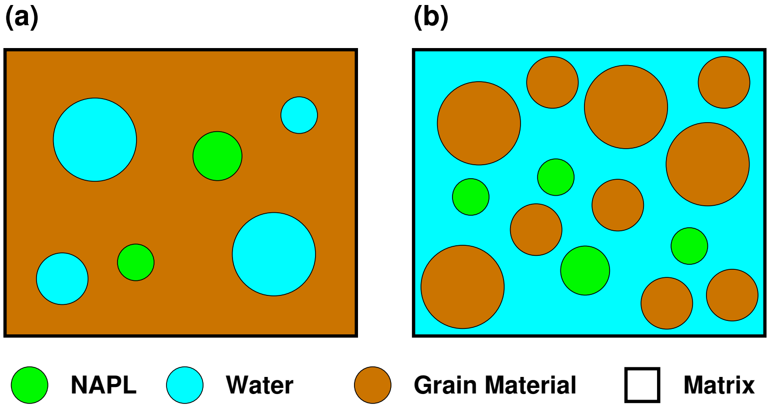

Figure 5.14: Geometric distributions for the Maxwell-Garnett model with two different mixing sequences. Panel (a) shows water and NAPL inclusions in a solid matrix while panel (b) depicts grains and NAPL spheres embedded in water. These geometries correspond to the bounds shown in figures 5.15 and 5.16

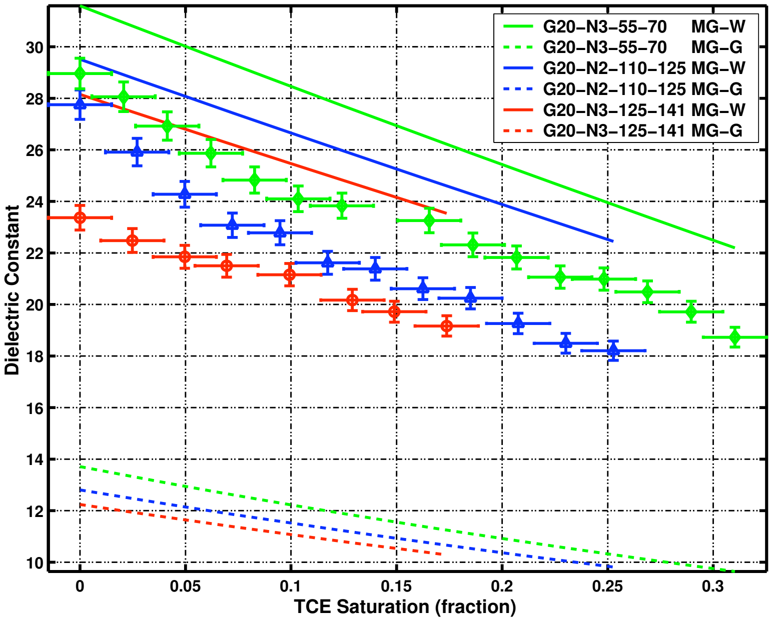

Figure 5.15: Maxwell-Garnett fits for the natural aquifer samples : Upper curves use water with spherical contaminant and grain inclusions while the lower curves assume a solid matrix with spherical fluid inclusions.

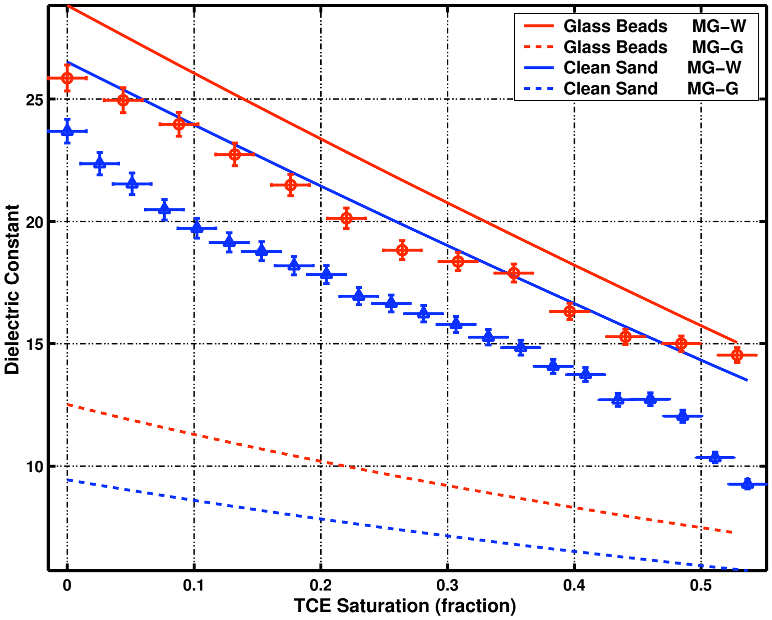

Figure 5.16: Maxwell-Garnett fits for the synthetic samples : Upper curves use water with spherical contaminant and grain inclusions while the lower curves assume a solid matrix with spherical fluid inclusions.

5.5.3 A Symmetric Self-Consistent Model

The Self-consistent (SC) model [156] [32] begins by assuming that the mean property value used in the perturbation analysis are equal to the effective property value i.e. $\kappa_o = \kappa_{eff}$ in equation 5.15. Evaluating equation 5.15 for this case yields an implicit formula since κ_{eff} is the value we are attempting to solve for. The resulting model is symmetric with respect to treatment of the constituent phases and does not require choice of either a host material or a mixing order,

$$\sum_{i=1}^{N} f_i \frac{\kappa_i - \kappa_{eff}}{\kappa_i + 2\kappa_{eff}} = 0. \tag{5.22}$$

Equation **??** assumes that all N phases are present as spherical components. This implicit formula can be converted into a form suitable for solution through fixed-point iteration,

$$\kappa_{eff} = \left(\sum_{I=1}^{N} f_i \frac{1}{\kappa_i + 2\kappa_{eff}} \right)^{-1} - 2\kappa_{eff}. \tag{5.23}$$

To solve equation 5.23 we make an initial guess at the value for κ_{eff} using CRIM and evaluate the right hand side to obtain an updated value. This process is repeated until the difference between κ_{eff} in two iteration has fallen beneath a threshold value indicating convergence. In principle, SC models should be valid at higher material contrasts and volume fractions then non-self-consistent models like Maxwell-Garnett. This property, and the symmetric treatment of components make the SC model attractive. However, comparison to our laboratory experiments (see figures 5.17 and 5.18) shows that the SC model in this form underestimates bulk dielectric constant for both the natural and synthetic samples.

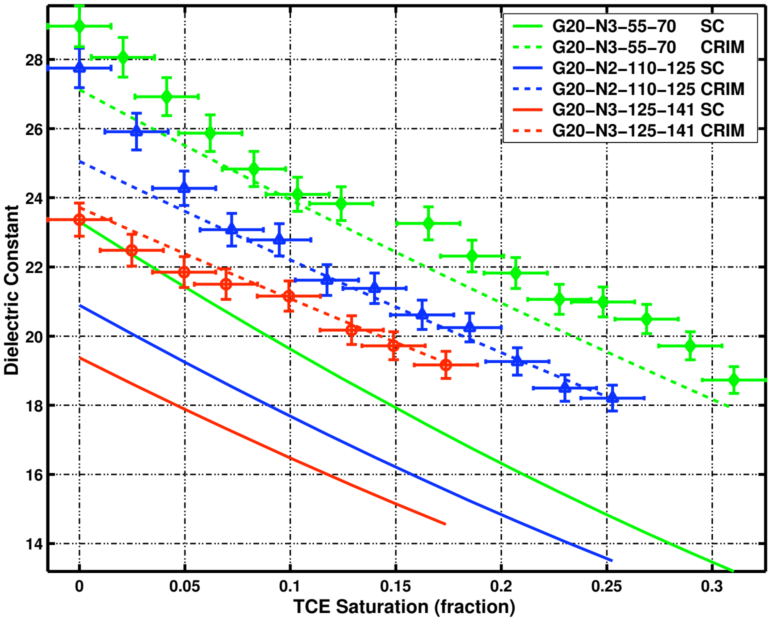

Figure 5.17: Self-consistent model vs CRIM fits for the natural aquifer samples : No assumed host material.

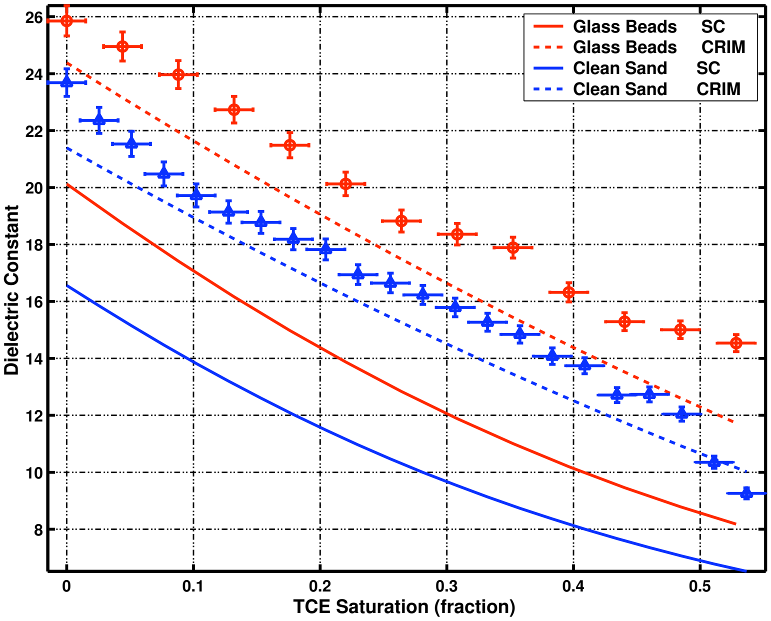

Figure 5.18: Self-consistent model vs CRIM fits for the synthetic samples : No assumed host material.

5.5.4 The Bruggeman/Hanai/Sen Self-Similar Model

Sen *et al.* [239], following previous authors, developed a self-consistent effective medium model by recursively embedding coated spheres and calculating the limit of this process at the correct volume fraction. Figure 5.19 depicts the theoretical geometry of this self-similar model where the coating of each coated sphere consists of other coated spheres. Sen *et al.* [239] exploits the closed form for polarizibility of a coated sphere due to Van de Hulst [78]. The resulting relationship, termed the Bruggeman/Hanai/Sen formula (BHS), can be written in terms of the volume fraction of inclusion material, f_1, as

$$\left(\frac{\kappa_m - \kappa_{eff}}{\kappa_m - \kappa_1}\right)\left(\frac{\kappa_1}{\kappa_{eff}}\right)^C = f_1 \tag{5.24}$$

where κ_m, κ_1, and κ_{eff} are the dielectric constants of the matrix, inclusion, and composite material respectively. C is a geometric parameter related to grain shape which is 1/3 in the case of spherical grains. A simple line-search algorithm is used to determine κ_{eff} given the requisite phase and geometry information. The BHS model, as described here, is non-symmetric with a preferred host material. Since the BHS model is not easy to extend to more than two material phases, we use a sequence of mixing operations to accommodate our grain/water/DNAPL composites. Numerical experiments revealed that the best fit for our data were generated by sequentially mixing grain and water followed by mixing this “wet rock” with DNAPL. In the first step, the grain material is chosen as the host while in the second case the water saturated rock is used in the same capacity. For all of our numerical studies we assume a C value of 1/3 since more detailed information on grain shape distributions were not available.

Figures 5.20 and 5.21 show our experimental results and the BHS estimates with CRIM as a reference. BHS was the most accurate physically derived EFM model with good fits for most of the examined samples. BHS overestimated the dielectric constant of the G20-N3-125-141 core but matched the experimental datasets better than CRIM for the other two natural aquifer samples. For the synthetic samples, BHS fit the clean sand experiment well, particularly at lower TCE saturations. For both the glass and sand samples, BHS faired better than CRIM.

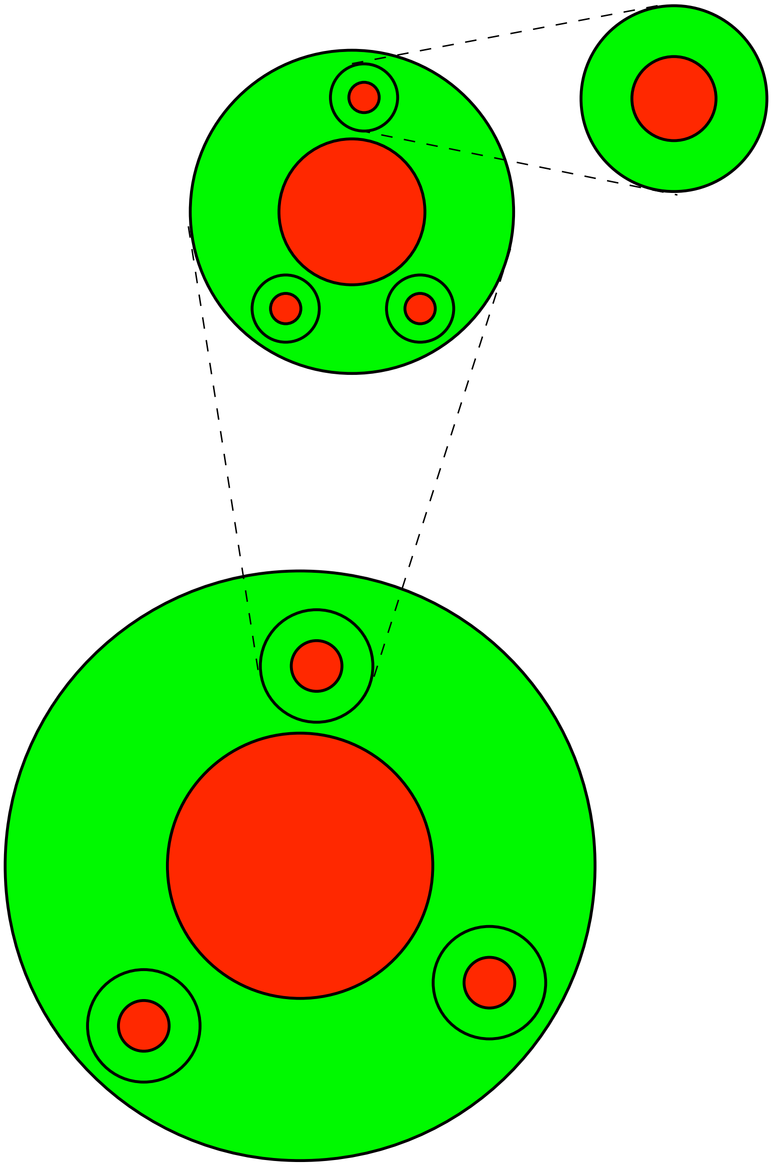

Figure 5.19: Geometric interpretation of the BHS model

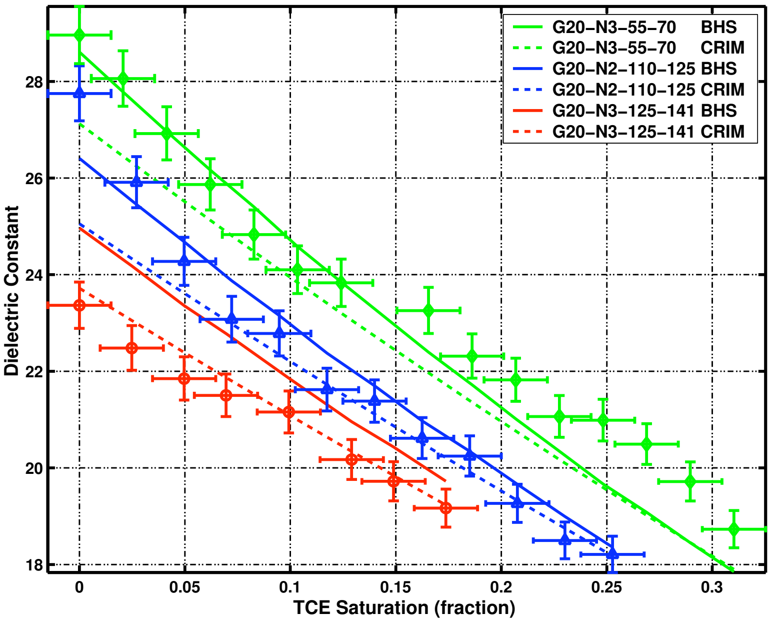

Figure 5.20: BHS model vs CRIM fits for the natural aquifer samples : Mixing sequence - 1. grain (matrix)/ water (inclusion) 2. wet grains (matrix) / DNAPL (inclusion)

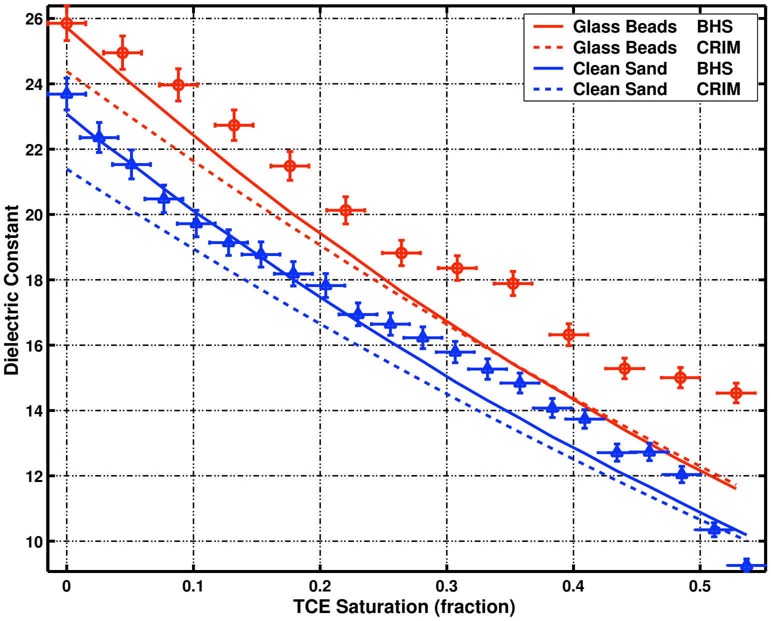

Figure 5.21: BHS model vs CRIM fits for the synthetic samples : Mixing sequence - 1. grain (matrix)/ water (inclusion) 2. wet grains (matrix) / DNAPL (inclusion)

5.6 Two Alternatives For A Five-Phase Dielectric Model

In our experimental investigations, we have considered only systems with three phases, a single insulating solid phase mixed with two fluids, water and DNAPL. This description should be sufficient for the case of clean sands in the saturated zone where the dielectric constant is determined primarily by porosity, water/DNAPL fraction, and to a lesser extent grain dielectric properties. Two factors which we have neglected but are often important in the analysis of field data are partial gas saturation and clay content. Our simplification should be valid for the majority of the radar surveys collected at Pinellas due to our acquisition geometry which extended from immediately below the water table to the top of the clay rich aquitard. Possible exceptions to our 3-phase model include the presence of isolated clay/silt lenses or residual gas left from seasonal changes in the water table. Biogenic gas production, possibly related to contaminant degradation, is another possible source of gas *in situ*. Although the inversion schemes we will discuss in later chapters make use of this 3-phase assumption, this section will discuss extensions of the two most useful EMT models we have tested, the BHS and CRIM models, to account for five-phase composites including clay and gas.

Since gas has a low dielectric constant (1), the radar signature of partial gas saturation is indistinguishable from changes in either DNAPL fraction or porosity (grain fraction) if only V_{EM} is measured. Clay content tends to increase both the real and imaginary components of the dielectric constant in most soils in addition to increasing increasing DC conductivity.

One simple model used in previous works [145] is the semi-empirical CRIM equation discussed previously,

$$\kappa_{eff} = \left[(1-\phi)V_{cl}\sqrt{\kappa_{cl}} + (1-\phi)(1-V_{cl})\sqrt{\kappa_g} + S_w\phi\sqrt{\kappa_w} + S_a\phi\sqrt{\kappa_a} + S_n\phi\sqrt{\kappa_n}\right]^2 \tag{5.25}$$

where S_w,S_a,S_n are water, air, and NAPL saturation respectively, V_{cl} is the fraction of clay present within the solid phase, with the κ_i variables indicating the dielectric constants of the appropriate phases. If changes in DC conductivity due to clay content are significant, the lossless propagation assumption used previously is invalid and calculation of V_{em} requires use of equation 5.4.

The BHS model has also been used to include the effects of clay in multiphase composites. Carcione *et al.* [51] modeled a five phase clay/sand/air/water/NAPL system using BHS with a C value of 1/3. He proposed a nested mixing sequence equivalent to (((air + NAPL) + water) + (sand + clay)). Both models can be interpreted in terms of a two component mixture of effective grain and fluid phases.

Figure 5.22 demonstrates the three-way non-uniqueness possible with variations in NAPL saturation, porosity, and gas content. Using the 4 phase version of CRIM, figure 5.22 shows the predicted effect of the addition of DNAPLs (red curves) or gas (blue curves) to clean sands with three different porosities, 0.3,0.4, and 0.5. The green line is shown to emphasize that a single dielectric constant could be generated by variations in porosity, DNAPL saturation, or gas content. This example

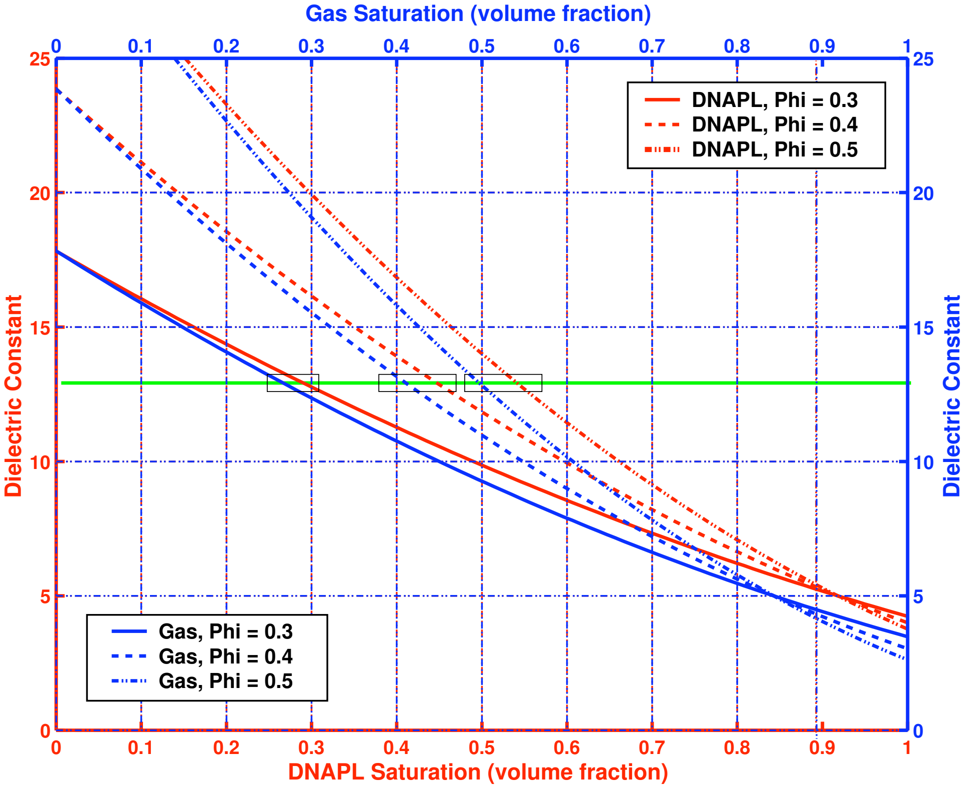

Figure 5.22: Non-uniqueness and dielectric measurements : The Gas/DNAPL/Porosity Tradeoff. The blue curves correspond to CRIM predictions for the change in dielectric constant due to the addition of gas to a water saturated sample while the red curves show the dielectric effects of adding DNAPL for three different porosity materials.

assumes dielectric constants of 5, 2.7, and 1 for grain material, DNAPL, and gas respectively.

5.7 Conclusions : Dielectric Signatures Of DNAPL Saturation At Pinellas

We conclude our discussion of dielectric properties with an estimate of the likely magnitude of DNAPL-induced radar signatures at Pinellas. To predict this signature we require a reasonable profile of both the DNAPL phase and the soil matrix at the site. Important topics that we will discuss in later chapters on imaging is the role of upscaling and target dimensions in the detection problem.

In chapter 3, we developed a dielectric profile for the DNAPL phase at Pinellas base upon constraints provided by samples from wells RW-06. Density and GCMS measurements revealed that the DNAPLs at this location were a mixture of TCE, toluene, heavy oil, and a large array of trace compounds with an approximate dielectric constant of 2.7. Porosity measurements on both the homogenized samples described in table 5.1 and on intact cores from Pinellas suggest an *in situ* porosity of between 0.35 and 0.46. Visual microscopy revealed that the sand fraction at Pinellas was primarily quartz ($\kappa = 4.27$ [140]) with small amounts of calcium carbonate in the form of shell micro-fragments ($\kappa = 7.8$ [140]) and potassium feldspar ($\kappa = 6.03$ [202]) yielding an approximate grain dielectric constant of 5.

Using the above parameters and the BHS/CRIM models discussed in the previous section we can make an educated guess as to the radar visibility of the DNAPL phase at Pinellas. Figure 5.23 shows the predicted bulk dielectric constant of five soils with porosities ranging from 0.3 to 0.5 as a function of DNAPL saturation. The BHS and CRIM estimates are very similar. Figure 5.24 shows the same dielectric estimates converted into radar velocities assuming the lossless wave propagation model. Velocity changes due to DNAPL saturation are significant; At a 20 % DNAPL saturation, a velocity difference of between 11 and 14 % with respect to the water saturated state would be expected. At a 40 % DNAPL saturation we might see velocities between 26 and 36 % greater than the water-saturated state. Velocity contrasts of this magnitude should be detectable using crosswell traveltime tomography assuming that the DNAPL saturated region has sufficient spatial extent. Figure 5.25 depicts the normal incidence reflection coefficient expected for a two-layer scenario where the top layer is fully water saturated and the bottom layer has a given DNAPL saturation. The expected reflectivities are significant, between 0.12 and 0.18 at a DNAPL saturation of 40 %, which is on the same order of magnitude as radar reflections generated by large changes in soil porosity or mineralogy.

One component which was neglected in the above calculations was the role of κ'', the lumped dielectric loss term, in the calculation of V_{em}. Although the DI water used in our laboratory experiments was relatively low conductivity, the groundwater at Pinellas probably has a significantly higher σ_{dc} and a correspondingly large κ'' term. The resulting change in $\tan\delta$ (see equation 5.5) could have a significant impact on the estimated V_{em} values in addition to attenuating the radar pulse.

All three numerical experiments demonstrate the non-uniqueness present in determining DNAPL saturation. As shown in figure 5.24, a given observed V_{em} can be explained by either differences in DNAPL saturation or differences in porosity. This non-uniqueness is most visible at low DNAPL saturations where small changes in porosity generate significant changes in water fraction. However, we can bound DNAPL saturation for a given measured velocity as long as our dielectric model is correct and we have prior bounds on porosity. Using the CRIM model discussed previously, DNAPL saturation (S_n) can be written in terms of grain, fluid, and measured effective dielectric properties as,

$$S_n = 1 - \left(\frac{1}{\sqrt{\kappa_w} - \sqrt{\kappa_n}}\right)\left(\frac{\sqrt{\kappa_{eff}} - (1-\phi)\sqrt{\kappa_g}}{\phi} - \sqrt{\kappa_n}\right). \tag{5.26}$$

Substituting bounds on porosity, ϕ_{max} and ϕ_{min}, into equation 5.26 yields bounds on DNAPL saturation, a useful diagnostic tool in the detection problem. Such bounds can be extended to include the possibility of gas saturation and changes in grain dielectric properties using the models provided in the last section. Gas content in particular can easily replicate the dielectric signature of

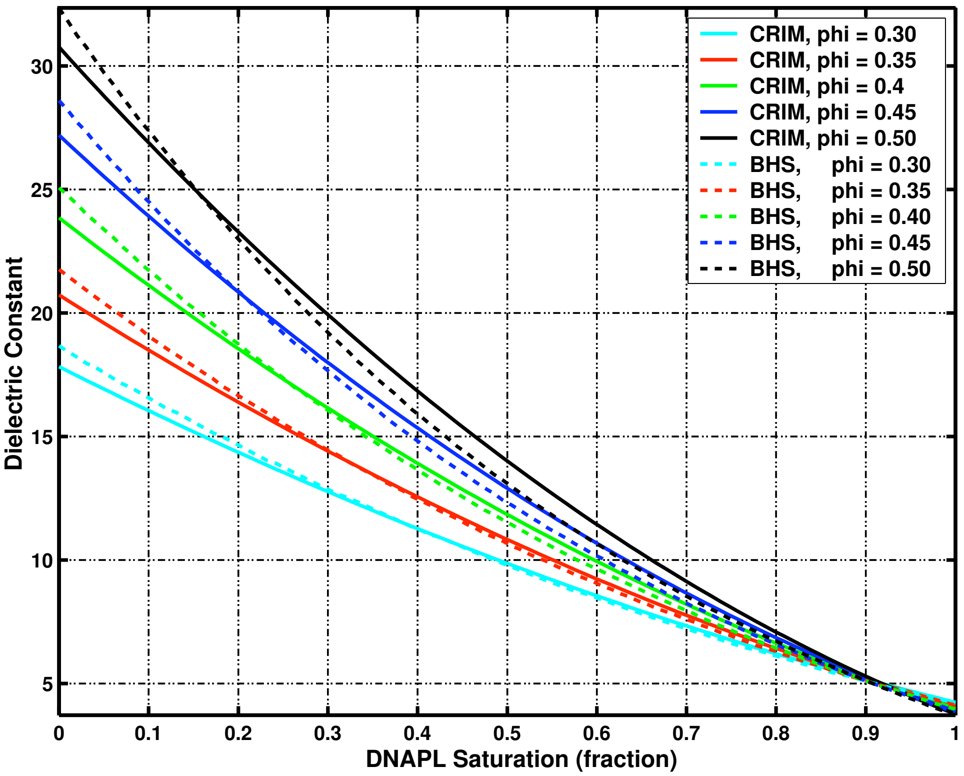

Figure 5.23: Dielectric Signature Predictions for the Pinellas NE DNAPLs

DNAPL saturation. With a low dielectric constant (~ 1), free phase gas might be interpreted as a high DNAPL saturation as was shown previously in figure 5.22.

In conclusion, partial DNAPL saturation has a demonstrable dielectric signature as shown in both our experimental efforts and the work of previous researchers. Our experimental database, which includes both synthetic and natural aquifer samples, provides an approach for confirming existing effective medium models. Ideally, core measurements might also be used for directly calibrating site response; in our case, the required sample homogenization process made use of our dataset in that capacity problematic. The CRIM and BHS models both provided good fits for our experimental dataset and seem to be candidates for estimating the properties of DNAPL saturated sediments in the field. Based on our best estimate of site soil properties and the characteristics of the DNAPL phase extracted *in situ*, we predict that high radar velocity is a likely signature of free-phase contamination at Pinellas. However, the non-uniqueness introduced by variations in matrix properties or the addition of small amounts of gas prevents a unique inversion for DNAPL saturation using only radar velocity information. This limitation might be overcome through use of additional datasets, possibly including seismic measurements and/or well logs.

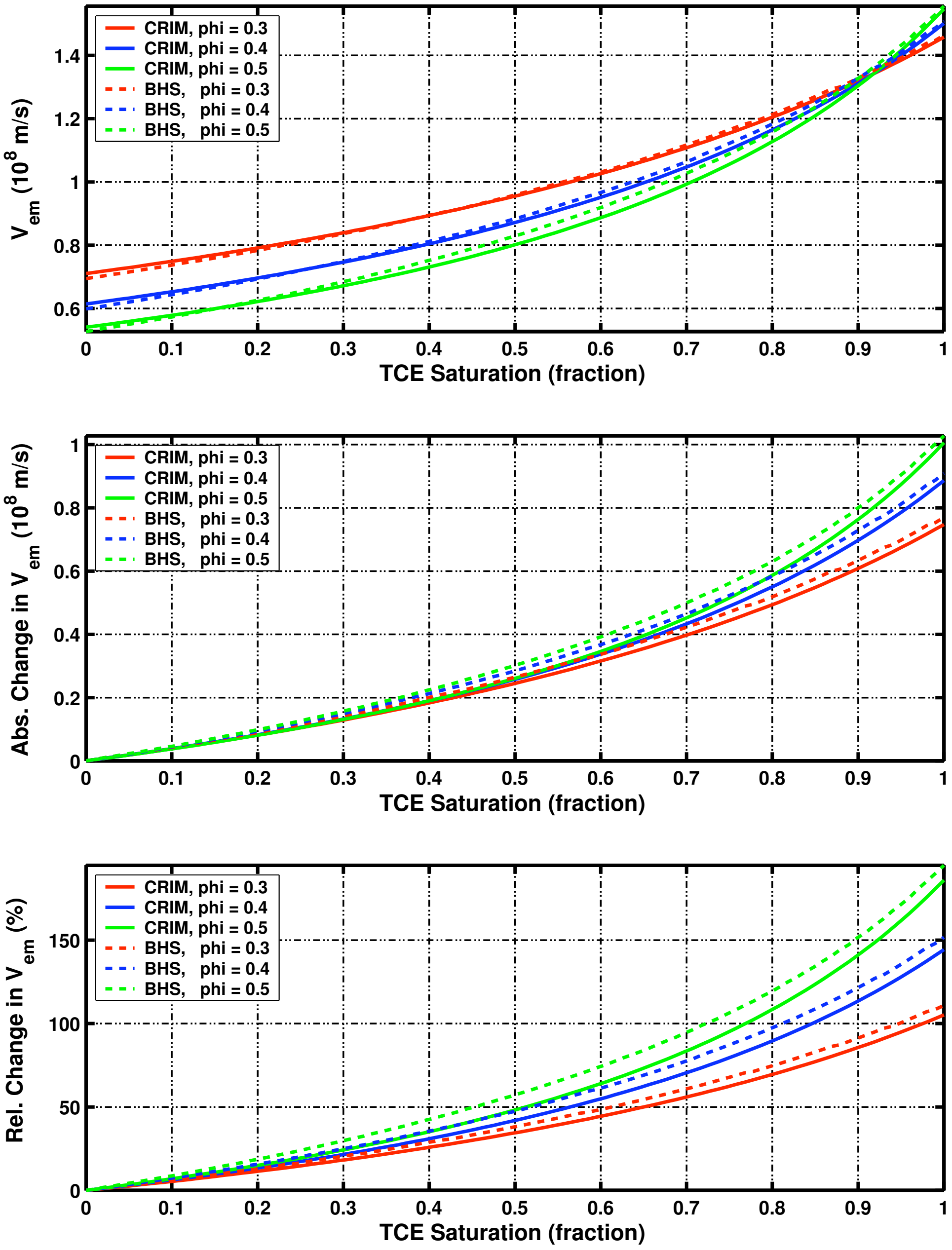

Figure 5.24: Radar Velocity Signature Predictions for the Pinellas NE DNAPLs : The top panel shows absolute velocity predictions, the center panel shows the prediction for change in velocity with respect to the water saturated state, and the bottom panel shows the same prediction in terms of relative change in velocity.

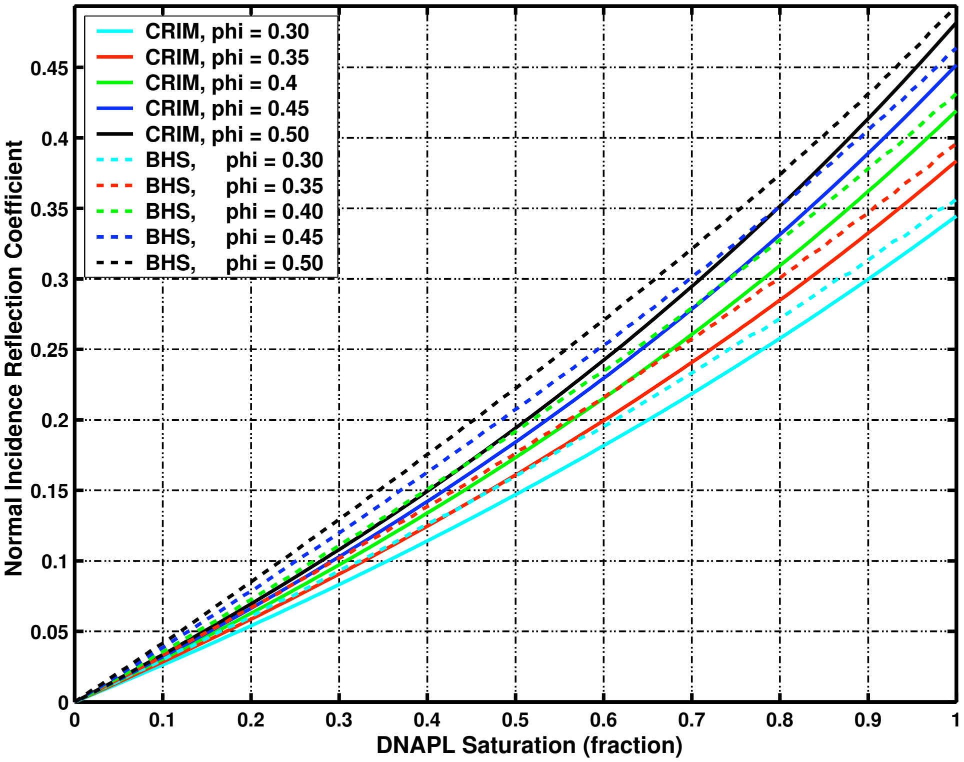

Figure 5.25: Normal Incidence Radar Reflectivity Signature Predictions for the Pinellas NE DNAPLs

Chapter 6

The Acoustic Properties Of DNAPL Saturated Granular Media

Seismic methods are one of the most commonly used techniques for acquiring high resolution images of near-surface targets. Both surface reflection methods [244] [245] [28] and borehole transmission measurements [129] have found broad application in hydrogeophysics and site characterization. While there are no field tests which have demonstrated the efficacy of seismic methods for DNAPL detection, a number of laboratory core [111] [234] [108] and physical model [146] [109] experiments have shown that DNAPL saturation possesses a measurable and sometimes significant acoustic signature. The goal of this chapter is to place seismic-based DNAPL detection on firm petrophysical footing by developing an experimental and theoretical framework for understanding the acoustic properties of sediments partially saturated with free-phase contaminants in the laboratory. Since the *ab initio* prediction of the acoustic properties of near-surface sediments is still in many ways an open problem, we focus only on the seismic signature of DNAPL saturation.

In this section, we analyze several previous studies of the seismic properties of unconsolidated sediments contaminated with a distinct NAPL phase. Due to the small number of available measurements on samples with partial DNAPL saturation, we also include a selection of LNAPL experiments which have some relevance to the applicable petrophysical models. We only consider measurements made at less than 1 MPa of confining pressure, corresponding to a maximum subsurface depth of approximately 50 meters. Additionally, we focus on samples without the presence of a gas phase making this study relevant to NAPL contamination below the water table. We present the results of several NAPL injection experiments monitoring P-wave velocity as a function of NAPL saturation for Pinellas core samples. We also contribute new measurements of the acoustic properties of glass bead samples fully saturated with either toluene or trichloroethylene [1]. We interpret the existing

---

[1] All new experimental data discussed in this chapter was collected with Jil Geller (LBNL) who performed the laboratory seismic component of the Pinellas project.

experimental database in terms of Biot-Gassmann theory with three models for the geometric distribution of fluids. We find that Biot-Gassmann theory provides a good lower bound on the P-wave signature of contaminant saturated sediments but does not always quantitatively match measured V_p values, particularly at higher NAPL saturations. These discrepancies might be explained through changes in frame shear modulus due to anomalous contact mechanics. An empirical model based on NAPL volume fractions provides a second approach to property estimation. The simple linear volumetric model we present seems to accurately predict changes in velocity due to NAPL saturation for a broad range of samples. Increased seismic attenuation has also been observed in NAPL injection experiments; we explore several possible explanations for these effects. We conclude with an estimate of the expected seismic signature for the DNAPLs present at the Pinellas site based on our previous estimates of NAPL phase properties. Based on our best estimate of soil properties at the Pinellas site and the expected characteristics of the extracted DNAPL phase, we predict a relatively small decrease in P-wave velocity as the most likely seismic signature for free-phase contamination at Pinellas.

6.1 Experimental Database For The Acoustics Of NAPL Saturated Granular Media

Although the acoustic properties of NAPL saturated granular media have not been heavily investigated, a small but growing body of experimental results exists for synthetic systems (glass beads), clean sands, and natural aquifer cores at low pressures. All laboratory experiments to date have shown that NAPL saturation reduces P-wave velocity and increases P-wave attenuation at frequencies between 60 and 1000 kHz. Only part of the observed velocity reductions can be attributed to the increased compressibility of pore fluids within the standard framework of poroelasticity as described by Biot and Gassmann which we discuss at length in the following sections. Although significant changes in waveform amplitude were observed in all cases, we focus our investigation on P-wave velocity which is the most accessible variable from a field perspective and the most robust parameter to extract from ultrasonic laboratory experiments. The scaling of attenuation measurements from ultrasonic to seismic frequencies further complicates the application of laboratory measurements to the analysis of field data. A discussion of possible attenuation mechanisms and their significance for site characterization will be postponed until the concluding sections. Table 6.1 includes the basic acoustic properties of the fluids used in the experiments which we will review. The reader is referred to chapter 4 for a detailed examination of pure DNAPL properties.

Geller and Myer [111] investigated the relationship between NAPL saturation, P-wave velocity, and attenuation using 1,1,2-trichloro-1,2,2-trifluro-ethane (freon 113), n-dodecane, and iso-octane as model contaminants. They made measurements on medium sub-rounded quartz sand samples (212-250 microns) with porosities of 42% at effective pressures of 140 kPa. Measurements examining both NAPL injection into water saturated samples and purely NAPL saturated samples were made using

Acoustic Properties Of Experimental NAPLs				
Fluid Type	Density (kg/m^3)	Bulk Modulus (Pa $\times 10^9$)	V_p (m/s)	Viscosity (Pa $\times 10^{-}3$)
Freon 113	1560	0.7997	716	0.711
n-Dodecane	745	1.2398	1290	1.378
Iso-octane	690	0.8655	1120	0.504
Trichloroethylene	1451	1.6317	1050	0.566
Silicone Oil (100)	968	0.9297	980	100
Silicone Oil (10)	940	0.8808	968	10
Castor Oil	942	2.1393	1507	800
Toluene	870	1.5182	1321	0.522
Water	997.07	2.2343	1497	1

Table 6.1: Acoustic properties for NAPLs previously used in experimental studies : The most relevant references are [111] [235] [234] [236] [108]. The reader is referred to chapter 4 for a complete review of pure NAPLs including auxiliary health/chemical information and citations.

an ultrasonic pulse transmission system operating at a central frequency of 500 kHz. Throughout this chapter, we use the abbreviation GM-95 to refer to Geller and Myer's 1995 dataset. The GM-95 measurements are an attractive dataset for testing theoretical predictions because of the variety of fluids examined, the large number of saturation levels attained, and the acquisition of independent data points for fully saturated samples. One short coming of the GM-95 experiments is the lack of S-wave velocity measurements, without which elastic moduli cannot be directly determined.

Seifert [234] [236] performed a similar set of measurements with a focus on varying fluid viscosity and wetting properties. P-wave velocity and attenuation were measured while saturating with two different grades of silicone oil (10 and 100 cs), castor oil, and n-dodecane. Seifert used the same sub-rounded quartz sand examined by Geller and Myer [111] (212-250 microns) but packed the samples to 35% porosities and used a higher effective pressure (690 kPa). Only pure phase measurements were made for the oils while n-dodecane was examined during both NAPL-to-water and water-to-NAPL injections. Measurements were made using a similar ultrasonic pulse transmission system operating at a central frequency of 900 kHz.

On a slightly larger scale, a series of physical model (0.61 m tank) experiments was performed by Kowalsky *et al.* [146]. In this experiment, n-dodecane was injected into a homogeneous sandpack maintained at a confining pressure of 140 kPa. Acoustic waveforms were acquired using a miniature accelerometer array and bar piezoelectric source operating at a frequency of 60 kHz. The resulting dataset was processed using a 2D straight-ray tomographic algorithm. The velocity decrease due to n-dodecane saturation appeared to be only 2% for the rays of maximum delay. However, amplitude anomalies of up to 65% were observed along high delay paths. Geller *et al.* [109] performed a similar experiment, using the same apparatus operating at 90 kHz, to image a lens of n-dodecane pooled at a capillary barrier. They observed reductions in amplitude and an increase in traveltimes for rays traveling through the NAPL zone. Subsequent asymptotic waveform tomography performed by Keers *et al.* [138] revealed peak velocity reductions on the order of 2.5 %.

Geller, Ajo-Franklin, and Majer [108] examined the effects of toluene and trichloroethylene (TCE) saturation on ultrasonic P-wave velocity and attenuation for a set of natural aquifer samples from the Pinellas site [112] [11] [12]. Samples with a variety of textures ranging from clean sands to clayey silty sands were tested with porosities ranging from 32% to 43% percent. Only NAPL-to-water injection sequences were performed. The maximum contaminant saturations achieved were less than 80% for all samples. Several auxiliary samples saturated only with water were also characterized to provide added information on the relationship between V_p and textural parameters. Measurements were made in the transmission mode at 500 kHz. These experiments will be our primary focus in this chapter due to their relevance to seismic detection of DNAPLs at Pinellas; we refer to this work as the G/A-F 02 dataset.

In this section, we will also extend the existing NAPL saturation database to include unpublished measurements on soda-lime glass beads, a well-characterized model system with known grain geometry and fixed homogeneous grain moduli. Following [108], TCE and toluene were used as saturating fluids and both injection and pure phase measurements were acquired. These measurements were also made in the transmission mode at 500 kHz; we refer to this work

6.2 Previous Theoretical Approaches For Modeling The P-Wave Velocity Signatures Of NAPL Saturation

Several previous attempts to develop petrophysical models for NAPL saturation have met mixed success. Geller and Myer [111] proposed using a variation of the Kuster Toksoz (KT) scattering model to describe NAPL saturation effects. The fluid mix was used as the background phase and effective fluid properties were estimated using a Voigt average. Quartz grains were added as inclusions. Unfortunately, the model could not fit the observed P-wave velocity data without significantly reducing the model porosity to between 30 and 35 %. Figure 6.1 shows the three Geller/Myer 95 datasets in addition to the KT scattering model and the Reuss suspension model evaluated at the correct porosities. The discrepancy between the KT model and the observed data could be attributed to several sources including the large concentration of inclusions which probably breaks the model's implicit single-scattering assumption. The use of the fluid as the background phase also assumes a suspension state with a shear modulus of zero which is probably not the case for the samples examined. Although no S-wave velocity measurements were acquired as part of the Geller/Myer dataset [111] measurements on similar sands made by Prasad [218] [220] [219] and Zimmer [283] [282] at low pressures show S-wave propagation demonstrating that grain contacts are indeed load bearing.

Seifert [234] and Seifert *et al.* [235] examine a 1D propagator matrix technique for understanding

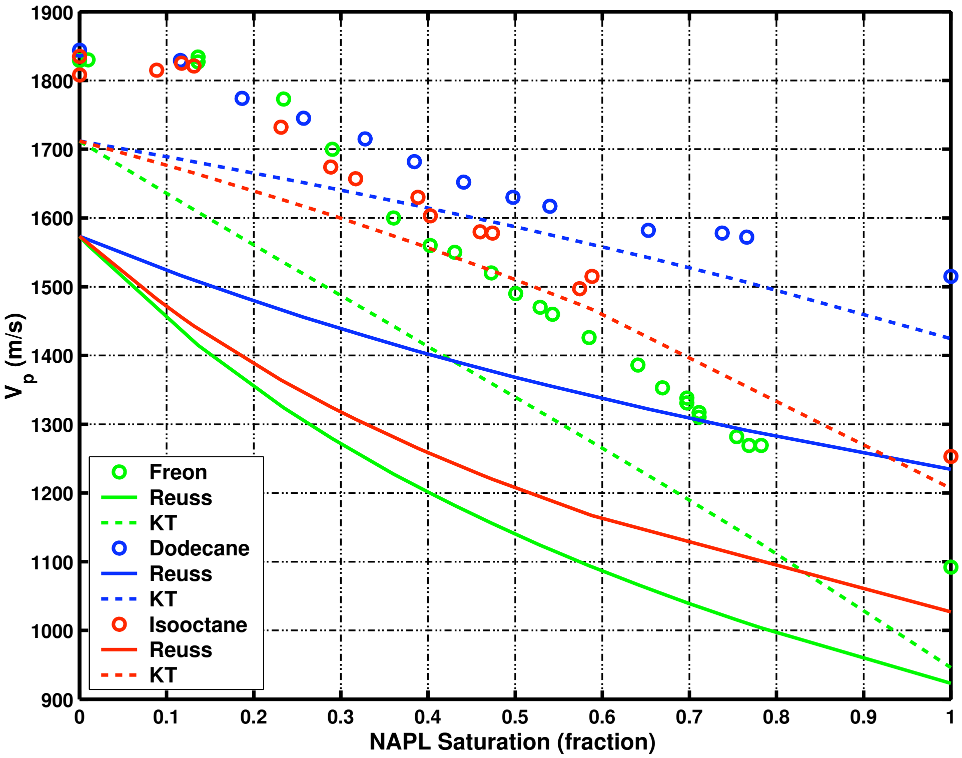

Figure 6.1: Comparison of the Geller/Meyer 95 dataset [111] to two suspension models : The lower set of curves are the Reuss lower bounds for the 3 phase (grain/water/NAPL) mixtures. The upper set of curves are the equivalent Kuster-Toksoz curves treating the system as grains embedded in a fluid mixture as is done in [111]. The GM-95 samples were clean sands with a uniform porosity of 0.42 .

Geller and Myer's [111] P-wave velocity and attenuation measurements. The geometric model assumed for the resulting simulations were stacks of 1D laminae where each layer has the properties of the appropriate NAPL, water, or quartz. The thickness of each quartz lamina was approximately 230 microns which is close to the grain dimensions used in the original experiments. A gaussian distribution of two or four component groupings of laminae (quartz/water or quartz/water/NAPL/water) were used while preserving the appropriate total porosity and NAPL saturation to within a fixed standard deviation. Each reported simulation point was the mean of 10 independent realizations. However, like the KT modeling results presented in [111], reasonable velocity fits could not be obtained without reducing the modeled porosities to 32% from the experimentally measured 42%.

Seifert [234] and Seifert, Kaelin, and Johnson [236] investigated the role of fluid viscosity in P-wave velocity and attenuation in sands at low pressure using the Dynamic Composite Elastic Medium model (DYCEM), the Local Flow Model (LFM) as described by O'Connel and Budiansky, and the unified Biot-Squirt model (BISQ). Seifert, however, focused on fitting the trends in frequency dependent attenuation observed using spectral ratio analysis and states that velocities estimated using DYCEM or Berryman's Self-Consistent model were unable to explain the NAPL measurements without making the frame bulk modulus strongly dependent upon the saturating fluid.

More recently, Carcione *et al.* [51] proposed a theoretical model for the acoustic properties of NAPL contaminated sediments which includes White's patchy saturation model. An extended Biot-Gassmann model including viscodynamic effects related to clay content was used to allow single phase patches to have a second relaxation mechanism. However, Carcione does not compare this model to any existing data set for NAPL saturated unconsolidated materials and only uses data from partial gas saturation experiments on cemented limestones and sandstones. His prediction that attenuation peaks at intermediate NAPL saturations due to patch pressure equilibration contradicts the attenuation data from the GM-95 experiments [111] where peak attenuation is observed at full NAPL saturation for two of the three fluids. The presence of a patch dimension term also makes testing of the theory difficult without X-ray CT images of the sample during fluid injection.

6.3 Ultrasonic Measurements On The Pinellas Core Collection

Interpreting seismic field data in terms of NAPL saturation requires both experimental confirmation of NAPL-induced seismic signatures and a theoretical framework for interpreting such datasets. The paucity of existing acoustic measurements of soils partially saturated with NAPLs motivated our laboratory investigation. Additionally, our use of sediment cores from the Pinellas site, saturated with the types of NAPLs present *in situ*, made the results relevant to calibration of our seismic field dataset. The experiments we will discuss examined changes in P-wave velocity and amplitude during the injection of either TCE or toluene into fully water saturated natural aquifer samples. This section presents the essential results from Geller, Ajo-Franklin, and Majer [108] relevant to the Pinellas investigation. The reader is referred to the aforementioned paper for more details on methods and experimental procedures.

Experimental Apparatus

The apparatus used for the Pinellas core seismic experiments was developed by Jil Geller (LBNL) for the measurement of P-wave velocities at ultrasonic frequencies using the pulse transmission method. This particular system was specifically tailored for use at low effective pressures ($\sim$ 50 kPa - 1 MPa) with reactive solvents as saturating fluids. Figure 6.2 shows a schematic of the apparatus. Independent control of axial, confining, and pore pressure allowed duplication of near-surface stress conditions expected at our field site. A set of ISCO 500D syringe pumps operating in a constant pressure mode were used for maintaining confining and axial stress in the triaxial cell. A similar pump was used for fluid injection and control of pore pressure. NAPLs were injected using a transfer cylinder to chemically isolate the solvent from the pump components. Endcaps were constructed from compression-molded polyphenylene sulfide (pps) which possesses both excellent solvent resistance and a superior impedance match ($V_p = 2519$ m/s, $\rho = 1329$ kg/m^3, $I_p = 3.347 \times 10^6$ kg/(m^2 s)) to low-pressure sediments in comparison to aluminum ($V_p = 6420$ m/s, $\rho = 2700$ kg/m^3, $I_p = 1.773 \times 10^7$ kg/(m^2 s)) or stainless steel. Saturating fluids were injected through two ports in the endcap assembly. The injection ports were mounted on an annular fluid distribution channel to promote a laterally uniform saturating front. The samples were jacketed using either teflon tubing or a viton elastomer. The viton jackets exhibited superior solvent resistance but the teflon tubes had the added advantage of transparency allowing visual monitoring of the injected fluids.

500 kHz Panametrics transducers bonded to the interior of the endcaps were used for the transmission measurement. The transducers were excited using a square wave with a 400 volt amplitude and an 8 μs peak width generated by an an IRCO model M1K-20 pulser. Waveforms were digitized using a Lecroy 9310A digital oscilloscope. One hundred pulses were stacked for each acquired trace.

Procedure

Measurements were performed on samples from the G13-N3, G13-N4, and G20-N4 core sections [2] , detailed in Chapter 2 where we refer the reader for complete information concerning core acquisition and sample locations. Each 7 cm long sample was removed from the larger core tube using a steel cutting plate, subcored to a diameter of 6.93 cm, and then frozen. The frozen sample was then inserted into the appropriate sample jacket and loaded into the triaxial measurement cell. Before injection, the pore water was vacuum deaired and allowed to equilibrate with the material in the subcore annulus to prevent dissolution of microstructural cements. The sample was saturated at a pore pressure of 350 kPa with axial and confining loads used to maintain an effective stress of 380

---

[2] The first component of each core label, e.g. G20, denotes the well from which the core was taken while the second component, e.g. N3, is a numeric label to distinguish different core sections taken from the same well. Smaller subsamples taken from the large core sections are labeled by the distance in cm from the top of the core to the top and bottom of the subsample e.g. G20-N4-31-38 is a subsample taken from the 4th core extracted from well G20 with top and bottom edges 31 and 38 cm respectively from the top of the core.

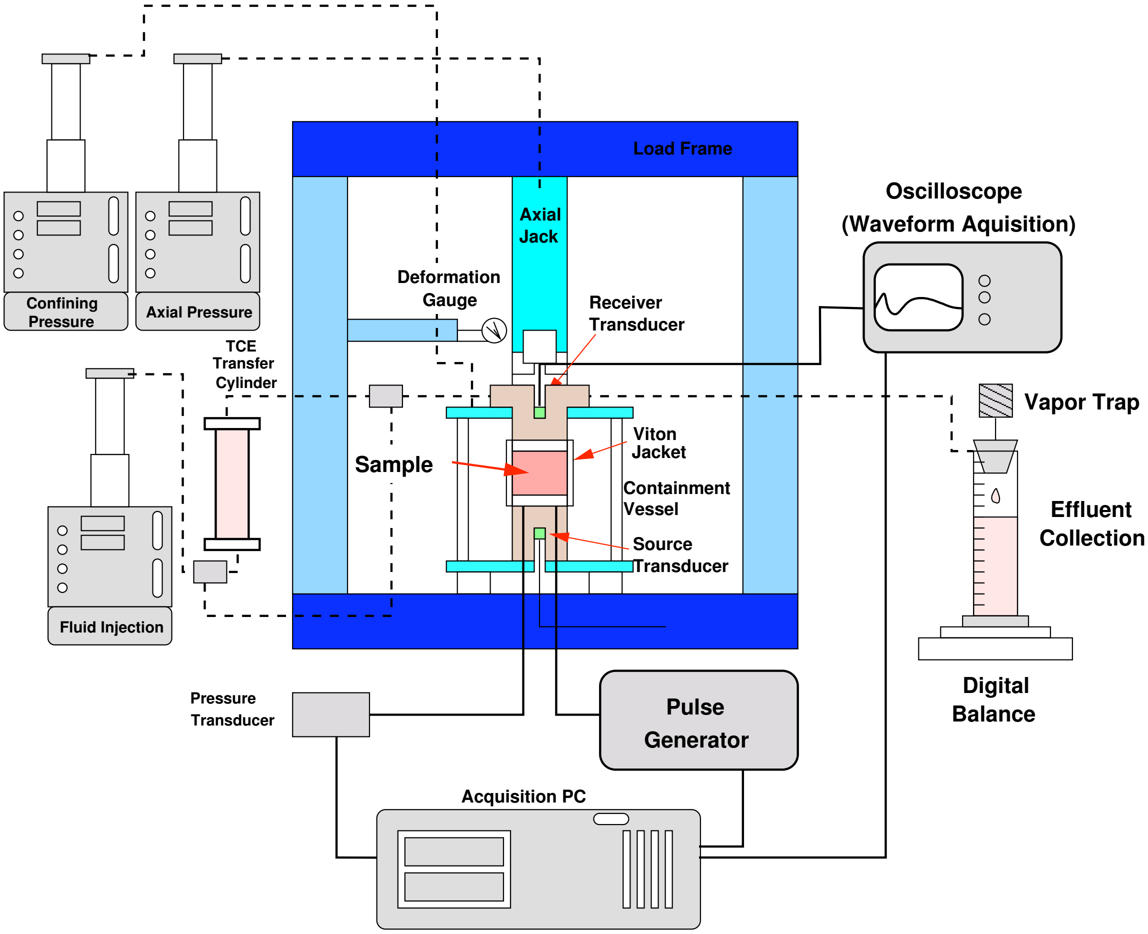

Figure 6.2: Schematic of the ultrasonic pulse transmission apparatus : diagram is a modified version the figure from Geller, Ajo-Franklin, and Majer [112].

Sample	**Elev.** (m)	ϕ	**Sand/ Silt/ Clay**	**Mean Eff. Stress** (kPa)	V_p Water Sat. (m/s)	**NAPL Type**	**Max** S_{NAPL}	ΔV_p (%)	ΔA (%)
G13-N3-52-59	-0.9	0.39	91/3/6	240	1780	-	-	-	-
G13-N3-59-66	-1.0	0.34	95/1/4	372	1780	TCE	0.59	12.16	40.77
G13-N3-59-66B	-1.0	0.41	91/8/2	230	1740	-	-	-	-
G13-N3-66-73	-1.4	0.32	89/3/8	360	1790	Tol.	0.81	8.9	43.24
G13-N4-57-64	-2.5	0.43	60/26/14	480	1730	Tol.	0.42	5.48	40.07
G13-N4-96-103	-2.9	0.43	59/28/13	-	1710	-	-	-	-
G13-N4-104-101	-3.0	0.42	62/21/17	327	1740	TCE	0.30	5.42	33.93
G13-N4-135-142	-3.28	0.41	55/24/21	355	1770	TCE	0.51	8.32	33.2
G20-N4-20-28	-2.0	0.43	57/30/13	-	1770	-	-	-	
G20-N4-31-38	-2.1	0.40	53/34/13	541	1760	Tol.	0.50	8.15	53.38

Table 6.2: Ultrasonic V_p measurements on the Pinellas samples. Elevations are the vertical locations at which the samples were collected and are absolute with respect to sea-level. Sand/Silt/Clay fractions were determined using the hydrometer method.

kPa. As the sample was saturated, P-wave velocity and amplitudes increased as gas was removed. The core was considered fully water saturated when P-wave response achieved a steady state. NAPL, dyed red for visibility (oil-red-O dye, Sigma Aldrich), was injected from the sample's top (for toluene) or the sample's bottom (for TCE) to prevent density-driven flow instability. NAPL injection volume was measured by both pump indicators and the mass of effluent collected. The experiment was considered complete when the NAPL injection pressures reached 280 to 350 kPa, indicating difficulty in displacement of the remaining pore water. Following each injection experiment, the samples were dried and weighed for dry bulk density, grain density, and porosity measurements. A section of the sample was taken for grain-size analysis using the hydrometer method.

P-wave traveltimes were determined by picking the first zero-crossing and calculating times with respect to de-aired DI water which was used as a calibration fluid. P-wave velocity was calculated from sample length and picked traveltime.

Four cores were injected with NAPLs, two with TCE and two with toluene. Three cores were used only for water saturated P-wave velocity and hydraulic conductivity measurements. Table 6.2 contains a summary of the experimental results for all of the Pinellas samples examined including textural parameters, effective stress levels during measurement, and the change in P-wave velocity and amplitude observed at maximum NAPL saturation. Full NAPL saturation was not attained in any of the injection experiments with peak saturations ranging from 30 to 78 %.

The core samples from the shallow N3 section were relatively clean sands while the samples from the N4 section were a mixture of sands and silts with a small clay component (clayey-silty sands). All N4 samples had similar porosities (0.40 to 0.43) and all cores examined had very similar V_p values at full water saturation (1710 to 1790 m/s) independent of porosity or texture. Figure 6.4 shows the lack of correlation between V_p and porosity, V_p and clay content, V_p and silt content, and porosity and clay content for the water-saturated Pinellas cores. Glass bead samples and curves for the Reuss suspension model are included for reference. The lack of correlation between textural

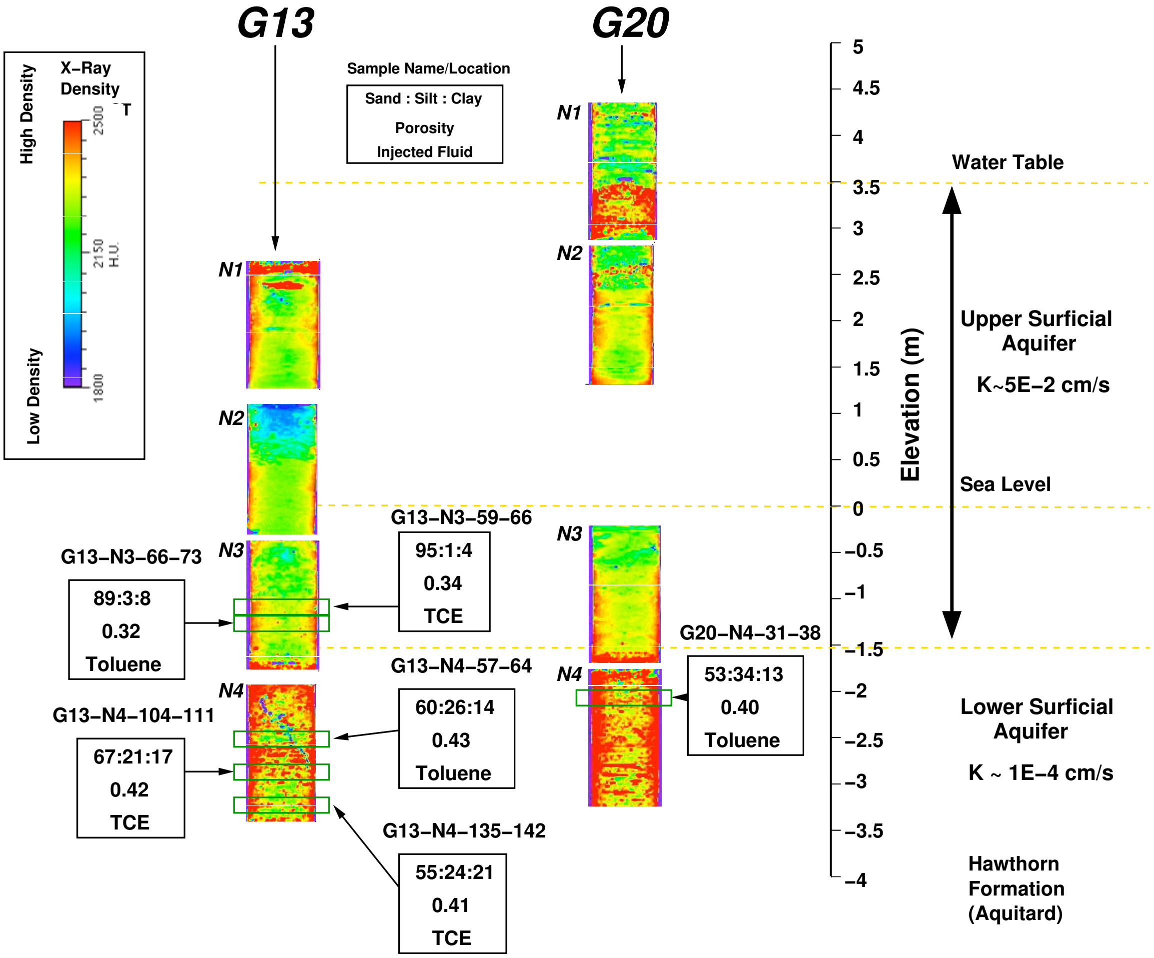

Figure 6.3: Vertical distribution of Pinellas core samples: Core color maps are generated from X-ray CT imagery with red colors indicating higher bulk densities. Since the cores were drained prior to imaging, fine soils with higher residual water saturations have a higher bulk density despite the fact that they have low porosities. Green boxes superimposed indicate the location of samples taken for injection experiments. Labels show the sand/silt/clay content and porosity of each sample in addition to fluid type used in the injection experiment.

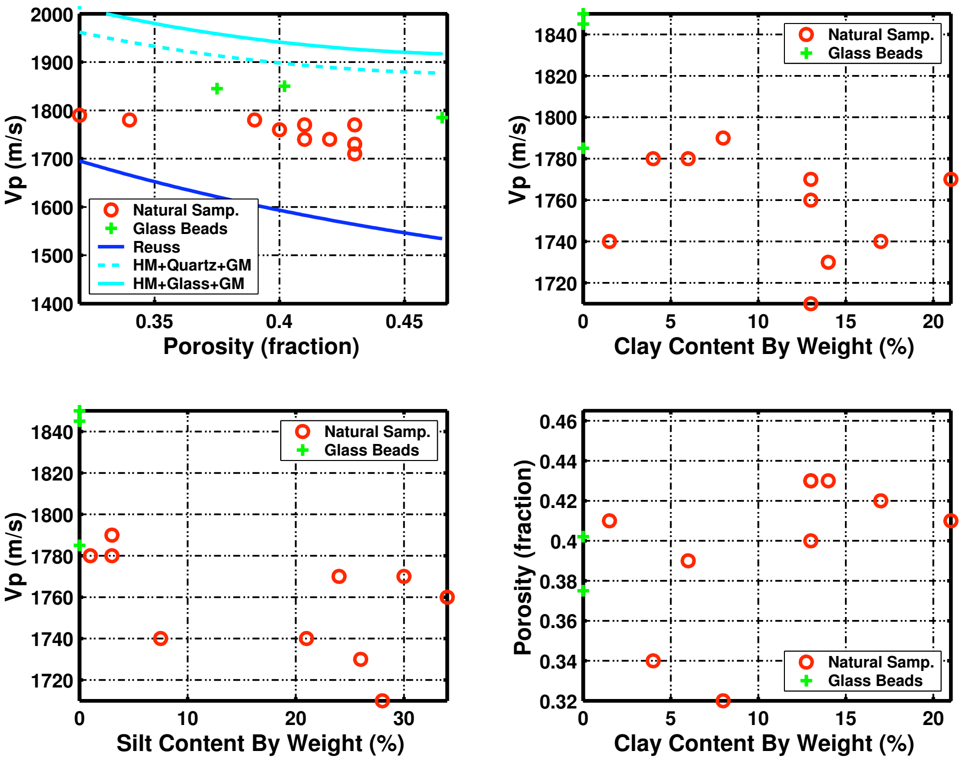

Figure 6.4: V_p vs. porosity, V_p vs. clay content, V_p vs. silt content, and porosity vs. clay content for the water-saturated Pinellas cores. The prediction of the Reuss suspension model is superimposed over the V_p vs. porosity plot as is the Hertz-Mendlin (HM) contact theory prediction using Gassmann to add water saturation. The HM model is used here only for reference with quartz and glass as two possible grain components. The HM model assumes a pressure of 50 kPa. Contact theory models will be discussed in more detail in the joint modeling section.

parameters and V_p suggests that the fluid bulk modulus dominates the properties of saturated soils at these pressures. However, the fact that suspension models predict a lower V_p than those observed is evidence that contacts are indeed load bearing and that the soils examined have a small but non-zero shear modulus in agreement with previous experiments at similar pressures [282]. In addition to curves for the Reuss model, figure 6.4 also includes predictions generated by the Hertz-Mendlin (HM) contact model saturated using Gassmann fluid substitution and assuming an effective pressure of 50 kPa. We will not discuss contact theories in detail until the joint modeling section but one should note that HM predicts a somewhat stiffer frame than is observed in our low pressure natural sediment measurements.

In all natural aquifer samples examined, NAPL injection decreased measured P-wave velocity and decreased peak waveform amplitude. NAPL injection decreased P-wave velocity by between 5.42 and 12.16 % depending upon the injected fluid, peak saturation, and sample porosity. Figure 6.5 shows some recorded waveforms for the G13-N3-59-66 and G13-N4-104-111 samples in the water saturated state and with maximum NAPL saturation. We will embark on a more detailed exploration of the results of the injection experiments in the following sections.

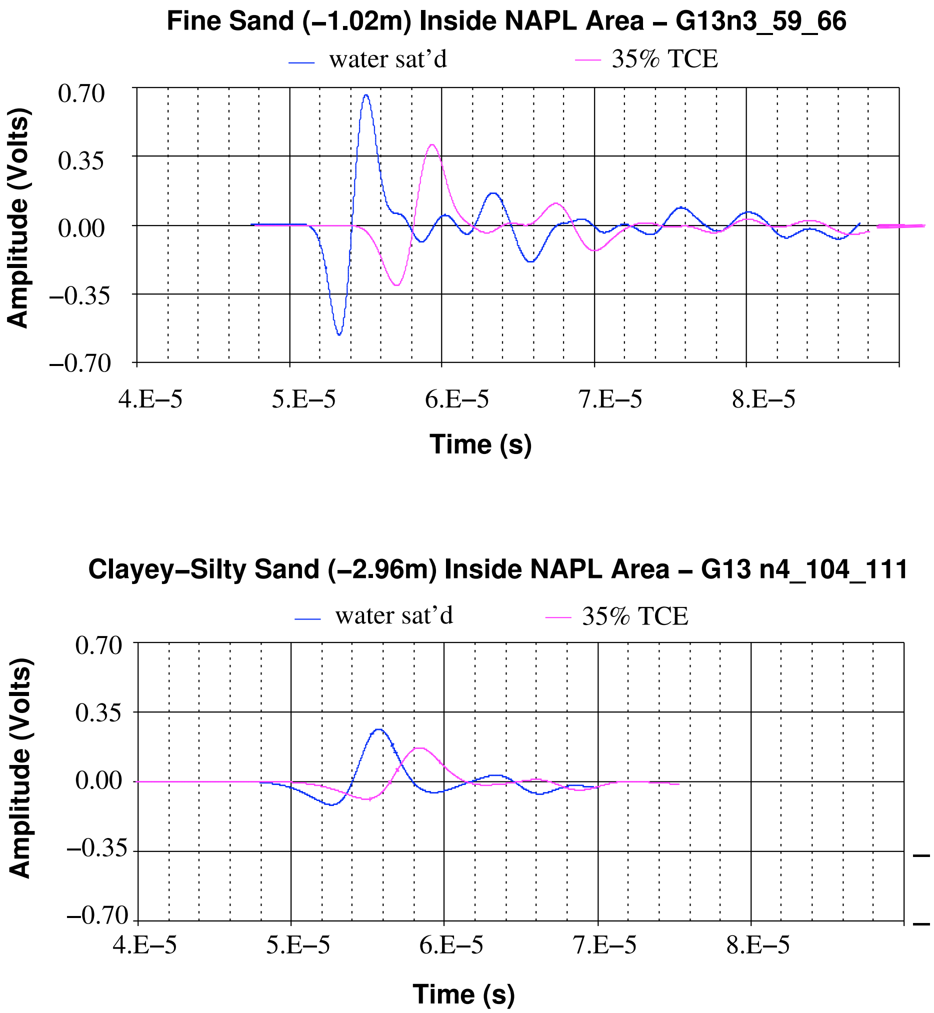

Figure 6.5: Ultrasonic waveforms from two injection experiments. Note that traveltime increased (a decrease in V_p) and amplitude decreased in response to NAPL injection.

6.4 Predicting The P-Wave Signature Of DNAPL Saturation

The primary goal of our investigation is to understand the changes in soil P-wave velocity due to partial DNAPL saturation. Biot-Gassmann theory [35] attempts to describe the effects of pore fluids on the bulk properties of porous materials. Fluids with a high bulk modulus tend to stiffen pores while at higher frequencies viscous losses can be generated due to motion of the saturating fluid with respect to the porous matrix. Significantly, the theory does not attempt to predict rock properties from *ab initio* information concerning individual phase properties and the geometry of the distribution of phases like the Differential and Self-Consistent effective medium theories (DEM and SCM) but limits itself to fluid effects. We will focus on the use of Biot-Gassmann theory for the prediction of P-wave velocities. Although seismic attenuation due to the presence of NAPLs has been noted in previous studies, the lack of laboratory measurements over a large frequency range makes diagnosis of the relevant mechanism difficult. We will consider some possible attenuation mechanisms in later sections.

When quantifying the effects of DNAPL saturation on rock properties, we must consider both the geometric distribution of the fluid in the solid matrix and the fluid volume fraction. We will explore the effects of fluid distribution through comparison of several extensions to Biot-Gassmann theory including the Reuss/Voigt effective fluid models, Hill's equation [127], and White's patchy saturation model [274] [84].

6.4.1 Biot-Gassmann : Theory

The Biot-Gassmann relations can generally be divided into a set of frequency regimes where different mechanisms are dominant. In the Gassmann or low-frequency regime, the measurement frequency, f, is considerably smaller than the Biot critical frequency, f_c, where f_c can be written as,

$$f_c = \frac{\phi\,\eta}{2\,\pi\,\rho_{fl}\,\kappa}, \tag{6.1}$$

with

ϕ = porosity
ρ_{fl} = fluid density
η = viscosity of the saturating fluid
κ = permeability of the porous media

Within this frequency range, the effect of the saturating fluid is primarily a stiffening or softening of the pore space; fluid pressure has sufficient time to equilibrate across the sample volume. As is clear from equation 6.1, both the properties of the fluid (η, ρ_{fl}) and the properties of the porous matrix (ϕ, κ) influence this transition frequency. One common application of Biot-Gassmann theory is the calculation of rock properties when the pore fluid is modified, a process called fluid substitution. Equation 6.2 is one form of Gassmann's formula. In this case, the dry frame bulk modulus (K_{dry})

is calculated from the grain bulk modulus (K_g), the bulk modulus of the fluid (K_w), the measured bulk modulus of the fluid saturated rock (K_{wsat}), and the porosity (ϕ),

$$K_{dry} = \frac{K_{sat_w}\left(\frac{\phi K_g}{K_w} + 1 - \phi\right) - K_g}{\frac{\phi K_g}{K_w} + \frac{K_{sat_w}}{K_g} - 1 - \phi}. \tag{6.2}$$

Likewise, this dry frame estimate can then be re-saturated with a second fluid using a similar equation, thus generating a bulk modulus estimated for the same sample with a second fluid within the pore space. One fundamental assumption of Gassmann's equations are that the dry and wet shear moduli are the same,

$$\mu_{dry} = \mu_{wet}. \tag{6.3}$$

Additional requirements include that the rock should be isotropic, the grain mineral properties homogeneous, and that the rock is fully saturated with a single fluid. Gassmann's equation does not make any assumption concerning grain contacts, coordinate number, or grain/pore aspect ratio.

Since we are interested in the signature of partial DNAPL saturation we must consider techniques for introducing multiple fluid phases into the Biot-Gassmann framework. One approach is to introduce an effective fluid model which treats the partially saturated rock as a fully saturated material with a modified fluid. The properties of this effective fluid are calculated through some type of volumetric average of the constituent fluids properties. We will consider Reuss and Voigt effective fluid models which can be seen as heuristic bounds on the properties of fluid mixtures within the porous frame. We will also consider two models which explicitly consider macroscopic zones with different fluid saturations. Hill's equation allows us to calculate the bulk modulus of a composite with uniform shear modulus but spatial variations in compressibility. Since shear modulus is independent of fluid saturation in Biot-Gassmann theory, Hill's equation allows us to calculate the properties of a material with patches occupied by different fluid phase. While Hill's equation is only valid in the quasi-static limit, White's model for patchy saturation includes effects due the equilibration of pore fluid pressure between patches.

6.4.2 Previous Experimental Confirmation Of Gassmann's Equations

Biot-Gassmann theory has been experimentally tested on a large array of core samples, including both unconsolidated and consolidated media, at pressures over 2 MPa. Even at high frequencies, Gassmann's equation has shown significant utility due to the relatively small velocity dispersion predicted by Biot mechanisms. Confirmation of Biot-Gassmann theory on unconsolidated sediments at pressure below 2 MPa is still incomplete and a full model for sands at low pressures is still being developed using contact theory formalisms.

Han *et al.* [120] examined a large number of Gulf Coast sandstones at pressures between 5 and 40 MPa using ultrasonic (1 MHz) pulse transmission techniques. Samples were analyzed for clay content, V_p,V_s, bulk density, and porosity. Comparison of saturated bulk modulus as calculated by Gassmann's equation to measured bulk modulus agreed well, particularly at porosities higher than 25%. Samples with significant clay content displayed measurable changes in shear modulus due to hydration of clay contacts.

Castagna *et al.* [54] demonstrate that with correct V_p and V_s values, Gassmann's equation agrees well with existing laboratory measurements. The Holt Sand example mentioned in [54] matched Gassmann predicted values to within 1%. Secondary plots presented in the same paper show a mild degree of deviation from Gassmann generated by the assumption that the dry bulk and shear moduli are equal, $K_{dry} = \mu_{dry}$. Another relevant examination of the validity of Biot-Gassmann theory for describing velocities in unconsolidated media was carried out by Domenico [82] [81]. Synthetic samples composed of clean Ottawa Sand ($\sim$ 89 microns mean diameter) and glass beads ($\sim$ 81 microns mean diameter) were investigated at effective pressures ranging from 2.8 to 34.5 MPa, considerably higher than the 100 to 700 kPa pressures we have focused on.

6.4.3 Literature Derived Estimates Of V_p/V_s

Since only V_p, ρ, and ϕ are directly measured in our core experiments, a technique to estimate V_s is required to calculate the elastic constants K and μ. We present some estimates of appropriate V_p/V_s ratios for our samples. We also demonstrate that calculations of K are relatively insensitive to the assumed ratio when $10 > V_p/V_s > 4$, which is likely the case for the measurements we consider. Assuming V_p, V_s, and ρ are known, K and μ can be expressed as,

$$\mu = \rho V_s^2 \tag{6.4}$$

$$K = \rho \left[V_p^2 - \frac{4}{3} V_s^2 \right]. \tag{6.5}$$

Equivalently, equations [6.4] and [6.5] can be rewritten in terms of V_p and the V_p/V_s ratio,

$$\mu = \frac{V_p^2 \rho}{(V_p/V_s)^2} \tag{6.6}$$

$$K = \mu \left[(V_p/V_s)^2 - \frac{4}{3} \right]. \tag{6.7}$$

As is clear from equation 6.5, when $V_p >> V_s$, K is only weakly dependent on V_s.

Several studies considering the V_p/V_s ratios of clean unconsolidated sands at low pressures exist within the literature [219] [283] [220] [218] [282] [228]. Zimmer [282] provides perhaps the most complete set of acoustic measurements on unconsolidated samples available within the low pressure regime. He acquired 200 kHz pulse transmission data for 13 samples ranging in texture from glass beads to natural sands at effective pressures between room pressure to 20 MPa. Figure 6.6 depicts the V_p, V_s, and V_p/V_s datasets from Zimmer which we use for our primary calibrations. Only water-saturated measurements acquired at effective stresses between 0 and 1000 kPa from Zimmer's first three loading cycles are included. All V_p/V_s values from the examined dataset were between 4 and 10. Similar results for wet V_p/V_s were also reported by Hamilton [119] who observed *in situ* values of between 9.3 and 13 for the first 10 meters of oceanic silts/clays and between 31 and 7.7 for the first 10 meters of oceanic sands.

For the clean sands examined by Geller and Myer [111], we use Zimmer's water-saturated Santa Cruz aggregate ($\phi = 0.4$, $D_{50} = 288 \times 10^{-6}$ m) dataset for our estimate of V_p/V_s [282]. Both porosity and mean grain dimension were comparable to the Geller/Myer sand and similar effective pressures were used in both experiments. The V_p values for Santa Cruz aggregate sample were weakly pressure dependent while V_s exhibited a strong pressure dependence from 0 to 1000 kPa. V_p/V_s ranged from 5.5 to 4.5 with V_p/V_s being inversely correlated with effective stress. We use a V_p/V_s value of 5 for all fits involving the Geller/Myer dataset although the fitting results are not sensitive to this choice as will be demonstrated later.

Since the silt/clay components of the natural aquifer samples might have a significant effect on the wet V_p/V_s ratio, we use values from Zimmer's water-saturated Meritt sand dataset ($\phi = 0.34$, $D_{50} = 225 \times 10^{-6}$ m). The Merrit sand is a Pleistocene dune sand composed primarily of Quartz and Plagioclase with 11 % clay by weight. V_p/V_s values ranged from 5 to 9.6 and we use a value of 7 for all fits involving our natural aquifer samples. Unfortunately, Zimmer's glass bead measurements were not performed in a water saturated state : we will use the Santa Cruz aggregate value of 5 for our glass bead V_p/V_s fitting experiments.

Having provided basic estimates of V_p/V_s for our measurements, we can also demonstrate that changes in the assumed V_p/V_s ratio in the range of 4 to 10 do not have a large impact on estimated bulk modulus and predicted V_p values from the Gassmann model. Figure 6.7 depicts Gassmann estimates of V_p as a function of saturation for the GM-95 freon-113 dataset using the fluid substitution model we will discuss in the next section. Curves using V_p/V_s values of 4,7, and 10 are shown with almost negligible differences in estimated V_p values : the peak relative difference between the curves corresponding to V_p/V_s values of 4 and 10 is only 1.2 %.

6.4.4 A Fluid Substitution Framework

In this section we present a simple work flow for estimating the properties of sands partially saturated with NAPLs using Gassmann fluid substitution, effective fluid models, and Hill's formula. Although Gassmann is the low frequency limit of Biot-Gassmann theory, the calculated velocity dispersion due to Biot flow is smaller than the observed departures from Gassmann's equation and also has the wrong trend. We will discuss Biot effects in the transition frequencies later in this chapter. Another argument in favor of using Gassmann's equations is the smaller number of guessed parameters; with the exception of the V_p/V_s ratio which we estimate using literature relations, all components of the model are experimentally known. In the Biot model, several parameters including tortuosity and

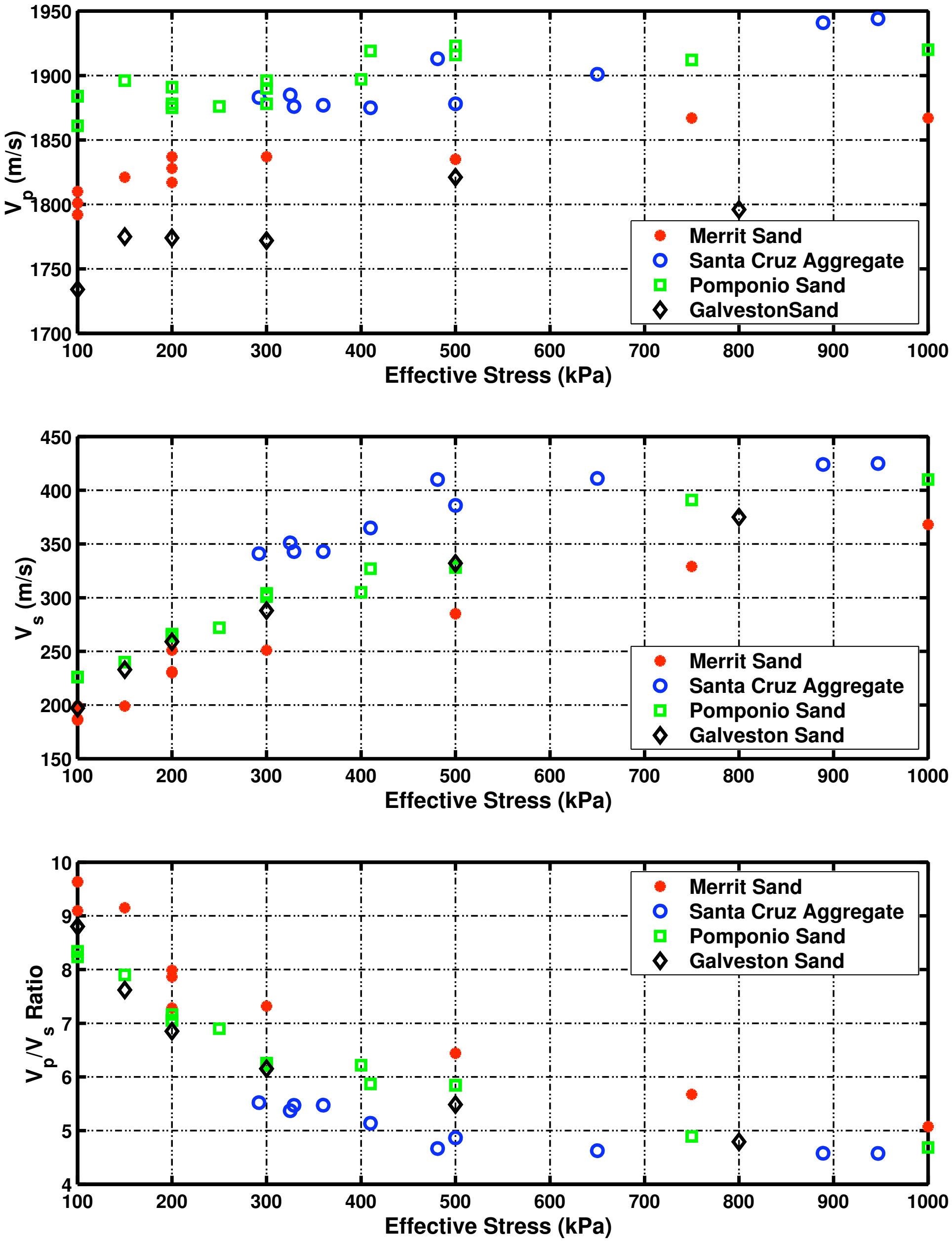

Figure 6.6: Vp/Vs measurements on wet sands from Zimmer 03 for pressures from 0 to 1000 kPa: Shown are data from the first couple of loading cycles for the Santa Cruz aggregate ($\phi = 0.4$, $D_{50} = 288 \times 10^{-6}$ m), the Merrit sand ($\phi = 0.34$, $D_{50} = 225 \times 10^{-6}$ m), the Pomponio Beach sand ($\phi = 0.339$, $D_{50} = 378 \times 10^{-6}$ m), and the Galveston Beach sand ($\phi = 0.397$, $D_{50} = 134 \times 10^{-6}$ m).

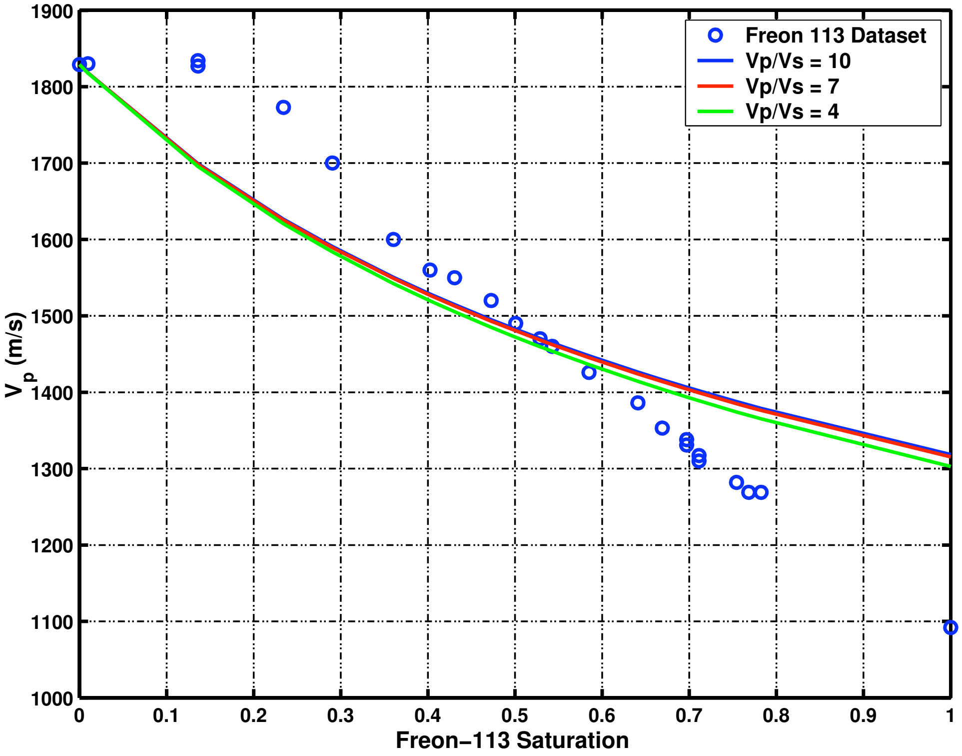

Figure 6.7: V_p predictions for the GM-95 freon-113 dataset for different assumed V_p/V_s ratios between 4 and 10. Gassmann fluid substitution with the Reuss effective fluid model is used for for V_p estimates.

sample permeability must be estimated. Tortuosity in particular is very difficult to measure and most calculations rely on theoretical estimates dependent on grain geometry.

Estimation Of V_p For Samples Partially Saturated With NAPLS

Since our goal is a quantitative comparison to laboratory data, the flow we will describe starts with available experimentally obtained parameters for a sample in the fully water saturated state and predicts V_p at a given NAPL saturation. The process is a relatively standard adaptation of Gassmann fluid substitution. In all of the experiments we analyze, grain properties (K_g,μ_g,ρ_g), fluid properties (K_n,K_w,ρ_n,ρ_w), and phase fractions (ϕ,S_w,S_n) are known while V_p is measured during the injection process. The following flow uses the effective fluid approach described previously. Since the water saturated state is used to extract frame parameters, any curves generated will be "anchored" at full water saturation.

1. Compute K_{sat_w}, the bulk modulus of the water saturated sample, and μ_{sat_w}, the shear modulus of the water saturated sample, from $V_{p_{sat_w}}$ (measured), ρ_{sat_w} (calculated from ϕ,ρ_g, and fluid information), and a literature estimate of wet V_p/V_s at a similar pressure as discussed previously [6.4.3],

$$\mu_{sat_w} = \frac{V_{p_{sat_w}}^2 \rho_{sat_w}}{\left(\frac{V_p}{V_s}\right)^2} \tag{6.8}$$

$$K_{sat_w} = \mu_{sat_w} \left[\left(\frac{V_p}{V_s} \right)^2 - \frac{4}{3} \right]. \tag{6.9}$$

2. Compute K_{dry}, the dry frame bulk modulus, using Gassmann's equation. For clean sands we assume that grains have the properties of pure quartz or ($\rho_g = 2650$ kg/m^3, $K_g = 36$ GPa, and $\mu_g = 45$ GPa) or sodalime glass beads ($\rho_g = 2530$ kg/m^3, $K_g = 43$ GPa, and $\mu_g = 30$ GPa). Our initial saturating fluid is water ($K_w = 2.205$ GPa). Porosity (ϕ) is known from volumetric measurements.

$$K_{dry} = \frac{K_{sat_w}\left(\frac{\phi K_g}{K_w} + 1 - \phi\right) - K_g}{\frac{\phi K_g}{K_w} + \frac{K_{sat_w}}{K_g} - 1 - \phi}. \tag{6.10}$$

   Gassmann implicitly assumes $\mu_{sat_w} = \mu_{dry}$ i.e. that the shear modulus is not changed by fluid saturation. In cases where contact mechanics are altered by fluid effects, this assumption is probably false.

3. Estimate the effective properties of the fluid mixture using either a well-mixed or heuristic patchy model. We test both the Reuss effective fluid model (K_{fl_R}), applicable in the case of well-mixed fluid phases, and the Voigt effective fluid model (K_{fl_V}), which is often used as a

bound for the impact of patchy saturation. The effective fluid properties can be written as,

$$K_{fl_R} = \frac{1}{\frac{S_w}{K_w} + \frac{S_n}{K_n}} \tag{6.11}$$

$$K_{fl_V} = (S_w \, K_w) + (S_n \, K_n) \tag{6.12}$$

$$\rho_{fl} = (S_w \, \rho_w) + (S_n \, \rho_n) \tag{6.13}$$

where S_w and S_n are the water and NAPL saturations respectively. NAPL bulk modulus and density are denoted as K_n and ρ_n. Since the Voigt fluid model has no theoretical basis, we will consider a second methods of including patchy saturation, the Hill's equation, in a moment.

4. Estimate the properties of the sample saturated with the NAPL/Water mixture using the K_{dry} and μ_{dry} values calculated from the water saturated sample and Gassmann's equation. In some cases a slightly different ϕ is used in the resaturation step in the situation where the water and NAPL measurements where made on similar but not identical samples. This assumes that the dry bulk and shear modulus of both samples are equivalent,

$$K_{sat_n} \;=\; K_{dry} + \left(\frac{\left[1 - \frac{K_{dry}}{K_g}\right]^2}{\frac{\phi}{K_{fl}} + \frac{1-\phi}{K_g} - \frac{K_{dry}}{K_g^2}} \right) \tag{6.14}$$

   where K_{sat_n} is the bulk modulus of the sample partially or fully saturated with NAPL. K_{fl} might be derived from either of the effective fluid models. Since we are assuming the validity of Gassmann's equation, $\mu_{dry} = \mu_{sat_n}$. The effective density, ρ_{sat_n} can be written as a simple arithmetic average of the component densities and saturation levels,

$$\rho_{sat_n} \;=\; (1-\phi)\rho_g \;+\; (\phi \, S_w \, \rho_w) \;+\; (\phi \, S_n \, \rho_n). \tag{6.15}$$

5. Calculate the predicted velocities for the NAPL contaminated sediment ($V_{p_{sat_n}}$ and $V_{s_{sat_n}}$) using K_{sat_n}, μ_{sat_n}, and ρ_{sat_n},

$$V_{s_{sat_n}} = \sqrt{\frac{\mu_{sat_n}}{\rho_{sat_n}}} \tag{6.16}$$

$$V_{p_{sat_n}} = \sqrt{\frac{K_{sat_n} + (4/3)\mu_{sat_n}}{\rho_{sat_n}}}. \tag{6.17}$$

Several of the key assumptions in this flow can be questioned, particularly the basic Biot-Gassmann assumption that $\mu_{wet} = \mu_{dry}$ and the applicability of the literature-derived V_p/V_s ratio.

If the above process is used for materials saturated with a single fluid phase, the effective fluid step can be neglected. In this case we do not have to choose a particular mixing strategy and the validity of Biot-Gassmann theory for our system can be directly explored.

Patchy Saturation Using Hill's Equation and White's Model

In cases where multiple fluid phases co-exist in a solid matrix, Biot-Gassmann theory cannot be directly applied without the introduction of an effective fluid. Another approach is to consider the effective properties of a set of regions where each region is saturated with only a single phase. This strategy honors both the volumetric constraints provided by saturation data and the theoretical limits of Biot-Gassmann theory.

Hill's equation [127] [32] [173] describes the effective bulk moduli of a composite where every component in the mixture has the same shear modulus (μ) but possibly different bulk moduli values (K). This general form, which is independent of the geometry of the constituent phases, can be written as

$$K_{eff} = \left(\sum_{i=1}^{n} \frac{x_i}{K_i + \frac{4}{3}\mu} \right)^{-1} - \frac{4}{3}\mu \tag{6.18}$$

where x_i and K_i are respectively the volume fraction and bulk modulus of the ith phase. In the case of fluid patches we can clearly see that since $\mu_{wet} = \mu_{dry}$ and μ_{dry} is equal at all points in the solid, Hill's equation is indeed applicable. The bulk modulus of the matrix saturated with each individual phase can be calculated by way of Gassmann's equation. The resulting patchy estimate of K_{eff} will always be stiffer than a combination of Gassmann and the Reuss effective fluid model but softer than Gassmann and the Voigt fluid model.

When a wave passes through a solid with zones of different bulk moduli, compression induces flow between these patches. The resulting diffusion of pore pressure across patch boundaries causes seismic attenuation consequently velocity dispersion. White's model [274] [84] for patchy saturation considers a solid composed of two Gassmann materials, each saturated with a different fluid phase, and the local flow between them. White explicitly formulates this problem in terms of spheres of material 1 with radius a embedded in a second sphere of radius b composed of material 2. White developed the model with the goal of understanding partial gas saturation but the technique is generally applicable to any problem involving two fluid phases. However, White's model is limited to cases where the patch dimensions are significantly smaller than the seismic wavelength but considerably larger than the dimensions of individual grains. In the case of our core experiments, the typical acoustic wavelength is on the order of 3 to 8 mm while grain dimensions are typically on the order of 0.5 mm leaving no room for valid application of White's model.

Figure 6.8 shows a synthetic comparison of the Reuss and Voigt effective fluid models with the Hill patchy saturation model. For this synthetic example, the grain material is taken to be quartz ($\rho_g = 2650$ kg/m^3, $k_g = 36 \times 10^9$ Pa, $\mu_g = 45 \times 10^9$ Pa) saturated with a mixture of water ($\rho_w = 997$

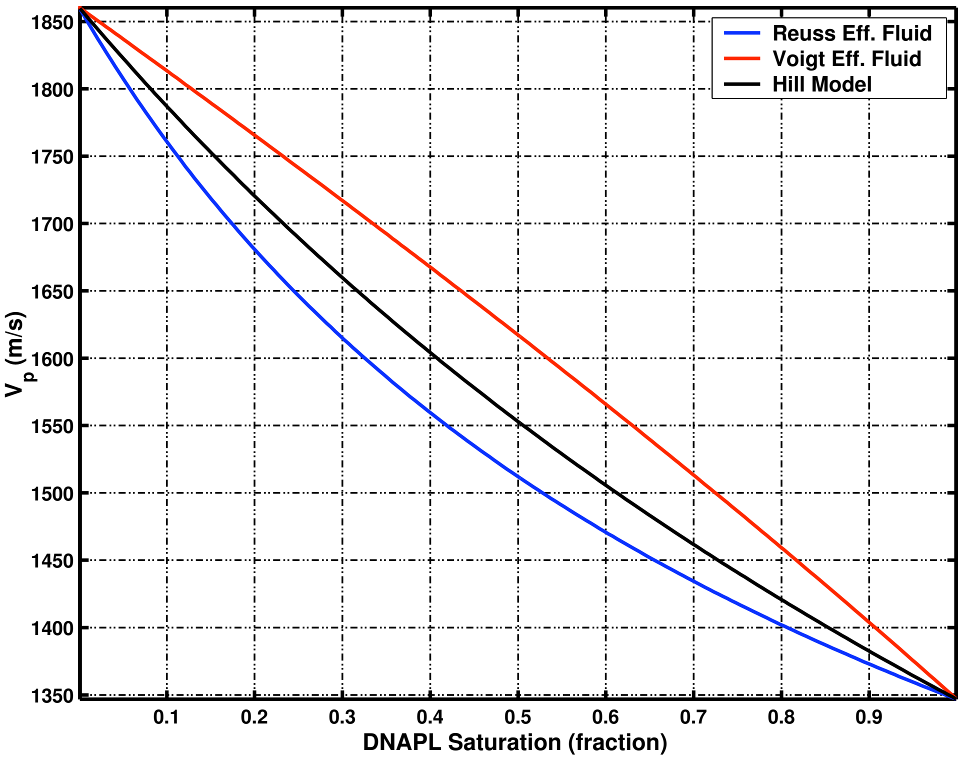

Figure 6.8: A synthetic comparison of patchy saturation models for a three phase system consisting of quartz grains saturated with a mixture of freon-113 and water (see below for fluid parameters). Shown are Gassmann fluid substitution with Reuss and Voigt effective fluid models and the Hill model for patchy saturation.

kg/m^3, $k_w = 2.205 \times 10^9$ Pa, $\eta_w = 1 \times 10^{-3}$) and freon 113 ($\rho_n = 1560$ kg/m^3, $k_n = 0.809 \times 10^9$ Pa, $\eta_n = 0.7 \times 10^{-3}$). The frame properties were chosen from previous experiments examining sands at low pressures with values of 2.181×10^9 Pa and 4.040×10^7 Pa used for frame bulk and frame shear moduli respectively. All three models are equivalent at the pure fluid endpoints. At mixed saturations, the Reuss effective fluid model predicts the softest composite while the Voigt effective fluid model provides a stiff upper bound. The Hill model takes on an intermediate value but tends to be closer to the Reuss model and has a similar inflection. A somewhat obvious but still important fact to note is that changing the fluid geometry through use of the above mentioned models only changes the path which connects the two pure fluid end points and thus cannot be invoked to explain systematic discrepancies for these bounding velocity values.

6.5 Experimental Results And Gassmann Analysis

With a relatively simplistic framework in place for analyzing the acoustic signature of NAPL saturation, we may apply these techniques to the results of both single-phase saturation experiments and NAPL injection experiments from previous studies [111]. More importantly, we will analyze the NAPL injection data acquired on the Pinellas core samples [108] and on synthetic glass bead packs

Sample	2nd Fluid	Porosity (fraction)	Eff. Stress (Pa $\times 10^3$)	V_p (water sat.) (m/s)	V_p (NAPL sat.) (m/s)	V_{pm} (NAPL gassman) (m/s)	Dev.G (%)
G/M 95 1	Freon 113	0.42	140	1829	1092	1319	20.8
G/M 95 2	Iso-Octane	0.42	140	1835	1253	1465	16.9
G/M 95 3	n-Dodecane	0.42	140	1844	1515	1609	6.2
S 98 1	n-Dodecane	0.32	600	2090	1655	1894	14.5
S 98 2	10cs Sili. Oil	0.35	690	1810	1289	1356	5.2
S 98 3	100cs Sili. Oil	0.35	690	1810	1326	1373	3.6
S 98 4	Castor Oil	0.34	690	1810	1747	1809	3.5
G/A-F 03 1	TCE	0.39	100	1850	1440	1574	9.3
G/A-F 03 2	Toluene	0.36	100	1850	1540	1652	7.3
G/A-F 03 3	Toluene	0.34	300	1840	1560	1645	5.5

Table 6.3: Single-phase NAPL experiments on granular materials. The GM-95 measurements were are from Geller and Myer [111], S 98 measurements are from Seifert [234], while the G/A-F 03 measurements are currently unpublished. The GM-95 and S 98 experiments both used clean sand samples while the G/A-F 03 measurements were made on glass beads. Values in the "V_p NAPL sat." column are the experimentally measured V_p values at full NAPL saturation.

as part of our laboratory investigation.

6.5.1 Single-Phase Experimental Measurements

As mentioned previously, examination of the single-phase fluid saturation endpoints allows testing of our fluid substitution strategy without assumption of a particular fluid geometry or mixing model. Table [6.3] includes all of the V_p measurements made to date on sediments saturated with a single NAPL phase and their departure from the V_p values estimated by Gassmann's equations using our fluid substitution flow.

Deviations from the predicted Gassmann velocities ranged between 5.5 and 20.8 % with the largest variation seen for the GM-95 freon-113 sample [111] . Gassmann consistently overpredicts the velocity of the NAPL saturated state and therefore underpredicts the relative change in V_p. The magnitude of these discrepancies is significantly larger than any effects related to traditional Biot relaxation phenomenon as will be discussed in later sections. Lowering the V_p/V_s ratio to approximately 1.4 eliminates disagreement at the NAPL saturated end-point but such a modification would contradict all existing data on the shear properties of granular materials at low pressures. One possible explanation for these deviations is an anomalous softening of grain contacts due to NAPL/surface interactions which we will discuss later in this chapter.

6.5.2 GM 95 Dataset

Plot 6.9 depicts the three datasets acquired by Geller and Myer [111] and the corresponding Gassmann modeling results. We assumed the grain properties were those of quartz ($\rho_g = 2650$

kg/m^3, $k_g = 36 \times 10^9$ Pa, $\mu_g = 45 \times 10^9$ Pa) since the samples were composed of clean quartz sand. The fluid properties used for modeling were discussed previously (see figure 6.1 and chapter 3). For each NAPL, three different Gassmann-type models were examined, a well-mixed model (Reuss fluid average), a heuristic patchy model (Voigt fluid average), and Hill's equation. All three models underpredict the velocity decrease due to NAPL saturation, with larger departures visible at higher saturations due to our anchoring the frame parameters at the fully water saturated end-point. One anomalous aspect of this injection dataset is the region of almost constant velocity at low NAPL saturations. This effect is due to irregular fluid geometry at low injected volumes which does not cross the acoustic transmission path. An important fact to note is that the fully NAPL saturated end-point measurements are separate experiments which start with dry samples; 100 % NAPL saturation is not achievable by directly injecting NAPLs into water saturated cores due to zones of irreducible water saturation. All three datasets appear to have relatively linear trends in V_p as a function of NAPL saturation with this trend extending to include the fully NAPL saturated end-point. This suggests that whatever mechanism is responsible for this deviation is dominated by volumetric effects. In addition to changes in velocity, we include plots showing changes in relative amplitude normalized to the water-saturated end-point. Although we will not present a quantitative model for describing the NAPL-induced attenuation effects we can clearly see that waveform amplitude decreases as a function of NAPL saturation.

6.5.3 Geller/Ajo-Franklin 2002 Data

The G/A-F 02 dataset consists of the Pinellas aquifer samples described previously. We assumed the grain properties were those of quartz ($\rho_g = 2650$ kg/m^3, $k_g = 36 \times 10^9$ Pa, $\mu_g = 45 \times 10^9$ Pa) despite the fact that substantial amounts of clay were present, particularly in the N4 samples. We felt that this choice was justified considering the lack of correlation between clay content and V_p displayed in our water saturated ultrasonic measurements (see figure 6.4) and the difficulty in choosing appropriate clay properties from a large database of contradicting estimates. Additionally, in 4 out of 5 of our experiments, treating grain bulk modulus as a free parameter in the model fitting process yielded a K_g value higher than that of pure quartz, the opposite trend expected when adding clay to a sand pack. The fluid properties used for modeling were discussed previously (see figure 6.1 and chapter 3). Figure 6.10 depicts the two N3 samples, one injected with TCE (G13-N3-59-66) and the second with toluene (G13-N3-66-73). The N3 samples were relatively clean sands with small amounts of silt and clay. The N3 samples also have a lower porosity (0.34 and 0.32) than most of the N4 samples with higher clay contents. Sample G13-N3-66-77 was the only core examined where our previously described Gassmann flow overpredicted the impact of NAPL saturation. Both samples show decreasing V_p as a function of NAPL saturation.

Figure 6.11 shows the same combination of fits for the N4 samples which are clayey silty sands with porosities between 0.4 and 0.43. XRD analysis of grab samples from other NE site wells indicate that the dominant clay minerals are kaolinite with traces of smectite [110]. Samples G20-N4-31-38

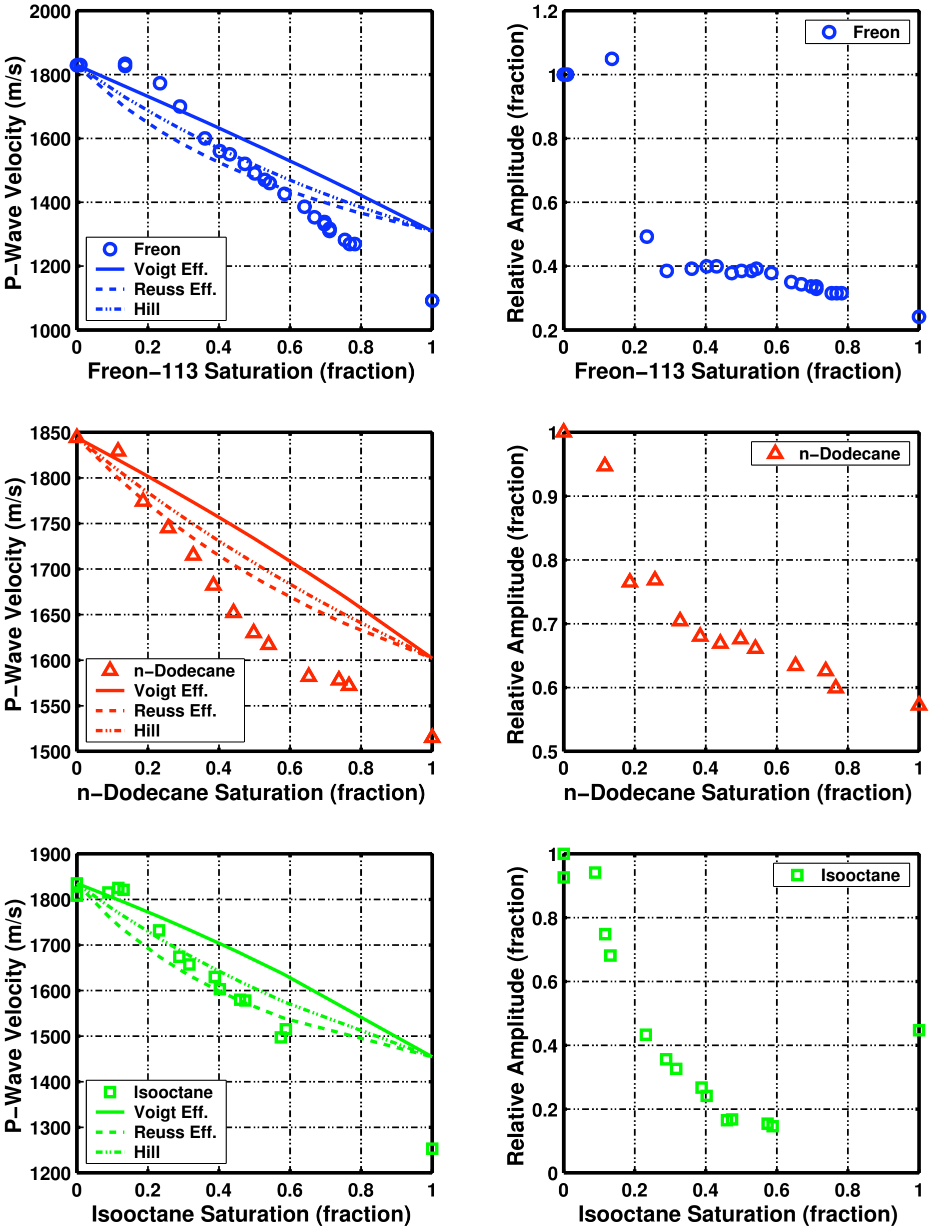

Figure 6.9: Geller-Myer 95 NAPL injection experiments with Gassmann predictions. Plots are shown sequentially (top to bottom) for freon-113, n-dodecane, and iso-octane injections. All experiments were conducted on identically packed clean sand samples with porosities of 0.42. Separate measurements were made for the fully NAPL saturated end-points. The right hand column depicts the relative amplitude plots corresponding to the velocity measurements on the left.

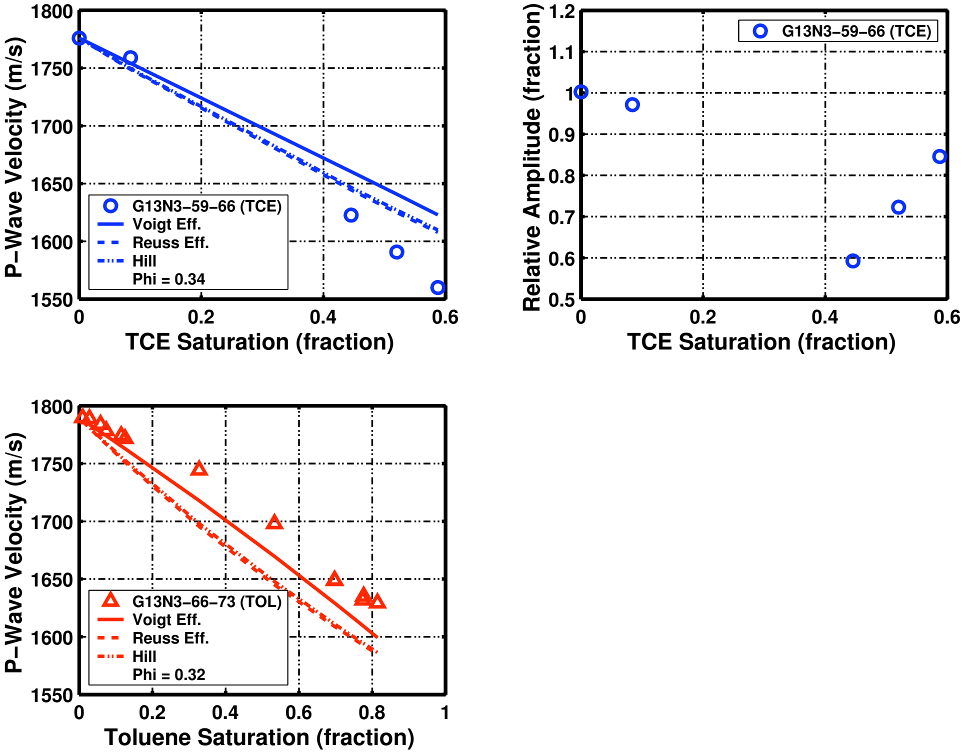

Figure 6.10: Geller/Ajo-Franklin 02 NAPL injection experiments with Gassmann velocity predictions for the N3 samples. The right hand column depicts the relative amplitude plots corresponding to the velocity measurements on the left. The N3 samples were relatively clean sands.

and G13-N4-57-64 were subjected to toluene injections while G13-N4-104-111 was injected with TCE. The Gassmann models provided a good match for the N4 measurements, particularly the Reuss effective fluid model and the Hill equation predictions, both of which were relatively similar for these samples.

6.5.4 Geller/Ajo-Franklin 2003 Data

Synthetic granular materials are useful tools for the investigation of rock physics models due to their established grain geometries and known grain properties. Since closed forms for many deformation problems are known only for simple geometric shapes including spheres, packs composed of identically shaped spherical beads are a good model system, particularly for contact-based theories. Although the complex textures of the natural aquifer samples were better approximations of the soils encountered in our field experiments, glass beads provide a way to factor out uncertainty due to grain shape, grain size distributions, and mineral moduli. For the 2003 bead experiments, soda lime glass beads ($\rho_g = 2530$ kg/m^3, $K_g = 43$ GPa, and $\mu_g = 30$ GPa) were used as the granular matrix. Figure 6.12 shows the results of two TCE injection experiments into bead packs with porosities of 0.402 and 0.465. Much like the results from the GM-95 datasets, our Gassmann substitution flow underpredicts the decrease in velocity due to NAPL injection.

6.5.5 Biot Effects Beyond Gassmann

Ultrasonic measurements are typically either in the intermediate or high frequency range with respect to the Biot critical frequency, especially in the case of high permeability samples. However, Gassmann's equations may be safe to use as an approximation to the full Biot formulation if the velocity dispersion generated by the Biot mechanism is sufficiently small. If the Biot-Gassmann P-wave velocities predicted for the low frequency and general case are written as $V_{p_{gassman}}$ and $V_{p_{biot}}(f)$ respectively, a convenient measure of departure from Gassmann behavior is

$$G_{dev}(f) = 100 \left[\frac{V_{p_{biot}}(f) - V_{p_{gassman}}}{V_{p_{gassman}}} \right]. \tag{6.19}$$

In equation 6.19, $G_{dev}(f)$ is simply the percent relative deviation from Gassmann behavior as a function of frequency. Figure 6.13 depicts this measure evaluated for the sand samples described in the GM-95 [111] dataset, fully saturated with either freon-113, n-dodecane, iso-octane, or water. Tortuosity was estimated at 1.69 using Berryman's theoretical expression for spherical packs. Three permeability values (0.1,1, and 10 Darcies) were tested to explore the relevance of the mechanism to different types of unconsolidated sediments. Permeability clearly plays a significant role in determining the transition frequency (see equation 6.1); at a permeability of 0.1 Darcies, velocity dispersion remains insignificant even at ultrasonic frequencies of 1 MHz. The maximum amount of velocity dispersion is controlled by the fluid density, assuming frame properties including tortuosity are not varied. Consequently, the freon-113 sample exhibits the highest level of velocity dispersion due to

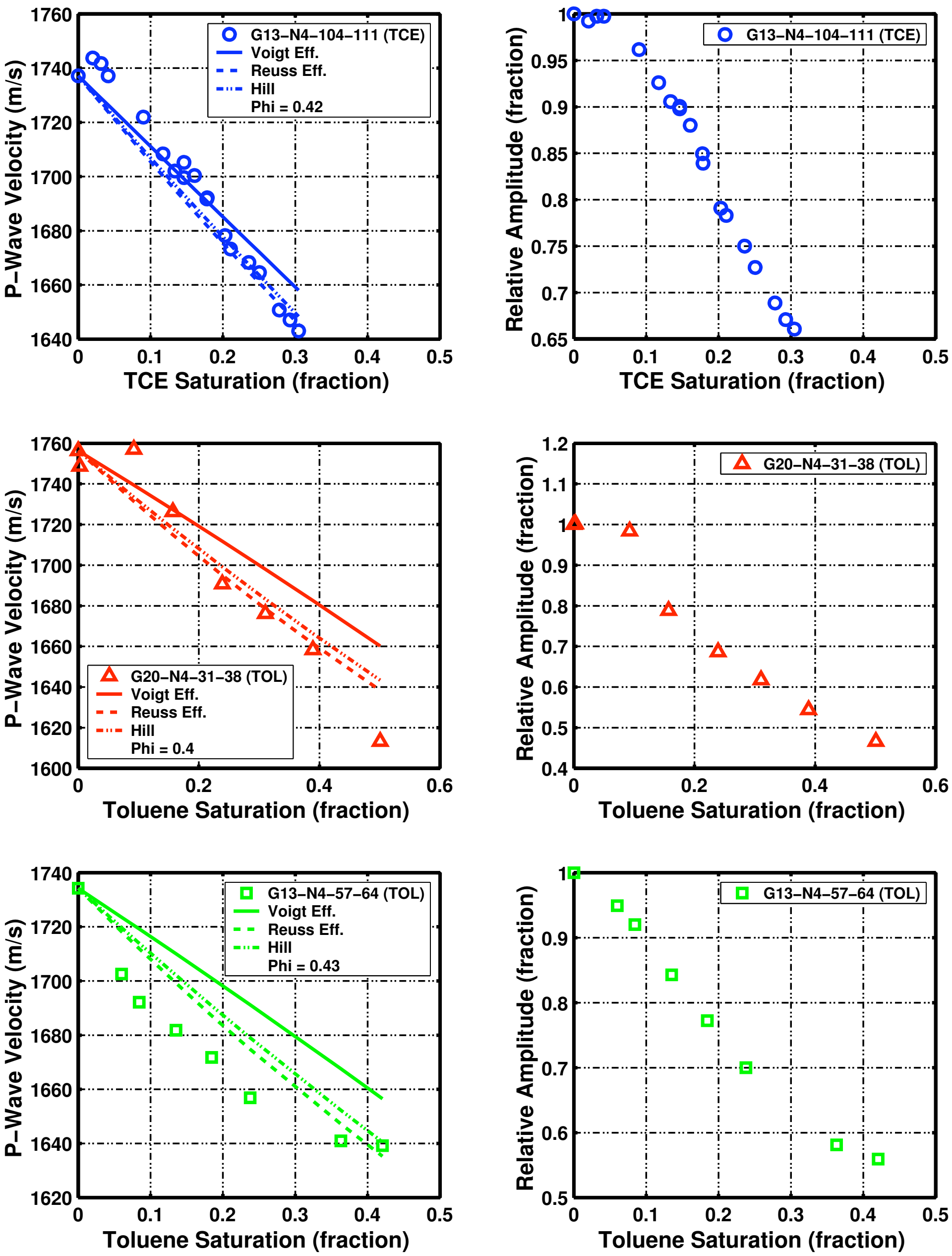

Figure 6.11: Geller/Ajo-Franklin 02 NAPL injection experiments with Gassmann velocity predictions for the N4 samples. The right hand column depicts the relative amplitude plots corresponding to the velocity measurements on the left. The N4 samples were sands with significant silt and clay components.

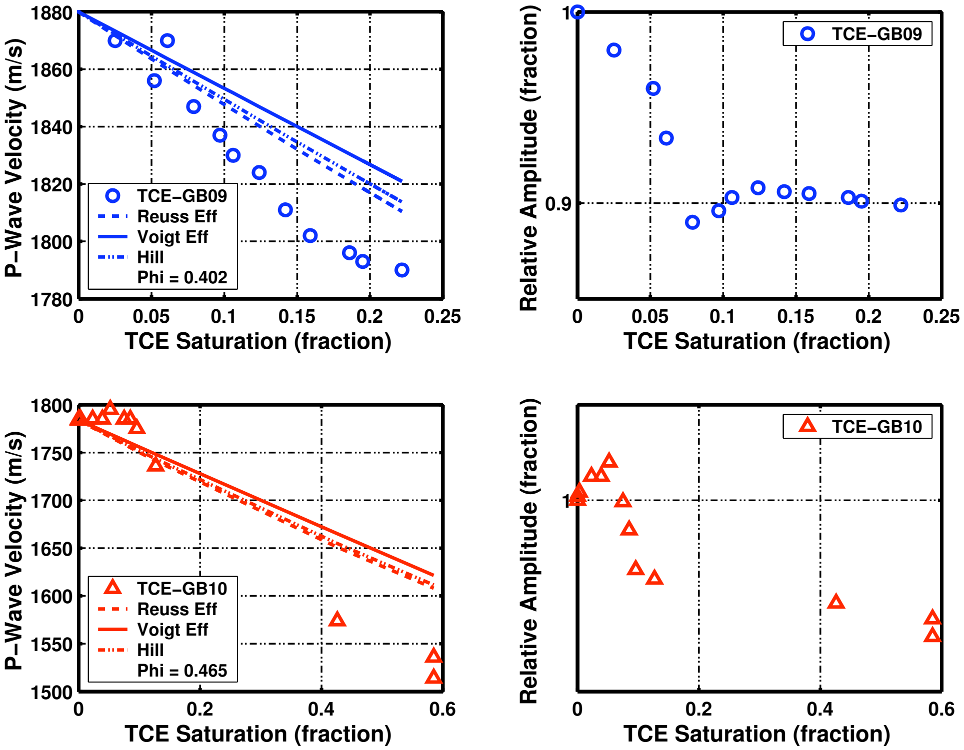

Figure 6.12: Geller/Ajo-Franklin 03 NAPL injection experiments with Gassmann velocity predictions for the glass bead samples. The right hand column depicts the relative amplitude plots corresponding to the velocity measurements on the left.

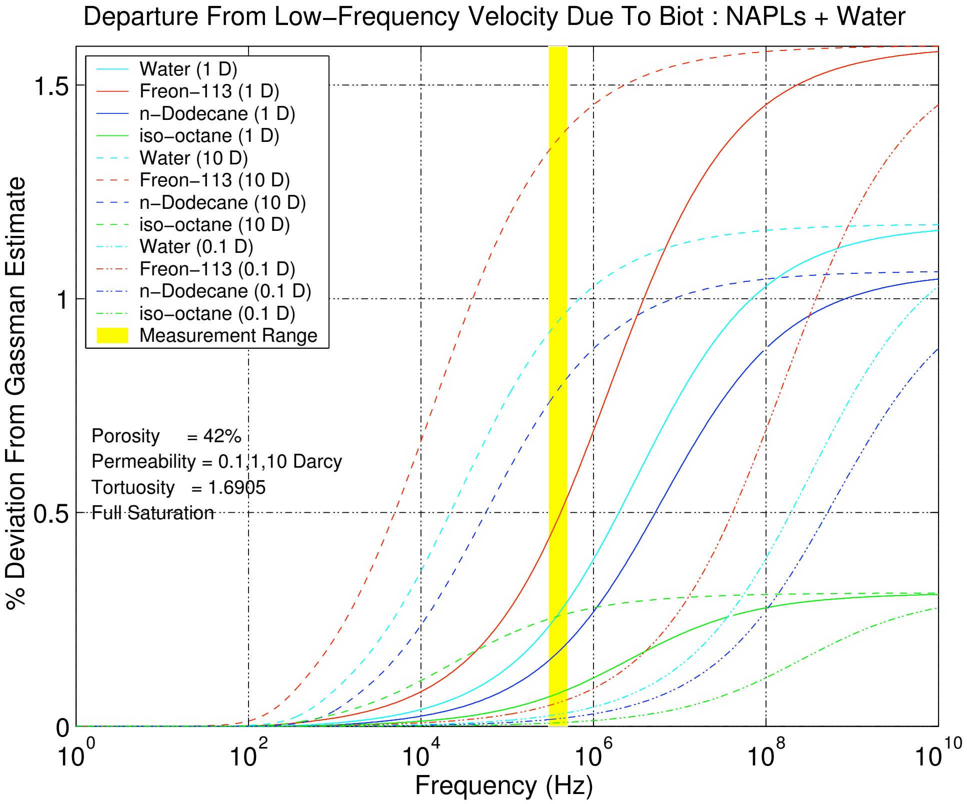

Figure 6.13: High frequency Biot effects for the GM-95 samples; Deviation from Gassmann as a function of frequency for 3 fluids and 2 permeabilities.

high fluid density.

As is clear from figure [6.13], the transition from low to high frequency behavior generates a maximum of 1.6% change in P-wave velocity, far too small to explain the observed deviations from Gassmann estimates. Additionally, the velocity change must be differential between fluids to generate this departure i.e. if both water and freon exhibit 10 m/s dispersion at frequency f, than the difference between the two cases (the departure we are trying to explain) remains constant. Despite the small predicted deviations from Gassmann, our measurement frequency falls directly within the transition zone where peak attenuation from Biot effects occurs. In conclusion, error due to use of the low frequency Gassmann model in opposition to the full frequency-dependent Biot model cannot explain observed deviations in V_p for NAPL saturated samples.

6.6 Empirical Volumetric Interpretation

A second approach for predicting the acoustic signature of NAPL saturation is to abandon mechanistic theories and develop an appropriately parametrized empirical model. For such a model to be useful, it should be based on as large a measurement database as can easily be described using the functional form chosen. Since any set of data can be fit exactly using a polynomial of sufficient order, care must also be given to selecting the appropriate fitting function with preference given to low-order or linear models.

If volumetric effects dominate system behavior as our previous analysis suggests, than a re-plotting of V_p measurements in terms of NAPL volume fraction seems appropriate. Casting the analysis in terms of NAPL fraction also serves to partially eliminate differences seen in saturation vs. V_p plots due to changes in porosity from sample to sample. Additionally, plotting the change in V_p from the water saturated state as a function of NAPL fraction normalizes against initial differences in frame properties, allowing a comparison of the change in bulk properties due to the fluid effects.

Figure 6.14 show the results from seven NAPL injection experiments using either TCE (left column) or toluene (right column) as the second saturating fluid. From top to bottom we plot V_{p_b}, ΔV_{p_b}, and relative (%) ΔV_{p_b} as a function of volumetric NAPL fraction where the extra b in the subscript indicates bulk P-wave velocity. Although the initial frame properties are clearly different at the water saturated end-point, the change in V_{p_b} due to NAPL saturation are remarkably consistent between all of the samples for a given fluid. We fit the ΔV_{p_b} data with a simple linear model of the form

$$\Delta V_{p_b}(F) = X + MF \tag{6.20}$$

where F is volumetric NAPL fraction and M and X are two fitting coefficients. M, the slope of the linear fit, is a good indicator of the sensitivity of V_{p_b} to saturation with a particular NAPL. Figure 6.15 shows the equivalent plots for all three fluids in the GM-95 dataset where similar trends are observed for both ΔV_{p_b} curves.

In both cases, extrapolating V_p to a NAPL fraction (F) of 1 yields an incorrect fluid velocity. Although we do not have data for higher NAPL fractions, we expect that once $1-F$ drops below some critical porosity the system will enter a suspension state which will converge on the fluid velocity at $F = 1$. Table 6.4 shows the M coefficients for the experimental fluids used in the injection experiments. Fluids are ranked by the magnitude of M which correlates most closely with fluid V_p with the exception of TCE and iso-octane. This particular reversal may be due to volatilization of iso-octane leading to a small amount of entrained gas.

The empirical relationships discussed above are most useful in cases where the contaminating fluid is known a-priori and an experimental dataset is available. This approach is difficult to apply to our field site where DNAPL samples, while collected for chemical analysis, were not available for direct geophysical measurements. Considering the correlation between fluid V_p and the M coefficients from the volumetric fitting described above, we can also build a simple model for describing this relationship. We choose a quadratic model of the form

$$M(V_{p_f}) = AV_{p_f}^2 + BV_{p_f} + C \tag{6.21}$$

where A, B, and C are fitting coefficients and V_{p_f} is the fluid velocity. Figure 6.16 shows the resulting

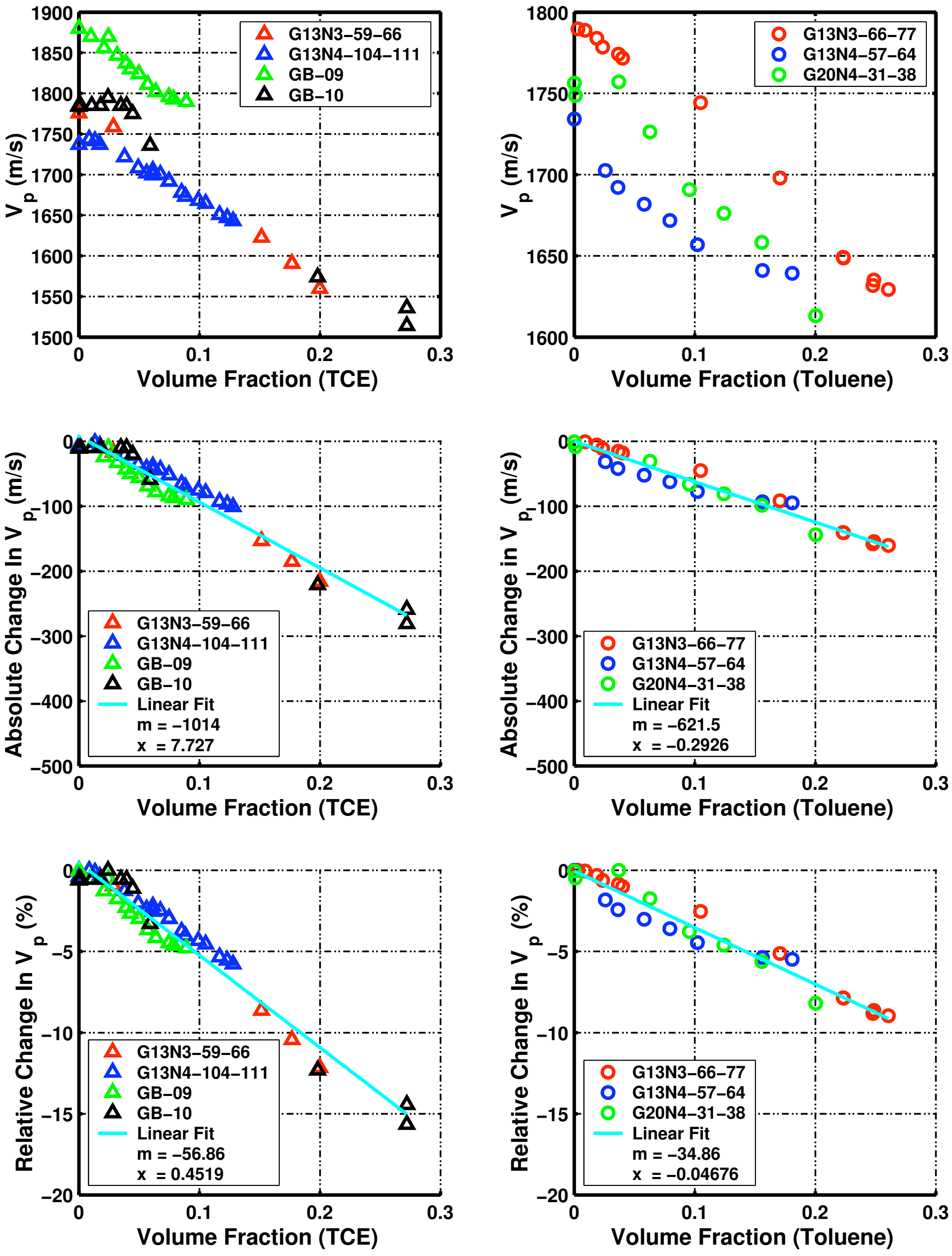

Figure 6.14: Fractional NAPL volume vs. V_p and change in V_p for the G/AF 02/03 datasets. Difference plots are normalized to the fully water-saturated state of a given sample.

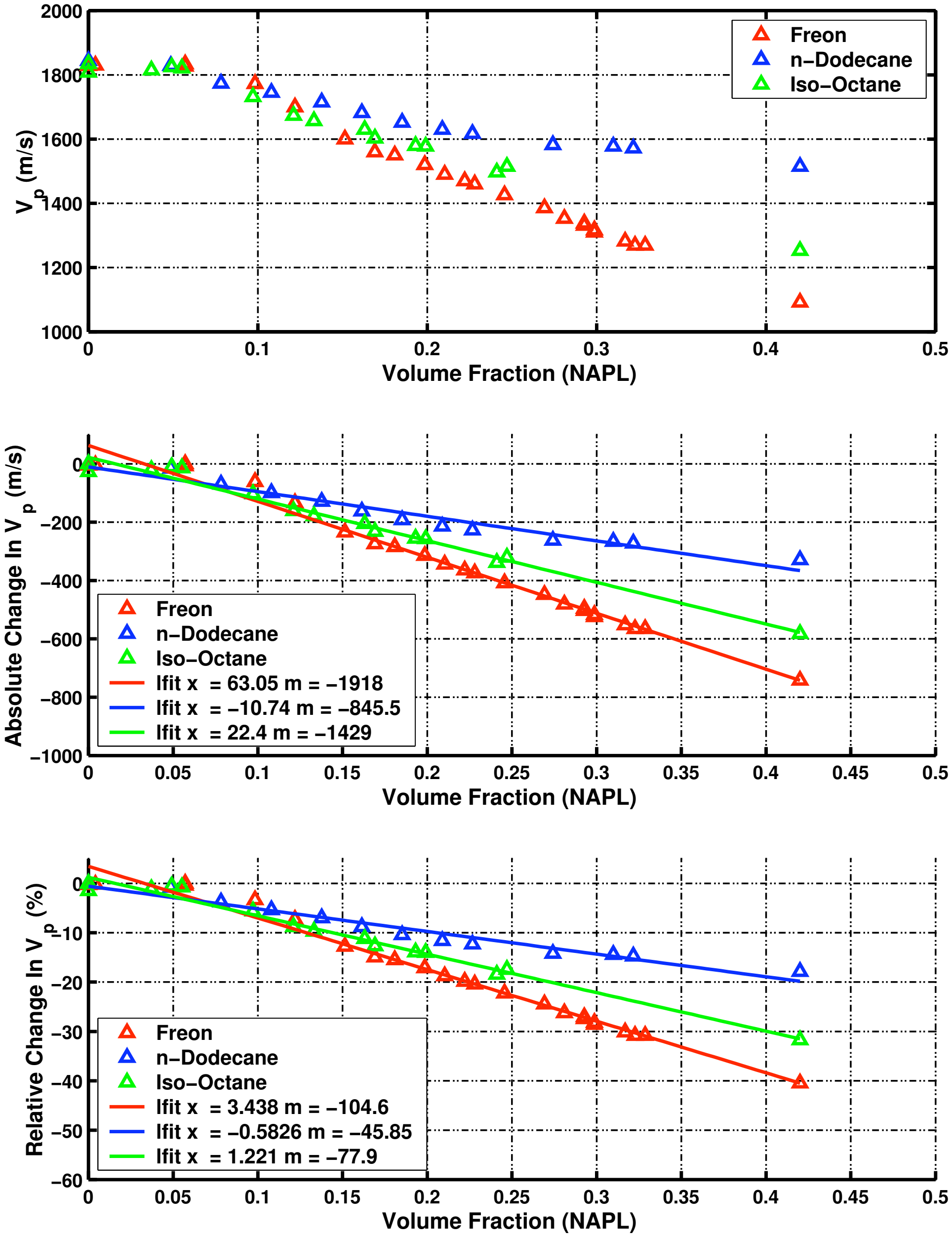

Figure 6.15: Fractional NAPL volume vs. V_p and change in V_p for the GM-95 dataset. Difference plots are normalized to the fully water-saturated state of a given sample.

Fluid Type	Density (kg/m^3)	Bulk Modulus (Pa $\times 10^9$)	V_p (m/s)	Impedance (kg/m^{2}s $\times 10^6$)	Abs. M. Coeff.	Rel. M Coeff.
Freon 113	1560	0.7997	716	1.117	-1918	-104.6
Iso-octane	690	0.8655	1120	0.773	-1429	-77.9
Trichloroethylene	1451	1.6317	1050	1.524	-1014	-56.9
n-Dodecane	745	1.2398	1290	0.961	-846	-45.9
Toluene	870	1.5182	1321	1.149	-621	-34.9
Water	997.07	2.2343	1497	0.493	0	0

Table 6.4: Empirical fits for NAPL fraction vs. V_p for several fluids. “Abs. M. Coeff” and “Rel. M. Coeff” denote the M-parameter values (see equation 6.20) for the absolute and relative changes in velocity respectively.

fit with the hard constraint that $M(V_{p_f}) = 0$ when V_{p_f} is that of water. Combining equations 6.20 and 6.21 with the constraint that $X = 0$ yields a simple equation for the change in seismic P-wave velocity due to NAPL saturation in terms of the NAPL fluid velocity and the volumetric NAPL fraction,

$$\Delta V_{p_b}(F, V_{p_f}) = (0.00175\, V_{p_f}^2 - 1.485\, V_{p_f} - 1714.6)\, F. \tag{6.22}$$

Equation 6.22 is based on a 131 measurement points collected over 11 fluid injection experiments using 5 different experimental NAPLs; the combined GM-95 and G/A-F 02/03 datasets. Some degree of scatter is expected since the sample set included clean sands, glass beads, and natural aquifer samples of widely varying porosity. In particular, the departure of the TCE datapoint from the curve suggests that a more detailed set of experiments might be required to bolster this empirical model. In the final section of this chapter, we compare this empirical model to Gassmann fluid substitution for a synthetic case using the DNAPL properties expected at the Pinellas site.

6.7 Interpreting Deviations From Biot-Gassmann In Terms Of Contact Theory

One possible explanation for the observed deviation from Gassmann’s equation is an anomalous effect at grain contacts generated by NAPL saturation. Description of the acoustic properties of sands in terms of contact theory has a long history [184] [42] [80] [267], but is still not complete as is apparent from recent measurements by Zimmer [283] [282] and others. Despite the theoretical inadequacies of contact models, they do capture a key aspect of unconsolidated media by emphasizing the strength of grain-to-grain interfaces as a crucial parameter. This insight allows estimation of both pressure dependent effects and the possible effect of fluids on contact strength. We give a brief overview of Hertz-Mindlin contact theory and then speculate on some NAPL-related effects at grain contacts. In later chapters, we use Hertz-Mindlin theory to derive rough guesses for dry frame properties as a

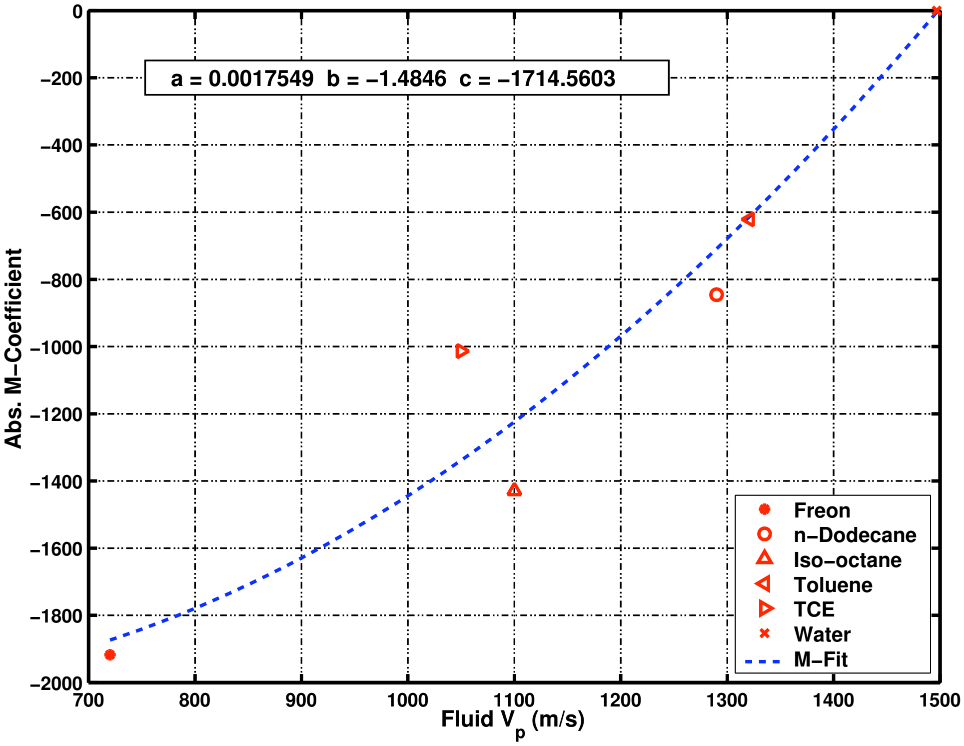

Figure 6.16: Empirical M-coefficients (see equation 6.20) as a function of NAPL type and the associated quadratic fit (see equation 6.21)

function of porosity and effective stress for use in predictive forward modeling.

One of the key parameters for describing granular media is the coordination number, the average number of contacts any given grain possesses. For regular packings of equal sized spheres, coordinate numbers are known exactly and range from 6 for a simple cubic pack to 12 for a hexagonal dense back [63]. Since quantitative estimates of packing behavior for randomly arranged spheres are notoriously difficult to derive, an empirical model relating soil porosity, ϕ, to the coordination number is a useful tool when generating property estimates based on contact theory. By using a cubic spline to interpolate the data pairs experimentally determined by Murphy [193], coordinate numbers for all porosity values can be estimated.

The Hertz-Mindlin (HM) model [184] describes the properties of a random packing of identical spherical grains. The HM model assumes that grain contacts are circular and that the tangential force along the contact is applied only after the contact is formed due to normal stresses. The model is parametrized in terms of grain shear modulus, G_g, grain Poisson ratio, p_g, coordination number, C_s, porosity, and effective pressure, P_{eff}. The expressions for the dry bulk modulus, $K_{eff(dry)}$, and dry shear modulus, $G_{eff(dry)}$, are

$$K_{eff(dry)} = \left[\frac{C_s^2 (1-\phi)^2 \, G_g^2 \, P}{18\pi^2 (1-p_g)^2} \right]^{\frac{1}{3}} \tag{6.23}$$

$$G_{eff} = \left(\frac{5 - 4p_g}{5(2 - p_g)} \right) \left[\frac{3C_s^2 (1 - \phi)^2 \, G_g^2 \, P}{2\pi^2 (1 - p_g)^2} \right]^{\frac{1}{3}} . \tag{6.24}$$

Several papers have investigated the effect of fluids on contact mechanics with a focus on consolidated sedimentary rocks. Murphy *et al.* [193] proposed a model combining elements of contact theory, Biot-Gassmann models, and squirt (local) flow effects. Tutuncu and Sharma [257] extend contact theory models by explicitly incorporating surface forces including Van der Waals attraction, electrostatic repulsion, and Born forces. One of the key parameters introduced was the fluid Hamaker constant which controls the Van der Waals force between grains. However, the Tuntucnu theory predicts that saturation with non-polar solvents will typically increase rather than decrease contact stiffness due to a decrease in equilibrium grain separation. The result is the prediction that water saturation increases peak attenuation. This contradicts existing experimental data on NAPLs in unconsolidated sands at low pressure.

Winkler [280] and Mavko *et al.* [173] provide simple expressions for dry frame moduli in terms of normal (T_n) and tangential (T_t) contact stiffness values,

$$K_{eff} \ = \ \frac{C(1 - \phi)}{12\pi R} T_n \tag{6.25}$$

$$G_{eff} \ = \ \frac{C(1 - \phi)}{20\pi R} (T_n + 1.5T_t). \tag{6.26}$$

By using the assumptions of Hertz-Mindlin theory, values for T_n and T_t can be estimated yielding the earlier expressions for K_{eff} and G_{eff} shown in equations 6.23 and 6.24. As is apparent from equations 6.25 and 6.26, changes in tangential contact stiffness can cause variations in G_{eff} without modifying K_{eff}. Although we cannot propose a mechanism for lowering T_t at this point, it seems possible that fluid replacement might modify contact stiffness. We will discuss contact theory in the context of loss mechanisms in the following section.

6.8 Observed Attenuation and Possible Mechanisms

As shown in figures 6.9, 6.10, 6.11, and 6.12 the injection of NAPLs into unconsolidated material consistently reduces signal amplitude in addition to reducing P-wave velocity. One should note that the observations in question are reductions in relative amplitude and not quantitative measurements of quality factor (Q). Decreases in amplitude can generally be ascribed to either scattering, intrinsic attenuation, or to secondary measurement effects such as changes in source coupling to the sample. One unusual aspect of the observed signal is that two out of three samples with end-point measurements exhibit the highest level of attenuation at full NAPL saturation. This seems to rule our attenuation mechanisms based upon equilibration between patches or due to scattering from regions of high NAPL saturation. Although we do not have a complete understanding of the observed amplitude reduction, we present evidence that such reduction is not due to variations in the sample/end-cap impedance match. We will also show that neither Biot nor modified squirt flow theories suitably describe the attenuation trends observed. To conclude we present some possible mechanisms yet to be explored and outline directions for future research on NAPL related attenuation mechanisms on the laboratory and field scales.

One possible source of amplitude reduction is an increase in the acoustic impedance mismatch between the sample and the transducer assembly. As shown in figure 6.17 some energy generated by the source transducer is reflected at the interface between the sample and the transducer endcap resulting in a decrease in observed amplitude unrelated to attenuation within the sample. Thus a change in amplitude could be generated by exchanging pore fluids such that the amount of energy reflected at this transition increases. The reflection coefficient for a P-wave normally incident to a planar transition in material properties can be written as

$$R_{12} = \frac{I_2 - I_1}{I_2 + I_1} \tag{6.27}$$

where I, the P-wave impedance is simply $V_{p1}\,\rho_1$ and numeric subscripts indicate the first and second materials. In the case of a uniform sample, the amplitude decrease is due to two interface reflections yielding a total transmissivity of $T_t \; == (1 - R_{12}) \times (1 - R_{21})$. Since our endcaps are constructed from polyphenylene sulfide ($V_p = 2519$ m/s, $\rho = 1329$ kg/m^3, $I_p = 3.347 \times 10^6$ kg/(m^2 s)) we can compute this reflection coefficent for both the water and NAPL saturated end-points through use of the observed V_p and a ρ calculated from porosity and phase density information. We will take the GM95 experiment is an example and consider the fully water-saturated ($V_p \;=\; 1829$ m/s, $\rho \;=\; 1957$ kg/m^3, $I \;=\; 3.58\; \times 10^6$ kg/(m^2 s)) and fully freon saturated ($V_p \;=\; 1092$ m/s, $\rho \;=\; 2192$ kg/m^3, $I \;=\; 2.39\; \times 10^6$ kg/(m^2 s)) samples. Replacing water with freon does indeed decrease the total transmissivity from 0.9989 to 0.9724 but this change in impedance mismatch can only explain an amplitude reduction of 2.65 %, far less than the observed reduction of approximately 80 % bolstering the case for attenuation of the transmitted wave within the sample.

Previous attempts to explain the seismic attenuation generated by NAPL saturation in unconsolidated materials have either used empirical models or chosen scattering as the relevant mechanism. Geller and Myer [111] analyzed their injection data using a simple model which assumed plug flow across the sample during NAPL saturation with fixed experimentally determined attenuation coefficients for the water and NAPL saturated sand regions. They did not posit a mechanism for the increased attenuation coefficient generated by NAPL saturation. As mentioned previously, Seifert *et al.* [234] attempted to fit the GM-95 dataset using a one-dimensional scattering theory but were forced to make several poorly justified modifications to their model parameters to generate a reasonable result. Modifications included using porosity as a fitting parameter despite the existence of reliable porosity measurements, the use of an arbitrary and artificially low Q value for NAPLs, and the addition of a gas layer. In the Seifert *et al.* analysis, scattering was assumed to be generated by laminar interfaces between quartz, water, and NAPL with the thickness of the layers determined by

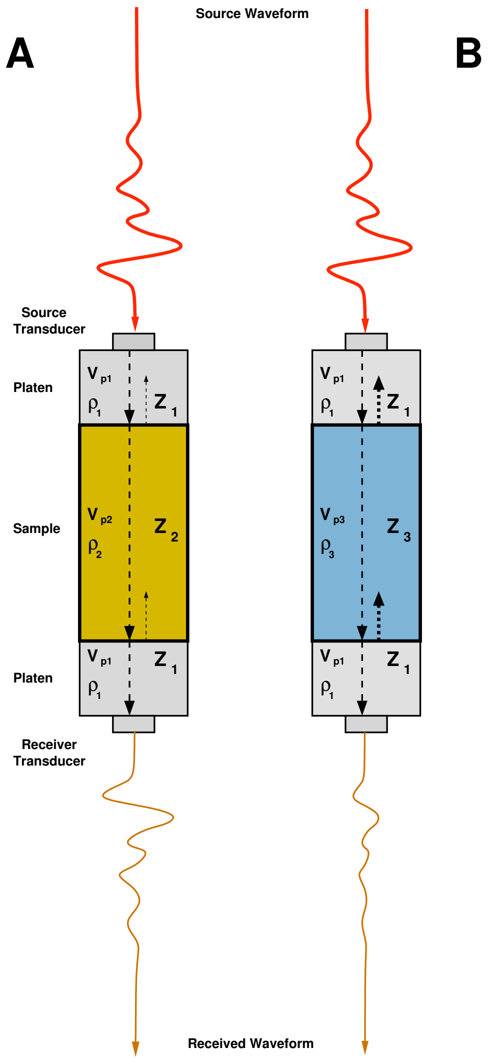

Figure 6.17: Schematic diagram of the effect of impedance mismatches on measured amplitudes

grain dimensions. In a second paper by Seifert *et al.* [236], the authors attempted to apply Dynamic Composite Elastic Medium Theory (DYCEM) to a similar dataset consisting of sand packs saturated with variety of oils with viscosities varying from 0.001 to 1 Pa s. The spectral ratio method was used to calculate frequency dependent Q values over the decade from 100 kHz to 1 MHz. In this case, DYCEM was not able to explain the velocity measurements without making frame properties dependent upon fluid type. The authors conclude that the DYCEM velocity discrepancy was due to contact effects but still insist that scattering is the dominant loss mechanism.

As mentioned previously, one unusual aspect of the GM-95 dataset is that two out of three samples with end-point measurements exhibit the highest level of attenuation at the fully NAPL saturated state. This observation eliminates the possibility that the observed attenuation is due to patch equilibration processes or to scattering from patches with different NAPL saturations. As shown in figure 6.18, damping due to hysteretic effects at menisci bridging grains is also eliminated as a possible

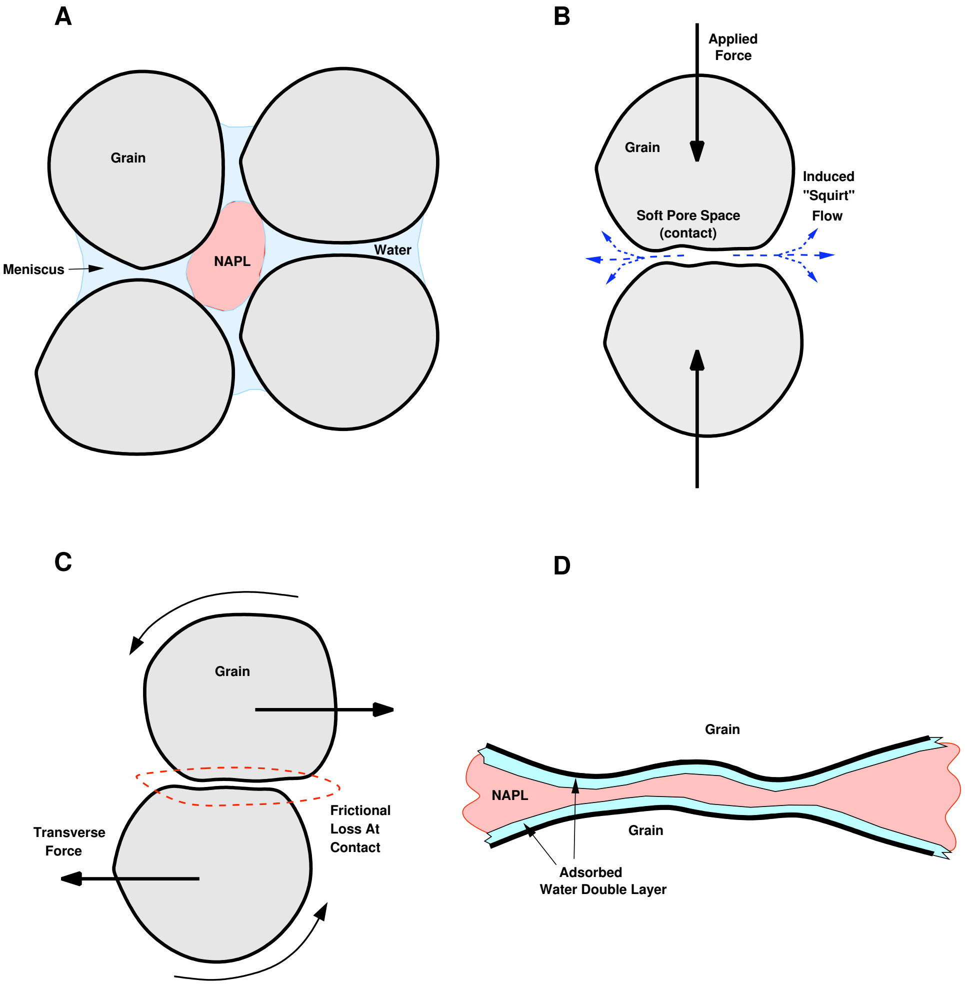

Figure 6.18: Schematic diagram of four loss mechanisms : a) meniscal damping, b) "squirt" or local flow, c) Grain/Grain frictional forces, d) unspecified contact mechanism

mechanism since no menisci exist in the fully saturated state. Fluid flow models including Biot's original theory discussed in earlier sections and the unified Biot-Squirt (BISQ) model d eveloped by Dvorkin and many others [87] [86] [85] [193] [174] are often appealed to when explaining seismic attenuation at laboratory frequencies. Squirt losses are due to flow induced by the compression of soft fluid-filled cracks during wave propagation (see figure 6.18). While we will not delve deeply into a comparison of the Biot and Squirt mechanisms a simple numerical experiment provides convincing evidence that neither model sufficiently describes the GM-95 dataset or subsequent NAPL injection experiments. The reader is referred to the literature, particularly [86] for details on the BISQ implementation.

We consider a synthetic case similar to that described for the patchy saturation model earlier in this chapter. Frame properties for our examples were chosen from our previous experiments examining sands at low pressures with values of 2.181×10^9 Pa and 4.040×10^7 Pa used for frame bulk and frame shear moduli respectively. Quartz is used for the grain material ($\rho_g = 2650$ kg/m^3,

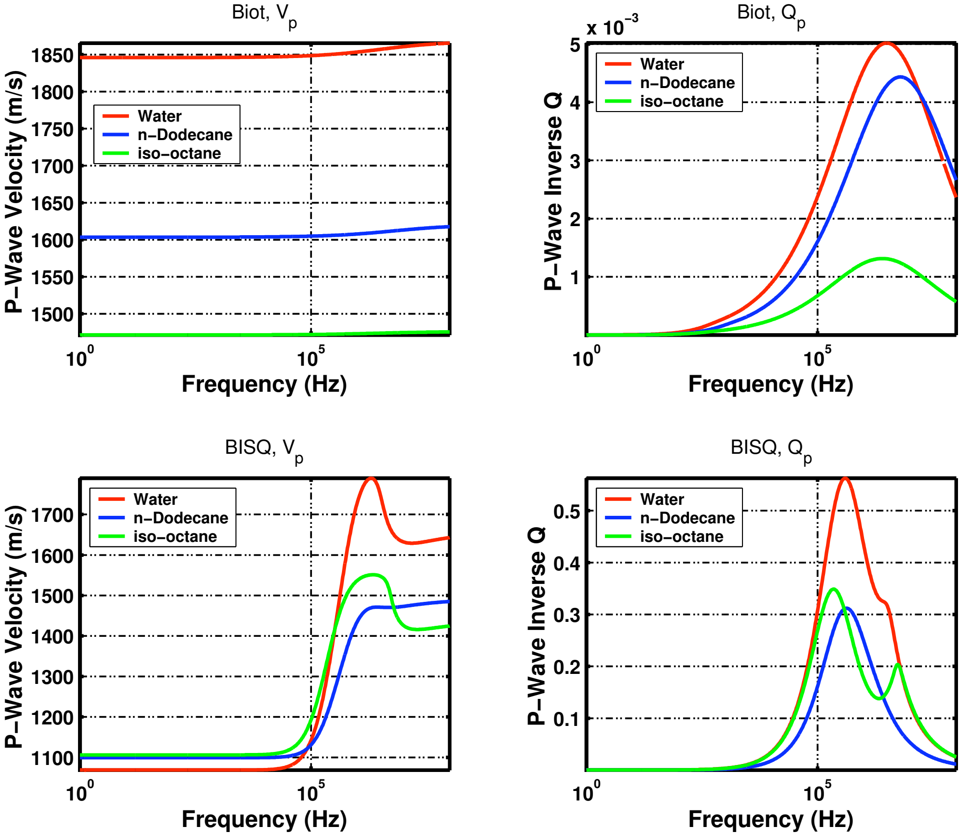

Figure 6.19: Application of the Biot and BISQ models to the GM-95 experiments. Saturated V_p and inverse Q_p are plotted for the fast P-wave as a function of frequency and fluid type. Detailed model parameters are included in the text.

$k_g = 36 \times 10^9$ Pa, $\mu_g = 45 \times 10^9$ Pa) and the sample is taken to be a sand pack with a porosity or 0.42, a permeability of 1 Darcy, and an average grain diameter of 225 microns, parameters very similar to those of the GM-95 sand samples. The sample is assumed to be fully saturated with either water, ($\rho_w = 997$ kg/m^3, $k_w = 2.205 \times 10^9$ Pa, $\eta_w = 1 \times 10^{-3}$), n-dodecane ($\rho_d = 745$ kg/m^3, $k_d = 1.24 \times 10^9$ Pa, $\eta_d = 1.38 \times 10^{-3}$) or iso-octane ($\rho_i = 690$ kg/m^3, $k_i = 0.835 \times 10^9$ Pa, $\eta_i = 0.504 \times 10^{-3}$). A tortuosity of 1.6905 was used based on Berryman's estimate assuming a spherical grain pack. Figure 6.19 depicts the Biot and BISQ estimates of V_p and inverse $1/Q_p$ as a function of frequency for all three fluids assuming a characteristic squirt flow length (R) of 0.001. For BISQ calculations, we use the high frequency formula advocated by Dvorkin *et al.* [86].

Several interesting features are evident in figure 6.19. The first and probably most important is that both Biot and BISQ predict *higher* levels of seismic attenuation for the case of full water saturation in comparison to saturation with either of the NAPLs. This trend contradicts all existing experimental evidence. The attenuation generated by the pure Biot mechanism is also far to small to explain the large reduction in amplitudes observed in laboratory experiments. However, our measurement frequencies are very near the relaxation frequency for both models suggesting that fluid dispersion mechanisms may play a role, albeit secondary to some other primary process.

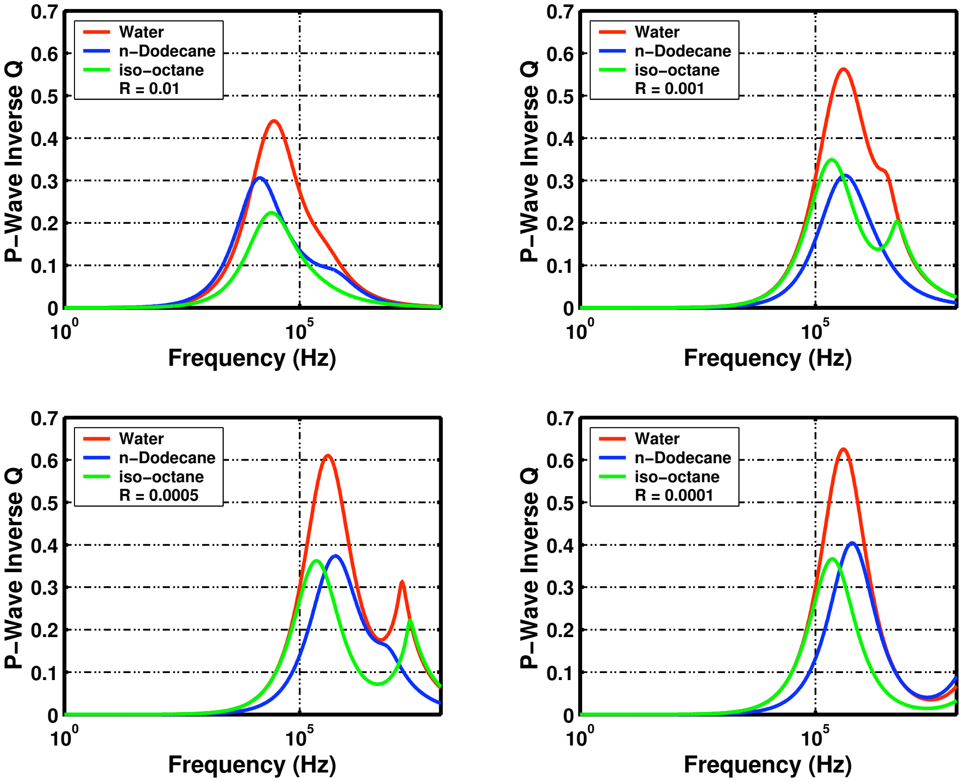

Figure 6.20: Sensitivity of BISQ computation to characteristic squirt length.

Additionally, the BISQ model has the unfortunate property of being highly sensitive to the choice of tortuoisty and the characteristic squirt flow length, neither of which can be directly measured in a satisfactory fashion. This sensitivity motivated several numerical experiments to explore the possibility that alternative parameter choices might generate the right ranking of attenuations as a function of fluid type. Figure 6.20 shows that this ranking is consistent across choice of squirt flow length with water always remaining the most attenuating fluid. Numerical experiments not shown in this text also suggest that tuning tortuosity cannot replicate the fluid attenuation rankings observed in our experiments.

Another possibility initially considered was that of entrained gas within the injected NAPLs reducing the fluid bulk modulus and increasing P-wave attenuation. However, measurements made on pure NAPLs within the same apparatus did not reveal any anomalous loss and the recovered fluid velocities agreed with literature values.

Having eliminated coupling issues, patch effects, scattering, and the usual flow related loss mechanisms from our list of possible suspects, we are left with the unsatisfactory situation of having to appeal to a poorly understood contact mechanism to explain the observed reductions in amplitude. Although frictional forces at contacts have been considered by Prasad [220] and others [257] as a source of attenuation in unconsolidated sands, the impact of replacing water with NAPL at the contact is unclear. Even in the fully NAPL saturated state, water probably still exists as a double layer on the grain surface since high vacuum was not applied before NAPL injection. This opens the possibility that interactions between adsorbed water and NAPLs might be relevant. Although outside the scope of this study, a more careful consideration of contact forces seems warranted. Direct measurement of these phenomenon on smooth samples might be accomplished through use of a surface force apparatus [131] yielding information on fundamental variations in contact stiffness due to fluid effects. The next step from a processing perspective is to perform spectral ratio analysis as a function of NAPL saturation on the recorded waveforms in the hope of illuminating the characteristic relaxation mechanism within the accessible frequency band (100 kHz to 2 MHz). One should note that none of the proposed mechanisms may be relevant at field frequencies and scales. Certainly the Biot and BISQ models typically have characteristic frequencies in the range of 10^5 to 10^7 Hz although some choices of parameters can push BISQ relaxation effects into the crosswell band. Patch equilibration models, such as White's model [274] [84] and scattering effects might be the most relevant mechanisms for our field data, a topic we will explore in later chapters.

6.9 Conclusions : The Acoustic Signature Of DNAPL Saturation At Pinellas

We will conclude our discussion of the acoustic properties of DNAPL saturation with some rough estimates of the DNAPL-induced seismic signature at Pinellas. In chapter 3, we developed an acoustic profile for the DNAPL phase at Pinellas based upon constraints provided by samples from wells RW-06. Density and GCMS measurements revealed that the DNAPLs at this location were a mixture of TCE, toluene, heavy oil, and a large array of trace compounds with an experimentally measured density of 1030 kg/m^3 and an estimated P-wave velocity of $\sim$ 1340 m/s yielding a fluid bulk modulus of 1.85 $\times 10^9$ Pa. Water ($\rho_w = 997$ kg/m^3, $K_w = 2.205 \times 10^9$ Pa) is the second phase of the fluid mixture *in situ*.

Visual microscopy revealed that the sand fraction at Pinellas was primarily quartz ($\rho_g = 2650$ kg/m^3, $k_g = 36 \times 10^9$ Pa, $\mu_g = 45 \times 10^9$ Pa) with small amounts of calcium carbonate ($\rho_g = 2700$ kg/m^3, $k_g = 63 \times 10^9$ Pa, $\mu_g = 31 \times 10^9$ Pa) in the form of shell micro-fragments and potassium feldspar ($\rho_g = 2620$ kg/m^3, $k_g = 37 \times 10^9$ Pa, $\mu_g = 15 \times 10^9$ Pa). Since quartz was the dominant sand/silt component and clay content was almost uncorrelated with V_p, we will assume for modeling purposes that the grain properties are those of quartz. The porosity and frame properties were obtained from two of the previously described natural aquifer experiments (see table 6.2) and our literature V_p/V_s ratios.

Figure 6.21 shows predicted values for V_p and change in V_p as a function of DNAPL saturation using the fluid and matrix properties described above. Two scenarios based on N3 and N4 samples with corresponding porosities of 0.39 (blue) and 0.43 (red) are shown. The solid lines are the estimates generated by the previously outline Gassmann + Hill's equation fluid substitution flow while the dotted lines were generated by our empirical volumetric relationship 6.22. The Gassmann model predicts a significantly smaller P-wave velocity signature for our model DNAPL in comparison to the empirical model. At DNAPL saturations of 0.4, probably on the high end of expected saturations in the field, Gassmann predicts $\sim 3\%$ change in V_p from the water saturated state while the empirical relation predicts a larger decrease in velocity on the order of $\sim 6\%$.

In conclusion, partial DNAPL saturation has a small but measurable acoustic velocity signature as shown in both our experimental efforts and the work of previous researchers. Our experimental database, which includes both synthetic and natural aquifer samples, provides a test for existing models describing the effects of saturation with a second fluid phase and empirical calibration information for the Pinellas NE field site. Gassmann fluid substitution combined with the Hill equation provides a good lower bound on the effects of DNAPLs on soil V_p values. We also develop an volumetric empirical model based on the 11 available NAPL injection experiments which predicts a larger change in V_p than Gassmann fluid substitution and effective fluid models or Hill's patchy saturation model. Based on our best estimate of site soil properties and the characteristics of the DNAPL phase extracted *in situ*, we predict that a small decrease in P-wave velocity and a possible increase in P-wave attenuation is a likely signature of free-phase contamination at Pinellas. Because of the relatively small changes induced by DNAPL saturation ($\sim 5-6\%$), high resolution seismic measurements are probably best suited for use as a supporting dataset in combination with radar data. Seismic measurements may have a more significant role in distinguishing regions of partial gas saturation due to large reductions in seismic velocity and increased levels of seismic attenuation.

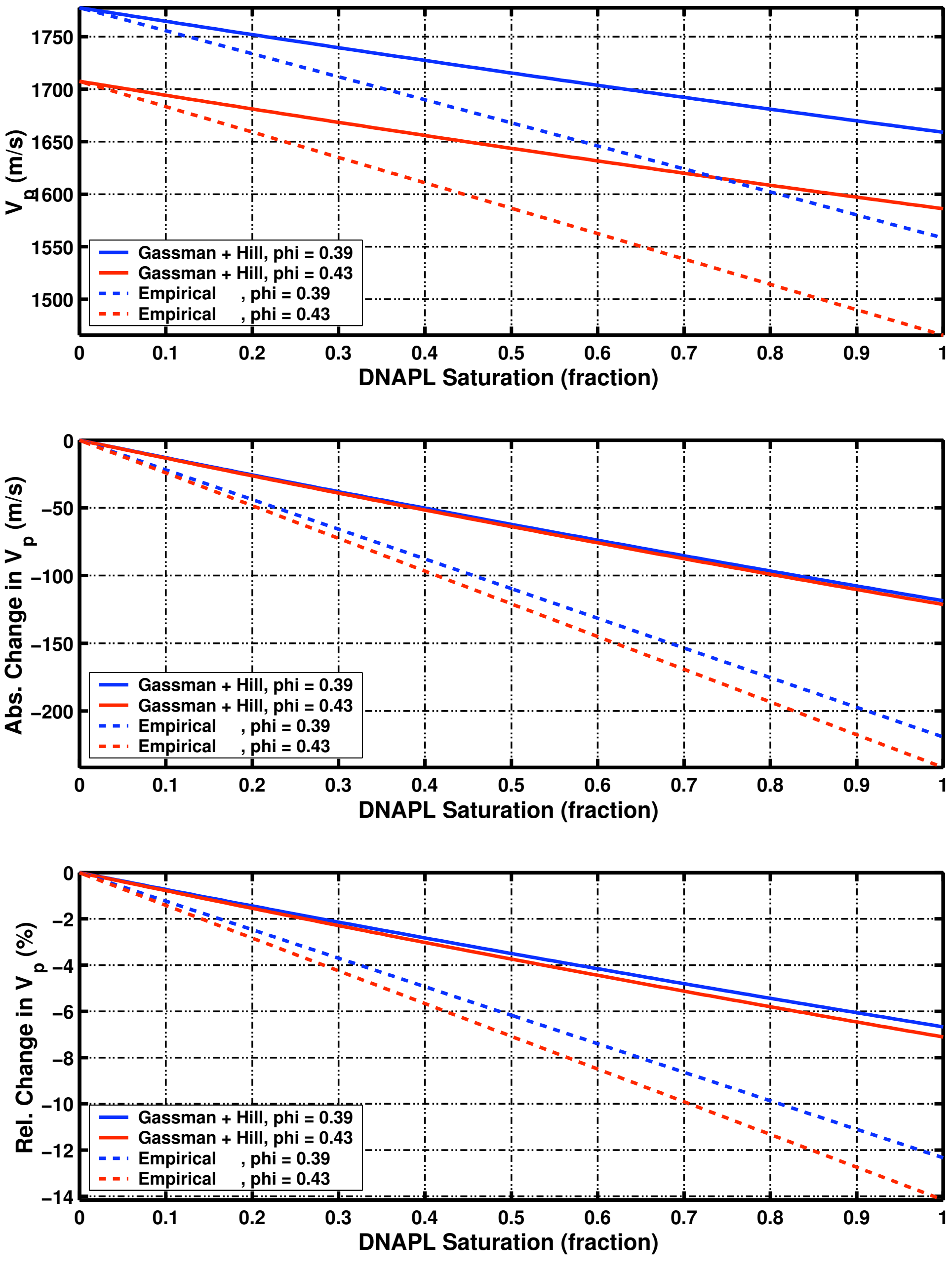

Figure 6.21: Expected seismic signatures for the Pinellas NE DNAPL phase : Shown are model predictions for two samples with different porosities. The Gassmann + Hill model is shown in solid while the volumetric empirical model is indicated by the dashed line.

Chapter 7

Joint Models For The Seismic/Radar Signature Of DNAPLs

In this chapter, we present a set of joint forward models for the acoustic and dielectric characteristics of sediments partially saturated with DNAPLs. In this case, the term “joint” indicates a mapping between the multitude of basic petrophysical properties (multiphase fluid saturation, porosity etc.) and several geophysical observables (V_p,V_{em}). We use these models to investigate some of the possible geophysical signatures of DNAPL contamination and the scenarios where joint measurements might enhance our ability to discriminate between contaminants and variations in lithology. As a simple demonstration, we exploit these forward mappings to build a geophysical model of a DNAPL pool with a realistic contaminant distribution generated by multi-phase flow simulations. We then apply full-wavefield crosswell modeling to predict the type of signatures which might be observed in the field.

7.1 A Joint Forward Model

At this point, we have developed a series of petrophysical models for predicting the effects of DNAPLs on the dielectric and acoustic response of soil samples. We have focused primarily on the effects of DNAPLs in particular and have not delved deeply into other variations in soil and fluid properties which might mimic the response of contaminants. In this section, we outline flows for joint property estimation for cases where minimal amounts of prior information concerning the site-specific response are available. Since small amounts of trapped gas might occur beneath the water-table at Pinellas, we provide extensions to previously considered models including partial gas saturation. We will also suggest two simple approaches for integrating calibration information to build more realistic

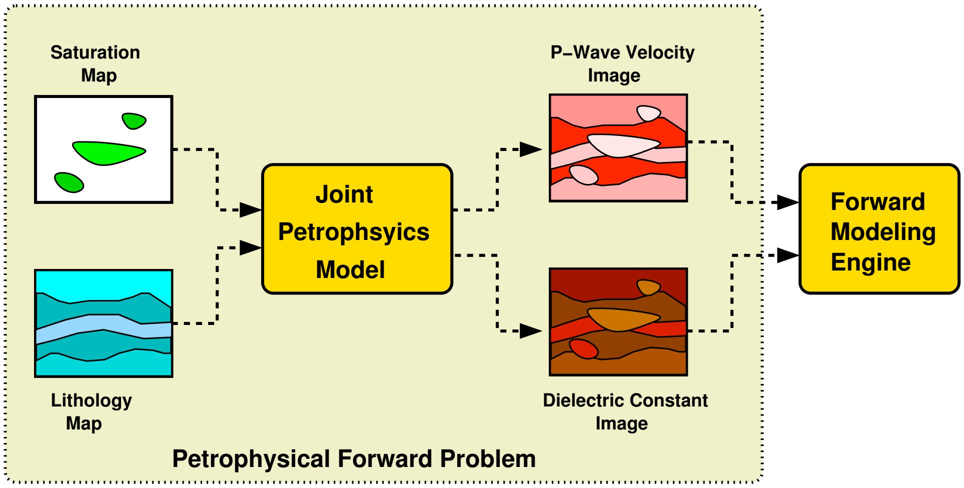

Figure 7.1: Forward petrophysical modeling : conceptual schematic. The forward petrophysics problem starts with information on lithology and saturation and attempts to map them to geophysical observables.

geophysical models. Figure 7.1 shows the general philosophy of our approach. In the case of the forward petrophysics problem, we might start with a model of the subsurface generated from geologic information, geostatisitcs, and the results of multiphase flow simulations. Our goal is then to transform these maps into corresponding maps of geophysically observable properties which will serve as the input to our suite of forward modeling codes. This process will allow us to perform synthetic investigations of geophysical contaminant signatures. Discussion of the actual wave field modeling process will be delayed: in this chapter we will develop only the block referred to as the petrophysical problem in figure 7.1.

The flows we will develop for estimating dielectric and acoustic properties will begin with the same inputs, a map of saturation values (water, NAPL, and gas), information on NAPL and grain composition, a map of porosity, and finally a detailed description of the properties of pure mineral and fluid phases. The output of these models will be maps of geophysical observables : in this case the resulting geophysical models will include dielectric constant, density, and effective bulk and shear moduli. The initial flows will assume that minimal prior information on the applicable petrophysical relations are available and hence will make several simplistic assumptions, particularly with respect to frame properties in the acoustic case.

7.1.1 A Dielectric Forward Model

Figure 7.2 depicts our initial processing flow for dielectric property estimation. One should view this particular flow as just one realization of a general approach since many of the individual steps could be easily replaced with the user's favorite model or a site-calibrated empirical relationship. The diagram is divided into tiers corresponding to different steps in the prediction process. The top tier consists of measured or literature information detailing the properties of pure material phases

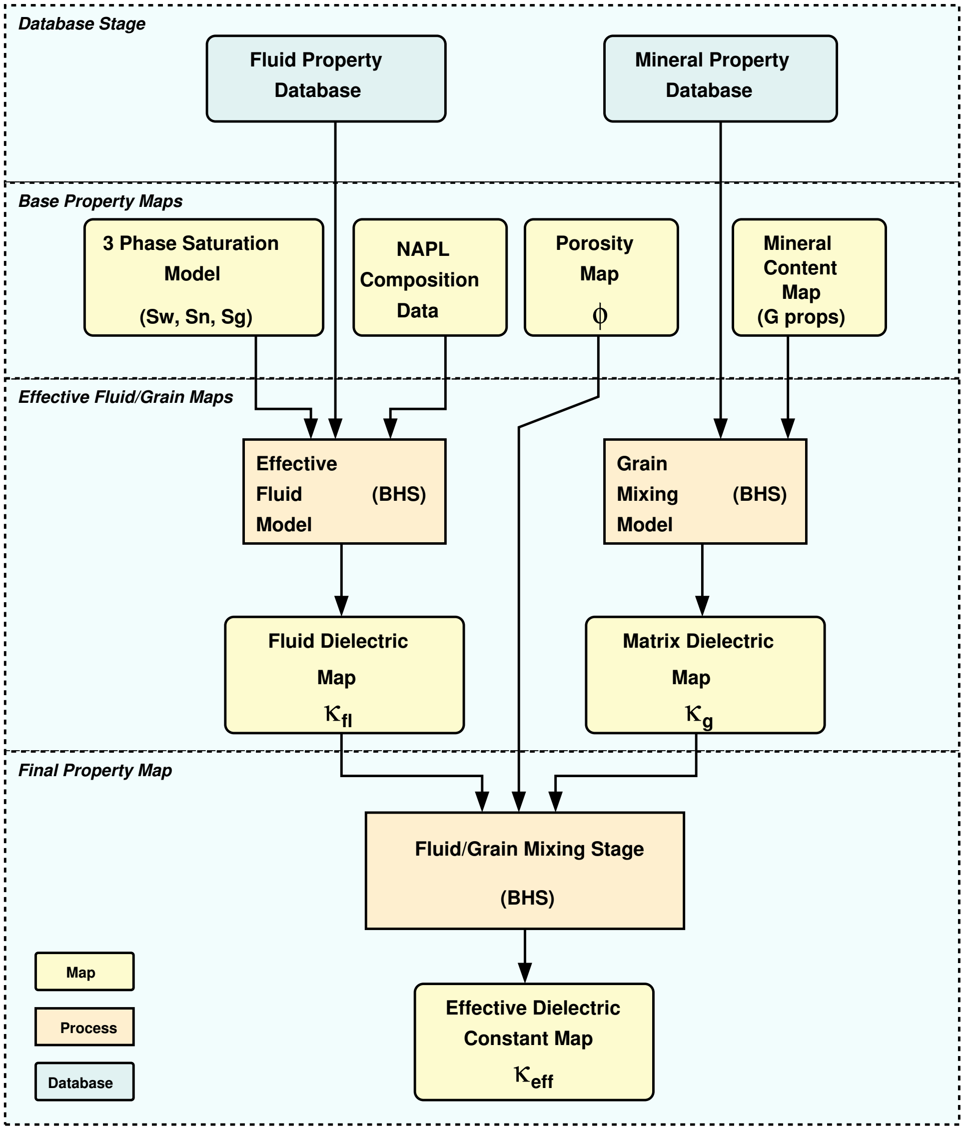

Figure 7.2: A forward model for the dielectric response of DNAPL saturated soils. As indicated in the legend, blue boxes indicate database components while tan and pink boxes represent property maps and processing steps respectively.

including NAPL components, relevant gases, water, and grain materials. We refer to this tier as the database stage since it is independent of the geological and saturation models being processed.

The second stage details the basic property maps which are provided as input to the forward mapping. The inputs provided in this stage are certainly problem dependent with our particular set of inputs biased in favor of examining saturation effects. Since DNAPLs are rarely in pure form in the field, we feel that compositional data for the NAPL mixtures present is a key component in parameterizing this portion of our model. Also included in this stage are porosity and mineral content, the later used to incorporate sand/clay fractions. These base property models could come from a variety of sources. Perhaps the most straight-forward is to place a contaminant hydrogeologist in a room with a cup of coffee and ask him/her what a DNAPL pool would look like at a particular site. Auxiliary information on porosity and mineral data would come from some educated guesses with perhaps a bit of calibration from exploratory boreholes. In the example we will present later in this chapter, porosity and mineral content will be derived from a single realization of a geostatistical model while the fluid saturation map will be generated by multiphase flow simulation. For the ambitious geophysicist with an interest in sedimentology, the lithology model could be generated using a micro-scale depositional model for the appropriate environment to replicate meso-scale textural features.

The third stage takes the initial subsurface lithology and saturation models and transforms them into a map of effective fluid and grain properties. We feel that this intermediate step is important since the inverse solution will often stop at an estimation of these two parameters. We use the Bruggeman-Hanai-Sen model [239] for both of these mixing steps because of its success in fitting our core-scale laboratory measurements. The same BHS model with various mixing sequences has also been used in previous NAPL synthetic modeling investigations carried out by Sneddon *et al.* [243], Carcione and Seriani [50], and Carcione *et al.* [51]. In this and later steps, the BHS model could be easily replaced with the CRIM model [227] [92] or a calibrated instance of the Lichtnecker-Rother equation [118] [173]. In practice, the effective fluid model box contains three steps, one sequentially mixing the NAPL components to produce an effective NAPL, a second mixing the gas fraction with the NAPL, and a third mixing the gassy NAPL with water. In the case of the CRIM model, all components are symmetric and the question of mixing order is avoided. For the BHS model, we have found that the model predictions are not highly sensitive to the choice of mixing order. However, when the generation of effective fluid and grain property maps is not a required step, we typically perform a mixing sequence by computing the properties of a water saturated rock first and then adding NAPL and gas components since this sequence yields a slightly better fit to our laboratory measurements.

In the last stage the BHS model is again applied, this time to generate a final spatial map of effective dielectric constant. The effective grain material is treated as the matrix component.

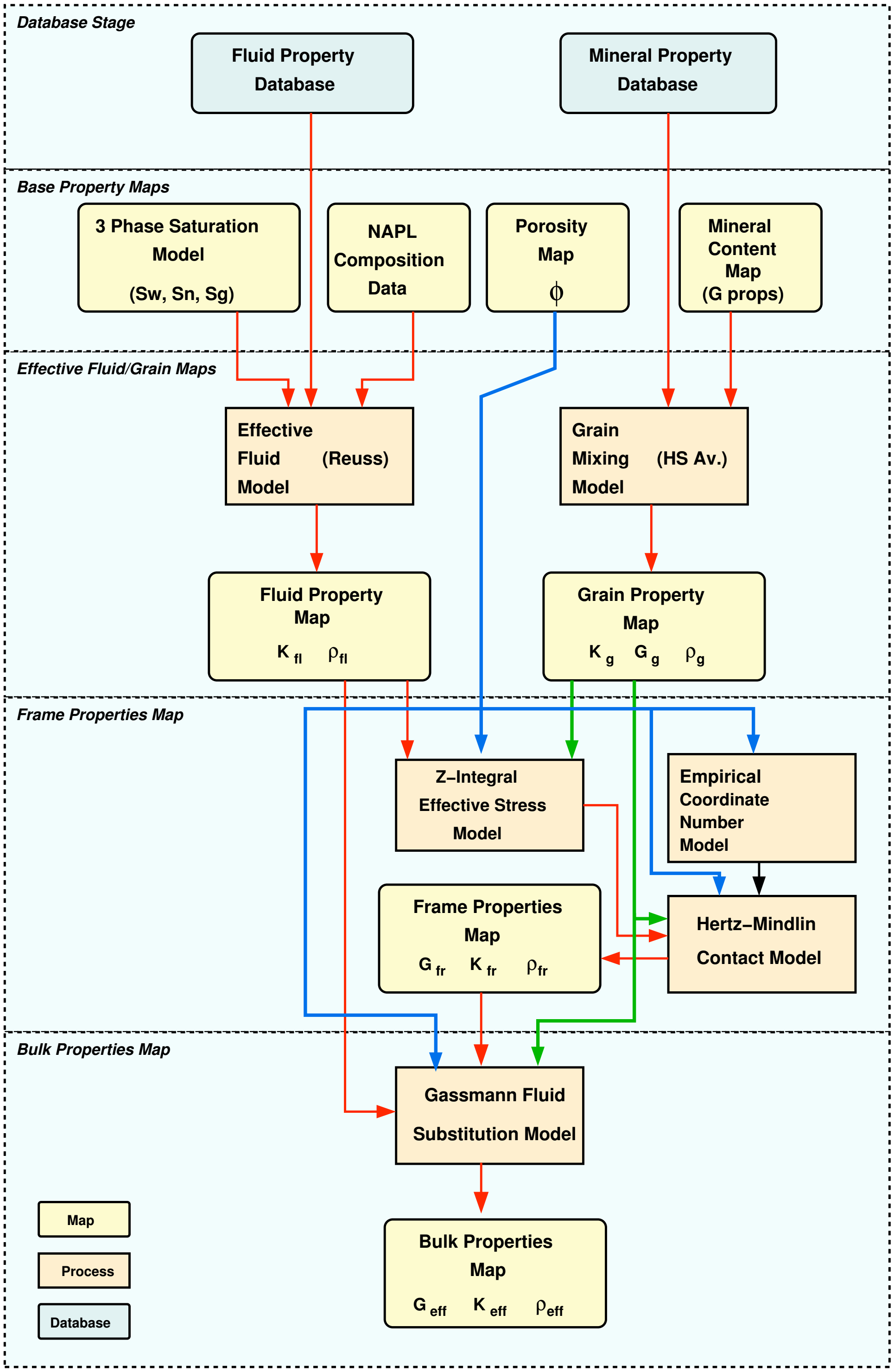

Figure 7.3: An initial forward model for the acoustic response of DNAPL saturated soils. As indicated in the legend, blue boxes indicate database components while tan and pink boxes represent property maps and processing steps respectively.

7.1.2 An Acoustic Forward Model

Figure 7.3 shows an equivalent zeroth-order flow chart for our acoustic forward model. The primary difference between the two flows is the addition of a frame property estimate stage based on a simple contact theory model. The database and base property maps components are identical to those shown in figure 7.2 since we desire a uniform set of inputs to our joint petrophysical model.

The effective fluid/grain property stage uses the Reuss isostress model discussed previously in the acoustics chapter for fluid estimates and a Hashin-Shtrikman average for effective grain properties. Since gasses have a very low bulk modulus, the addition of a small quantity of gas into a harmonic mean (Reuss) greatly increases the effective fluid compressibility. The effective grain properties are computed using a Hashin-Shtrikman average as suggested by Mavko *et al.* [173]. These averages can be written as,

$$K_{HSA} = \frac{K_{HS+} + K_{HS-}}{2} \tag{7.1}$$

$$G_{HSA} = \frac{G_{HS+} + G_{HS-}}{2}, \tag{7.2}$$

where $HS+$ and $HS-$ in subscript denote the Hashin-Shtrikman upper and lower bounds. These bounds for a two-phase composite can be written as,

$$K_{HS\pm} = \frac{f_1}{\frac{1}{K_2 - K_1} + \frac{f_1}{K_1 + 4/3G_1}} \tag{7.3}$$

$$G_{HS\pm} = \frac{f_2}{\frac{1}{G_2 - G_1} + \frac{2f_1(K_1 + 2G_1)}{5G_1(K_1 + 4/3G_1)}}, \tag{7.4}$$

where f_1 and f_2 are the volume fractions of two components with bulk moduli K_1 and K_2, and shear moduli G_1 and G_2. When the stiffer of the two materials is chosen as component 1, equations 7.3 and 7.4 yield the Hashin-Shtrikman upper bounds (K_{HS+} and G_{HS+}). Likewise, by exchanging the two components the lower bounds (K_{HS-} and G_{HS-}) can be calculated. Berryman [32] presents a formulation of the Hashin-Shtrikman bounds valid for an arbitrary number of phases. The effective fluid (ρ_{fl}) and grain densities (ρ_g) are calculated using a volume weighted arithmetic mean of the constituent phases.

Before the effects of fluids can be integrated into our model the acoustic properties of the dry frame must be estimated. This stage involves the most significant assumptions and hence should be treated as an educated guess rather than a truly predictive value. We use Hertz-Mindlin (HM) contact theory [184], discussed in the previous chapter on acoustic properties, for estimation of the frame properties K_{fr} and G_{fr}. The HM model assumes an isotropic random packing of identical spherical grains all with the same elastic properties, a series of assumptions which are broken in all real soils except the rare case of homogeneous natural deposits consisting only of glass beads. We have also implemented the Walton smooth and Walton rough models [267] which can be easily interchanged with the HM model in this step. As a contact theory, the moduli generated by the HM model are dependent on the *in situ* hydrostatic stress state which we must also estimate. We assume that effective pressure (P_{eff}) can be written as the difference between overburden pressure (P_o) and pore pressure (P_p),

$$P_{eff} \; = \; P_o \; - \; P_p. \tag{7.5}$$

If a one dimension columnar model is used to represent the subsurface, effective pressure as a function of depth can be written as the difference between two density integrals,

$$P_{eff}(z) \; = g \left[\int_0^z \, \rho_{fr}(z) \, dz - \int_w^z \, \phi(z) \, \rho_{fl}(z) \, dz \right], \tag{7.6}$$

where g is the acceleration due to gravity, w is the depth to the water table, and ρ_{fr} is the effective density of the frame or $(1-\phi)\rho_g$. We assume negligible pore pressures in the vadose zone. In practice, equation 7.6 is discretized into a summation over vertical slabs of thickness Δz. Coordinate number, another key input into the HM model is calculated using an empirical porosity-based equation as described in the previous acoustics chapter.

The final step in the forward acoustics flow calculates the impact of fluid saturation on the effective elastic moduli using the Gassmann fluid substitution model presented in chapter 5. The resulting spatial maps of effective bulk K_{eff} and shear G_{eff} modulus and effective density ρ_{eff} provide the basic inputs to our lossless acoustic and elastic modeling codes.

7.1.3 A Lossy Acoustics Model For Studying Gas And NAPL Based Attenuation

The previous flow for acoustic property estimation considered only the impact of DNAPL and/or partial gas saturation and elastic moduli and gave no hint as to the attenuating effects of either. Anticipating later analysis of the Pinellas seismic dataset, we will introduce a second flow which includes attenuating effects due to patchy saturation via White's model [274] [84]. As discussed in the the acoustics chapter, White's model describes the changes in bulk modulus and attenuation due to pore pressure equilibration between patches saturated with different fluids. White casts the problem in terms of spheres of radius a saturated by fluid one surrounded by a cubic volume saturated with fluid two. In the case of full saturation with either of the two fluids, the moduli predicted by White's model reduce to Gassmann fluid substitution and the corresponding $1/Q_p$ takes a value of 0. Although other sources of intrinsic attenuation are likely operative at Pinellas, we will limit ourselves to patchy effects in addition to the apparent attenuation due to macroscopic scattering.

The first and second stages of the patchy flow are identical to those shown in the previous acoustic property model. However, in the effective fluid/grain property calculation stage we treat the 3-phase fluid combination as a mixture of 2 effective fluids, one "soft" phase of gas or NAPL and a second

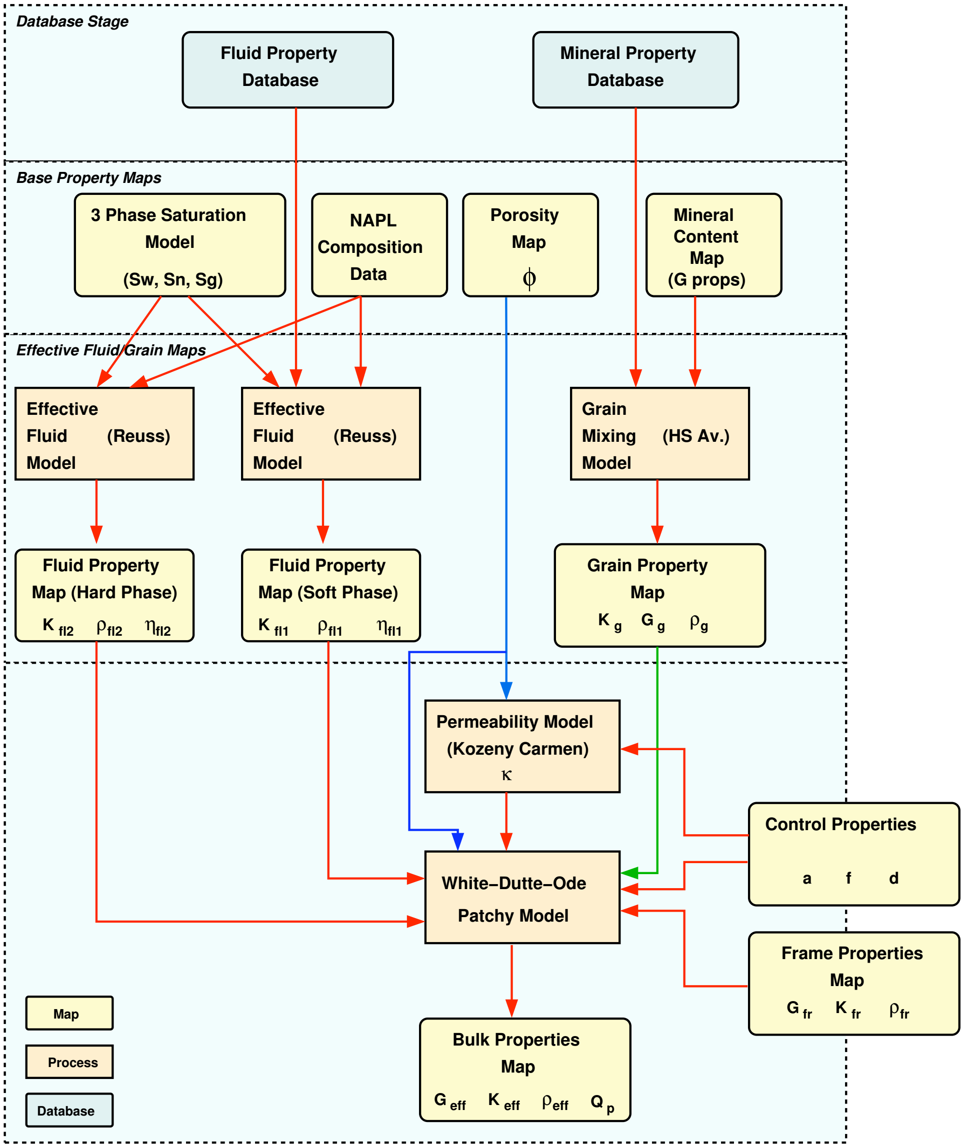

Figure 7.4: A Lossy Acoustics Flow Based On The White-Dutta Model As indicated in the legend, blue boxes indicate database components while tan and pink boxes represent property maps and processing steps respectively.

"hard" phase usually consisting of water. These two effective fluids correspond to the the interior and exterior fluids in White's model. The bulk moduli of the effective fluids are calculated using a Reuss average while the density and viscosity are calculated using volume-weighted arithmetic means. The treatment of grain moduli through Hashin-Shtrikman averaging is identical to that described in the previous section.

In the next and final phase in our lossy acoustics flow, we apply White's model to the soft/hard fluid combination. In figure 7.4 we assume that the frame properties are available, either through the Hertz-Mindlin model as used for the last flow or from empirical relations calibrated at the site in question. Since White's model describes relative flow at the boundaries of a patch, local permeability is an important input parameter. In cases where we have no prior estimate of permeability from site cores we use the extended Kozeny-Carman relation with a percolation threshold [175] [173] to estimate permeability (k_{kc}) assuming spherical grains of diameter d and the porosity map as input. The relation can be written in the form,

$$k_{kc} \;=\; B\,\frac{(\phi-\phi_c)^3}{(1-\phi_c-\phi)^2}\,d^2, \tag{7.7}$$

where B is a geometric factor and ϕ_c is the percolation threshold, the lowest permeability for which a rock of a particular grain structure will have an internally connected flow path. In the absence of any constraints on B or d for a given site we used a form of equation 7.7 fitted to glass bead measurements (250 micron) from Mavko and Nur [175] for a rough guess on permeability,

$$k_{kc} \;=\; 5\,(\phi \;-\; 0.025)^3\,(250\;\times\;10^{-6})^2. \tag{7.8}$$

The White model also requires information on the seismic frequency at which the measurements are made (f) and a characteristic patch radius (a) mentioned previously. For the analysis of field data, frequency information can be obtained from measured power spectrum at the site, in our case within the range from 500 to 10000 Hz. In some situations a guess for a might be available from spatial analysis of lab scale DNAPL flow experiments.

Having provided a general forward mapping for describing the effects of DNAPLs on near-surface acoustic and dielectric properties we would like to once again state that the above flows should be viewed as rough estimates suitable for use in sensitivity testing but not suggested for quantitative predictions requiring significant accuracy. As we will discuss later in this chapter, the use of site calibration data or site reference images allows us to avoid some of the more egregious simplifications we have made. Having said this, we feel that the core fluid saturation models, BHS for the dielectric case and Gassmann for the acoustic case, have sufficient experimental confirmation to allow relatively confident application to this type of problem, particularly to estimate a lower bound on DNAPL effects.

7.2 Joint Signatures In Kappa/V_p Space

With a developed a series of models for describing the combined dielectric and acoustic signature of DNAPLs, we will now consider graphical techniques for exploring these results. Property crossplots, a well established technique in petrophysics, are a useful approach for examining the discriminating power of multiple datasets. One of the most relevant plots for our case is that of V_p against dielectric constant, the property pair which would be extracted in the case of spatially collocated crosswell seismic and radar surveys. By using the previously generated forward mappings, we can now investigate the types of trends which would be expected if a given zone were perturbed by the addition of DNAPLs or gas.

Taking this approach we will start with a model sandy soil, fully water saturated, with a porosity of 0.38, and examine the changes induced by modifying, porosity, adding DNAPLs, or adding a small quantity of free-phase gas. Figure 7.5 shows the changes predicted by the combination of our BHS dielectric prediction flow and the lossless acoustics flow based on the Gassmann model. Dry frame properties for the starting point were obtained from the Pinellas core scale experiments discussed in the acoustics chapter. Grain properties were assumed to be those of quartz [1]. The red path depicts variations in porosity from 0.1 to 0.55 while the two blue paths depict increasing DNAPL saturations up to 80%. The dashed blue line corresponds to the addition of pure TCE [2] while the solid line shows the same saturation process with the predicted properties of the Pinellas DNAPL phase [3] where in both cases DNAPL displaces water [4]. The green path shows the effects of adding up to 40 % free phase gas [5]. As is clear from the crossplot, any dielectric value below the initial state can be explained by either partial DNAPL saturation, partial gas saturation, or decreased porosity. However, the addition of V_p allows us to make an easy distinction between gas and DNAPL saturation due to the significantly smaller P-wave velocity exhibited in the gas case. The two DNAPL saturation curves show that the our characteristic DNAPL phase as determined by the RW06 sample components has a smaller acoustic signature than pure TCE. Based on this analysis, we would expect Pinellas DNAPL phase to significantly decrease subsurface dielectric constant with a minimal acoustic signature. However, acoustic measurements would serve as a good discriminator between DNAPL induced effects and the signature of partial gas saturation or changes in porosity.

While figure 7.5 assumed the lossless acoustic model described previously, we can also explore the signature of DNAPLs and gas saturation using the patchy acoustics flow which incorporates White's model to estimate P-wave attenuation. The top panel in figure 7.6 depicts the results of applying our joint flow with the lossy acoustics component to the previously discussed example. Since losses in the White model are due to relative flow at the boundaries of fluid patches, the porosity trend does not change from the lossless case. The DNAPL addition trend is barely effected by use of the White model due to the relatively small contrast between DNAPL and water impedance. In this case, the

---

[1] Quartz : $\kappa = 4.5$, K = 36 $\times 10^9$ Pa, G = 44.9 $\times 10^9$ Pa, $\rho = 2650$ kg/m^3

[2] TCE : $\kappa = 3.35$, $V_p = 1015$ m/s, $\rho = 1451$ kg/m^3, $\eta = 0.566 \times 10^-3$ Pa s

[3] P-DNAPL : $\kappa = 2.7$, $V_p = 1340$ m/s, $\rho = 1030$ kg/m^3, $\eta = 0.566 \times 10^-3$ Pa s

[4] Water : $\kappa = 80$, $V_p = 1497$ m/s, $\rho = 997$ kg/m^3, $\eta = 1 \times 10^-3$ Pa s

[5] Gas : $\kappa = 1$, $V_p = 331.8$ m/s, $\rho = 1.19$ kg/m^3, $\eta = 1.73 \times 10^-5$ Pa s

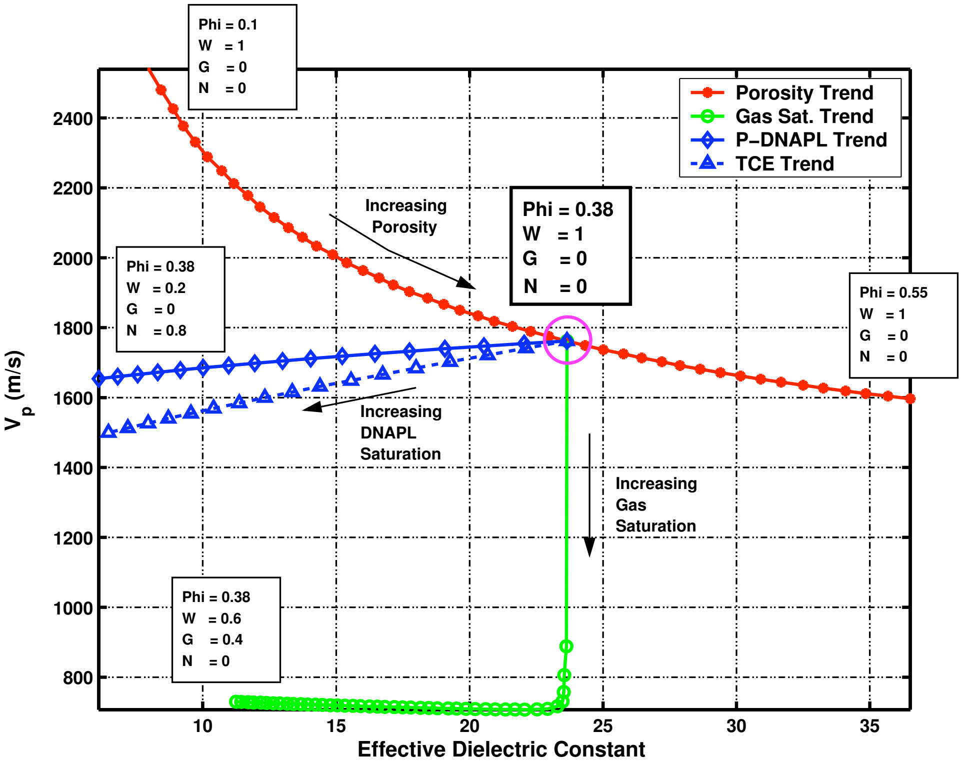

Figure 7.5: Three trends in V_p/dielectric space for a model soil : Acoustic predictions were generated with the lossless forward model based on Gassmann's equation with a Reuss effective fluid. Dielectric predictions were generated using the BHS-based forward model.

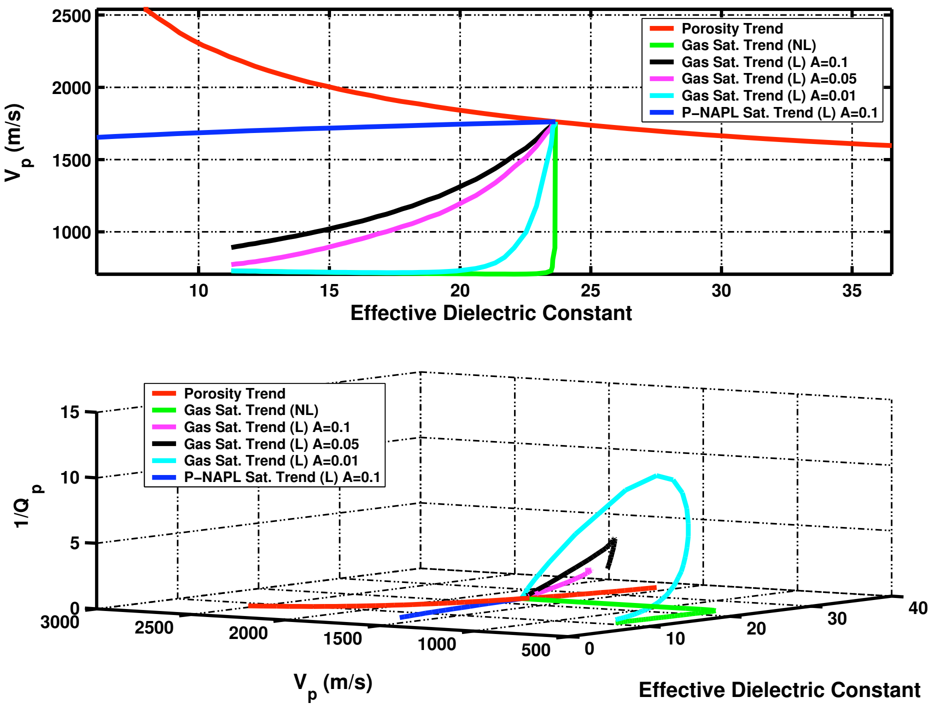

Figure 7.6: Trends in V_p/dielectric space including patchy losses : Results are shown for the idealized sample discussed previously with a porosity of 0.38. A frequency of 5 KHz was used for the loss calculations

lossy and lossless model curves are virtually identical. Significant differences are observed in the case of partial gas saturation. Assuming an investigation frequency of 5 KHz and a permeability of 15 Darcies, changing patch size in the White model from 0.1 to 0.01 causes large variations in V_p as a function of gas saturation. The green gas curve is the previous lossless case using Gassmann and the Reuss effective fluid model. As patch size become smaller, the White prediction converges on this profile. Another approach for looking at the acoustic signature of gas saturation is to "unfold" our V_p/dielectric crossplot into a 3rd dimension where the z-axis is P-wave attenuation as shown in the lower panel of figure 7.6. In this case, attenuation levels are also dependent on patch dimension but any amount of gas generates a larger attenuation signature than that exhibited for the DNAPL profile.

7.3 A Forward Example : The Kueper PCE Model

In this section, we apply our joint forward petrophysics mapping to a realistic DNAPL spill model developed by Kueper and Gerhard [151] [6] to understand the type of property perturbations expected in the field. We then apply full-waveform FD modeling techniques to the resulting property fields in order to explore the seismic and radar signatures of this particular DNAPL distribution.

Kueper and Gerhard [151] examined the infiltration statistics of point-source PCE spills for a set

---

[6] The flow results were generously provided by J.I. Gerhard. and B.H. Kueper of Queens University.

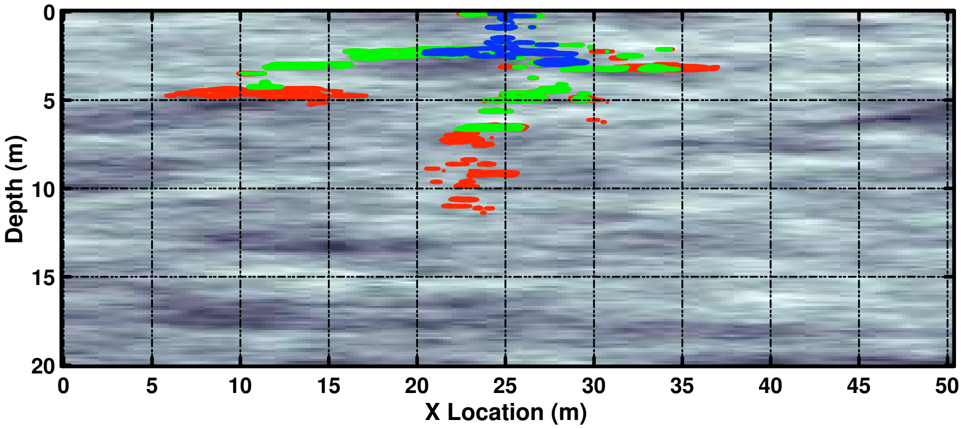

Figure 7.7: The Kueper PCE spill model at 3 times : The blue region shows the extent of the DNAPL after 1 day of infiltration while the green and red regions correspond to infiltration at 3 and 5 days. The solid region at each time corresponds to the region with PCE saturation greater than 20%. Log(permeability) is shown in the background for reference.

of 25 spatially correlated random permeability models by conducting two-phase flow simulations with identical initial and boundary conditions. The models generated for their numerical experiments were 50.5 × 20.125 m two dimensional permeability fields with anisotropic exponential autocorrelation functions and correlation lengths of 5.0 m and 0.5 m in the horizontal and vertical directions respectively. They used an adaptation of the two-phase flow code presented in Kueper and Frind [149] [150] to simulate the release of 5.0 m^3 of PCE (ρ_{fl} = 1460 kg/m^3, η = 0.00057 Pa s) from a surface point source. Although permeability was treated as a random variable, they assumed a constant porosity of 0.34. We use several flow snap-shots from one of their realizations as starting points for our numerical experiments. Figure 7.7 shows the results for one of their flow simulations with a background image of log permeability structure. The blue, green, and red zones correspond to regions with 0.2 PCE saturation

Since the stochastic models developed by Kueper and Gerhard were not tailored to our particular petrophysical flow, we adapted them to provide the requisite input parameters. The goal of using the Kueper models was a realistic DNAPL pool geometry linked to a spatially variable permeability field, not a precise simulation of any particular site; we felt comfortable with modifying both the characteristics of the DNAPL and using a porosity map scaled from the permeability values. The log of the initial permeability models were linearly mapped to porosities ranging from 0.3 to 0.48 with more hydraulically conductive regions mapped to higher porosities. Panel (a) of figure 7.8 shows the porosity map generated through this process. The porous matrix was assumed to be a clean quartz sand with permeability variations induced by sorting. Effective stress values were calculated using the one-dimensional overburden model described previously 7.6 and are shown in panel (b) of figure 7.8. Small lateral variations are caused by porosity variations but these changes tend to be averaged out at depth leaving an almost one-dimensional trend.

Also depicted in figure 7.8 are the results of applying our joint petrophysics forward model to the

DNAPL saturation values at day 5 in Kueper and Gerhard's flow simulation. Panel (c) shows the saturation values at this time step where a series of horizontal pools have been generated through the pooling of DNAPLs above low permeability regions. Saturation values as high as 0.68 are present in this particular realization. For our geophysical property estimation process we replaced the fluid used in the flow simulation (PCE) with the characteristics of the Pinellas DNAPL phase ($\kappa = 2.7$, $V_p = 1340$ m/s, $\rho = 1030$ kg/m^3). The previously discussed BHS-based dielectric model and the lossless acoustic model were used for these calculations. Panel (d) shows the computed P-wave velocity for this saturation map while panel (e) shows the equivalent map of dielectric constant. Consistent with our previous discussion, the DNAPL's dielectric signature is significantly more visible than the changes in P-wave velocity.

To gain insight into the type of seismic and radar responses which might be generated by realistic DNAPL geometries, we performed full-wavefield modeling on the sequence of Kueper flow results. For simulating both seismic and radar responses we used a time-domain finite-difference solution to the scalar wave equation with an added first-derivative loss term. The numerical scheme was 2nd accurate in time and 8th order accurate in space allowing a relatively coarse sampling of the wavefield. Appendix A describes our wavefield modeling approach in detail. Since our goal was to understand the type of signature which might be visible within our Pinellas surveys, we extracted a 10 x 20 m subsection of the Kueper model centered on the DNAPL region and used a crosswell geometry for acquisition of our synthetic dataset. An array of 25 sources were positioned at X = 0.1 m and the resulting wavefields were recorded with an array of 100 receiver located at X = 9 m. The initial velocity models were sampled at a 0.07 m interval resulting in a 130 X 260 point computational mesh with an additional 40 point absorbing buffer on all sides. Figures 7.9 and 7.10 show the results of two radar modeling runs with a Ricker source wavelet centered at 70 MHz. Both figures show the time evolution of the V_{em} model on the left and the corresponding common shot seismograms on the right.

Figure 7.9 depicts the synthetic radar results from a single common-shot gather with the source (red dot) located near the most significant DNAPL pool. The top row shows the background velocity model and the baseline synthetic radargram while the subsequent rows show the model and radargrams corresponding to 1, 3, and 5 days of DNAPL infiltration. As can be seen in the figure, the DNAPL pools have a significant effect on the first arrival, increasing apparent velocity and significantly decreasing amplitude. Scattered events and increased coda energy are also visible. Figure 7.10 shows a similar set of gathers for a shot located at 15 m depth, well below the zone of DNAPL infiltration. In this case, several coherent down-going reflections from individual DNAPL pools are visible. Small velocity changes are also visible at high receiver locations, the only zones where the direct arrival passes through the zone of DNAPL saturation. These numerical experiments suggest that three possible radar signatures of DNAPL pools *in situ* are increased transmission velocity, decreased first arrival amplitude due to scattering losses, and coherent reflections or strong scattered arrivals. These signatures are certainly not unique since lithological variations or a zone gas saturation could generate the same velocity variations. In our analysis of the combined Pinellas

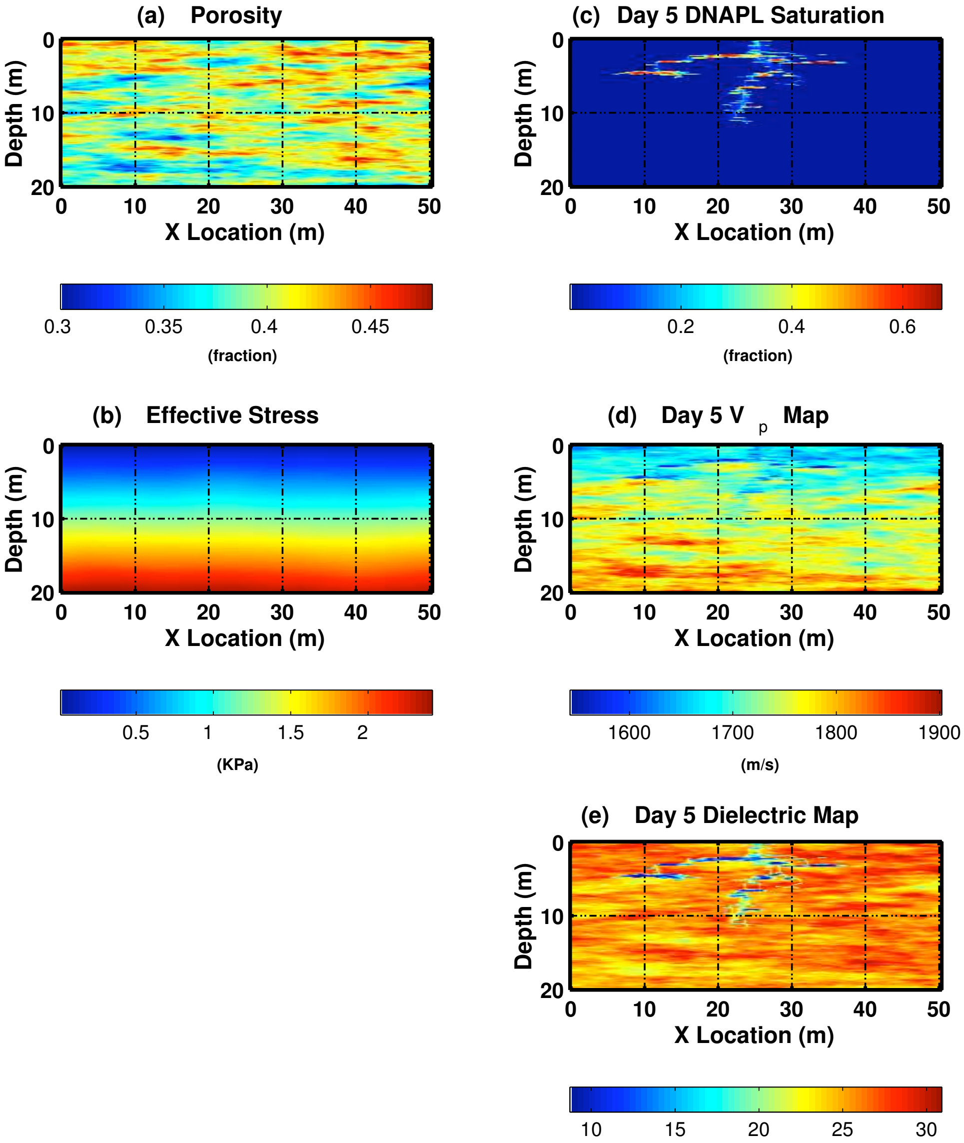

Figure 7.8: The Kueper PCE Spill Model, Geophysical Parameters : Panel (a) shows the porosity model. Panel (b) shows the effective stress map determined using a 1-D density integral. Panel (c) shows the DNAPL distribution on day 5 of the flow simulation while panels (d) and (e) show corresponding maps of V_p and dielectric constant.

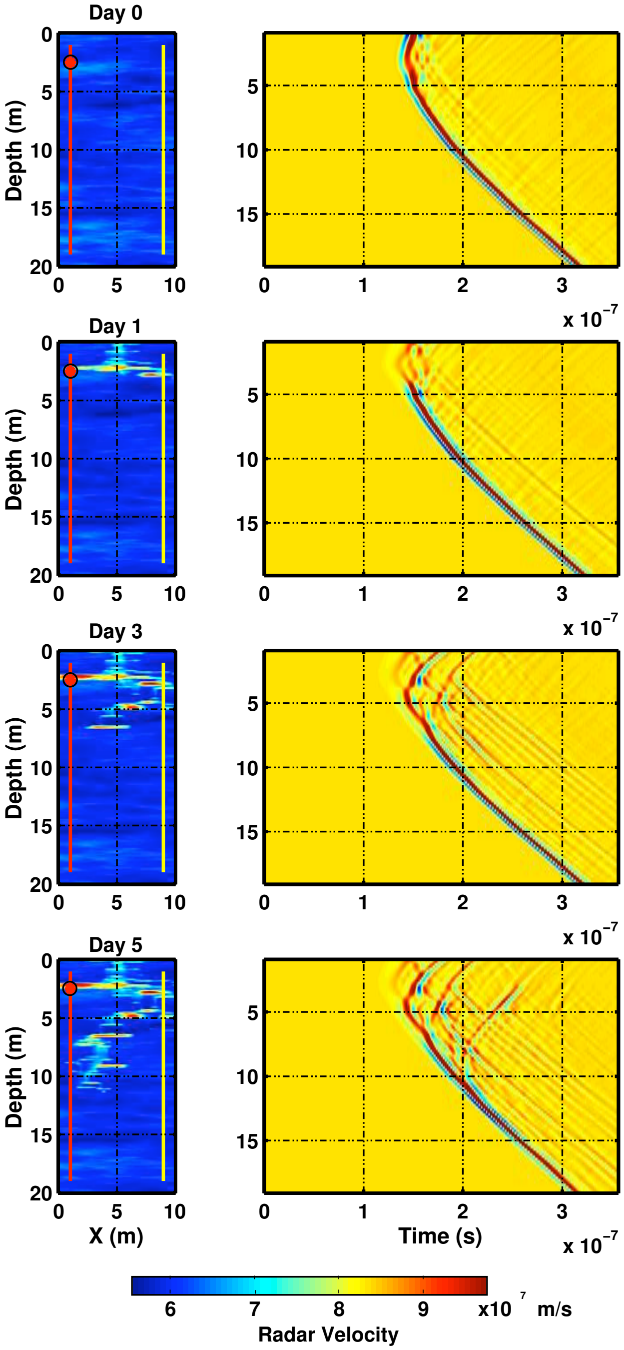

Figure 7.9: Time-lapse wavefield modeling results for crosswell radar : Left hand column depict radar velocity models for each flow step with the source location marked in red and the receiver well marked in yellow. Right hand column depicts the corresponding common shot gathers created using a Ricker wavelet with a 70 MHz central frequency. Note the changes in first arrival traveltimes and amplitudes in the vicinity of the DNAPL pool as well as reflected arrivals later in the wavefield.

datasets we will attempt to use auxiliary information from logs and seismic surveys to constrain the possible sources of observed radar anomalies.

Figure 7.11 shows a similar set of results except for the seismic case, using a 2500 Hz Ricker wavelet as the source. Unlike the radar modeling results, the DNAPL pool network has virtually no seismic signature in either the direct or later arrivals. This is due to the low acoustic contrast between the predicted Pinellas DNAPL phase and water. Similar numerical experiments using pure TCE or carbon tetrachloride as the saturating fluid yield minor but visible acoustic signatures which are nonetheless much smaller than their radar counterparts. One should note that the V_p models were generated using our lossless acoustic flow and therefore can only account for amplitude reductions related to scattering off of discrete DNAPL zones. However, our previous sensitivity studies indicate that losses due to patch equilibration would probably be insufficient to allow the direct identification of DNAPLs (see figure 7.6). Since we have not yet characterized the seismic loss mechanisms present in our lab scale DNAPL experiments (see chapter 6) we cannot rule out the existence of secondary attenuation effects in the field. These results suggest that high-resolution seismic methods might be successfully used to constrain the interpretation radar imagery since seismic measurements are relatively insensitive to DNAPLs but highly sensitive to gas saturation.

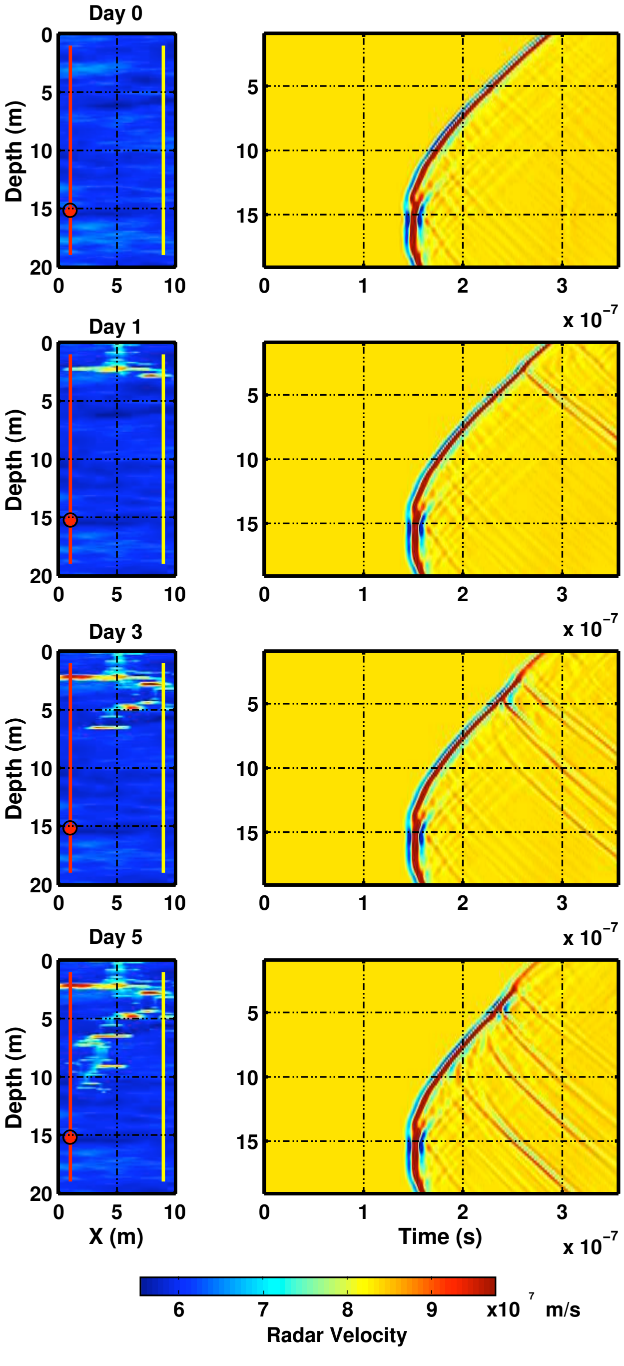

Figure 7.10: Time-lapse wavefield modeling results for crosswell radar, oblique shot : Left hand column depict radar velocity models for each flow step with the source location marked in red and the receiver well marked in yellow. Right hand column depicts the corresponding common shot gathers created using a Ricker wavelet with a 70 MHz central frequency. Note the several down-going reflections generated by individual DNAPL pools and the small change in first-arrival move-out and amplitude at the top of the gather.

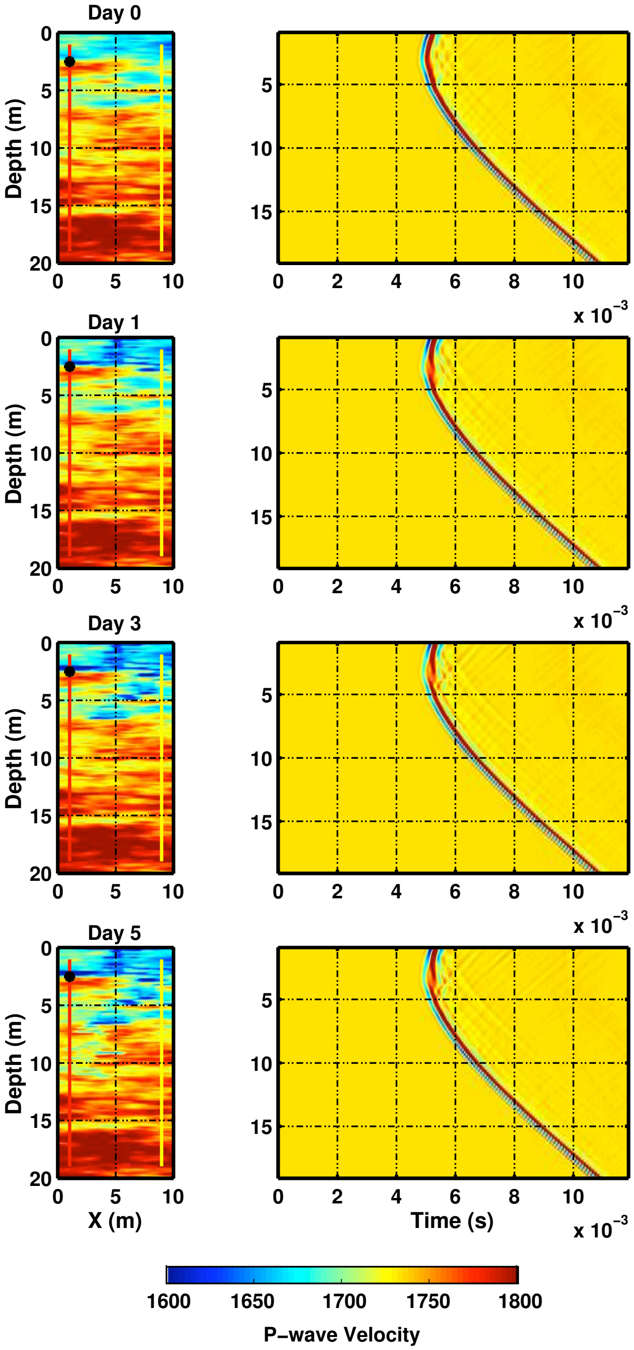

Figure 7.11: Time-lapse wavefield modeling results for crosswell seismic, head-on shot : Left hand column depict seismic velocity models for each flow step with the source location marked in red and the receiver well marked in yellow. Right hand column depicts the corresponding common shot gathers created using a Ricker wavelet with a 2500 Hz central frequency. Minimal variations are seen in the synthetic seismograms.

Chapter 8

Numerical Techniques For Adaptive Near-Surface Tomography

The goal of our sequential crosswell acquisition strategy was to create continuous high-resolution seismic and radar velocity images stretching from a clean region of the site to one with known DNAPL contamination. We decided that simultaneous inversion of the entire dataset was a crucial step in creating a single depth-consistent site image with spatial resolution on the order of 0.5 meters. The largest problem in the effective tomographic processing of our multi-well seismic dataset was the presence of irregular regions of high attenuation. In some zones, no transmitted signal was observed for wells with lateral separations as short as 2 meters. Despite the fact that datasets were acquired with similar source/receiver depth spacings and stacking levels, the number and quality of pickable traces varied dramatically between crosswell sections. The end result of these attenuating zones was a combined seismic profile with highly irregular ray density, angular aperture, and S/N ratio. As can be seen in figure 8.1, the zone of high attenuation stretches between wells G19 to G16 with varying vertical extent between the different well pairs. We set out to develop a tomographic algorithm which would gracefully handle irregular ray geometries while preserving high spatial resolution in zones with sufficient coverage. To solve this problem, we exploit an adaptive mesh refinement algorithm to construct a high quality parametrization for the traveltime tomography problem [1].

In this chapter, we provide a brief introduction to traveltime tomography and the resulting linear and non-linear inverse problems. We then present a traveltime tomography method which exploits a greedy mesh refinement algorithm to construct adaptive parameterizations with guarantees on model resolution. The refinement strategy is implemented on an unstructured trigonal mesh of cells, each

---

[1] Jaime Urban (Stanford) participated jointly in the development of the raytracing and regularization scheme presented in this chapter.

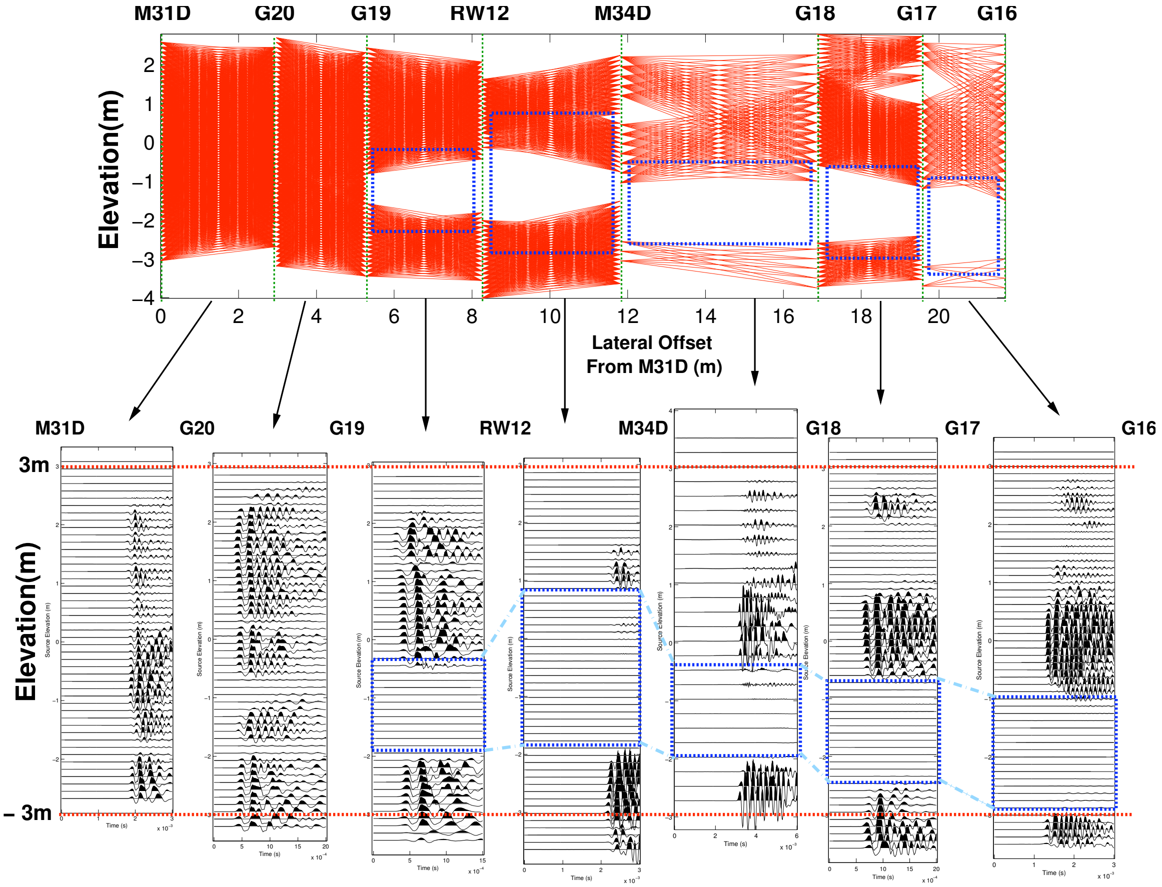

Figure 8.1: Raypaths and zero-offset (ZOFF) sections for the M31D-G16 combined seismic profile : The zero-offset sections for each well pair are plotted in true amplitudes. Note the large region with no signal at approximately -1 to -2 meters. Elevations are absolute with respect to sea-level.

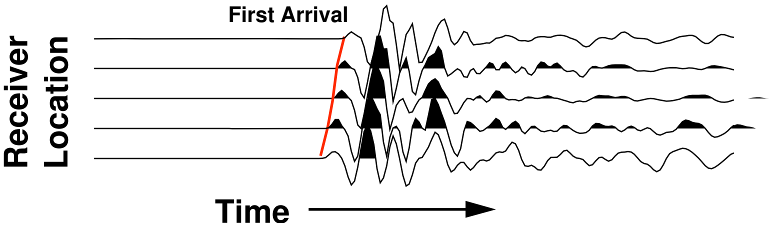

Figure 8.2: First arrivals in a seismic dataset

with a constant gradient of slowness. We extend previous work on this topic by adding a new class of refinement operations which produce higher quality meshes with fewer poorly formed triangles. The algorithm is tested on both a synthetic reconstruction problem and one of the Pinellas seismic profiles which exhibits highly irregular ray coverage.

8.1 An Introduction to Traveltime Tomography

Near-surface geophysical characterization relies heavily on numerical algorithms for transforming raw data collected in the field into quantitative models of subsurface properties. In the case of radar and seismic methods, our experiment involves generating either an acoustic or electromagnetic impulse and recording the resulting wavefield at a set of locations in space. From these waveforms, we would ideally like to build a high resolution image of elastic (V_p, V_s, ρ) and electromagnetic (κ, σ_{dc}) properties suitable for determining petrophysical parameters relevant to hydrogeology such as porosity and saturation state. While the perfect inversion scheme might utilize the entire waveform for solving such problems [2], we will primarily use the temporal location of the first arriving wave at each receiver, a datum better known as the *first arrival traveltime*. Figure 8.2 shows several sample seismic waveforms with first arrivals picked in red. We will also make limited use of the amplitude and spectral characteristics of the first detectable phase for quality control purposes. By ignoring the rest of the waveform, we lose all of the information encoded in later arrivals, particularly the reflected phases which provide constraints on short wavelength features. If only traveltime data are used, we can at best hope to recover maps of V_p, V_s (if a shear arrival is detected), and V_{em}.However, posing the inversion in terms of traveltimes has several advantages over full wavefield processing in terms of algorithmic convergence, computational cost, and most importantly robust behavior in the presence of errors. We will postpone discussion of the mechanics of pre-processing waveform data and picking traveltimes for later chapters.

The word *tomography* can be broken into two Greek roots, *tomo* and *graphika* with the respective literal translations of “slice” and the verb “to write”. In common parlance, tomography now refers to techniques for inferring the internal properties of objects using external sources of radiation, often involving some type of wave based component. In the case of traveltime tomography using

---

[2] Exploitation of the entire wavefield for tomographic imaging has been developed in both the time-space [187] [249] and frequency-space [222] [223] domains.

seismic and radar techniques, we are attempting to recover spatial variations in velocity, $v(x, z)$ in two dimensions. To recover this velocity model we need to develop a mapping between $v(x, z)$ which we will refer to as model vector m, and our observed traveltimes, which we refer to as the data vector d. In reality, traveltimes are dependent not only upon the velocity model but also the temporal bandwidth of the recorded data. Although several methods exist for calculating and inverting band-limited traveltime data [117] , we will use what is commonly referred to as the ray theory approximation which assumes infinite frequency and bandwidth [58]. In this case, the traveltime along a particular curve through space can be written in terms of a path integral of the form,

$$T(x_s, x_r, s, c) \; = \int_c s(x, z) dx dz = \int_{t_a}^{t_b} \|c'(t)\| s(x(t), z(t)) dt, \tag{8.1}$$

where T is the traveltime for a ray traveling along path c through slowness field $s(x, z)$ ($s = 1/v$) and the source/receiver locations are denoted by x_s and x_r respectively. c is a bounded parametric curve in t, i.e. $c(t)$, $t_a \leq t \leq t_b$, $R \Rightarrow R^2$. For the curve to connect x_s and x_r we constrain c to appropriate values at the limits of integration or, $x_s = c(t_a)$ and $x_r = c(t_b)$.

Equation 8.1 merely provides us with a traveltime when the raypath c is known *a priori*. However, with an infinite number of possible curves available, we must choose the one associated with the first arriving phase and evaluate T along this path. Fermat's Principle states that raypaths will be extremum i.e. for c to be a valid path it must be a local minimum or maximum in T for given values of s, x_r, and x_s [39] [31] . The path c_{min}, associated with the global minimum in T, is the path of the first arrival, hence T_{fa} should be,

$$T_{fa}(x_s, x_r, s) = min(\int_c s(x, z) dx dz) = \int_{t_a}^{t_b} \|c'_{min}(t)\| s(x(t), z(t)) dt. \tag{8.2}$$

This formulation suggests that one approach to evaluating T_{fa} is to limit c to a functional form of a few variables and minimize T through a search across the parametrization of the path, a process referred to as the bending method [189]. [3] Figure 8.3 is a schematic diagram of the path integral.

Since T_{fa} is our measured dataset (d) and $s(x, z)$ is the model we wish to recover (m), we can write our problem in terms of a non-linear traveltime operator, G, such that $d = G(m)$ [4] . In cases where velocity perturbations are relatively small, we can assume that raypaths (c) will be straight allowing us to remove the minimization term from equation 8.2. Since integration is a linear

---

[3] Although we appeal to Fermat's principle, this minimization process can be thought of as one particular boundary value solution of $\frac{d\theta}{dl} = \frac{1}{s}\left(\frac{\partial s}{\partial y}\cos\theta - \frac{\partial s}{\partial x}\sin\theta\right)$, the ray equation, where θ is the local orientation of the ray [31]. One popular approach to solving for the path connecting a particular source/receiver pair is through sequential initial value solutions of the ray equation, a process referred to as the *shooting method* [58]

[4] An alternative approach for traveltime calculation involves direct solution of the eikonal equation which in two dimensions is $\frac{1}{v^2} = \left(\frac{\partial t}{\partial x}\right)^2 + \left(\frac{\partial t}{\partial z}\right)^2$. Many techniques ranging from finite-difference methods [262] [258] [240] to modified shortest path algorithms [190] are available for solving this non-linear PDE.

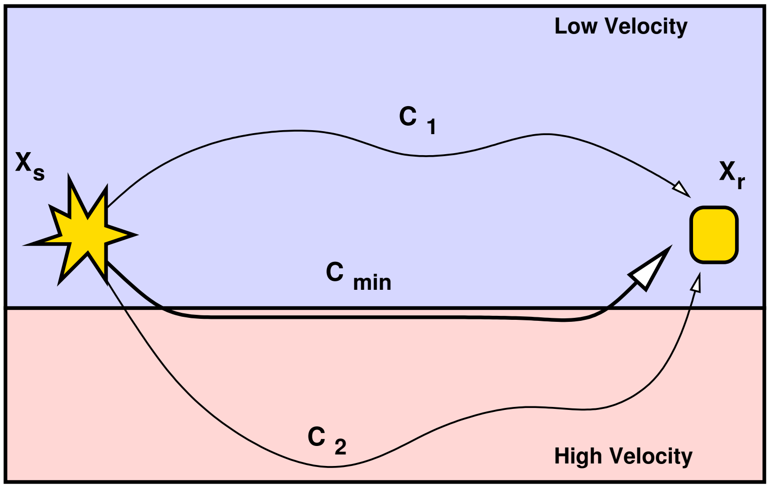

Figure 8.3: The path of minimum time

operation, we can then write the forward problem in its classical form

$$G\,m \;=\; d, \tag{8.3}$$

where the details of G depend upon how the model is discretized. The validity of the straight ray assumption depends largely on the velocity contrasts present and the source/receiver geometry used. As a rule of thumb, local velocity variations less than 10 % can usually be handled accurately using straight rays. This assumption is usually invalid in cases where waves traverse the vadose/saturated zone boundary or soil/bedrock contacts, two scenarios which are not relevant to the Pinellas dataset.

The most illuminating approach to explaining traveltime tomography is to choose a discretization for m and provide a step-by-step explanation for constructing the operator G. A rectilinear mesh of constant velocity blocks is one of the simplest and most commonly used ways to represent the subsurface with the first application of this parametrization dating back to Aki and Lee's [14] work in the late 1970's. In this case equation 8.1 reduces to a summation of the form,

$$T(x_{s_k}, x_{r_k}, s) \;= \sum_{i=1}^{n} s_i\, l_{ki}, \tag{8.4}$$

where s_i is the slowness value for the ith cell and l_{ki} is the length of the kth ray in the ith cell. Figure 8.4 shows one possible source/receiver configuration for the crosswell geometry. The bottom panel shows the subsurface partitioned into 9 rectangular cells of constant slowness and three raypaths through this model. The full expansion of $G\,m \;= d$ for this case is then,

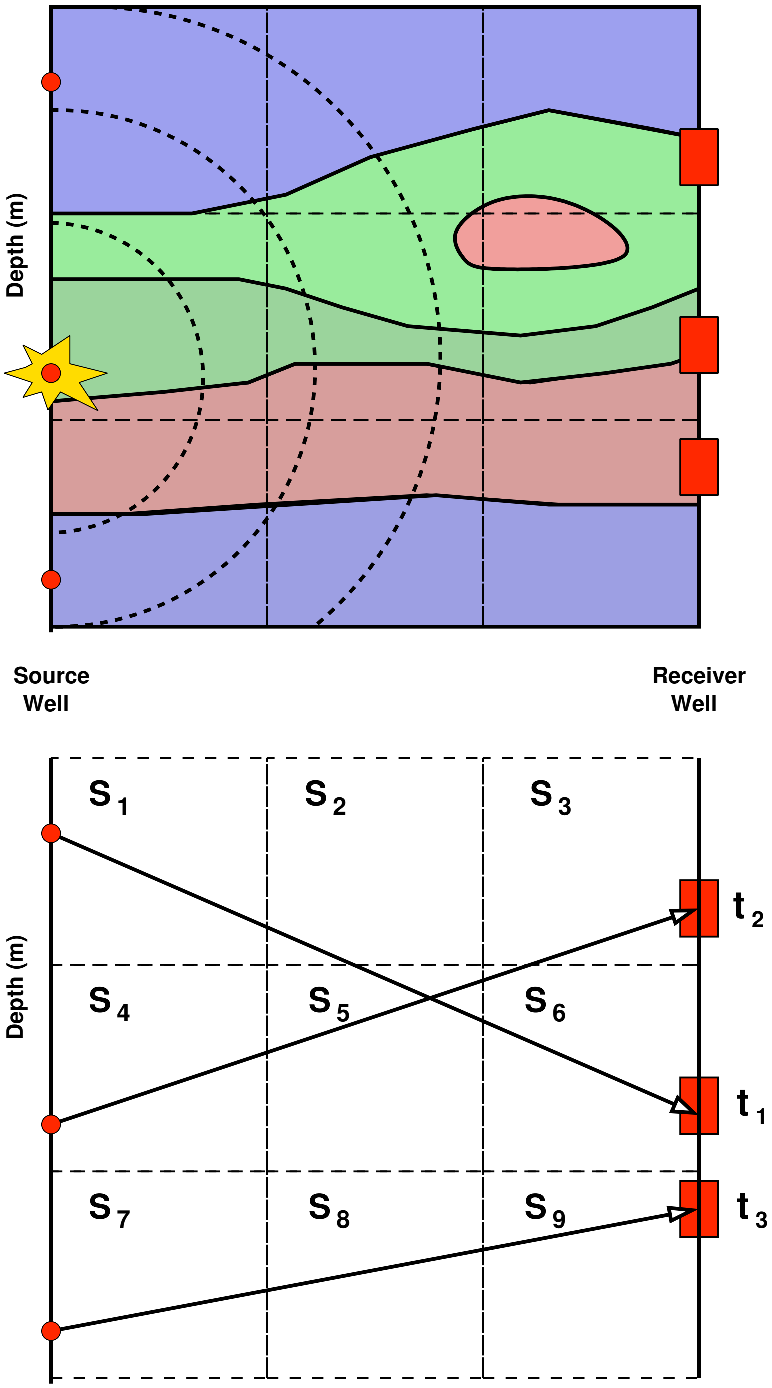

Figure 8.4: Crosswell geometry and a piece-wise constant parametrization

$$\begin{bmatrix} l_{1,1} & l_{1,2} & 0 & 0 & l_{1,5} & l_{1,6} & 0 & 0 & 0 \\ 0 & 0 & l_{2,3} & l_{2,4} & l_{2,5} & l_{2,6} & 0 & 0 & 0 \\ 0 & 0 & 0 & 0 & 0 & 0 & l_{3,7} & l_{3,8} & l_{3,9} \end{bmatrix} \begin{bmatrix} s_1 \\ s_2 \\ s_3 \\ s_4 \\ s_5 \\ s_6 \\ s_7 \\ s_8 \\ s_9 \end{bmatrix} = \begin{bmatrix} t_1 \\ t_2 \\ t_3 \end{bmatrix},$$

where again l_{ki} is the length of the kth ray in the ith cell. In our tomographic algorithm we use trigonal cells with a constant gradient of slowness rather than constant slowness pixels. Since our goal is to recover m given d, we are tempted to write a solution in terms of the inverse of G,

$$m = G^{-1}\, d. \tag{8.5}$$

However, in most cases a true inverse for G does not exist because, as is shown in our simple example, G is not square ($i_{max} \neq j_{max}$) and is also typically rank deficient and poorly conditioned. We can calculate an operator which "undoes" the work of G, a so-called generalized inverse,

$$m = G^{-g}\, d. \tag{8.6}$$

G^{-g} is not an inverse in the strict sense since in most cases $G^{-g}G \neq GG^{-g} \neq I$. Before deciding how to calculate G^{-g}, we can describe several interesting matrices which give insight into the solutions which G^{-g} generates. The model resolution matrix, R, describes the way in which model parameters can be independently resolved and can be defined as,

$$R = G^{-g}G. \tag{8.7}$$

R can be seen as a filter which shows how the imaging experiment and the choice of G^{-g} modify the true model, i.e.

$$m_{est} = R\, m_{true}. \tag{8.8}$$

By the same token if R is equal to I, the identity matrix, all model parameters are fully resolved and $m_{est} = m_{true}$. Each row of R provides information on how the true model is averaged to produce a single element in m_{est}. The diagonal elements of R measure the degree to which a given estimated model parameter (m_{est_i}) is correlated with the same parameter in the true model (m_{true_i}) and is thus a good first order measure of how well resolved the parameter is. The unit covariance matrix, $[cov_u\, m]$, defines the way in which error is mapped from data into the estimated model when solving the inverse problem. Assuming uncorrelated data with uniform Gaussian errors quantified by variance σ^2, $[cov_u\, m]$ can be written as,

$$[cov_u\, m] \;=\; \sigma^{-2} G^{-g} [cov\; d] G^{-g\,T} \;= G^{-g} G^{-g\,T}. \tag{8.9}$$

A final special matrix which can be derived from G^{-g} is the data resolution matrix, H, which is defined as,

$$H \;=\; G\, G^{-g}. \tag{8.10}$$

H can be seen an operator which maps the measured data to those predicted by the combined forward and inverse schemes or,

$$d_{pred} \;= G\, m_{est} \;= G\, G^{-g}\, d_{meas} \;=\; H\, d_{meas}. \tag{8.11}$$

At some point we must consider a concrete approach to calculating G^{-g} or a plan for duplicating the action of G^{-g} on the data vector. In our tomographic algorithm, we use a spatially anisotropic regularized least-squares formulation for the traveltime inversion problem where the generalized inverse is defined as

$$G^{-g} \;=\; (G^T G + \lambda_x^2 D_x^T D_x + \lambda_z^2 D_z^T D_z)^{-1} G^T \tag{8.12}$$

where D_x and D_z are directional spatial differencing operators and the λ parameters describe the amount of weight given to model simplicity in terms of D versus L_2 data fit. This is equivalent to the least-squares solution of

$$\begin{bmatrix} G \\ \lambda_x D_x \\ \lambda_z D_z \end{bmatrix} m \;=\; \begin{bmatrix} d \\ 0 \\ 0 \end{bmatrix}. \tag{8.13}$$

When the λ parameters are large, the $D\, m$ products are minimized regardless of whether $Gm \;=\; d$. These model space regularization operators provide smoothness constraints on model structure. By choosing a particular ratio between the horizontal and vertical regularization parameters, $r_\lambda \;=\; \lambda_z/\lambda_x$, we can also provide a prior bias towards layered models, a valid approach in many shallow sedimentary environments. Many techniques exist for solving problems of the form 8.13 but we generally prefer the LSQR algorithm of Paige and Saunders [211].

Choosing the appropriate value for the regularization parameter(s) is not always an easy task. The Generalized Cross-Validation technique (GCV) [265] is one approach for determining an appropriate regularization without having to assume *a priori* a particular noise level. The GCV technique attempts to choose a regularization parameter resulting in a "robust" solution, i.e. a λ value which allows reliable prediction of the model if any single data point is discarded. $GCVC(\lambda)$, the metric which the GCV technique uses to judge the fitness of a particular choice of regularization or parametrization is

$$GCVC(\lambda) \;=\; \frac{\|(I \;-\; H)\, d\|^2}{Trace(I \;-\; H)^2}, \tag{8.14}$$

where H, the data resolution matrix, implicitly contains λ since $H = G\,G^{-g}$. The GCV criterion is minimized over the space of reasonable regularization parameters. This is a 1D minimization problem requiring calculation of G^{-g} and H for a large number of λ_1 values. The λ_1 value that minimizes equation [8.14] is then used to evaluate the tomography solution. One common problem with this approach is that the GCV metric (8.14) often has a wide shallow minimum resulting in uncertainty as to the appropriate λ [121]. With a general framework for the traveltime tomography problem established, we will now move to our specific implementation using unstructured trigonal meshes with greedy refinement.

8.2 Traveltime Tomography on Unstructured Trigonal Meshes

The application of traveltime tomography algorithms to near-surface seismic datasets is often complicated by irregular acquisition geometries, variable signal quality, and the underdetermined nature of the resulting inverse problems. In the case of the Pinellas seismic investigation, one of the most difficult processing problems was the existence of large regions of high attenuation. Although the acquisition geometry was regular at Pinellas, the loss of signal in the attenuating region prevented us from picking all of the acquired traces. The result is a ray geometry with significant spatial gaps as is shown in figure 8.1. Intuitively, regions of space with higher ray densities and more complete angular coverage should allow examination of smaller features, assuming the fundamental wave-theoretic limitations of imaging are honored. In addition to large coverage gaps, differences in interwell spacing and S/N levels can produce significant variations in angular aperture between well pairs. If we consider the entire profile as a single dataset for the purposes of inversion, the choice of a regular mesh and an appropriate regularization operator becomes difficult. We are forced to either use a fine mesh and deal with a large number of totally unconstrained parameters or to select a coarse mesh where individual cells are well-constrained but spatial resolution is greatly decreased. Several approaches exist for dealing with the case of sparse data or variations in resolving power. One approach uses a fine discretization of regular pixels to generate an underdetermined inverse problem, similar to the continuous case, and then adds information to this system in the form of a spatially adaptive regularization scheme as implemented by Yi *et al.* [281] for the resistivity inversion problem. A second commonly used technique extrapolates the data set to full aperture and interpolates all measurements onto a regular geometry thus generating a spatially uniform problem

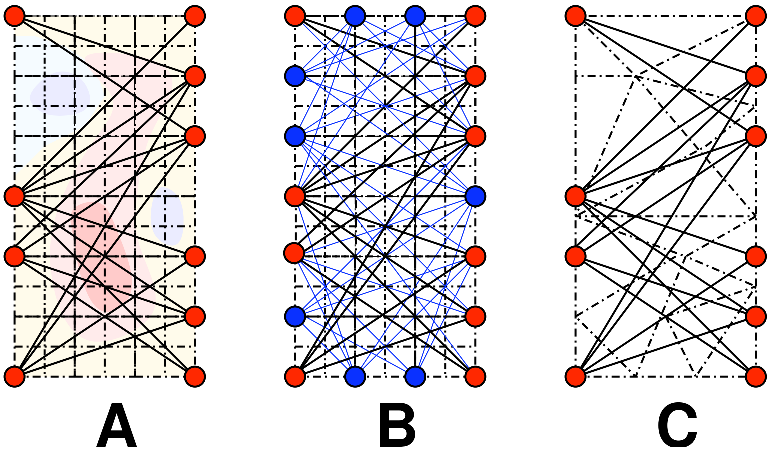

Figure 8.5: Three approaches to dealing with coverage problems in tomography : panel (a) depicts a fine mesh with colors schematically representing zones a spatially variable regularization parameter, $\lambda(x, z)$ [281] . Panel (b) shows the irregular geometry extrapolated to full aperture with added sources and receivers shown in blue [161] . Panel (c) shows a trigonal mesh adapted to the ray geometry [62].

as is done by Li and Nowack [161]. The problem in this case is to predict missing data, a non-trivial task but one which has seen significant advances through the development of autoregressive signal analysis and optimal prediction-error filters [97].

We will consider a third approach, the problem of finding an optimal parametrization with spatially varying cell dimensions where mesh quality is judged by the properties of the model resolution matrix. This strategy allows us to construct a mesh adapted around irregular ray-coverage with formal constraints on how different zones of the problem are resolved. We will solve the limited problem of finding high quality meshes for crosswell seismic experiments assuming straight ray-paths and a consequently linear inverse problem.

The goal of tomographic mesh adaptation is to generate a parametrization with some stipulated property, possibly fulfilling or optimizing a formal quality measure of the resulting inverse problem such as eigenspectrum metrics [64], various properties of the model resolution matrix [62], or null-space power [38]. For larger problems, heuristic measures of mesh quality including cellular hit count [34] are often used. In some cases, mesh adaptation is instead driven by structural goals such as the effective representation of zones with high velocity gradients [37]. The actual choice of mesh can be obtained through global optimization schemes [64], greedy refinement [62], or even manual interpretation [37]. Our general approach will be to locally refine the mesh in regions with sufficient model resolution values using a greedy algorithm similar to that presented by Cox [62]. Although this approach might not yield the globally optimum mesh, we can guarantee by construction that it will fulfill our resolution constraints and is also less expensive than global search techniques.

Curtis and Snieder [64] provide a compelling argument for using properties related to problem eigenspectrum and null-space components instead of ray density for determining mesh quality. Consider a 2×2 tomography problem with constant slowness cells and the two parameterizations shown

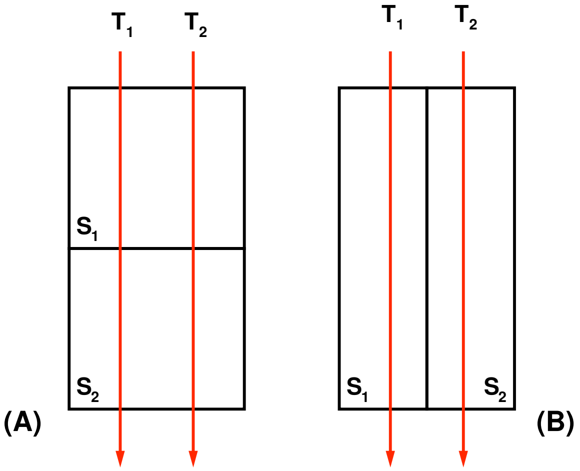

Figure 8.6: Ray density vs. Resolution : this trivial example from Curtis and Snieder [64] demonstrates that a model with a higher cell-by-cell hit-count (A) can have a larger null-space than a comparable model with a lower hit-count (B).

in figure 8.6. If ray density, the number of rays passing through a given cell, is used as a measure of mesh quality then parametrization (A) with hit counts of 2 in both cells is superior to parametrization (B). However, the tomographic system resulting from parametrization (A) has a significant null-space since any perturbation to S_1 and S_2 such that $\Delta S_1 + \Delta S_2 = 0$ has no effect on either measured traveltime. Furthermore, either cell S_1 or S_2 can be subdivided into an arbitrary number of horizontal layers without altering ray density. In parametrization (B), each model parameter is uniquely resolved even though the ray density is lower than in (A).

Curtis and Snieder [64] advocate the use of a normalized eigenspectrum flatness measure Ω of the form,

$$\Omega = \frac{1}{\lambda_1} \sum_{i=1}^{N} \lambda_i, \tag{8.15}$$

where λ_i is the ith eigenvalue of operator matrix G. This metric can conveniently be computed in $O(n^2)$ time in comparison to the full SVD of G which requires $O(n^3)$. However, the Ω-metric is intrinsically non-local since all spatial information is encoded in the right eigenvectors for which the eigenvalue spectrum only provides appropriate weighting. Non-local metrics cannot be used for greedy refinement since we have no way of deciding where to add control nodes. Curtis and Snieder [64] side-step this problem by fixing the number of unknowns *a priori* and executing an expensive global search over all possible model parameterizations. We follow the approach of Cox [62] and use the diagonal of the model resolution matrix as a local measure of mesh quality. In the following sections, we formulate the forward and inverse traveltime tomography problems in terms of unstructured trigonal meshes and propose a mesh adaptation scheme based on model resolution properties.

8.2.1 Formulation of the Forward Problem on Unstructured Meshes

Unstructured parameterizations, and trigonal meshes in particular, have several advantages over traditional Cartesian meshes for solution of both the forward and inverse problems. Unstructured meshes can be easily constructed to conform to geological interfaces or surface topography. Accurately representing curved features using a regular Cartesian mesh requires spatial oversampling which increases the cost of evaluating the forward problem. The location of interfaces or mesh density can also be used to introduce prior structural information directly into the parametrization of the inversion. Most importantly, unstructured meshes can be adapted to increase mesh quality where the quality metric might include ray coverage, model resolution, or posteriori covariance. From the perspective of the forward problem, unstructured meshes have an advantage over regular Cartesian representations when large spatial regions are homogeneous. In this situation, a small number of irregular cells can be used to effectively represent an area requiring an larger number of regular pixels. In cases where the density of unstructured control nodes/cells approaches that of a regular Cartesian mesh, the higher book-keeping costs of irregular grids makes them less attractive for the forward computation.

Several parameterization methods have been considered for use in adaptive tomography including cubic-B splines [181] [182], Voronoi polygons [37] [38], lumped Cartesian blocks [34], and trigonal meshes with constant velocity [64] and squared slowness interpolating functions [62]. Cubic-B spline representations have desirable second-order continuity properties but require numerical integration procedures to calculate the Frechet derivatives when solving the inverse problem. Voronoi polygons are attractive for adaptive inversion due to their compact support but greatly complicate the ray-tracing phase due to their variable number of cell edges. Cartesian meshes with cells grouped for the inversion process are computationally efficient for certain types of adaptation but lack the flexibility of truly unstructured parametrization, particularly for interface representation. Trigonal meshes are a useful building block for tomographic imaging due to their natural relationship to constant gradient interpolating functions. Since a gradient can be uniquely defined by three points, trigonal meshes enable local linear interpolation with continuity at cell boundaries. Although we use straight rays for our formulation, semi-analytic closed forms exist for curved ray paths in trigonal cells with constant gradients in velocity [273] or the square of slowness [57].

For our parametrization we have chosen to use a trigonal mesh where slowness varies linearly within each cell. Figure 8.7 illustrates the key parameters for a triangular cell and the associated control points. For the more general equations, both numeric and alphabetic subscripts should be treated as variables applicable to any triangle while the subscripts in the concrete examples are explicitly labeled in figure 8.7 The slowness at any point $\mathbf{r}$ can be written as a summation of linear basis functions operating on s_j, the slowness value corresponding to control node r_j,

$$s(\mathbf{r}) = \sum_{j=1}^{N} s_j \phi_j(\mathbf{r}), \tag{8.16}$$

where ϕ can be calculated using

$$\phi_j(\mathbf{r}) = \begin{cases} \frac{(\mathbf{r}-\mathbf{r_1})\times(\mathbf{r_2}-\mathbf{r_1})\cdot\mathbf{e_3}}{(\mathbf{r_j}-\mathbf{r_1})\times(\mathbf{r_2}-\mathbf{r_1})\cdot\mathbf{e_3}}, & \text{if } \mathbf{r} \text{ is inside of a triangle with vertex } \mathbf{r_j} \\ 0, & \text{otherwise} \end{cases} \tag{8.17}$$

$\mathbf{r_j}$ is the position vector of node j, $\mathbf{r_1}$ and $\mathbf{r_2}$ are the position vectors of the other two nodes of the triangle containing $\mathbf{r}$ and $\mathbf{r_j}$. $\mathbf{e_3}$ is the unit vector normal to the plane. To clarify equation 8.17 consider a location r_{k1} within triangle k_1 (see figure 8.7). We can express the slowness at r_{k1} explicitly using the indexing conventions from the our schematic as,

$$s(\mathbf{r_{k1}}) = \quad s_1 \frac{(\mathbf{r_{k1}}-\mathbf{r_2})\times(\mathbf{r_3}-\mathbf{r_2})\cdot\mathbf{e_3}}{(\mathbf{r_1}-\mathbf{r_2})\times(\mathbf{r_3}-\mathbf{r_2})\cdot\mathbf{e_3}} + s_2 \frac{(\mathbf{r_{k1}}-\mathbf{r_1})\times(\mathbf{r_3}-\mathbf{r_1})\cdot\mathbf{e_3}}{(\mathbf{r_2}-\mathbf{r_1})\times(\mathbf{r_3}-\mathbf{r_1})\cdot\mathbf{e_3}} + s_3 \frac{(\mathbf{r_{k1}}-\mathbf{r_1})\times(\mathbf{r_2}-\mathbf{r_1})\cdot\mathbf{e_3}}{(\mathbf{r_3}-\mathbf{r_1})\times(\mathbf{r_2}-\mathbf{r_1})\cdot\mathbf{e_3}} \quad . \tag{8.18}$$

Given our slowness interpolation function 8.16, we can write the tomographic matrix in terms of the ith ray and the jth nodal basis function as,

$$G_{ij} = \int_{\text{ray } i} \phi_j dl, \tag{8.19}$$

where for our case the raypath is known *a priori* as a straight segment connecting source and receiver. For this class of basis functions, the elements of G_{ij} have a simple analytical expression of the form,

$$G_{ij} = \sum_{\substack{\text{cells that share node } \mathbf{r_j} \\ \text{and are intersected by ray } i}} \|\mathbf{r_a}-\mathbf{r_b}\| \frac{(\frac{\mathbf{r_a}+\mathbf{r_b}}{2}-\mathbf{r_1})\times(\mathbf{r_2}-\mathbf{r_1})\cdot\mathbf{e_3}}{(\mathbf{r_j}-\mathbf{r_1})\times(\mathbf{r_2}-\mathbf{r_1})\cdot\mathbf{e_3}} \tag{8.20}$$

where $\mathbf{r_a}$ and $\mathbf{r_b}$ are the intersections of the raypath with the cell edges. For the concrete case of the example shown in figure 8.7, the entry for ray i and node r_3 would be a summation over contributions from cells *k₁*, *k₂*, and *k₃* and could be written explicitly as,

$$\begin{aligned} G_{ij} &= \|\mathbf{r_a}-\mathbf{r_b}\| \frac{(\frac{\mathbf{r_a}+\mathbf{r_b}}{2}-\mathbf{r_1})\times(\mathbf{r_2}-\mathbf{r_1})\cdot\mathbf{e_3}}{(\mathbf{r_3}-\mathbf{r_1})\times(\mathbf{r_2}-\mathbf{r_1})\cdot\mathbf{e_3}} + \\ &\|\mathbf{r_b}-\mathbf{r_c}\| \frac{(\frac{\mathbf{r_b}+\mathbf{r_c}}{2}-\mathbf{r_2})\times(\mathbf{r_4}-\mathbf{r_2})\cdot\mathbf{e_3}}{(\mathbf{r_3}-\mathbf{r_2})\times(\mathbf{r_4}-\mathbf{r_2})\cdot\mathbf{e_3}} + \\ &\|\mathbf{r_c}-\mathbf{r_d}\| \frac{(\frac{\mathbf{r_c}+\mathbf{r_d}}{2}-\mathbf{r_4})\times(\mathbf{r_5}-\mathbf{r_4})\cdot\mathbf{e_3}}{(\mathbf{r_3}-\mathbf{r_4})\times(\mathbf{r_5}-\mathbf{r_4})\cdot\mathbf{e_3}} \end{aligned} \tag{8.21}$$

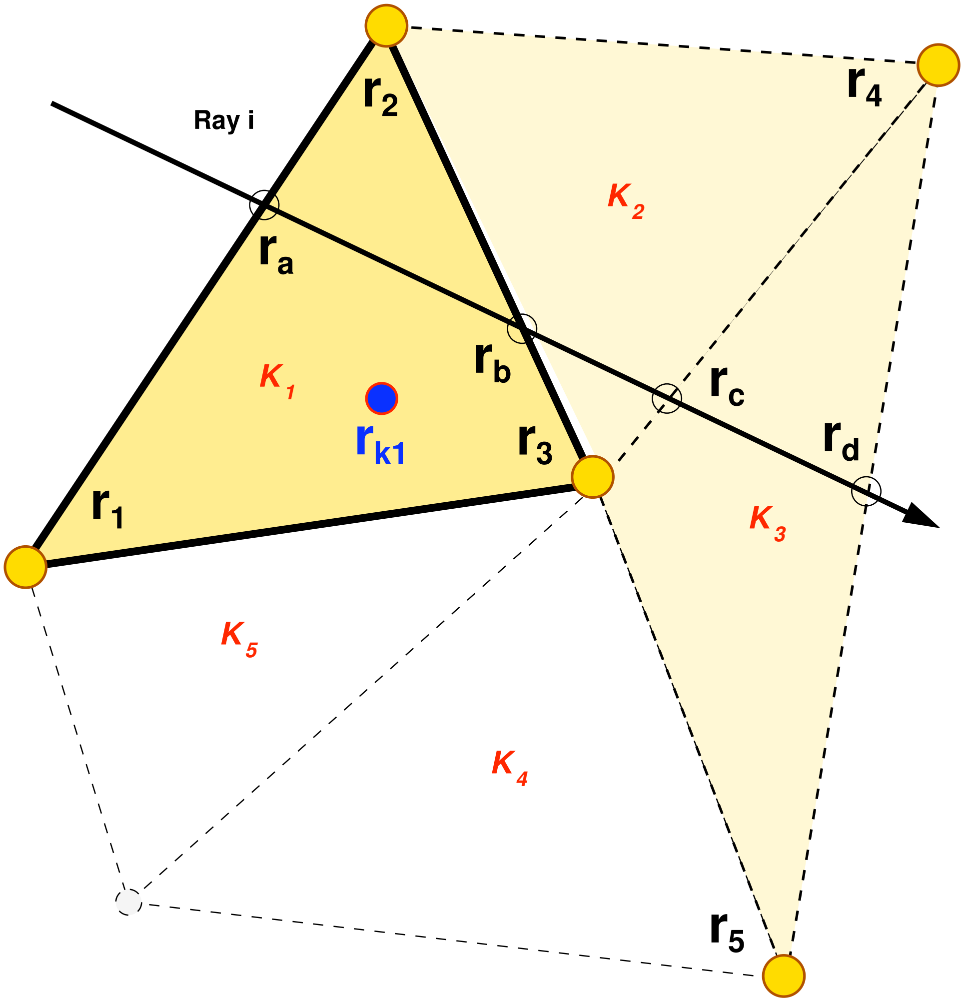

Figure 8.7: Illustration of the parameters used for the trigonal model

8.2.2 Formulation Of The Inverse Problem

If the trigonal mesh geometry is known *a priori*, we may apply the standard techniques of linear inverse theory to obtain a model estimate. In our case we use a least-squares method with an anisotropic first derivative regularization scheme to solve our tomography problem. Using the definition of G_{ij} from equation 8.20 we seek the least-squares solution of

$$\begin{bmatrix} \mathbf{G} \\ \lambda_x \mathbf{D_x} \\ \lambda_z \mathbf{D_z} \end{bmatrix} \mathbf{m} = \begin{bmatrix} \mathbf{d} \\ 0 \\ 0 \end{bmatrix} \tag{8.22}$$

which has the normal equation

$$\mathbf{m} = (\mathbf{G}^T\mathbf{G} + \lambda_x^2 \mathbf{D}_x^T \mathbf{D}_x + \lambda_z^2 \mathbf{D}_z^T \mathbf{D}_z)^{-1} \mathbf{G}^T \mathbf{d} \tag{8.23}$$

where $\mathbf{m}$ is the slowness model, $\mathbf{d}$ is the travel time vector and $\mathbf{D}_x$ and $\mathbf{D}_x$ are non-uniform first derivative operators. The coefficients λ_x and λ_z are regularization parameters in the appropriate direction. A useful secondary variable to consider is the ratio of the x and z regularization parameters, $r_\lambda = \frac{\lambda_z}{\lambda_z}$ which takes on large values as we bias $\mathbf{m}$ towards layered models.

$\mathbf{D}_x$ and $\mathbf{D}_x$ are defined in terms of a mixed notation where subscript k refers to trigonal cells while j refers to control nodes. The derivative contribution for the jth node and the kth cell is then,

$$\mathbf{D}x_{kj} = \frac{\mathbf{e_1} \times (\mathbf{r_2} - \mathbf{r_1}) \cdot \mathbf{e_3}}{(\mathbf{r_j} - \mathbf{r_1}) \times (\mathbf{r_2} - \mathbf{r_1}) \cdot \mathbf{e_3}} \tag{8.24}$$

$$\mathbf{D}z_{kj} = \frac{\mathbf{e_2} \times (\mathbf{r_2} - \mathbf{r_1}) \cdot \mathbf{e_3}}{(\mathbf{r_j} - \mathbf{r_1}) \times (\mathbf{r_2} - \mathbf{r_1}) \cdot \mathbf{e_3}} \tag{8.25}$$

where e and r are the appropriate unit normal and nodal location vectors respectively,

$$\mathbf{r} = \begin{bmatrix} x & z & 0 \end{bmatrix}^T \tag{8.26}$$

$$\mathbf{e_1} = \begin{bmatrix} 1 & 0 & 0 \end{bmatrix}^T \tag{8.27}$$

$$\mathbf{e_2} = \begin{bmatrix} 0 & 1 & 0 \end{bmatrix}^T \tag{8.28}$$

$$\mathbf{e_3} = \begin{bmatrix} 0 & 0 & 1 \end{bmatrix}^T \tag{8.29}$$

We typically use the iterative LSQR algorithm of Paige and Saunders [211] to solve equation 8.22. Constant values for λ_x and λ_z are typically chosen by observation since we do not have a prior estimate of data variance. Application of the GCV technique [265] for determination of λ values was attempted on several datasets but failed due to the existence of very broad minima on the GCV curve. When applying the GCV method, we assumed a regularization anisotropy ratio, r_λ, and performed the 1-D search in terms of λ_z values with λ_x defined implicitly. Additionally, we know that one component of error within our experimental traveltime data consists of correlated non-Gaussian noise due to picking bias. Since errors of this type break GCVs assumption of Gaussian noise with a fixed variance, this correlated noise is interpreted as a model component and the resulting GCV value for λ is often unrealistically low.

8.2.3 Mesh Refinement Algorithm

With an approach to tomographic reconstruction on arbitrary trigonal meshes established, we will now consider the problem of automatically generating parameterizations with the appropriate resolution properties. Several classes of mesh refinement algorithms exist, ranging from manual guidance of the refinement process [38] to global searchers for an optimal mesh [64]. These techniques are distinguished by the geometric form used for the parametrization (triangles, arbitrary polygons, etc.), the metric chosen for evaluating mesh quality, and the search or construction method utilized for generating the final mesh.

Bohm and Vesnaver [38] advocate an interpretive approach to mesh adaptation guided by prior knowledge of structure and graphical measures of null space properties. However, the inclusion of manual interpretation steps is both time consuming for large problems and generates a human bias for the geometry in the final mesh. They parametrize the forward and inverse problem in terms of constant velocity Voronoi cells. Another approach examined by Curtis and Snieder [64], chooses a fixed number of control nodes and uses a global non-linear optimization scheme to determine the best triangulation defined by these control points. They use a quality metric based on the flatness of the eigenvalue spectrum which does not require the full SVD of the operator matrix. We have found that Curtis' approach, while conceptually attractive, is not feasible for significant problems due to the large number of iterations required for the global search to converge. They parametrized the forward and inverse problem in terms of constant velocity triangles and used straight rays. A related method proposed by Michelini [181] uses the gradient of data misfit with respect to perturbations in the parametrization to adapt the position of velocity model control points. While Michelini's method converges for simple cases, it is easily trapped by local minimum in parametrization space and additionally is not posed in terms of a mesh quality metric.

We examined several greedy algorithms for mesh generation. These algorithms sequentially add control vertices until the resolution properties of the problem degrade below a threshold value. The technique is similar to that presented by Cox [62] with a new scheme for choosing the location of added nodes. In contrast to the Curtis/Snieder search methodology, the mesh generated by greedy algorithms fits a quality constraint by construction and there is no guarantee that the mesh is globally optimal. Refinement and coarsening techniques are two possible approaches to greedy mesh adaptation. Refinement techniques begin with a coarse mesh and iteratively add points until a threshold criterion is met whereas coarsening techniques begin with a fine mesh and remove low quality nodes until the quality metric is fulfilled. Our technique is a combination of the two approaches. We start with a coarse mesh and sequentially add nodes until no allowable refinements exist. We then prune remaining nodes from the control point set which do not fulfill the resolution criterion. The primary differences between our approach and the technique outlined by Cox [62] are the way in which nodes are added during the refinement process and the rules used for halting mesh adaptation. The general algorithm is outlined in the following pseudo-code,

```
1. Start with a coarse mesh enclosing the S/R array
2. While valid refinements exist
    (a) Compute Delaunay triangulation for the control point set
    (b) Compute tomography kernel for the triangulation
    (c) Compute model resolution matrix
    (d) If even iteration
        • Collect all edges where
            – both endpoints satisfy the resolution criterion ($R_{ii} > R_c$)
            – the edge satisfy the minimum length requirement ($L_{12} > L_c$)
        • Choose $n$ longest valid edges - add bisection points to the control point set
    (e) If odd iteration
        • Collect triangles where
            – all nodes satisfy the resolution criterion ($R_{ii} > R_c$)
            – the triangle satisfies the minimum area requirement ($A_{123} > A_c$)
        • Choose $n$ largest valid triangles - add centroids to the control point set.
3. While coarsening locations exist
    (a) Compute Delaunay triangulation for the control point set
    (b) Compute tomography kernel for the triangulation
    (c) Compute model resolution matrix
    (d) Scan nodes which do not fulfill the resolution criterion
    (e) Remove $m$ worst nodes
```

Figure 8.8 shows in visual form the core refinement loop. At any given step in the refinement process we begin with a set of control points and compute the associated trigonal mesh. The resolution properties of the mesh are evaluated and the location for the next node is chosen using

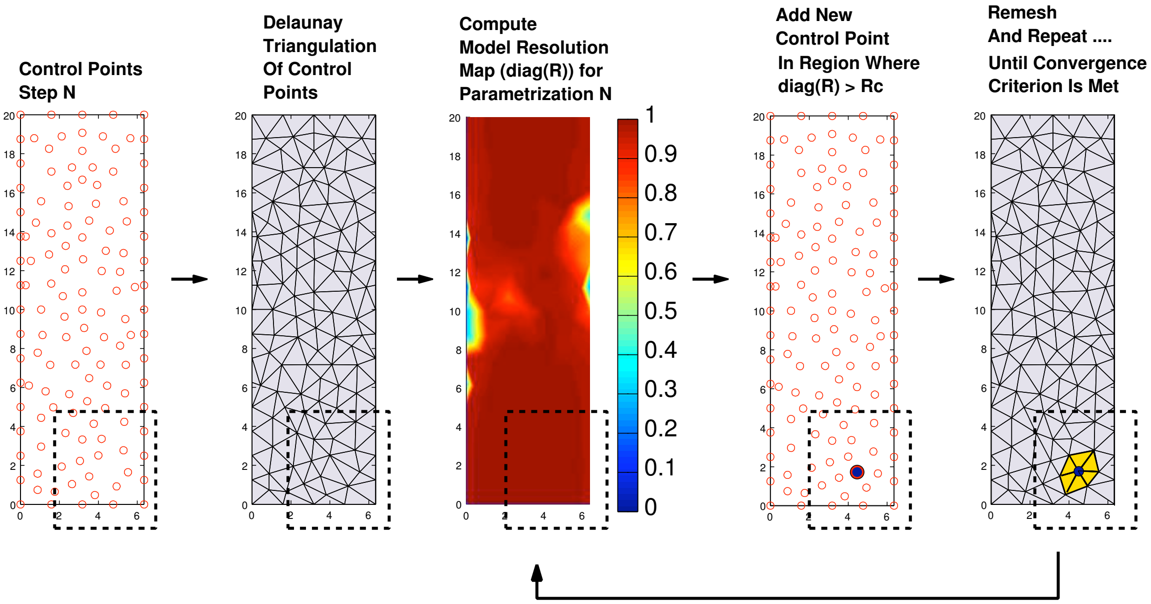

Figure 8.8: A schematic view of the mesh refinement process : Starting with a set of control points at iteration n we calculate a Delaunay triangulation, compute the associated model resolution metric, add another control point and repeat this process until no valid updates exist.

a rule set which we will outline. As mentioned previously, this process is repeated until no valid update locations are available.

One underlying component in the algorithm is the conversion between the set of control points and their associated trigonal mesh. Since a given set of points can have a large number of possible triangulations, we choose the Delaunay triangulation as a unique mapping between the two structures. The Delaunay triangulation, the dual of the Voronoi diagram, is straightforward to compute and is guaranteed to be locally optimum with respect to minimum angle in the mesh [77]. We use J. Shewchuck's Delaunay triangulation code, *Triangle*, [241] to generate our mesh. In addition to providing neighbor information *Triangle* can also accommodate constraints on edges which must be included in the triangulation. This would allow prior information on lithologic boundaries to be explicitly included in the triangulation.

We use a point-by-point estimate of the diagonal elements of R, the model resolution matrix, as the central component of our mesh quality metric. The goal in our mesh refinement process is a parametrization where each point is as close as possible to a threshold resolution value, R_c, with the hard constraint that $R_{ii} \geq R_c$. This metric maximizes the spatial density of control points in a given region as long as all unknowns are resolved to within R_c. A possible improvement to our metric might use the off-diagonal components of R to provide a threshold in terms of locality i.e. exploit a Backus-Gilbert style norm.

Computing the mesh quality metric is the most time consuming component of the adaptive refinement algorithm since R must be calculated. For problems of small dimensions, the dense SVD can be used for the calculation of R. The examples described in this chapter have dimensions on the

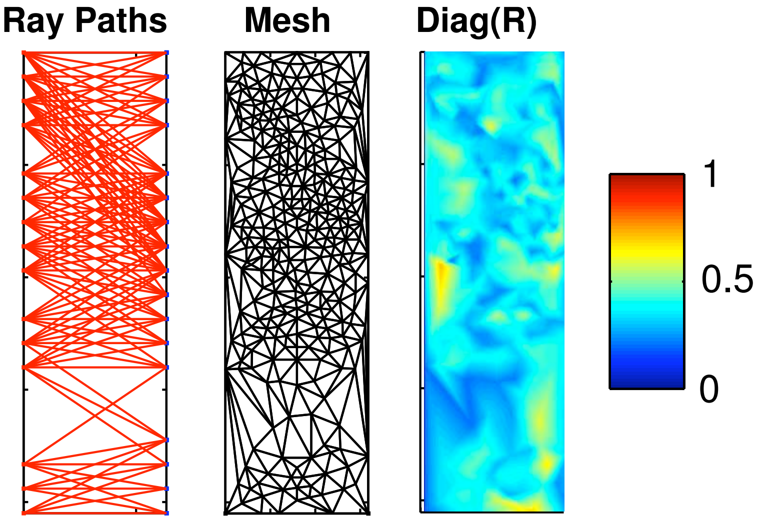

Figure 8.9: An example of mesh refinement and the corresponding values for $diag(R)$: The left most panel shows a crosswell S/R/ geometry and a set of raypaths. The center panel shows one possible refined mesh with the right panel providing a map of $diag(R)$ for this particular parametrization.

order of 5000 data and 1000 to 4000 unknowns. Following Menke [179], we use the SVD factorization to decompose the operator matrix, G, into the matrix product,

$$G \;=\; U\,\Lambda\,V^T \;=\; U_p\,\Lambda_p\,V_p^T \tag{8.30}$$

where U is an $N \times N$ matrix of eigenvectors spanning the data space, Λ is the diagonal $M \times N$ eigenvalue matrix, and V is the $M \times M$ model eigenvector matrix. The subscript p denotes that the SVD is truncated at some small index. In this case the truncated SVD model estimate is $m_{est} \;=\; V_p\,\Lambda_p^{-1}\,U_p^T\,d$ and R can then be written as,

$$R \;=\; G^{-g}\,G \;=\; \left[V_p\,\Lambda_p^{-1}\,U_p^T\right]\,\left[U_p\,\Lambda_p V_p^T\right] \;=\; V_p\,V_p^T. \tag{8.31}$$

The choice of the truncation point, p, is taken as a prior parameter; we tend to choose a large p value to approximate the unregularized problem. Figure 8.9 provides a visual example of $diag(R)$ for a set of crosswell ray paths and a refined mesh with a quality constraint of $R_c = 0.1$.

Considering the N^3 asymptotic complexity of the dense SVD calculation, iterative algorithms that sequentially calculate elements of R seem necessary for large scale problems. Cox [62] uses an adaptation of the LSQR algorithm [211] to calculate components of R without having to explicitly form G while Fomel [96] uses a similar modification to the traditional conjugate gradient method. In both cases only the action of G and G^T on m are required for implementation.

The primary difference between our approach and the method outlined by Cox [62] is the fashion in which points are added during the refinement process. At each iteration, the Cox algorithm adds control nodes at the centroid of all triangles where the R_{ii} values of the bounding nodes are greater than R_c. Section A of figure 8.10 shows a single step of centroid refinement and the result of re-meshing with the additional control points. Within this refinement scheme no points will ever be added to the boundary of the domain resulting in long skinny triangles at the edge of the parametrization if too coarse a starting grid is chosen. This effect is particularly problematic in crosswell scenarios where a paucity of points at the domain boundary make the addition of prior information from well logs difficult.

A second possible approach is to add points so as to bisect triangle edges where both bounding nodes fulfill the R_c criterion. This approach allows control nodes to be added on the domain boundary resulting in a parametrization which is not biased towards refinement on the interior. Section B of figure 8.10 depicts an edge bisection refinement step. The one failing of the edge bisection update is the generation of preferential alignment of triangles in the end model.

We alternate between the two updating schemes at each iteration to produce meshes without preferential point distribution or preferential triangle alignment. Figure 8.11 shows the result of centroid refinement (A), edge bisection refinement (B), and the alternating scheme (C).

In addition to the R_c criterion, we also apply a size constraint to the point update process. Triangles below a minimum area and edges below a minimum length are not refined. The motivation for the size constraint is to avoid parameterizations which include many triangles far below the resolving power of finite bandwidth field data. In this case, resolving power refers to the smallest feature which can be successfully imaged using the full waveform and not to the elements of R which are based on our ray-theoretic forward operator G. Since our inversion scheme is based on ray-theory, an infinite bandwidth approximation to the wave equation, no notion of wave-theoretic resolution is present in the actual tomography scheme. We typically choose minimum edge lengths on the order of $\lambda/2$. This limit is not intended to be a true estimate of the wave-theoretic resolving power of the dataset, but merely a heuristic lower bound to prevent high levels of mesh refinement. In reality, spatial resolution in traveltime transmission tomography is limited by both λ and the experimental geometry and is variable within a given imaging plane. Although there is no closed form for the spatially varying wave-theoretic resolution, Williamson and Worthington [278] present a rough estimate of the maximum resolving power (r_{min}) of transmission data using Rytov theory,

$$r_{min} \sim \sqrt{L\,\lambda} \tag{8.32}$$

where L is the length of the transmission path. r_{min} is greater than $\lambda/2$ if $L > \lambda/4$, as is the case for all of our experiments. Reiterating the previous discussion, the size constraint is not meant to replace a more complete treatment of resolution but serves simply as a check against refinement far below a reasonable length scale.

Another relevant aspect of the updating scheme is choosing the number of control points (m) to add or remove at each iteration of refinement. For large values of m, the refinement algorithm converges quickly with few required calculations of $diag(R)$. However, we have found that adding a moderate number of points at each iteration generates meshes with a slightly higher quality, possibly because the sequential updating of R allows better choice of point locations.

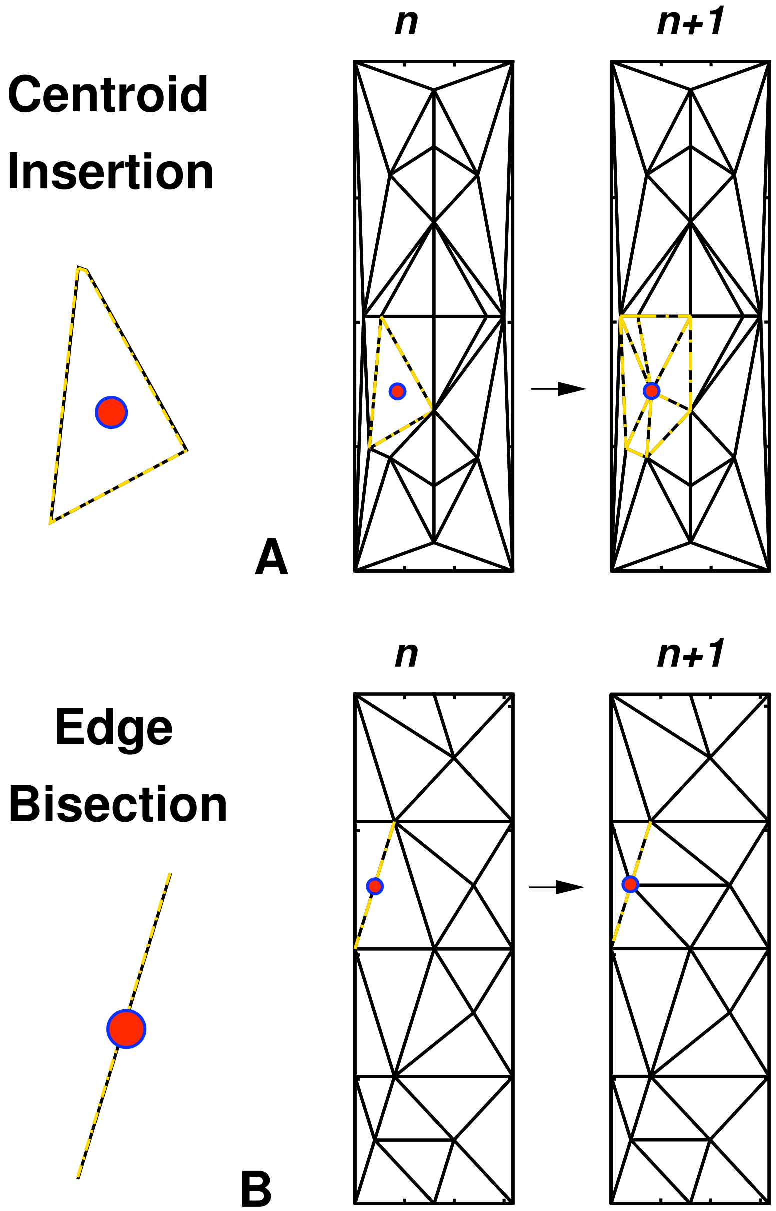

Figure 8.10: Two control point updating schemes. (A) centroid refinement, of Cox [62] (B) edge bisection refinement.

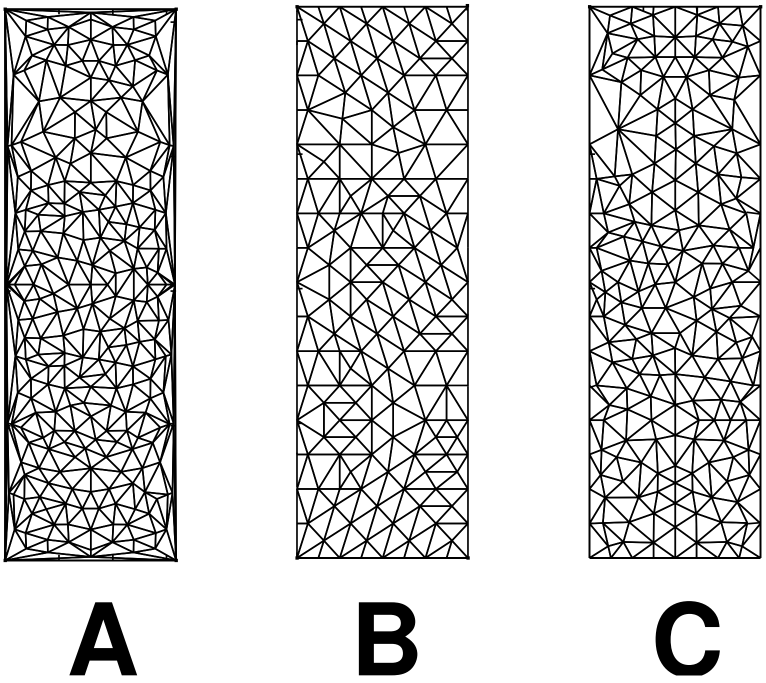

Figure 8.11: Meshes generated by the three insertion algorithms. (A) centroid refinement of Cox [62], (B) edge bisection refinement, (C) alternating update method.

The coarsening stage is handled in a similar fashion to the mesh refinement. If a given node has a $diag(R_{ii})$ value less than R_c, that node is a candidate to be removed during the coarsening phase. At each iteration of coarsening we remove n poorly resolved nodes and then recompute the resolution metric. Since only n nodes are removed at each step, some freedom exists as to which part of the model nodes are initially removed from. We use a heuristic distance measure to preferentially cull points from the domain interior in early iterations, however we have found that final mesh is generally insensitive to the choice of removal order. After the mesh refinement and coarsening steps are complete, the inversion algorithm described in section 2 is applied to generate the final tomogram.

8.3 A Synthetic Application

Our refinement and inversion algorithm was first tested on a synthetic crosswell dataset with a realistic irregular source/receiver configuration. Panels (a) and (b) of Figure 8.12 depict the true velocity model used for the synthetic test and the ray path set respectively. The sparse ray geometry has a spatially variable angular aperture, a zero transmission zone between 6 and 7 m depth, and several missing source and receiver locations. Synthetic traveltime data were generated using a finely discretized regular mesh and the same straight ray algorithm described in the previous sections. Gaussian noise with a 2% magnitude was added to the synthetic traveltimes. Some features in the true velocity model will not be visible in any tomogram given the sparse source/receiver geometry.

In these cases, particularly the coverage gap between 6 and 7 meters depth, the most we can hope for is a clean interpolation between bounding slowness values.

Three tomograms were calculated for this dataset, one adaptive mesh inversion and two regular mesh inversions with different Δx and Δz spacing values (see figure 8.12). Panel (c) depicts the adaptive mesh generated by the algorithm described previously. For the adaptive meshing phase, the resolution threshold was set to a low value of 0.1 and a minimum edge length of $0.3\,m$ was used. The regular mesh inversions were performed on both fine and coarse parameterizations. Panel (e) depicts the tomogram for a 20x75 sample regular mesh while Panel (f) shows the equivalent results for a 10x40 regular mesh. The number of unknowns in the inversions were 744, 1500, and 400 for the adaptive, fine regular, and coarse regular meshes respectively. For both regular mesh inversions, control points with no constraining rays were discarded. When these control points were included in the inversion, the results were not usable due to overwhelming image artifacts. As can be seen in panel (c) of figure 8.12, zones with the densest ray coverage and the highest model resolution values are represented with a fine parametrization while zones with poor coverage are appropriately coarsened. As can be seen in the tomograms, the adaptive scheme both gracefully handles the variations in ray coverage and does a better job of recovering velocity boundaries. Improvements are visible in the small high velocity lens at 3.5 m depth and the high velocity feature at the bottom of the model.

Figure 8.13 shows ray-hit and $diag(R)$ maps for the same three meshes. As can be seen from panels (a) and (d), although the adaptive mesh fulfills our resolution constraints, neither ray hits nor $diag(R)$ values are uniform. Since the refinement and sparsening operations are intrinsically discrete, the greedy scheme does not have sufficient flexibility to generate parameterizations where the quality metrics of triangles are smoothly distributed. One possible remedy to this problem is the use of a second round of mesh optimization which operates by perturbing nodal locations rather than adding or subtracting nodes.

8.4 Application To A Multi-offset Crosswell Profile

The dataset which drove the development of our adaptive tomography approach was the large multi-well crosswell seismic survey acquired the Pinellas site. As discussed in previous chapters, the seismic dataset was acquired as a sequential curtain of seven crosswell surveys extending from a region of the site without free-phase contaminants to a zone where DNAPLs were observed from borehole water sampling. By using a sensitive 24 level hydrophone string and a small piezoelectric source, we were able to acquire data with a center frequency in excess of 5 kHz. One of our processing goals was to jointly invert the entire dataset to allow more effective interpretation of lateral velocity variations.

The most challenging aspect of the Pinellas seismic dataset was a zone of high seismic attenuation which prevented us from picking first arrivals in a large region of the site. The resulting source/receiver geometry was highly irregular with differences in both vertical coverage and angular aperture between consecutive well pairs. Figure 8.14 shows the ray coverage map, the adaptive mesh

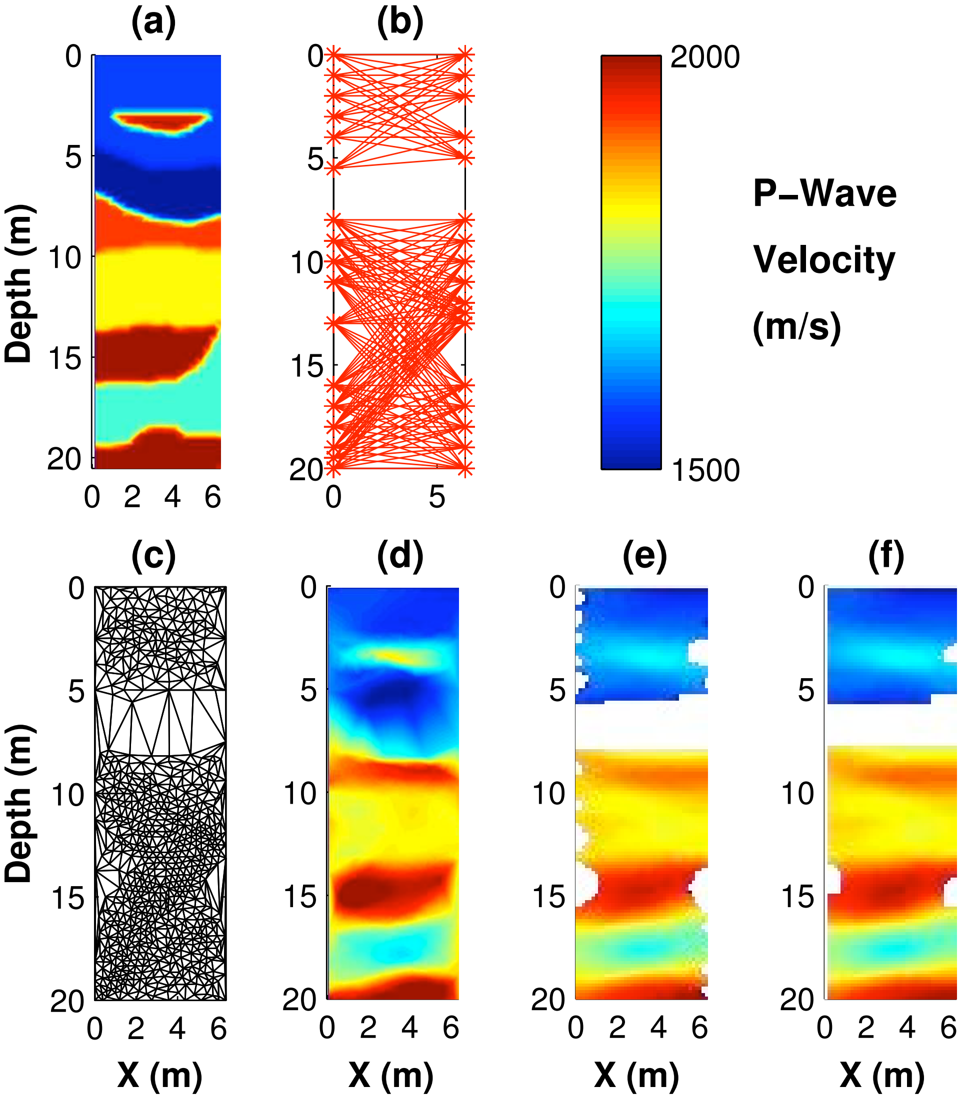

Figure 8.12: A synthetic example of our adaptive tomography scheme : (a) the true velocity model, (b) the ray paths used for the inversion, (c) the optimal mesh obtained from our greedy updating scheme, (d) the tomogram calculated using mesh c, (e) the tomogram calculated using a fine (20x75) regular mesh, (f) the tomogram calculated using a coarse (10x40) regular mesh. The white regions in (e) and (f) correspond to parameters which were not inverted for.

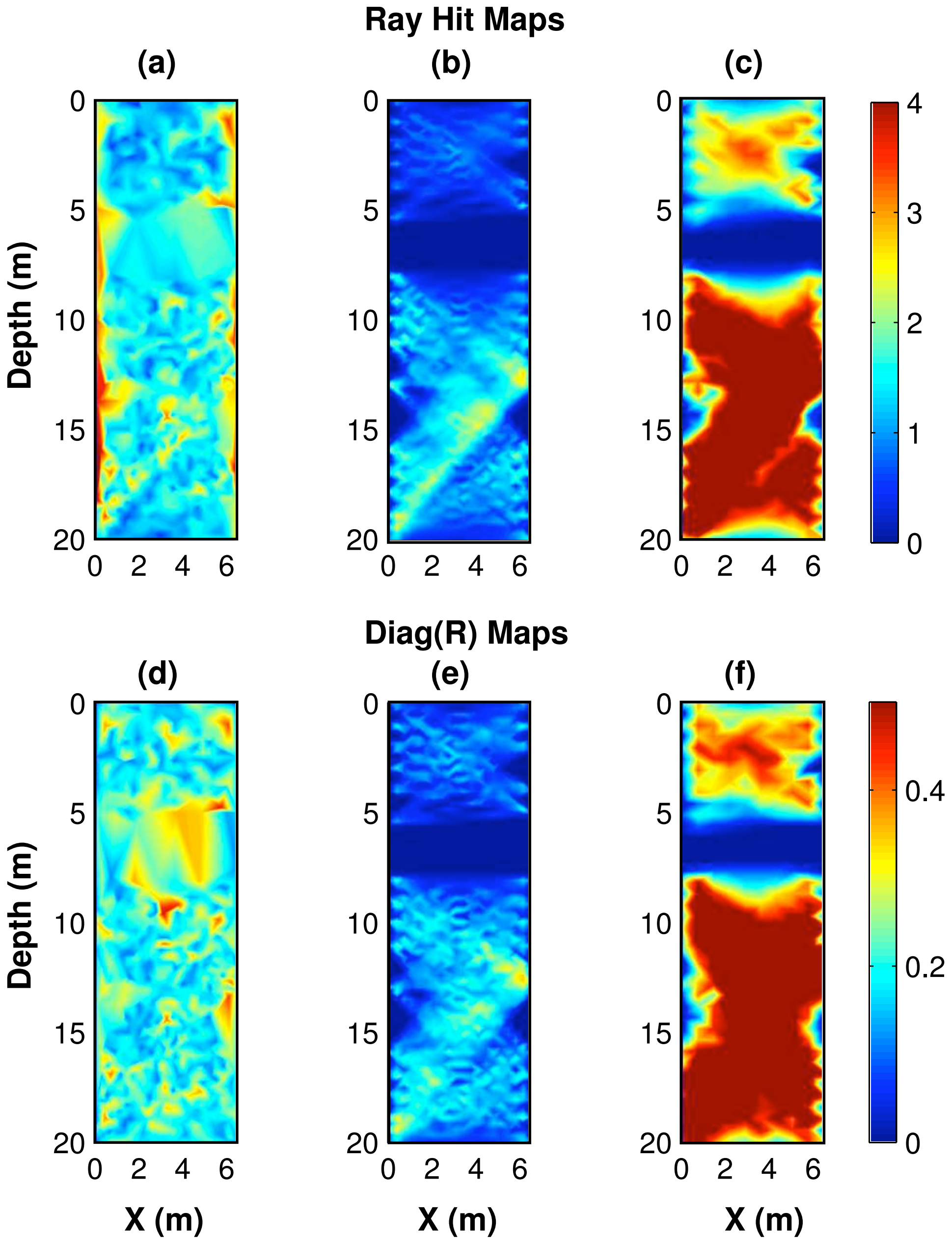

Figure 8.13: Maps of ray coverage and resolution properties for the synthetic example : the top row shows the ray hit maps for the adaptive (a), fine regular mesh (b), and coarse regular mesh (c) with a clip of 4 hits applied. The bottom row shows $diag(R)$ for the same three cases with a clip of 0.5.

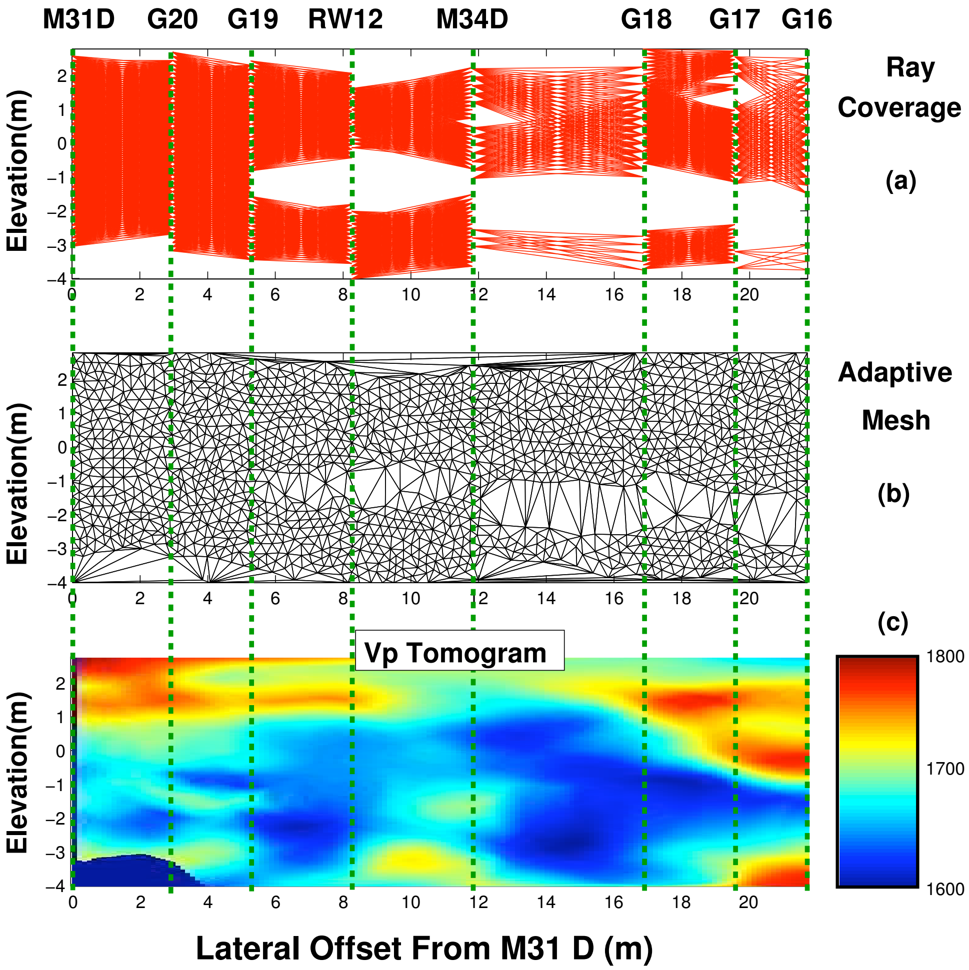

Figure 8.14: Multiwell seismic tomography results from the Pinellas site : the M31D-G16 profile

generated by our algorithm, and the resulting V_p tomogram. In particular, the M34D-G18 profile had very limited angular aperture, large regions without ray coverage, and low S/N in comparison to the M31D-G19 and G19-G20 sections. For the adaptive meshing step, the resolution threshold was set to a relatively low value of 0.1 and a minimum edge length of 0.2 m was used to prevent meshing below $\lambda/2$.

Visible in panel (b) of Figure 8.14, our mesh generation algorithm avoided overparametrization of the low coverage region and provided a velocity estimate in these zones consistent with data recorded above and below. In regions with sufficient coverage, the mesh is refined down to our prespecified $\lambda/2$ limit. Like the synthetic examples, the values for the $diag(R)$ metric are not uniform across the tomogram with the worst values present in the lower regions with poor angular aperture including the lower portions of the M34D-G18 and G17-G16 sections. Since triangles are not aligned at profile boundaries, some information from the adjacent wells is used in poor coverage regions; in the case of G17-G16, the dense coverage on the boundary with G17 constrains the region between -2 and -3 m elevation.

The observed velocity variations for this dataset were on the order of 200 m/s or approximately 11 % of the peak velocity; the tomogram would probably benefit somewhat from the inclusion of ray curvature.

8.5 Conclusion And Future Work

Our current adaptive tomography strategy is limited to relatively small problems with model and data dimensions of less than 10^4, more than sufficient for the datasets acquired at Pinellas but trivial in comparison to large crosswell or VSP surveys with dimensions on the order of 10^6 or 3D reflection surveys with dimensions upward of 10^8. This scaling problem is largely due to our computation of the SVD of the operator matrix G at each of several hundred refinement steps. Each SVD has an asymptotic cost of $O(n^3)$ in both memory and computational time which makes scaling the algorithm to larger problems very difficult. As mentioned previously, this problem could be partially eliminated through use of an iterative scheme for computing elements of R as described by Fomel *et al.* [96] and Cox [62]. Even with an iterative scheme in place, the cost of computing even a few elements of R is still expensive for large problems. Another possible alternative is to develop a cheap mesh quality heuristic based on a combination of ray density and local angular coverage. In this case, angular coverage might provide a secondary constraint to help prevent excessive refinement in cases like geometry (A) in Curtis and Snieder's double-cell scenario [64] (see figure 8.6).

A second limitation of the current scheme is our inability to include ray curvature and therefore handle the full non-linear problem. While we have written several codes capable of calculating of curved raypaths on regular Cartesian grids, the extension of these techniques to unstructured trigonal meshes is somewhat more complex. We are in the process of developing raytracing schemes based on the semi-analytic closed form for rays within trigonal cells with a constant gradient of slowness squared [57] and Vinje *et al.*'s wavefront construction algorithm [263]. Even after completion of a curved ray tracer for trigonal or tetrahedral meshes, we still must contend with the problem of handling mesh adaptation at each gradient step in the non-linear problem; modification of ray geometry during convergence will force some iterative re-adaptation of the mesh. One approach to solving this problem would be to only add a small number of additional control nodes at each step in the non-linear problem, a strategy analogous to methods which successively relax model-space constraints such as Nemeth *et al.*'s dynamic smoothing technique [203].

In this chapter, we have succeeded in developing an adaptive traveltime tomography algorithm based on greedy mesh refinement. Our formulation provides formal guarantees on model resolution and can be easily applied to problems with irregular S/R geometries. We have improved upon previous adaptation schemes by incorporating a new mesh refinement operator which reduces the number of high aspect ratio triangles. Using a complex synthetic test case, we demonstrated that our algorithm both improves tomogram quality in regions of good coverage and provides consistent property estimates in regions with insufficient data. We have also successfully inverted a substantial field dataset, the M31D-G16 multi-offset crosswell seismic profile. In the next chapter, we apply these same techniques to our extensive collection of crosswell surveys acquired at the Pinellas NE site.

Chapter 9

Tomographic Characterization Of The Pinellas NE Site

High-resolution tomographic imaging techniques are a powerful tool for obtaining semi-quantitative estimates of near-surface properties suitable for understanding site lithology and hydrogeology [129] [128] [67]. The purpose of our geophysical investigation at the Pinellas NE site was to evaluate the applicability of high-resolution tomograms from a combination of crosswell radar and seismic methods for the detection of DNAPLs *in situ*. We also hoped to use tomographic images to aid in the development of a more comprehensive model of site lithology relevant to contaminant flow processes. As discussed in previous chapters, a chain of crosswell surveys was acquired stretching from a zone of the site with confirmed DNAPL contamination, in the vicinity of wells RW6 and M17D, to a region with low aqueous contaminant levels near wells M31D and G20 (see chapter 3). This chapter details our processing of the NE site geophysical profiles using adaptively parametrized traveltime tomography and our integrated interpretation of the resulting images, a process aided by laboratory petrophysical measurements conducted on site core samples. We examine in detail two regions, one zone with high seismic attenuation and a second partially coincident region of high radar velocities, both of which may be indicative of partial gas or NAPL saturation. We explore the possibility of biogenic gas generation in more detail and propose a consistent site model which includes partial gas saturation as a possible biogeophysical signature of active methanogenesis. Although this hypothesis is by no means proven, it should provide an interesting starting point for future environmental investigations using radar and seismic imaging techniques.

9.1 Imaging Target And Expected Geophysical Signature

As discussed in chapter 4, DNAPLs have physical properties that are distinct from those of water, including a high density, low dielectric constant, and a low P-wave velocity. In the same chapter, we estimated that the mixed DNAPL phase present at the Pinellas NE site has a dielectric constant of ≈ 2.7, a P-wave velocity of ≈ 1341 m/s and a measured density of 1030 kg/m^3. Chapters 5 and 6 describe a series of laboratory experiments carried out on core material collected at Pinellas, the results of which suggest that the geophysical signature of DNAPLs at Pinellas would include measurable reductions in dielectric constant with a small decrease in P-wave velocity and a moderate increase in P-wave attenuation. Considering a porosity range of 0.3 to 0.5 we would expect that 40% saturation with our characteristic DNAPL would generate an increase in measured V_{em} between 26% and 36% with reductions in V_p on the order of 3% to 8% in addition to an undetermined increase in $1/Q_p$. Based on Parker *et al.*'s excellent review of DNAPL distributions *in situ* [213] we expect that the peak DNAPL saturation which we might encounter would be approximately 50% with significantly lower levels if only residual material is present. Since the results of multiphase flow modeling [149] [150] [151], controlled field tests [152], and direct fluid sampling at depth [213] suggest that the highest DNAPL saturations occur at permeability transitions, our imaging target was the contact region between the upper surficial aquifer and the less permeable lower surficial aquifer located at an absolute elevation of -1.5 and -2.5 m. We had also hoped to target the transition zone between the lower surficial aquifer and the Hawthorn group but drilling limitations prevented us from acquiring data with sufficient coverage of this region. Figures 2.7 and 3.2 from chapters 2 and 3 provide approximate lithology columns for the site with the target units marked in blue.

The signature of DNAPLs described above is by no means geophysically unique and accordingly we must carefully consider other processes which might produce similar petrophysical variations. Partial gas saturation in particular can cause a reduction in seismic velocity and an increase in radar velocity, the same trends we expect with DNAPL saturation. Since the dielectric constant of gas is approximately 1, a small quantity of gas can generate a change in bulk dielectric properties equivalent to a larger volume of DNAPL. Gas also has a much higher compressibility than DNAPLs; less than 2% volumetric gas saturation can generate significant changes in V_p. As we described in our discussion of joint petrophysical properties in chapter 7, we expect that seismic attenuation is one possible way to discriminate between partial gas saturation and DNAPLs *in situ* since very small amounts of gas can produce substantial seismic attenuation through a variety of mechanisms including patch equilibration and scattering phenomenon. Since our investigation is restricted to the saturated zone, if we appeal to partial gas saturation as the cause of a geophysical signature we must provide a plausible argument for how significant quantities of gas could be entrained or generated at depth. Variations in seismic and radar response due to changes in lithology are always present but we expect somewhat different petrophysical trends from these processes. Increasing clay content tends to decrease radar velocity (increase bulk dielectric constant) unlike either gas or DNAPLs. While decreasing porosity can produce an increase in radar velocity, we would also expect an increase in seismic velocity. Additionally, of the 20 porosity measurements available from cores (see chapter 6 and Fernandez [172]) none are below 0.31 which provides an upper bound for the effects of porosity on radar response. Figures 7.5 and 7.6 in chapter 7 depict some of the possible trade-offs between DNAPL saturation, gas saturation, and variations in porosity.

To increase our chance of identifying a DNAPL pool, we acquired a chain of surveys stretching from a region with confirmed DNAPL contamination in the vicinity of wells RW6 and M17D, to a region with low aqueous contaminant levels near wells M31D and G20. Figure 9.1 shows a site map with the crosswell profiles used for our analysis marked with red and green dashed lines. Note that the one DNAPL sample from this region analyzed for chemical composition was extracted from well RW06 which is closest to survey well G12. Aqueous TCE concentrations at M31D have historically been very low at less than 5 μg/L while dissolved values along the profile increase by several orders of magnitude, to 59 μg/L at RW12, 500 μg/L at M34D, and 21000 μg/L at M17D. We had hoped to invert the entire profile as one dataset but we were unable to acquire either seismic or radar data across the long lateral offset between wells G15 and G12. We were also unable to acquire radar data from wells M31D and RW12 due to metallic casing. Even with these restrictions, our crosswell profiles provide a high-resolution cross-sectional view of this region with effective λ values of between 30 cm (seismic) and 60 cm (radar). Chapter 3 provides the full details of our field acquisition effort.

9.1.1 Data Characteristics

The quality of the collected crosswell seismic and radar data was generally good with the exception of a large zone of high seismic attenuation observed extending across a section of the site. Chapter 3 includes example shot gathers from both the seismic (3.10) and radar (3.13) surveys. Figure 9.2 shows a sequence of true amplitude zero-offset seismic gathers acquired across the M31D-G16 profile in addition to secondary information on lithology, well offsets, and aqueous contaminant levels. As can be seen from the section, data quality steadily decreases when moving away from the M31D-G20 survey with substantial zones of pore transmission extending from G19 to G16. The zone of maximum signal loss seems to be located directly above the upper/lower surficial aquifer contact ($\approx$ -1 to -2 m elevation) but varies in vertical extent across the site. One common feature is a recovery in signal strength within the deeper clay-rich soils present in the lower surficial aquifer. Although the high attenuation region is clearly indicative of some unusual process, it also encompasses a large section of our target region and prevents us from quantitative evaluation of V_p and Q_p within these zones.

While picking the Pinellas NE crosswell datasets several problems were encountered. In the seismic datasets, we were plagued by large regions with no pickable first-arrival. In true amplitude these traces were effectively blank; boosting the gain sufficiently often revealed noise with some superimposed packets of very low and very high frequency waves. Traces which were clearly in the zero signal regions were not picked and removed from the tomography dataset. The ambiguity arose when choosing the point at which traces should be discarded. Typically the signal died out over 4-5 traces with changing character in the waveform and sharply decreasing apparent velocity. We tended to take a conservative approach and discarded waveforms where the phase in the first arriving wavelet changed enough to make consistent picking difficult. From experimentation we found that more speculative picking strategies often introduced errors which were difficult to recover from in

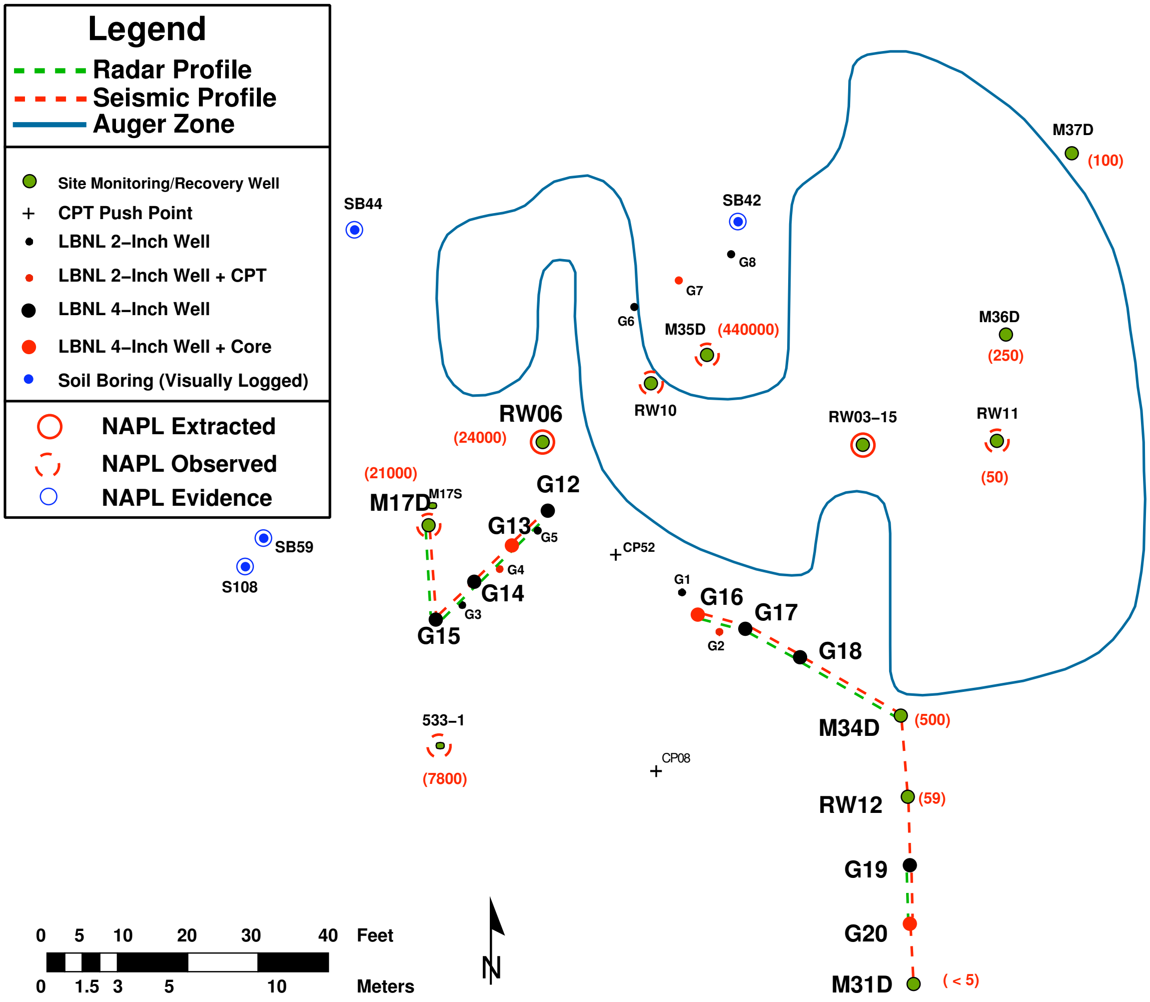

Figure 9.1: Map-view of the Pinellas geophysical study area with tomography profiles : The tomography profiles (shown in dashed red and green) are the subset used for analysis in this chapter. Red numbers near well labels indicate aqueous TCE concentrations in μg/L as recorded in April of 2002.

the tomographic imaging step and the small increase in angular aperture was of minimal benefit. Another problem in some seismic datasets were phase reversals in areas of excellent S/N. In these situations we picked true first breaks in both cases (up or down) with added uncertainty in the region where the phase of the first arrival was actively changing in character. More information concerning data preprocessing, QC, and picking methods is included in appendix A.

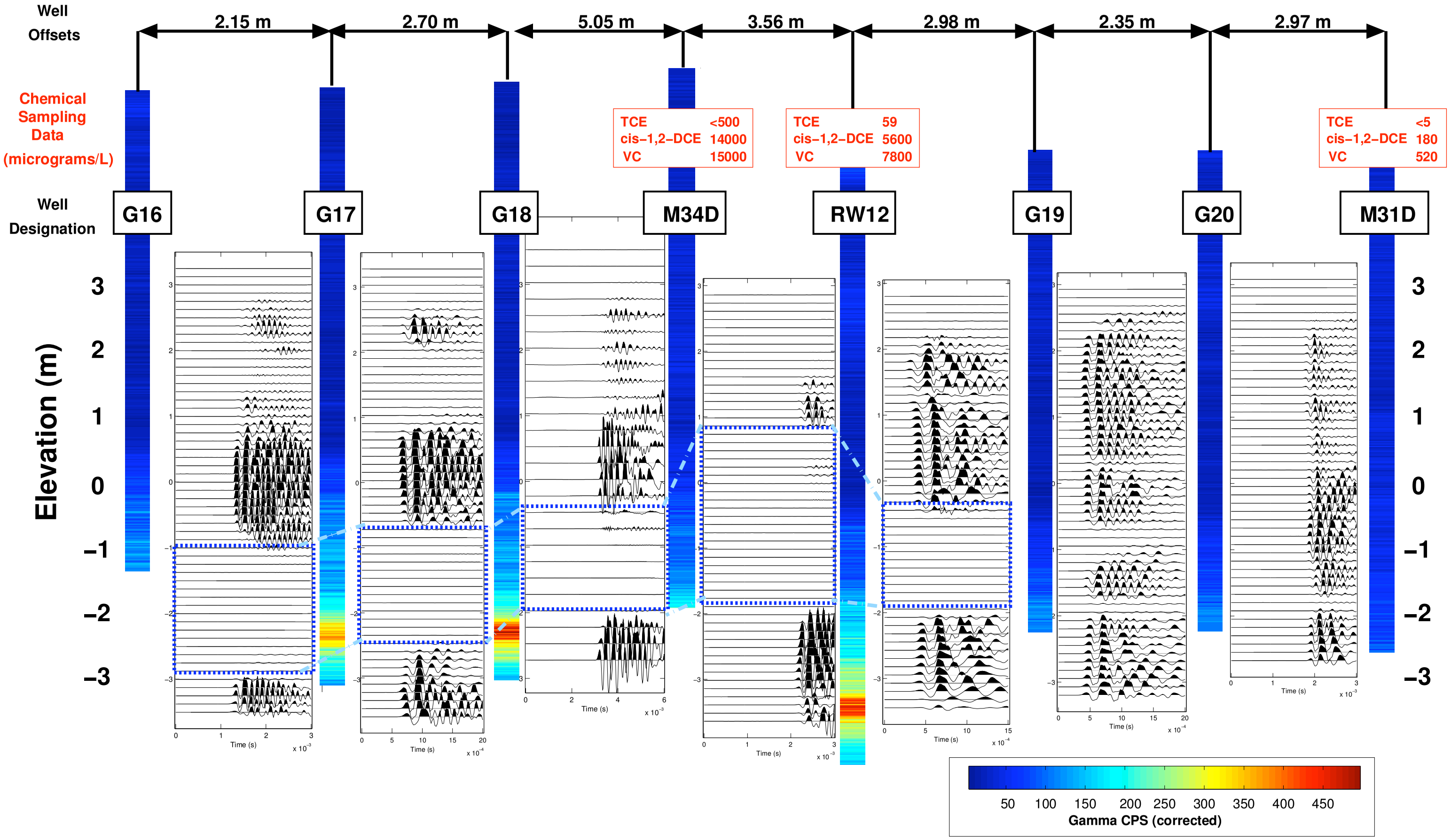

Figure 9.2: Zero-offset gathers of the seismic attenuation zone : Seismic gathers are shown in true amplitudes with a fixed instrument gain applied to each survey. The dashed blue boxes show the interpreted extent of the attenuating zone. Boxes are not shown for the G19-G20 and G20-M31D sections; their low amplitude traces have visible arrivals if trace relative gain is applied. Gamma logs, shown in CPS with no clip, are included for reference. The top lines include lateral well offset measurements and aqueous contaminant concentrations. Contaminant concentrations are noted in terms of μg/L. Listed contaminants include TCE, cis-1,2-dichloroethane (cis-1,2-DCE), and vinyl chloride (VC). Concentration measurements were made during April of 2002.

9.2 Adaptive Tomography Results

Using the adaptive velocity tomography methods discussed in chapter 8 we successfully inverted our primary multi-well profiles, the G12-M17D and M31D-G16 well sequences for the seismic case and the G19-G20, G18-G16, and G12-M17D well sequences for our radar surveys. We decided that all available spatially contiguous data should be inverted simultaneously to allow generation of a consistent image of large cross-sections of the site with guaranteed velocity ties at all well locations. Although acquisition limitations prevented us from building a continuous profile, we were able to simultaneously invert up to seven crosswell surveys. Our tomography algorithm, based on the use of an unstructured trigonal mesh, was able to generate adaptive parameterizations with guaranteed model resolution properties even in the presence of high irregular ray coverage.

9.2.1 Seismic Velocity Images

Figure 9.3 shows V_p tomograms (bottom) for the two primary seismic profiles displayed with the corresponding ray geometries (top) and adaptive meshes (middle). All results were generated with a resolution constraint (R_c) value of 0.1 . The G16-M31D inversion system, built from seven crosswell surveys, had dimensions of 4632 × 1419 (data by model) while the smaller M17D-G12 profile based on four surveys had dimensions of 2814 × 1016. In both cases the resulting inverse problem was overdetermined and fulfilled the pre-specified resolution constraints. As can be seen in figure 9.3, our algorithm generates a fine quasi-uniform mesh in regions of the site with good ray coverage and a much coarser mesh in the attenuating region. In both meshes, the smallest cell dimension is chosen based upon an estimate of the $\lambda/2$ length scale. The G16-M31D mesh is somewhat coarser than the G12-M17D mesh due to the lower mean centroid frequency of the included surveys and the correspondingly longer mean wavelength. Control points on region boundaries with no supporting data are also discarded and displayed as blank regions on the tomogram, as can be seen in the lower corners of the G12-M17D image. Subsurface velocities ranged from 1600 to 1800 m/s, values typical of fully saturated shallow soils.

Figure 9.4 shows a 3D perspective view of the seismic tomography results with semi-quantitative clay content estimates at wells based on calibrated gamma logs. The image is dominated by a large region of low seismic velocity which cuts across lithological boundaries and partially coincides with the high attenuation region. Since no data could be acquired in the high attenuation zone, the velocity estimates in these regions are constrained by ray-paths crossing the boundaries of the relevant tomographic cells. Although the algorithm described previously guarantees that all parameters are well-resolved with R_{ii} values are greater than R_c, the algorithm cannot guarantee velocity images with high *spatial* resolution in regions with poor ray coverage and consequently large mesh spacings. In this case, a distinction must be drawn between the formal resolution of the inverse problem, as encapsulated in the model resolution matrix (R), and the ability of the dataset to uniformly resolve spatial heterogeneity at a specified scale.

One point to note is the consistency between the velocity estimates on right boundary of the

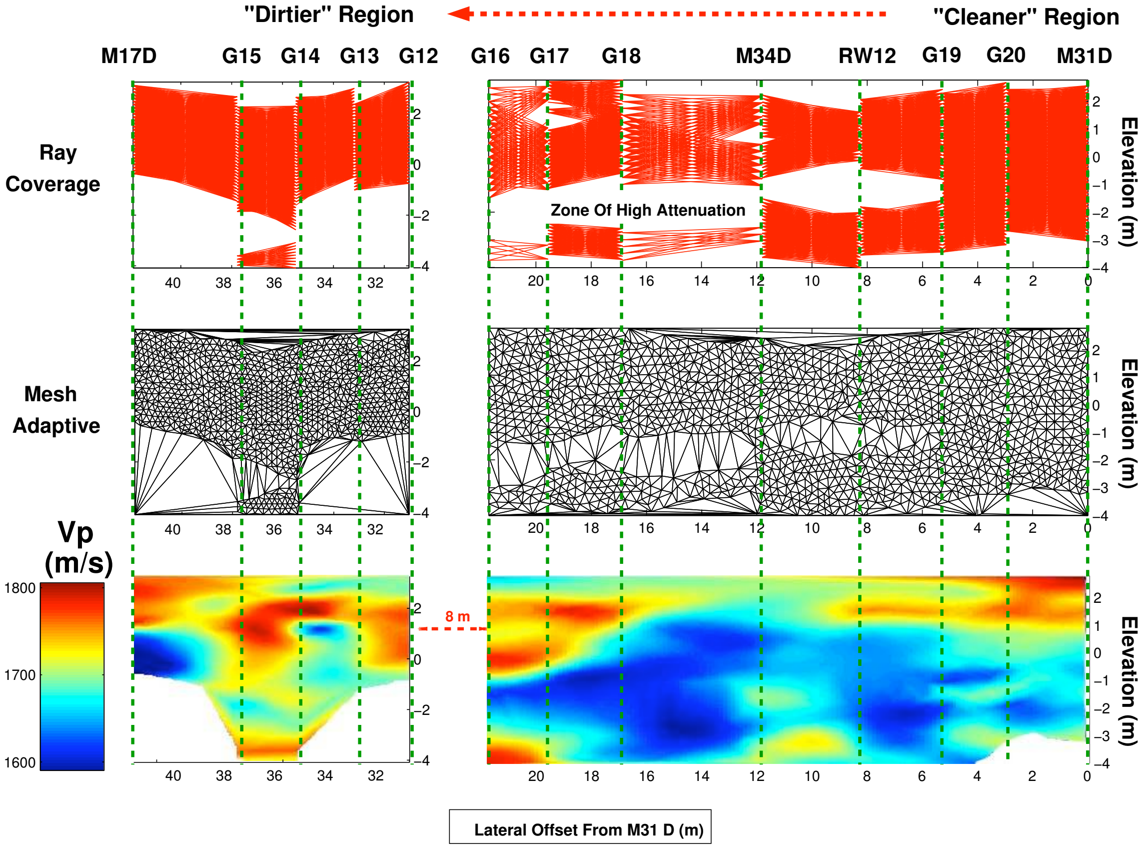

Figure 9.3: Adaptive seismic tomography result, M31D-G16 and G12-M17D sections : The top panel shows the ray geometry, the middle panel shows the parametrization used for the inversion, while the bottom panel shows the resulting P-wave tomogram.

M17D-G12 image and the left boundary of the G16-M31D image. Since no constraints between the two profiles were added, this match gives us added confidence in both inverted images. Interpretation of the tomogram set will be delayed until the following section where we will examine lithological boundaries and the attenuating region in more detail.

9.2.2 Radar Velocity Images

The results shown in figure 9.5 are traveltime inversions for the three radar profiles. In these cases ray coverage (not shown) was relatively uniform and the resulting meshes have minimal lateral variation. As mentioned previously, wells RW12, M34D, and M31D, all with steel casing, could not be used for our crosswell radar surveys. Like the seismic surveys, an R_c value of 0.1 was used during mesh generation. The problem dimensions were 1661 × 699, 2941 × 935, and 3470 × 1589 for the G19-G20, G16-G18, and M17D-G12 profiles respectively. The colormap for figure 9.5 is clipped between 5.4 $\times 10^7$ m/s and 6.5 $\times 10^7$ m/s due to very small regions of high and low velocity at the top and bottom edges. As in the seismic tomograms, close unconstrained matches at section boundaries give us additional confidence in the recovered images. Figure 9.6 shows a 3D perspective

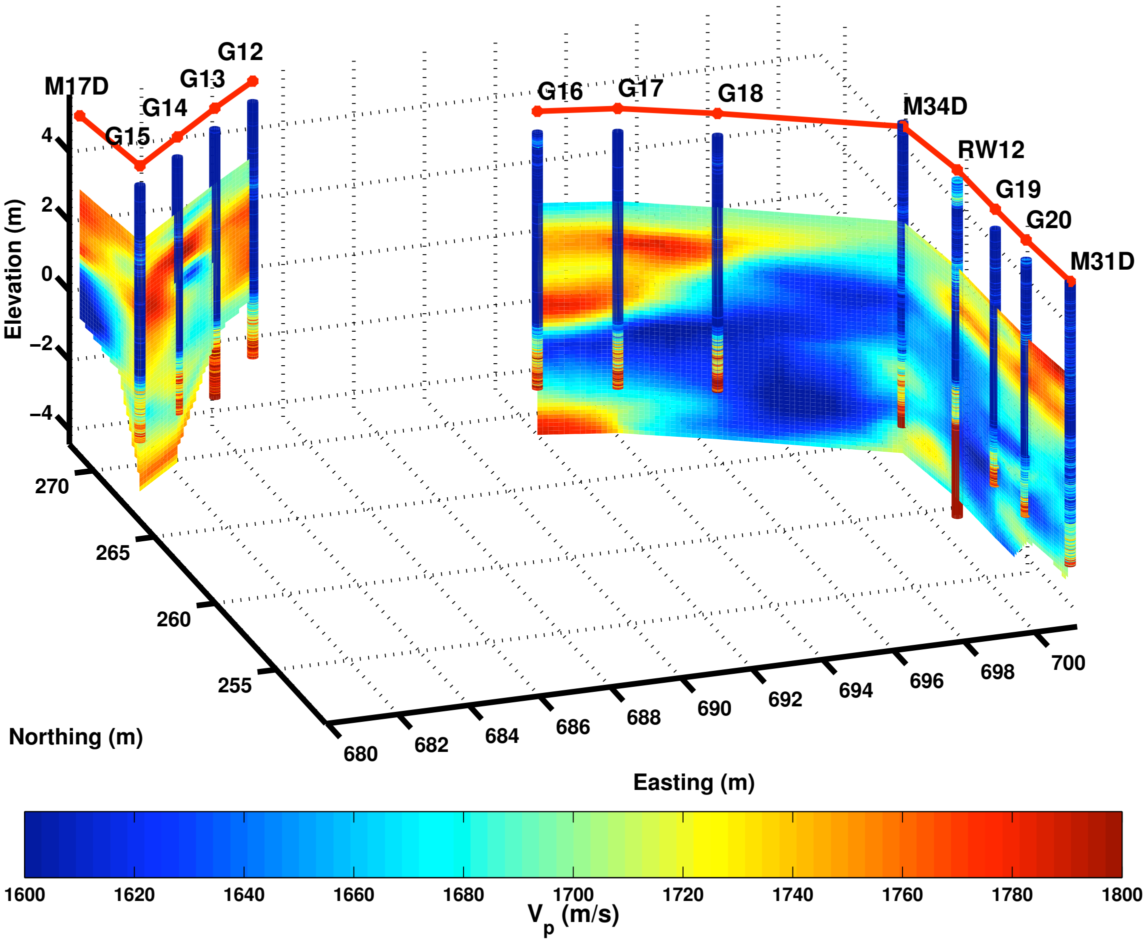

Figure 9.4: 3D perspective view of the seismic tomography results : Colors are P-wave velocity in m/s. Colored cylinders at well locations show gamma measurements empirically converted to clay content and clipped between 0 (dark blue) and 0.1 (dark red). The red line laterally connecting wells indicates surface elevation. with respect to sea level.

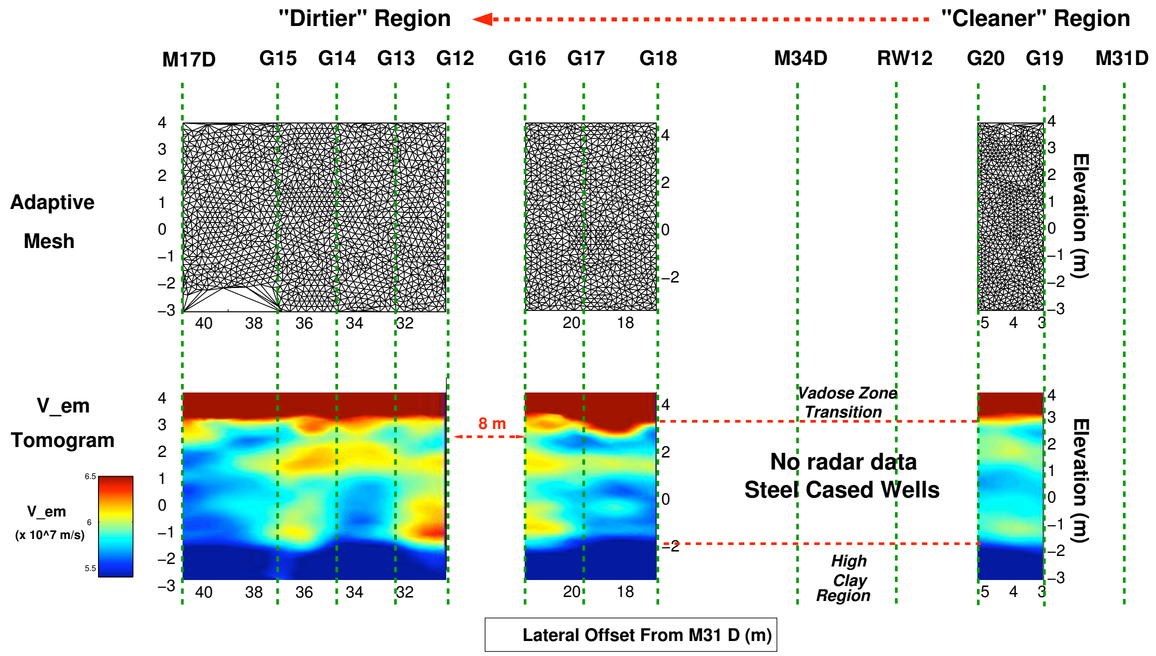

Figure 9.5: Adaptive radar tomography result, G19-G20, G16-G18, and G12-M17D sections : The top panel shows the parameterization used for the inversion, while the bottom panel shows the resulting V_{em} tomogram.

view of the radar tomograms with the same viewing angle and lighting as figure 9.4.

One unfortunate characteristic of our combined dataset is the variation in maximum sensor depth between our seismic, radar, and log measurements; this mismatch is due to significant differences in tool lengths.

9.2.3 Lithologic/Hydrogeologic Interpretation

In the previous section, we refrained from providing any explanation of the observed variations in seismic or radar velocities. In this section, we will attempt to classify which features in our crosswell imagery can be correlated with lithologic and hydrogeologic features visible in logging. Remaining features will be examined in more detail as perspective NAPL regions. When viewing figures 9.7 and 9.8, care should be taken in interpreting the lines linking the profiles since the distances between these boundaries are on the scale of the profiles themselves as can be seen in the 3D representations (9.6 an 9.4).

Figure 9.7 shows our crosswell radar profiles with secondary lithology information (CPT/gamma) and a basic interpretation. Several laterally continuous units are visible including the transition into the vadose zone (≈ 3 m) and the contact between the upper and lower surficial aquifers (≈ -2 m). The region of high radar velocity at the top of the profiles corresponds to the gradual transition into the vadose zone where the increase in velocity is due to partial gas saturation. A high velocity layer of irregular thickness can be seen between absolute elevations of 1 and 2 m. This unit, labeled as upper surficial aquifer unit B, does not have a significant signature in our gamma/clay logs and

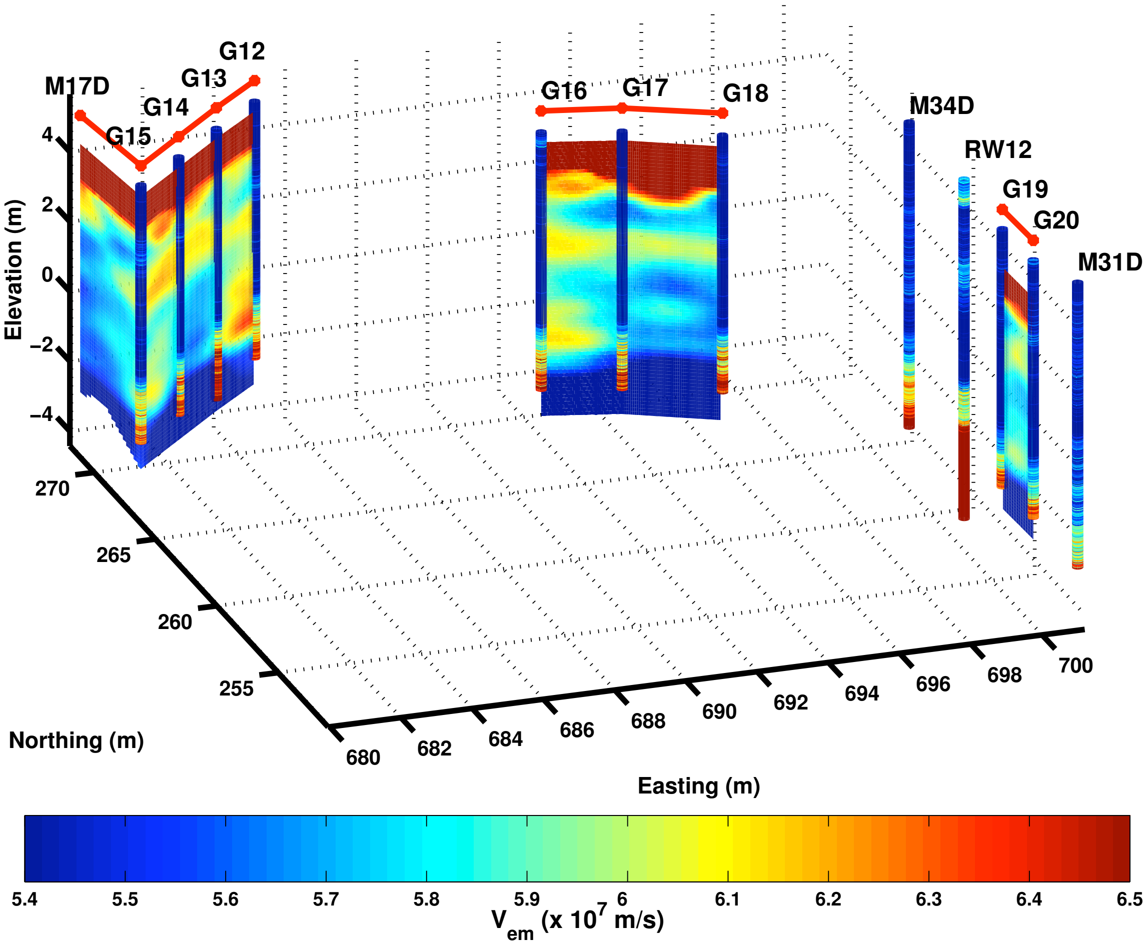

Figure 9.6: 3D perspective view of the radar tomography results : Colors are radar velocity in m/s $\times 10^7$. Colored cylinders at well locations show gamma measurements empirically converted to clay content and clipped between 0 (dark blue) and 0.1 (dark red). The red line laterally connecting wells indicates surface elevation. with respect to sea level.

could be due to variations in porosity related to sorting. Despite having an irregular geometry, evidence of B layer is visible in all acquired crosswell radar sections. The lower surficial aquifer (unit D) exhibits a lower radar velocity due to increased clay content and tracks well with variations in contact depth observed in gamma logs. The G4 CPT log, acquired midway between survey wells G13 and G14, provides a similar depth for the upper/lower aquifer transition. Several high velocity lenses, labeled as components of unit C2, are also visible directly above the upper/lower surficial aquifer contact. These features are not laterally continuous; while the most significant anomalies are located within the G12-G13 and G16-G17 sections, several smaller features are visible in the G14-G15, and G17-G18 sections. Since the C2 units are the only radar feature which cannot be readily explained, we consider them in more detail in the following sections.

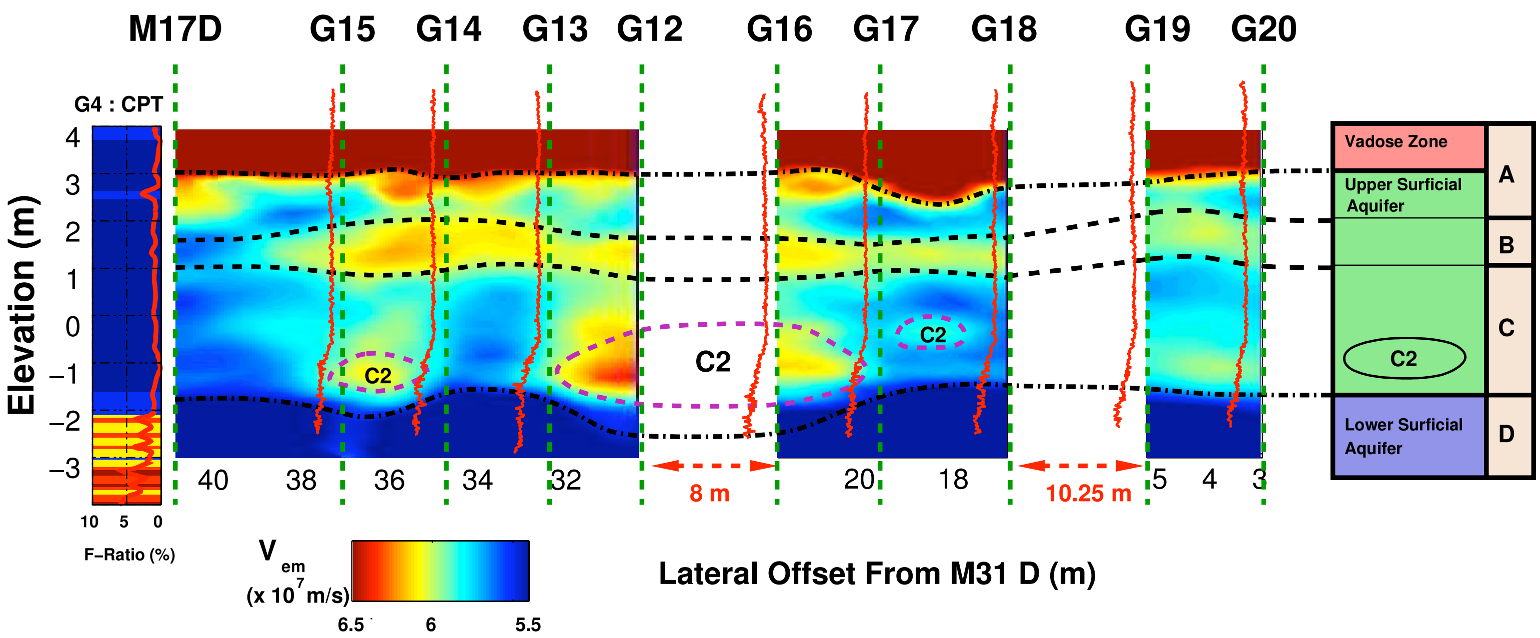

Figure 9.7: Radar profile interpretation : Shown are the G19-G20, G16-G18, and G12-M17D radar tomograms with gamma logs (red) and CPT data. Interpreted units are overlain. The water table and upper/lower surficial aquifer contacts are both visible as is a high radar velocity unit (B) in the upper surficial aquifer and several high velocity zones directly above the lower surficial aquifer (Q). CPT, gamma logs, and radar provide a relatively consistent location for the upper/lower surficial aquifer contact. The CPT log shown is from CPT well G4 which is between wells G13 and G14 in the survey profile.

Figure 9.8 shows a similarly interpreted image of the G12-M17D and M31D-G16 seismic tomograms. In general, the seismic images show a greater amount of spatial heterogeneity and are dominated by a large region of low velocity (LV) and the high seismic attenuation zone. As mentioned previously, since no picks are available in the attenuating zone, velocity estimates in this region are largely interpolated values constrained by rays on the boundary. The LV zone seems to cut across lithologic boundaries, occurring both above and below the upper/lower surficial aquifer contact. Considering the vertical extent of the LV region, clay content does not seem to be a reasonable explanation. The attenuating zone is partially correlated with the upper/lower surficial aquifer contact but is not visible in the G19-G20 and G20-M31D sections and varies significantly in thickness. The combination of co-localized regions of low seismic velocities and high seismic attenuation suggests a gas or DNAPL mechanism, two hypothesis we will discuss in the next section. Two layers of higher velocity, labeled units SA and SB, are visible in the upper portion of the profile, possibly caused by a region of reduced porosity. The irregular vertical thickness of unit SA and the truncation of unit SB between G17 and G18 might not be reflective of a lateral variation in lithology but of a secondary change related to fluid properties, particularly the presence of gas. Several smaller features are also apparent including two "tongues" of higher velocity material between G19 and M31D at a depth of -2 to -4 m and a highly localized patch of low velocity between G14 and G13.

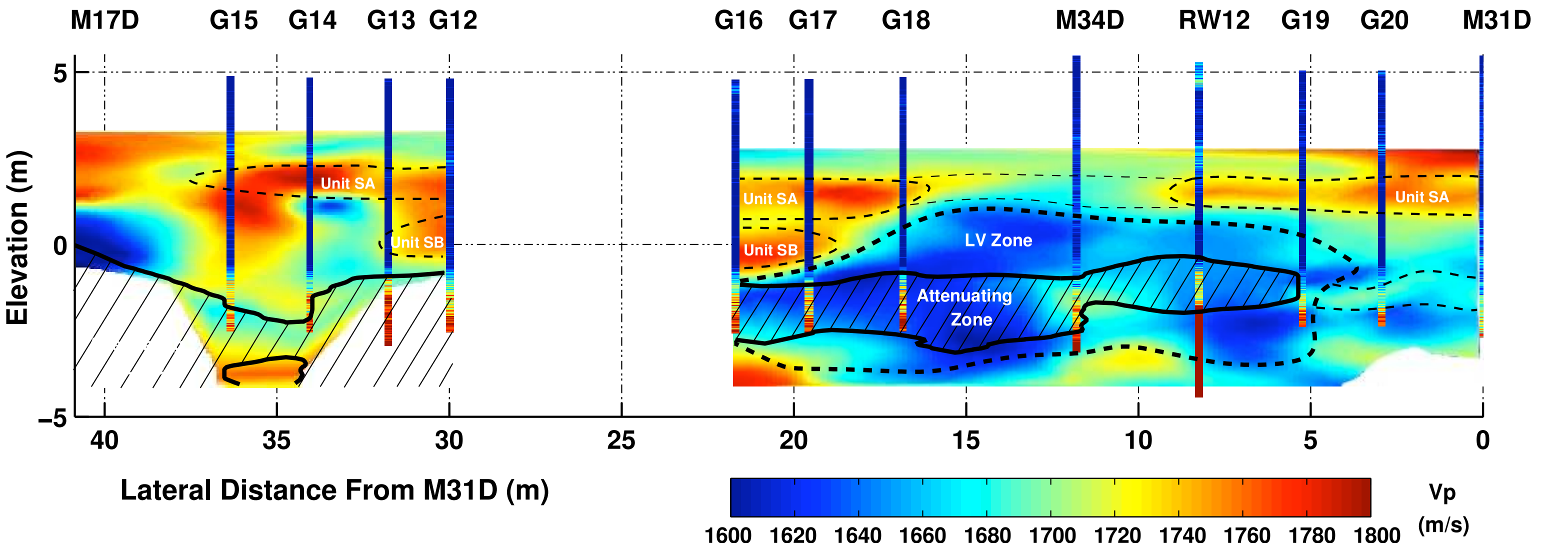

Figure 9.8: Seismic profile interpretation : Shown are the G12-M17D and M31D-G16 seismic tomograms with the colored bars at well locations showing gamma measurements empirically converted to clay content and clipped between 0 (dark blue) and 0.1 (dark red). The two most prominent features are a large zone of low velocity (LV) which cuts across lithologic boundaries and the high attenuation region. Several layers within the upper surficial aquifer with varying thickness (SA and SB) are also visible.

9.3 Data Integration

Several features visible in our seismic and radar profiles are not clearly linked to established lithologic or hydrogeologic features. In these cases, a qualitative examination of common units in our two tomographic datasets can provide a greater degree of insight as to the origin of the observed features. The first component of such a comparison is to in fact link the common features between the datasets, a task which is complicated by differences in the spatial extent and lateral variability of the reconstructed images. In figure 9.9 we visually integrate the two datasets by superimposing seismic velocity data (color contours) against background colormaps displaying radar velocity. The outline of the seismic attenuation zone is drawn over both images and auxiliary data detailing clay content and aqueous contaminant concentrations are also included. Red colors indicate high velocities for both velocity scales.

From figure 9.9 we can see that seismic SA unit mentioned previously coincides with the upper surficial aquifer B unit observed in the radar tomograms at an elevation of approximately 2 m. The combination of high radar and high seismic velocities suggests that the feature is a sandy region of lower porosity, probably indicative of a change in sorting within the clean sands of the upper surficial aquifer. Since the majority of the seismic low velocity zone is located between wells G18 and G19, for which we have no radar coverage, establishing a joint signature for this feature is difficult. Varying radar velocities in the zone of seismic attenuation indicate that this feature is probably not due to a significant change in clay content or porosity which would have a visible radar signature. The attenuating zone does however coincide with the largest of the high radar velocity features, the C2 unit in figure 9.7, visible in the G13-G12 and G16-G17 radar tomograms.

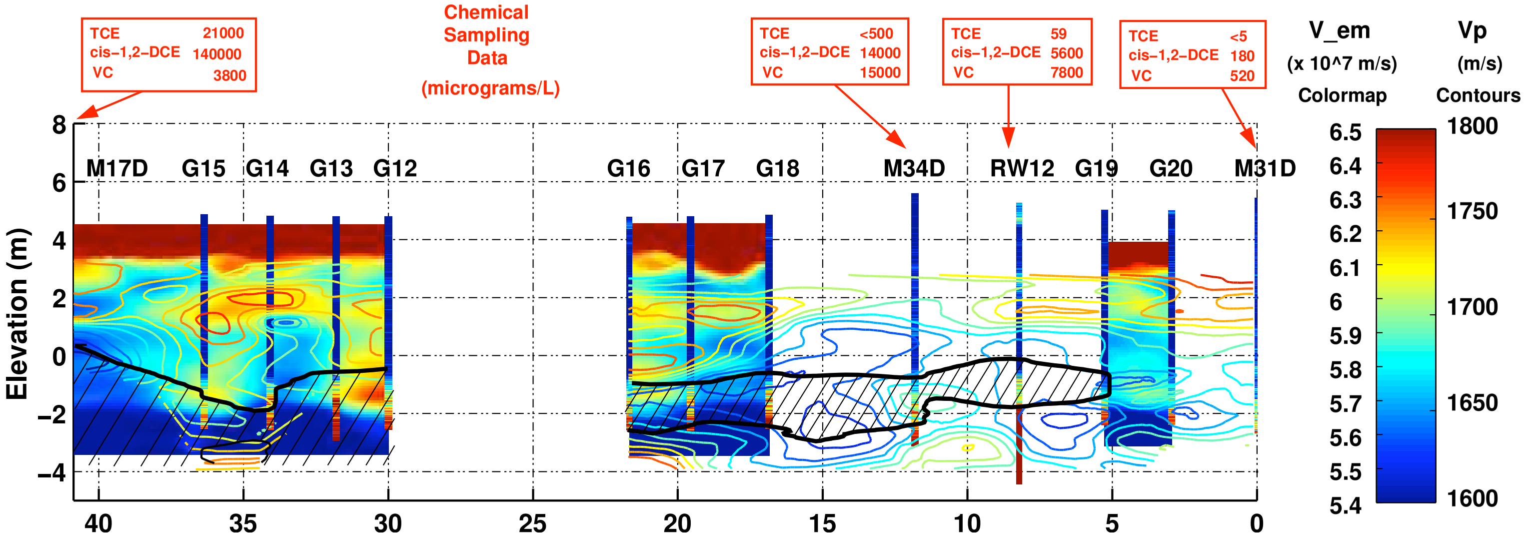

Figure 9.9: Integrated radar/seismic velocity display : Colored contours are seismic velocities for the M17D-G12 and M31D-G16 profiles while the background colormaps are radar tomograms for the G19-G20, G16-G18, and M17D-G12 survey sets. The shaded black outline indicates the zone of high seismic attenuation and colorbars at the well locations are gamma measurements empirically converted to clay content and clipped between 0 (dark blue) and 0.1 (dark red). Aqueous concentrations of the primary DNAPL component, TCE, and the break-down products cis-1,2-DCE and VC are also provided where available.

The petrophysical aspects of the C2 unit, a zone of high radar velocity located directly above a permeability barrier, qualitatively fit our model for the signature of a DNAPL pool. However, as discussed previously, this signature is hardly unique and several other processes could produce similar responses. Our approach will be to generate a series of scenarios where we assume that the C2 anomaly is due to a particular cause, in this case gas, DNAPL, or porosity variations, and then estimate the perturbation from background properties required to produce such a change in radar response. These estimates will then be evaluated in terms of both our seismic tomography results and our existing knowledge of site lithology from logs, CPT measurements, and core data.

As mentioned in chapter 7, there are many caveats for this type of analysis since theoretical models validated on quasi-homogeneous core samples are used to map velocity values estimated from tomography to petrophysical properties on a larger scale. This up-scaling problem is strongly effected by the averaging process inherent in tomographic imaging and is compounded by the fact that most imaging algorithms do not honor wave-theoretic resolution limits. Adding to the confusion is the effect of regularization and in our case adaptive parametrization, both of which generate an imprint on the map of recovered properties. Both the averaging effects of the imaging process and the secondary smoothing caused by regularization would tend to smear localized anomalies and thereby lead to underestimates of the peak magnitude of a given localized feature. Although progress is being made towards solving the problem of scale dependence in tomographic property estimates [75] [192] a generally accepted approach has not yet been developed. Another aspect of the up-scaling problem is the frequency dependence of some petrophysical properties; estimates of Q_p at 1 MHz laboratory frequencies will likely be different than estimates obtained from 1 kHz field data, particularly if fluid related loss mechanisms are operative. Ideally, petrophysical relationships would be handled in a stochastic fashion to allow for uncertainty within the core scale relationships as has been done by Hubbard *et al.* [128]. We will proceed with the knowledge that all of these problems can generate uncertainty in our final analysis and that the resulting numbers should not be viewed with too quantitative an eye.

The first step in our analysis of C2 anomaly was to extract a vertical column from our radar tomogram, a data format we refer to as a pseudo-log, which passed through the anomaly close to well G12. Since we are not attempting to generate an image but simply to explore several petrophysical scenarios, we selected the 1D format of a log which is simpler to both visualize and process. For an estimate of background properties, we selected a second radar pseudo-log at the point midway between wells G13 and G14 where the C2 anomaly is not visible. The tomographically estimated V_{em} pseudo-logs were converted to dielectric constant using the lossless model previously shown in equation 5.6. Panel A of figure 9.10 shows the G12 dielectric pseudo-log (solid red) and the reference measurement from G13-G14 profile (dashed red). Interpretation of the different vertical units is shown in the background of panel A including the upper surficial aquifer unit B (a low dielectric zone), the upper/lower surficial aquifer contact, and the beginning of the transition into the vadose zone. The C2 subunit of the upper surficial aquifer is the location of the anomaly as is apparent from the decreased dielectric values of the G12 log in comparison to the reference log. Panel

B of figure 9.10 shows the absolute difference in dielectric constant between the two pseudo-logs with only the section near the unit of consideration, between 2 m and -2.5, included.

We will consider three scenarios which might explain this change in dielectric constant, a reduction in porosity, partial DNAPL saturation, or partial gas saturation. We assume that the reference log represents an accurate estimate of background properties in a fully water-saturated state with only a single mineral phase present. Before testing each of the scenarios we used the previously verified Bruggeman-Hanai-Sen (BHS) model [239] to calculate background porosity values from the reference log. In these calculations we assumed a grain dielectric constant of 5 estimated from mineralogy in chapter 5. For the inversion of the BHS model we used the simplex search method to minimize the difference between the observed and calculated dielectric values for a given free variable, in this case varying porosity in our two phase system to match the dielectric constant derived from the radar tomograms. A closed-form CRIM estimate was used for the initial guess in this optimization process. The resulting porosities ranged from 0.4 to 0.43 for the upper surficial aquifer A and C units and between 0.38 and 0.4 for the upper surficial aquifer B unit. These values are within the range measured by the USGS on 10 retrieved core samples [172] and the measurements we have carried out on the G13, G16, and G20 cores.

If we assume that all perturbations in dielectric constant are caused by variations in porosity we can perform the same porosity inversion on the pseudo-log containing the C2 anomaly and determine the change required to produce the observed reduction in dielectric constant. As shown in panel C of figure 9.10, the C2 perturbation in κ could be explained by a 7% reduction in porosity, a change which would decrease bulk porosities in this region to values of 0.33 to 0.35, somewhat low but still within the range of values observed in recovered cores. We performed similar BHS inversions assuming that porosity values for the C2 pseudo-log were equivalent to the reference profile and allowing DNAPL saturation to be the free variable. In this case we used the site-specific DNAPL dielectric constant of 2.7 (derived in chapter 3) in our BHS calculation and followed the mixing procedure outlined in chapter 5. The results of this inversion are shown in blue on panel D of figure 9.10 which indicates that the same signature could be reproduced by a zone with a 13% DNAPL saturation, which is within the range of saturations observed by Parker *et al.* [213] in push sampling measurements. Conducting the same type of inversion using volumetric gas fraction as the free variable yields a peak gas saturation of 11% to replicate the anomaly as is shown in red on panel D.

In all three cases the changes in porosity or gas/DNAPL saturation inferred by our petrophysical inversions are physically reasonable requiring the introduction of secondary measurements to distinguish between our three hypotheses. We will consider seismic tomography results, CPT data, gamma logs, core information, and details of site history in this stage of our investigation.

The possibility of a porosity change, although reasonable given the geological setting is not fully consistent with our secondary measurements. We do not observe the C2 anomaly in our gamma logs which is not surprising since a porosity change could be easily generated by variations in sorting without an increase in clay content. Although we do not have CPT data which penetrates the C2 anomaly between G12 and G13 we do have information from wells G4 (between G13 and G14), push

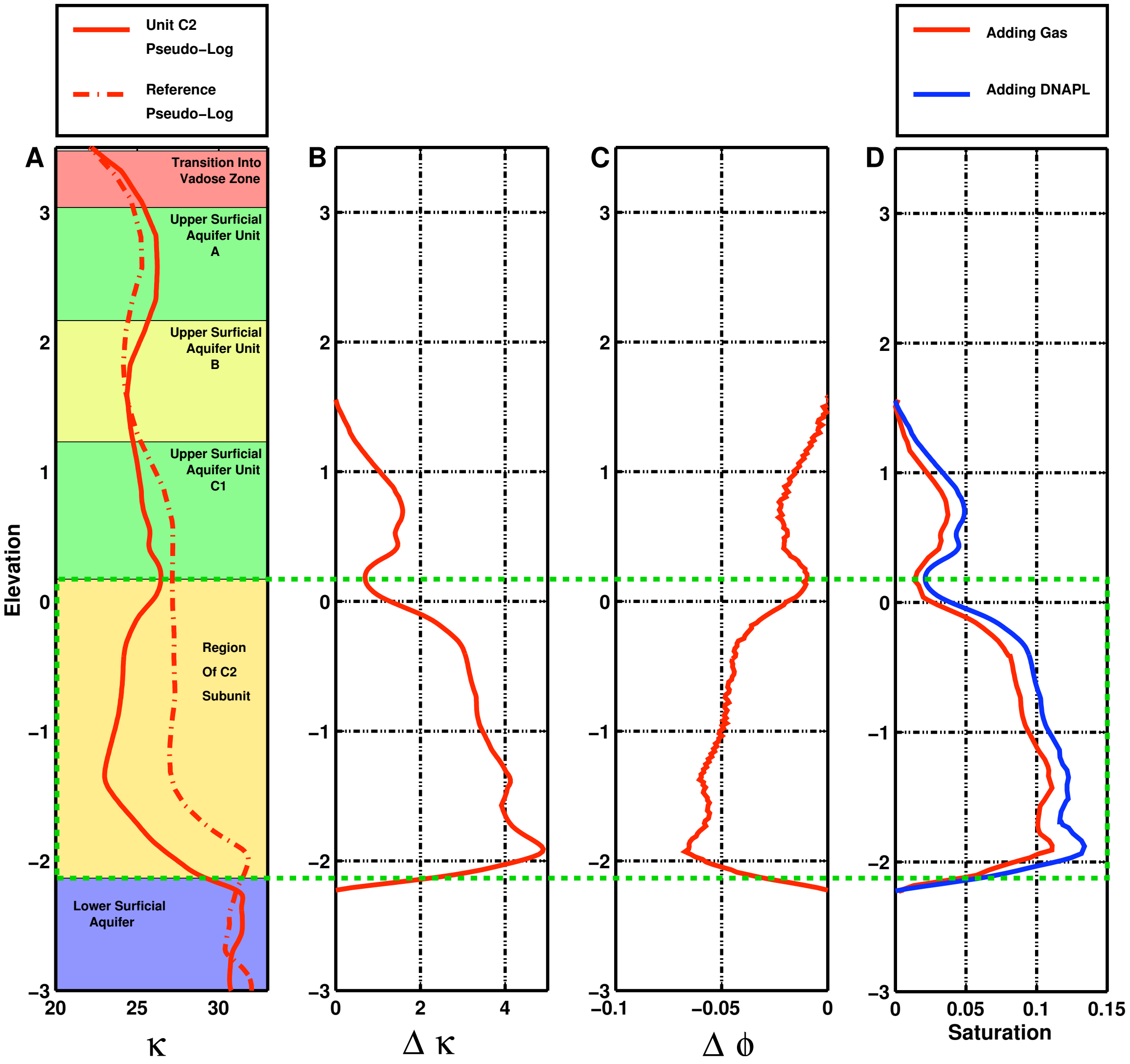

Figure 9.10: Using pseudo-logs to test the gas, DNAPL, and porosity hypotheses : Panel A are dielectric pseudo-logs extracted from the relevant tomograms. The C2 curve is from near well G12 within the G12-G13 crosswell profile while the reference curve corresponds to a pseudo-log located midway across the G13-G14 profile. Panel B is the absolute difference in dielectric constants between the two curves for the elevation range of 2 to -2.5 m. Panel C is the porosity required to produce the observed $\Delta\kappa$ values using our BHS inversion scheme. Panel D shows equivalent results where a reference porosity profile is assumed and the inverted perturbation corresponds to partial saturation with either DNAPLs or gas.

point CP52 (between G12 and G16), and G2 (between G16 and G17) all of which are marked on the site survey map, figure 9.1. The G2 push-point penetrates the edge of the C2 feature and the CP52 log may also pass through this region although our lack of radar data between wells G12 and G16 makes this difficult to determine. Figure 9.11 shows the two dielectric pseudo-logs next to the three mentioned CPT datasets. As can be seen in the figure, the depth of the upper/lower surficial aquifer contact as determined by CPT shows excellent agreement with our radar interpretation. The upper surficial aquifer unit B also seems to have a transient but visible CPT signature near 2 m elevation. The CPT response for the upper surficial aquifer's C unit is remarkably consistent as can be seen in panel E of figure 9.11 where the three F-ratio logs are superimposed. The lack of variation in CPT response between G02, G04, and CP52 suggests that the cause of the C2 anomaly is not strongly linked to lithology. Interestingly, an inflection in the F-ratio curve is replicated in the dielectric pseudo-logs, probably indicating a region of transition into the lower surficial aquifer. Seismic evidence also seems to contradict the porosity hypothesis. As can be seen in figure 9.9, the C2 anomaly overlaps with the seismic attenuation zone and is bounded by regions of low seismic velocity. Lower porosities tend to increase P-wave velocity and decrease P-wave attenuation, two predictions which contradict our observations. Although we do not have cores from the G12 well which intersects the thickest section of the C2 feature, we did obtain core from the G16 well which passes through a similar lens within the same sub-unit. When examining the CT imagery of the cores, no striking differences were noted in the C section between G16 and the corresponding core from G20. In conclusion, although a reduced porosity could generate the observed radar anomaly, secondary evidence including CPT data, seismic measurements, and core sampling suggest that this is probably not the case.

Having eliminated porosity as a likely source of the C2 anomaly we will now consider partial DNAPL saturation as an alternative cause for the observed zone of low dielectric constant. Unfortunately, the gamma and CPT measurements which have proven so useful in other aspects of site characterization do not provide any information on fluid saturation or fluid properties. Several pieces of circumstantial evidence point towards DNAPLs. The fact that the anomaly is located at the upper/lower surficial aquifer contact, a significant permeability transition, is consistent with DNAPL accumulation. The largest observed C2 dielectric anomaly is also in close proximity to well RW6, the only well in this region of the site from which substantial volumes of DNAPLs have been collected (see figure 9.1). The peak saturation levels which we estimated from our petrophysical inversion are well within the range of saturation levels measured at other DNAPL contaminated sites of similar age [213]. One inconsistency is the dimension of the proposed region of DNAPL accumulation; of all of the DNAPL regions characterized by Parker *et al.* [213] none were thicker than 30 cm. A naive interpretation of the C2 anomaly observed near well G12 would suggest a contaminated zone of approximately 1.5 m in height with a lateral extent greater than 3 m. These dimensions are inconsistent with the "pool" DNAPL architecture but could be interpreted as a patch of residual material. Additionally, we might posit the existence of a compact DNAPL source pool with the large apparent dimensions being a result of smearing in the tomographic reconstruction

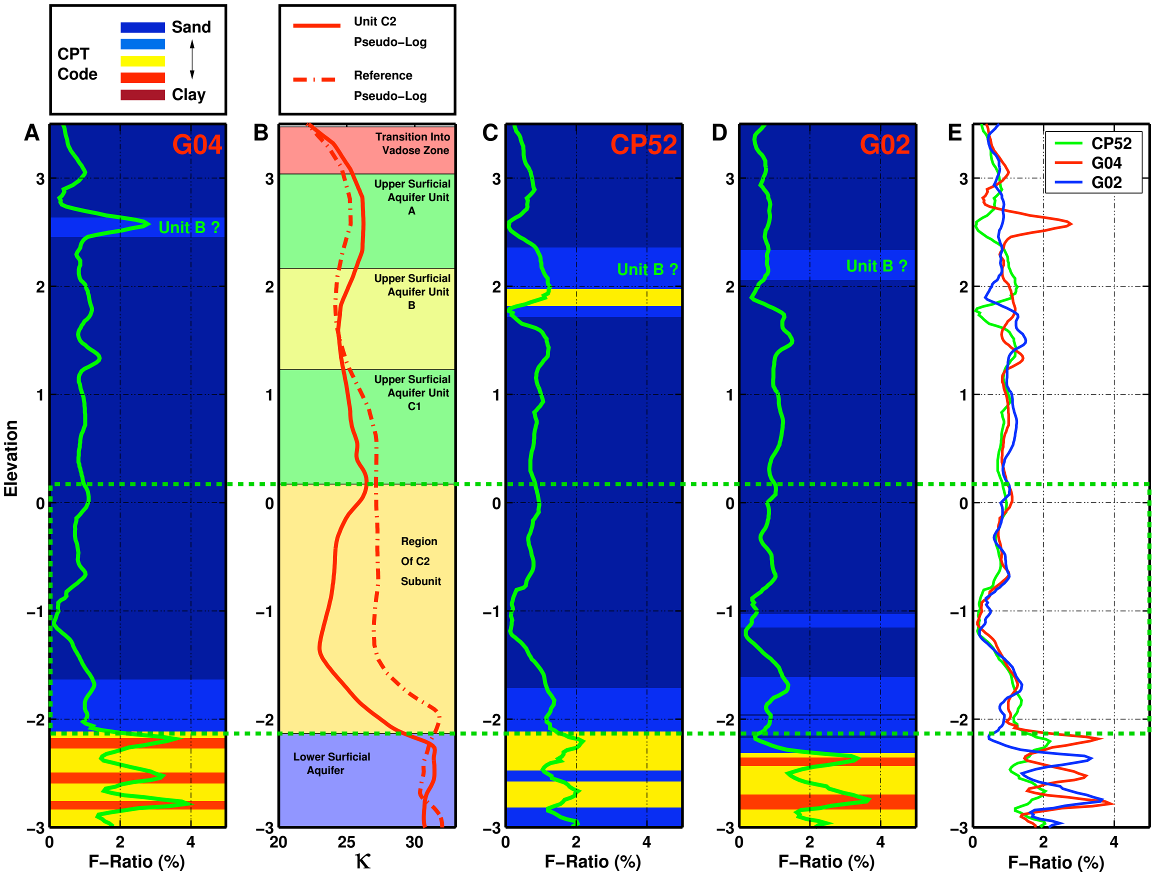

Figure 9.11: Comparison of dielectric pseudo-logs and CPT data for the C2 subunit : The CPT charts show F-ratio in green and empirical lithology estimates in color with red indicating high clay content. The lithology estimates are not perfectly correlated with F-ratio because piezo pore pressure (not shown) is also included in the lithology regression.

process. However, if we assume that the causal mechanism of the C2 anomaly is related to the seismic attenuation zone, we can make several arguments against the DNAPL hypothesis. Although the laboratory measurements discussed in chapter 6 document increased seismic attenuation in soil samples caused by DNAPL saturation [108] [111], the volumetric quantities required to observe this effect are significant, typically requiring at least 20% free-phase saturation to reduce normalized waveform amplitude to 0.8 from a starting value of 1. The observed levels of seismic attenuation would probably require even larger volume fractions but we will delay a detailed discussion of this line of inquiry until the following section. If we posit that the entire region of seismic attenuation is caused by these levels of DNAPL saturation, we would expect to see a correspondingly large region of high radar velocity. Referring back to the integrated radar/seismic tomography map shown in figure 9.9, we can see that such a high velocity zone is not visible, particularly in the G17-G18 and G15-M17D profiles. If the observed seismic attenuation were caused by significant DNAPL saturation we would also expect high aqueous contaminant levels in wells M34D and RW12 which intersect this region. Chemical sampling data (also shown in figure 9.9) reveals aqueous TCE levels of only 59 μg/L at RW12 and $\approx$ 500 μg/L at M34D, values which do not suggest the presence of DNAPLs within the vicinity of these wells.

Partial gas saturation is a third possible explanation for the C2 zone of high radar velocities and one which has the added advantage of being consistent with our seismic observations. Based on our previous petrophysical estimates, free gas saturations on the order of 11% could generate a radar velocity anomaly of the correct magnitude. Substantially lower gas levels are capable of causing both reductions in P-wave velocity and large increases in P-wave attenuation as demonstrated by both *in situ* sea floor measurements [275] and laboratory experiments [104]. P-wave losses can be generated by scattering from gas patches, patch equilibration mechanisms [274], or by direct bubble resonance [18] [19] [106] [105]. Since relatively low gas levels ($\approx$ 2%) could cause large seismic attenuations, as high as 200 dB/m between 1 and 3 kHz [33], but not have a detectable radar signature, the high attenuation region need not have a corresponding radar response. We could imagine a scenario where the C2 anomaly is caused by a patch of high gas saturation surrounded by trace gas levels responsible for the larger lateral extent of the seismic attenuation region. The total absence of seismic signal within the high attenuation region seems to be more consistent with a gas mechanism than DNAPLs; From a qualitative perspective similar "blank" regions have been observed in sea-floor transmission measurements within gassy sediments [275]. If we assume that patch equilibration [274] is the relevant seismic loss mechanism, then we predict gas to have a much more significant effect on Q_p than DNAPLs as demonstrated in our numerical examples in chapter 7. Unfortunately the unambiguous diagnosis of gas as the source of the observed radar and seismic signatures is difficult. None of the available logging datasets provide significant secondary constraints. Although gas volume determination has been carried out on cores using X-ray CT [33], the poor structural integrity of our core sections, the lack of pressure control on the sample volume, and the low resolution of our CT measurements eliminated the possibility of carrying out similar measurements. A dissolved gas content (CH_4, CO_2 etc.) dataset acquired in our survey wells would have provided another piece of circumstantial evidence for the gas hypothesis but unfortunately such data is not available. A main component missing for our arguments in favor of the gas mechanism is a plausible story for the origin of the gas regions, a topic we will explore later in this chapter.

Of the three proposed mechanisms for explaining the C2 radar anomaly, we believe that the gas hypothesis is the most consistent with seismic measurements and secondary site constraints. However, the possibility remains that porosity/lithology or partial DNAPL saturation could be responsible, particularly if the seismic attenuation anomaly is related to a subtle change in lithology which lacks a distinct radar response.

9.4 Conceptual Models For Gas Distribution And Generation

We will now attempt to build a consistent site model under the previously discussed assumption that partial gas generation is the source of both the C2 zone of high radar velocity and the encompassing region of high seismic attenuation. Such a model should include a plausible story describing the source of gas in the subsurface and its resulting spatial distribution. Figure 9.12 shows a tentative model for lithology and the proposed gas region within our survey profile. The vadose zone transition, all three upper surficial aquifer units (A/B/C), and the lower surficial aquifer are shown. Superimposed are the hypothesized gas regions constructed from features visible in crosswell radar and seismic tomograms. The C2 subunit is shown as a zone of high gas saturation which should be on the order of 11 % to fulfill our earlier petrophysical constraints from the radar velocity signature. Two secondary gas regions have also been interpreted on the basis of our seismic measurements. The first zone coincides with the high seismic attenuation zone and is hypothesized to be a region of relatively low gas saturation (≈ 1 %) surrounding the core gas patch in the C2 anomaly. This level of gas should be enough to have a significant seismic signature without dramatically changing radar velocities. The second region does not contain any free gas but has a sufficient quantity of gas in solution to reduce seismic velocities by approximately 100 to 150 m/s ; like the low gas region, the dissolved gas zone should not have a significant radar signature. In this scenario, dissolution at the boundary of the attenuating zone would generate large enough aqueous gas concentrations to produce the low velocity region interpreted in our seismic tomography profile (see figure 9.8). We should once again point out that while this interpretation is consistent with our observations it is certainly not conclusively proven since we lack direct data on either DNAPL or gas saturation within the region of interest.

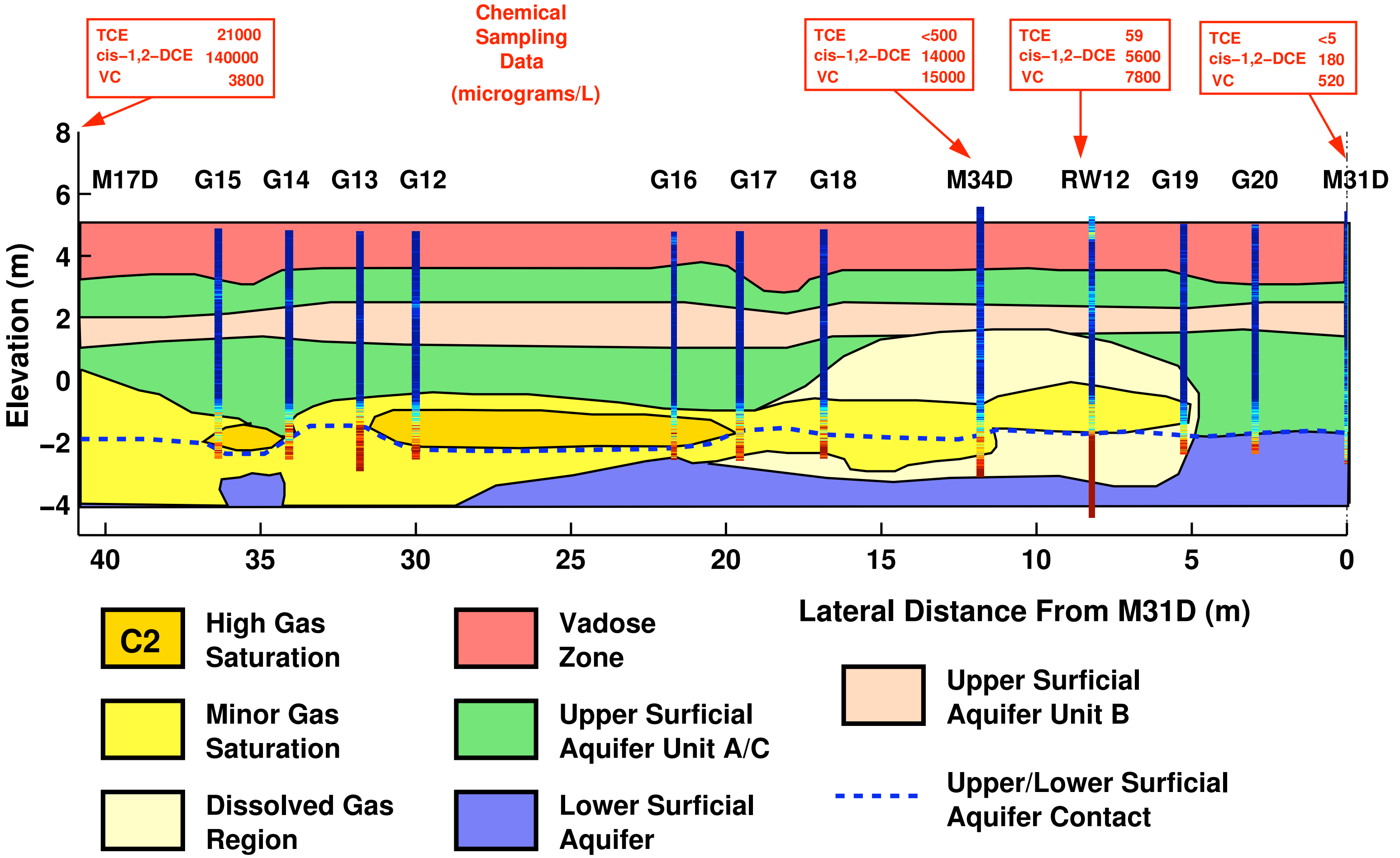

Figure 9.12: A local site model based on the gas hypothesis : Interpreted lithological and hydrogeologic boundaries are derived from radar and seismic tomography profiles with additional constraints from CPT measurements and gamma logs.

With the spatial distribution of the hypothesized gas body established, we will now propose several possible sources for subsurface gas at the NE site, some of which we can subsequently eliminate using secondary site data. Residual gas left by short-term fluctuations in water-table elevation is one possible source that we considered for our hypothesized gas body. Variations in water table levels at the NE site are caused by high rates of extraction from local recovery wells and by seasonal changes in recharge rates within the surficial aquifer. For residual gas from this process to be present in our C2 target region, the water table would have to have been lowered to an absolute elevation of -2 m. Figure 9.13 shows the recorded water table levels at the three monitoring wells which are contained by our site profile; this dataset was extracted from available Pinellas quarterly monitoring reports eg. [7]. As can be seen from the figure, although water levels do fluctuate by as much as 2 m for monitoring wells M17D, M31D, and M34D, at no point in the measurement record has the water table dropped to within 3 m of the C2 anomaly's elevation. Another conceivable scenario for generating a zone of partial gas saturation would invoke depressurization caused by site pumping activities. A quick reduction in pressure might cause existing aqueous gas to come out of solution and form localized patches. The maximum observed variation in water table elevation at the available monitoring wells is close to 2.2 m which corresponds to a pore pressure drop of approximately 8 kPa assuming a porosity of 0.38. Although tidally induced depressurization has been observed to cause small variations in sediment free gas content [33], larger decreases in pressure (30+ kPa) over shorter time scales ($\approx$ 6 hrs) were required to produce measurable changes. If we assume that the pore water is fully saturated with methane (CH_4) we can use Henry's law (methane, $K_c = 62.2 \times 10^6$) to calculate the change in free gas saturation induced by an 8 kPa pressure drop. Assuming a porosity of 0.38, a temperature of 25^o C, and a 2 m water column we can produce a maximum 0.25 % change in gas saturation in this scenario, which is approximately two orders of magnitude smaller than what our petrophysical estimates require to explain the C2 radar anomaly. Additionally, although wells M31D and M34D experience almost identical pressure variations as can be seen in figure 9.13, seismic attenuation levels are considerably higher in the M34D profiles suggesting that water table height is not the controlling variable. The depressurization scenario begs the question of where the dissolved methane comes from; one possible source is anaerobic methanogenesis, a topic which we will discuss in the following subsections.

As mentioned in chapter 2, the Pinellas NE site has been the location of several remediation projects including a pilot experiment examining rotary auger steam treatment during 1996 and 1997 [125]. This treatment method involves the use of a large crane mounted dual auger bit which vertically tills a column of soil of up to 10 m depth while injecting steam. DNAPLs present are volatilized and captured by a shroud. Figure 9.1 shows the proximity of the augered zone to our study region. The steam injected in this remediation process could have conceivably entered the region sampled by our crosswell tomography profiles through localized flow paths similar to those invoked to explain long distance gas transport during the biosparaging pilot project [8] at the Pinellas 4.5 acre site. However, in the case of auger treatment we believe that most of the injected steam would take a fast return path through the tilled soil column, a region of very high permeability, rather

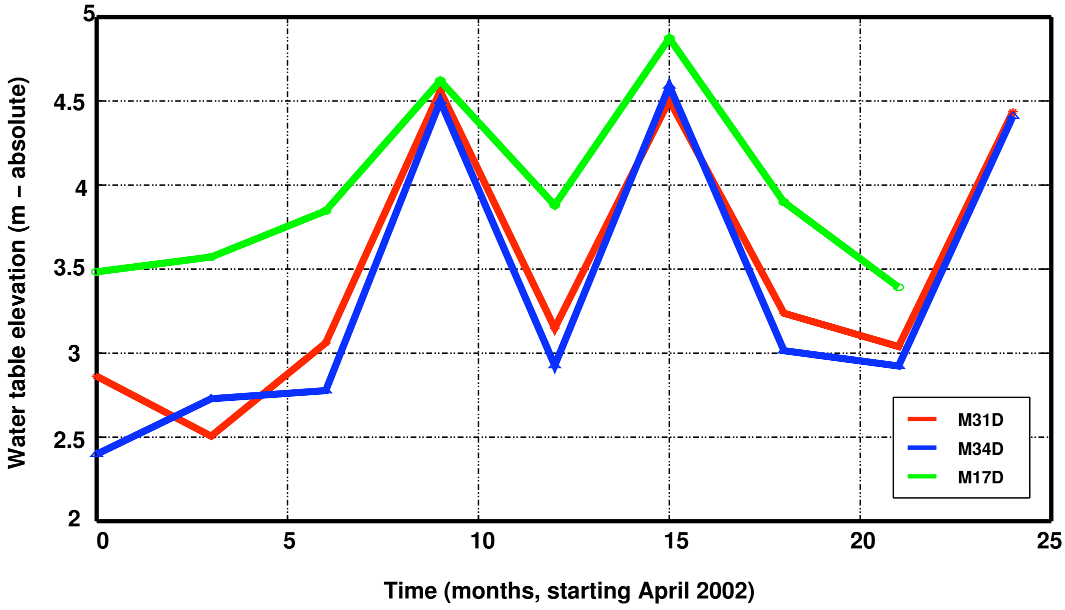

Figure 9.13: Water table fluctuations in the M17D, M31D, and M34D monitoring wells : Data was obtained from Pinellas sitewide quarterly reports eg. [7]

than penetrating into undisturbed formation. This process is enhanced by the low vacuum applied to the auger shroud. A second argument against this scenario is the relatively long time-span (5 yrs) between the injection pilot and our geophysical surveys, which would allow for small amounts of gas to re-enter solution. A final problem with the steam hypothesis is the detection of similar levels of seismic attenuation in preliminary surveys at the G9-G10-G11 profile [1] which is over 80 meters distant from the augered region. Although we cannot completely eliminate the steam auger treatment as a source of persistent subsurface gas we consider our next proposed scenario, biogenic methane production, to be more plausible.

9.4.1 A Story For Biogenic Gas Generation

Anaerobic methane production is one of the largest sources of biogenic gas in both shallow and deep subsurface environments. Volumetric methane saturations upwards of 50 % have been detected in wetland soils below the water-table [254] in units with vertical thicknesses on the order of meters. Methane production is also one of the few biogeochemical processes that has been observed *in situ* using seismic methods [275] [33] albeit in marine settings. A region of high biogenic methane production, possibly coupled to DNAPL degradation processes, is one explanation for the C2 radar anomaly and the correlated zone of seismic attenuation. This hypothesis, like other elements of our discussion, is speculative but may provide an interesting starting point for future research.

Seismic attenuation caused by methane bubbles in marine sediments has been a topic of research for the past several decades with recent focus on estimating the climatic contribution of oceanic

---

[1] This profile was one of the datasets initially acquired in the CPT emplaced boreholes 100 m. north of our current study region. This dataset was never successfully processed due to borehole deviation problems

methane sources and mapping shallow marine hazards. Many of the quantitative models for seismic attenuation induced by methane bubbles use the resonance theory for spherical bubbles proposed by Anderson and Hampton [18] [19]. Wilkens and Richardson [275] used a novel acoustic measurement device mounted on a gravity coring system to make seismic measurements on gassy sediments *in situ*. They observed attenuation levels of 40-50 dB/m at 15 kHz in the soft sea-floor muds of Eckernforde Bay (Baltic Sea). Best *et al.* [33] used a pulsed mini-boomer system to examine fluctuations in methane bubble attenuation induced by tidal pressure variations and successfully fit the resulting Q_p measurements to Anderson's theory. They observed attenuation levels as high as 200 dB/m between 1 and 3 KHz [33] in the shallow muds of Dibden Bay. The relevance of bubble resonance mechanisms at our site is uncertain due to the strong dependence of Anderson's theory on sediment shear strength and the characteristic bubble dimensions. Local flow [274], induced by pressure differentials across gas patch boundaries, is another possible mechanism for intrinsic losses within gassy sediments. For further information on this mechanism we refer the reader to the petrophysical modeling carried out in chapter 7. Gas zones can also attenuate seismic waves through scattering; since localized regions of gassy sediment have a considerably lower bulk modulus than the surrounding soils, the patch can act as an efficient scatterer independent of intrinsic loss mechanisms due to bubble resonance or patch equilibration.

Although free-phase methane can certainly generate a seismic attenuation signature and, in sufficient quantities, higher radar velocities ($\kappa_{methane} \approx 1$), additional evidence that methanogenesis is a significant process at the NE site is still required. One prerequisite for methanogenesis is an anaerobic environment. Water samples acquired from wells M34D and RW12 during 2000 [5] indicate an anaerobic environment with dissolved oxygen (DO) levels of 0.06 mg/L and 0.12 mg/L respectively over the screened interval of 0 to -3 m elevation. Low redox potentials also indicate that methanogenesis, in addition to sulfate reduction, should be dominant reactions. M17D, one of the wells within the seismic attenuation zone had a measured redox potential of -153 mV while M31D, outside of the attenuation zone, had a potential of 45.8 mV suggesting that spatial variations in redox state could control gas levels. Another necessary component for methanogenesis is a source of carbon; in the case of the NE site, this requirement could be fulfilled either through pre-existing organic carbon, which were found to be in the range of 1000 to 73000 mg/kg in the zone of interest [4], or from dissolved hydrocarbons, particularly BTEX compounds known to be present. The best evidence for supporting this hypothesis would be dissolved methane measurements from the monitoring wells; for free-phase gas to be a significant, local groundwater would have to be near full methane saturation. Measurements of dissolved nitrate, sulfate, iron, and carbon dioxide would also be useful in constraining bacterial processes in our zone of interest. Unfortunately, chemical sampling data of these types are not available for our analysis.

Several pieces of evidence indicate that significant anaerobic biodegradation of DNAPLs is occurring at the Pinellas NE site. As mentioned previously, several types of bacteria are capable of reductively dechlorinating organic solvents [176] in anaerobic environments. TCE can be sequentially transformed into cis-1,2-dichloroethane (DCE), vinyl chloride (VC), and finally ethene, a non-toxic end-product. Depending on geochemical conditions, different portions of this reaction chain may be more efficient, causing the accumulation of one or more daughter products. At the Pinellas NE site considerable levels of VC, a gas at near-surface pressures and temperatures, have been detected as can be seen in the chemical sampling data as shown in figure 9.12. Since VC was not a component of any of the initial liquid contaminants, significant levels at the site are conclusive evidence of bacterially mediated dechlorination of DNAPLs. Interestingly, VC levels are not well correlated with aqueous TCE concentrations as can be seen comparing the contaminant levels at M17D and RW12. RW12, which has a relatively low aqueous TCE concentration of 59 μg/L has a significantly higher VC level (7800 μg/L) than well M17D (3800 μg/L) despite the fact that M17D has much higher TCE concentrations (21000 μg/L). There may or may not be a link between the anaerobic processes responsible for DNAPL degradation and co-located regions of methane production. In some situations dehalogenation may not be energy-producing but a co-metabolic reaction mediated by existing methanogenic bacteria [159]. In this case, subsurface methane might be a signature of higher levels of active biodegradation but not necessarily regions of higher contaminant concentrations. In the case of energy-producing dechlorination of contaminants, referred to as dehalorespiration, it seems unlikely that the the daughter products (DCE, VC, ethene) are present as a separate phase.

9.5 Conclusion : Success Of The Tomographic Imaging Experiments

In conclusion, our tomographic imaging experiments produced an interesting picture of site structure but no definitive evidence of DNAPLs *in situ*. The crosswell radar tomography images were very effective in mapping all of the hydrogeologic and lithologic units observed in CPT and gamma logs including the vadose zone transition, the upper/lower surficial aquifer contact, and the B subunit within the upper surficial aquifer. The simultaneous inversion of several crosswell profiles allowed mapping of subtle variations in these features including the irregular thickness of the B subunit, which we infer to be a region of sand with a lower porosity than the A and C sections of the upper surficial aquifer. Several lenses with high radar velocities, which we refer to as the C2 subunit, were detected at the upper/lower surficial aquifer contact; no corresponding features were apparent in co-located gamma logs or nearby CPT push-points. Our crosswell seismic measurements yielded a less conclusive view of site structure. Although two layers, one corresponding to the B subunit, were visible across a section of the site, the seismic dataset was dominated by a large region of seismic attenuation and a second region of low velocity which do not seem to be linked to lithology. In an effort to understand possible sources for the C2 radar anomaly we performed a series of petrophysical inversions and determined that a region of low porosity, partial DNAPL saturation, or partial gas saturation were consistent with the zone of high radar velocity. Based on the hypothesis that the C2 anomaly and the region of seismic attenuation were signatures of a linked process, we were able to use seismic and site constrains together with radar velocities in our interpretation. After examination of the composite dataset, we decided that partial gas saturation was the most reasonable solution, particularly since it provided a consistent explanation of both the C2 radar feature and the high observed levels of seismic attenuation. Using the two sets of tomograms, we then built a tentative site model including the regions of possible gas saturation. We ended our discussion with a review of possible sources of free-phase subsurface gas at the NE site including depressurization effects and biogenic methane production.

Independent of the successful detection of DNAPLs, the Pinellas dataset was a useful case study of high-resolution near-surface imaging; in the crosswell radar tomograms we were able to track a lithological subunit of less than 1/2 m thickness. Although surface radar techniques can provide reflectivity images with even higher resolutions, the NMO velocity models generated from GPR reflection data can seldom approach the spatial resolution of our tomograms, particularly in regions lacking large numbers of discrete reflectors. The same comparison is equally valid in the seismic case where the velocity models inverted from surface reflection and refraction datasets seldom have the spatial resolution afforded by our 4+ kHz of bandwidth. We found that the interpretability of our site tomograms were increased by our simultaneous inversion of large profiles, a process which yielded consistent images of cross-sections as large as 22 x 7.5 m with spatial resolutions on the order of 1/2 m. Spatial integration of the two tomographic datasets proved difficult; the zone of seismic attenuation was severe enough to completely block transmitted P-waves thus preventing us from performing either velocity or attenuation tomography within these regions. Unfortunately, the seismic attenuation zone also overlapped with the most interesting radar feature seen at the site, the C2 subunit, which forced us to rely on a qualitative approach to integrated interpretation. Numerous site restrictions and funding limitations prevented us from acquiring the auxiliary ground-truth datasets which would have been useful in building a more complete assessment of our crosswell imaging results. In our final chapter, we will use our experience at Pinellas as a starting point for examining the future role of geophysical techniques in both DNAPL detection and environmental site characterization.

Chapter 10

Conclusion : The Way Forward

In this dissertation, we have investigated the applicability of high-resolution borehole geophysical measurements for the *in situ* detection of DNAPLs. As part of this investigation, we acquired a large series of crosswell seismic and radar surveys at a site of known DNAPL contamination, the DOE's Pinellas facility. We developed a new class of adaptive tomographic algorithms which allowed us to effectively perform traveltime inversion on our multi-well profiles despite the existence of significant gaps in ray coverage. The results of our tomographic imaging flow were integrated with logging results to generate a detailed model of site lithology. Although non-aqueous contaminants were not conclusively identified at this facility, we did detect several regions below the water table with high radar velocities and high levels of seismic attenuation, signatures which are consistent with soils partially saturated with either gas or DNAPLs. We also performed an extensive laboratory investigation into the dielectric and acoustic properties of Pinellas core samples partially saturated with trichloroethylene (TCE) or toluene, two contaminants of concern at our field site. The combined results of these laboratory experiments provide insight into the possible joint seismic/radar signatures of subsurface DNAPLs and partial confirmation of existing effective medium models used to describe such systems.

In this concluding chapter, we attempt to retrospectively evaluate both our results and the methods which we originally selected for our field and laboratory experiments. In light of our experience, we provide some possible directions for both field and laboratory approaches to DNAPL detection and DNAPL site characterization. We leave the reader with a more general analysis of the application of geophysical methods to this class of environmental problems.

10.0.1 The Success Of The Pinellas Field Experiment?

The field component of the Pinellas geophysical experiment yielded results which, while useful from a site characterization perspective, could not conclusively confirm the presence of DNAPLs. The next logical step would have been direct sampling of fluids from the C2 radar anomaly using CPT techniques [213]. The resulting fluids could have been analyzed for DNAPLs, high concentrations of contaminants dissolved in the aqueous phase, and dissolved gas levels (CH_4, CO_2) allowing us to resolve some of the questions concerning the source of the anomaly. Unfortunately, project funding limitations prevented us from collecting this data component. Independent of the successful detection of DNAPLs, our multi-offset crosswell radar and seismic datasets yielded high resolution velocity images of key cross-sections of the site with spatial resolutions sufficient to track lithological subunits of less than 1/2 m thickness. In particular, our radar tomograms allowed us to map shallow lithologic/hydrogeologic units at the site including the vadose zone transition, the topography of the upper/lower surficial aquifer contact, and the B subunit within the upper surficial aquifer. Our results showed good agreement with CPT and gamma logs giving us increased confidence in the quality of both the seismic and radar tomograms. We believe that our simultaneous tomographic inversion of 8 crosswell seismic surveys covering a 22 x 7.5 m plane is among the highest resolution shallow velocity images acquired with significant lateral extent.

10.0.2 The Role Of Crosswell Geophysics?

Our application of crosswell techniques at Pinellas highlighted several traditional strengths and weaknesses of such geometries. The first and most significant problem was the lack of areal extent in our crosswell measurements. Although the velocity images we generated were high resolution by near-surface standards, they only extended across one relatively small cross-section of the site and were therefore difficult to use for detection purposes. This problem is fundamental to the crosswell geometry and can only be solved by the installation of more wells, a procedure which can seldom be justified solely for geophysical data acquisition. For crosswell imaging, coverage is traded for high spatial resolution and an attractive S/R geometry for velocity reconstruction.

As in the case of petroleum reservoir characterization, the ability to image over longer interwell spacings would have allowed us to build more continuous site profiles. At the same time, longer offsets would also have required deeper monitoring wells to allow preservation of angular aperture, a key parameter in the reconstruction process. Increasing source strength or decreasing source frequency are two obvious solutions to this problem applicable for both radar and seismic acquisition. Slim-hole orbital vibrators [66], sparkers, and low-volume air guns may offer some possible alternatives to piezoelectric sources for long-offset shallow seismic imaging.

The capacity to consistently acquire high-quality shear wave data would also greatly enhance the utility of near-surface crosswell seismic surveys by offering greater discrimination between lithologic and fluid-induced anomalies. Regions with partial gas saturation should have a particularly low V_p/V_s ratio since μ should be unchanged by a modification of fluid properties. A combination of slim-hole vibrators [66] [67] and multi-level 3-component receivers would probably be the first step in acquiring data of this type. The downside of locking arrays is decreased acquisition speed but in the case of environmental sites with relatively shallow wells this constraint becomes less significant. At Pinellas, our crosswell seismic surveys typically required only 4 depth offsets of a 24 channel hydrophone array; the addition of locking time would have been relatively small in comparison to the total acquisition time.

As mentioned previously, one advantage of crosswell imaging in comparison to surface or VSP geometries is higher signal bandwidth which increases the maximum spatial resolution of the recovered image. At Pinellas, the average crosswell seismic gather typically had a bandwidth of 4 to 5 kHz in comparison to 500 to 700 Hz for our near-offset VSP measurements. Although the mean λ value for our seismic surveys was approximately 30 cm, the smallest features which we believe were reliably imaged, sections of the upper surficial aquifer B subunit, were closer to 50 cm in thickness. Nonetheless, by linking together and jointly inverting multiple crosswell surveys we were able to generate velocity images with both significant lateral extent (22 × 7.5 m) and vertical resolutions on the order of 50 cm. This type of velocity image could not be generated any traditional technique. NMO velocities recovered from surface seismic reflection surveys generally have low resolution and additionally require coherent reflectors for velocity estimation. Surface seismic refraction surveys also have significantly lower resolutions with signal bandwidths typically less than 400 Hz.

10.0.3 The Next Generation Of Field Experiments

With the benefit of hindsight, we now envision crosswell methods as part of a multi-tiered approach to the geophysical detection and characterization of DNAPLs. A surface method with significant areal extent, possibly IP or surface GPR with AVA/AVO analysis, would be initially applied to locate prospective targets. High-resolution VSP and crosswell methods would then be used to provide a detailed view of the target region using either existing wells or CPT platforms for acquisition. Final confirmation of DNAPLs would be carried out with push-based fluid sampling [213]. All three datasets would also be used for a simultaneous hydrogeophysical characterization of the site, possibly in concert with shallow logging data. The areal coverage of surface-based methods is particularly useful in building site-wide flow models where key hydrogeologic units, such as the surficial aquifer and the Hawthorn clays at Pinellas, must be delineated. The final product passed to site hydrogeology and engineering staff would combine geological structure and information on NAPL distribution into a form suitable for inclusion in modeling contaminant transport and planning remediation activities.

Crosswell techniques as stand-alone methods seem better suited to monitoring or characterization problems where the area of concern is known *a priori* as is the case in remediation. In these cases, areal coverage is less important than high spatial resolutions and the recovery of semi-quantitative images which can be converted into maps of petrophysical properties. Past applications of crosswell methods to remediation problems include the monitoring of air sparging [90] and enhanced bioremediation [158]. The active monitoring of remediation is particularly valuable in cases where the geophysical results might allow dynamic adjustment of process parameters. In the case of enhanced bioremediation, an accurate image of the spatial distribution of bacterial feedstock would allow site managers to plan additional delivery wells or increase injection rates at selected locations to maximize biodegradation of contaminants. The same ideas could also be applied to thermal remediation processes where the *in situ* temperature field must be monitored and power distribution to subsurface heating electrodes is the quantity to be optimized. Dynamic imaging of tracer injections to recover permeability variations is another application well-suited to crosswell methods [74] [242] as are vadose zone infiltration experiments [170]

10.1 Soft Sediment Petrophysics For Site Calibration?

The laboratory component of our research project was relatively successful. We were able to place radar-based DNAPL detection on a firm petrophysical footing by performing some of the first high frequency core-scale dielectric measurements of aquifer sediments partially saturated with TCE. Using the results of our solvent injection experiments, we were able to confirm the applicability of the Bruggeman-Hanai-Sen (BHS) and complex refractive index (CRIM) models for the prediction of the bulk dielectric constant of DNAPL contaminated soils. Acoustic measurements [1] performed on similarly saturated Pinellas core materials observed the same trends seen in previous measurements of this type [111], a reduction in P-wave velocity and an increase in P-wave attenuation. Gassmann fluid substitution combined with the Hill equation provided a good lower bound on the effects of DNAPLs on soil V_p values. We were also able to develop a volumetric empirical model based on the 11 available NAPL injection experiments which predicts a larger change in V_p than Gassmann fluid substitution. Although we were not able to fully explain P-wave attenuation trends, the possibility of modulus changes induced by fluid effects at grain contacts seems to be an interesting topic for future research.

Unfortunately, the results generated during our laboratory study were more effective at evaluating basic petrophysical relationships than calibrating site seismic and radar response. The main barriers to site calibration were difficulties with maintaining sample integrity and matching core dimensions to the sample volume/shape required for property measurements. The process of coring, transport, de-watering, and consolidation altered the soil fabric enough to make us hesitate in explicitly using laboratory V_p values as even soft constraints on our tomographic images. Additionally, the laboratory measurements were carried out at ultrasonic frequencies in contrast to the 4 kHz peak frequencies observed in the field; this discrepancy further complicates the calibration process, particularly in cases where attenuation plays a significant role. In the case of our dielectric measurements, the shape of the required sample, a long narrow cylinder with an interior hole, forced us to homogenize our samples and then pack the resulting material into the column. Surprisingly, in both the acoustic and dielectric cases the V_p and κ values measured in the lab were well within the range observed in the field despite significant alteration of the matrix materials. Another constraint on our petrophysics database was the time-intensive nature of soft sediment laboratory measurements; if sample preparation, secondary analysis, and saturation times are considered, each experiment took between 3 and 5 days to conduct assuming no equipment failures. Building a true petrophysics

---

[1] All new experimental acoustics data discussed was collected with Jil Geller (LBNL) who performed the laboratory seismic component of the Pinellas project.

database is difficult when every data point requires a week of effort in the lab not including the months involved with building, testing, and calibrating the measurement system.

One approach to increasing the available database would be to assemble a acoustic/dielectric core scanning system which allow continuous, non-contact measurements on long core sections. In addition to obtaining higher resolution V_p and κ measurements, such an approach would eliminate the need to subsection core and reduce the chance of sediment alteration. A serious near-surface core analysis project might use ODPs strategy of building a high-speed "assembly line" for the measurement of core properties immediately after excavation. Another strategy might exploit high-resolution log measurements for use as the petrophysical calibration dataset, a common practice in petroleum industry. The problem with this approach is the low quality of near-surface logs, particularly sonic logs. Even if our sonic logging attempts had been successful, the 2 m tool length insured that the resulting velocity model would have had a lower vertical resolution than the crosswell seismic measurements which we wanted to calibrate (!). As near-surface logging techniques are refined, this approach may become more attractive since it has the potential for providing local petrophysical measurements in the field without the laborious and possibly disruptive process of coring and lab analysis. Additionally, logs guarantee that acoustic measurements are made at true *in situ* stress states, a key component which is difficult to replicate in the lab at low pressures.

10.2 Concluding Thoughts

Over the next several years the DOE anticipates finishing remediation of the NAPL source regions at the NE site, afterwards entering a period of monitoring to ensure that site water quality achieves federal and state standards. DOE presence at the site will be gradually phased out and eventually development will proceed in this rapidly growing community. In this sense, the characterization and remediation of Pinellas is a finite problem which is being solved with current technologies, albeit at higher costs than we might expect. The DOE "mega-sites" such as Hanford, Savannah River, and Rocky Flats, are entirely different animals in comparison to Pinellas; all three have large long-term budgets, tremendously complex contamination problems which are not solvable using current methods, and the additional constraint of unrealistically short clean-up timeframes agreed to by federal authorities. At places like Hanford, the clean-up costs are so enormous that development of highly specialized geophysical characterization techniques can be justified, particularly considering the large spatial dimensions and high costs of direct sampling. Pinellas is more typical of the thousands of existing NAPL contaminated sites in the US, being relatively small with a limited budget. Consequently the role of geophysics at Pinellas is fundamentally different from Hanford, in that geophysics has a finite temporal window for which it is useful in the characterization process and must be applied in a fashion to considerably reduce costs with a relatively low risk of failure. While the results of our investigation arrive too late in the lifespan of Pinellas to significantly change the course of remediation activities, the lessons learned are applicable to a large number of sites still at earlier stages of development.

Appendix A

Wavefield Modeling

In previous chapters we have shown several full-wavefield sensitivity tests using velocity models generated from the results of two-phase flow simulations. In this short appendix we provide details of the numerical schemes used to generate these examples and a brief demonstration of their capabilities.

A.1 Simulating Radar Response

Forward modeling techniques for ground penetrating radar vary greatly in both physical realism and computational complexity. While simple models based upon ray theory [114] are often used for quick predictive simulations and tomographic inversion, 2D and 3D solutions to Maxwell's equations including multiple frequency dependent loss mechanisms, anisotropy, and realistic antenna radiation patterns have also been developed [268] [47] [48] [30] [49]. To effectively model full GPR surveys consisting of hundreds of shot locations and multiple models, a compromise must be made between an efficient simple techniques which quickly yield unrealistic results and methods with very complete descriptions of the physics which can only be applied to trivial problems due to their computational complexity. Considering these trade-offs we had four basic requirements for our choice of modeling technique,

A Wave-based Approach To allow a realistic understanding of spatial resolution as a function of frequency we decided that a wave approach (vs. asymptotic ray-theory) was required.

Conductive Losses Since the ability to collect radar data in the field is largely controlled by soil conductance, lossless wave propagation models are less useful for numerical estimation of penetration depth and cannot be used in synthetic imaging experiments where a significant clay fraction exists.

2D Property Heterogeneities While layered models are useful in some situations, we felt that true 2D property (dielectric,conductivity) variations were required to explore relevant near-surface problems, including the modeling of realistic DNAPL spill geometries.

Full Survey Modeling Since the goal of our work has always been the modeling of full radar surveys over complex environments, a significant requirement for an effective simulation technique is high computational efficiency.

The physical requirement of a wave-based approach disallows most ray and eikonal equation models for solution of the radar problem. Requiring 2D heterogeneities eliminates the class of semi-analytic RT solvers which can be efficient for 1D models. Computational efficiency requirements eliminated several of the more realistic governing equations for radar modeling including a full solution to Maxwell's equations like Yee's method. A good compromise was the TE-Mode E_y solution used by Casper and Kung [53] which is essentially a scalar wave equation with a conductive loss term. The model equation solved is only rigorously valid under the following assumptions,

1. All material properties are 2D i.e. vary only in the x-z plane.
2. Electric and magnetic field intensities are invariant in the y direction (also only 2D)
3. Relative magnetic permeability is constant
4. Electric charge density is zero everywhere
5. Antenna radiation is mainly into the E_θ and H_ϕ fields

A more complete description of these limitations and a full derivation from Maxwell's equation is included in [53]. The resulting lossy wave equation we solve can be written as,

$$\frac{1}{V^2}\frac{\partial^2 E_y}{\partial t^2} + \mu_o\,\sigma\frac{\partial E_y}{\partial t} = \frac{\partial^2 E_y}{\partial x^2} + \frac{\partial^2 E_y}{\partial z^2} \tag{A.1}$$

,

where E_y is the y component of the electric field, σ is conductivity, μ_o is the permeability of free space, and V is the effective radar velocity, which can be written in terms of c, the speed of light in a vacuum, and κ the relative dielectric permittivity,

$$V = \frac{c}{\sqrt{\kappa}}. \tag{A.2}$$

To solve equation (A.1) for complex heterogeneous media, we must discretize both the space and time variables and their associated partial derivatives. One approach is to use the well-developed time-domain finite-difference (FDTD) technique [251]. In the following sections we use (i, j) subscripts for specifying spatial locations on the computational grid and (n) superscripts are used for specifying time step. We discretize the time derivatives using a second order central difference operator for $\frac{\partial^2 E}{\partial t^2}$ and a first order forward difference operator for $\frac{\partial E}{\partial t}$, both of which can be expressed as,

$$\frac{\partial^2 E}{\partial t^2} = \frac{E^{n+1} - 2E^n + E^{n-1}}{(\Delta t)^2} \tag{A.3}$$

$$\frac{\partial E}{\partial t} = \frac{E^{n+1} - E^n}{\Delta t}. \tag{A.4}$$

Substituting equations A.3 and A.4 into equation A.1 yields,

$$\frac{1}{V_{i,j}^2}\left[\frac{E_{i,j}^{n+1} - 2E_{i,j}^n + E_{i,j}^{n-1}}{\Delta t^2}\right] + \mu_o\,\sigma_{i,j}\left[\frac{E_{i,j}^{n+1} - E_{i,j}^n}{2\Delta t}\right] = \left[\frac{\partial^2 E^n}{\partial x^2} + \frac{\partial^2 E^n}{\partial z^2}\right]. \tag{A.5}$$

Note that the spatial derivatives have not yet been discretized. By factoring equation (A.5) in terms of time steps we can write an explicit time evolution equation for the E field,

$$E_{i,j}^{n+1} = C_1\left[\frac{\partial^2 E^n}{\partial x^2} + \frac{\partial^2 E^n}{\partial z^2}\right] + C_2 E_{i,j}^n - C_3 E_{i,j}^{n-1}, \tag{A.6}$$

where C_1, C_2, and C_3 are three time independent coefficients which can be pre-calculated for every grid location for additional computational efficiency.

$$C_1 = \left[\frac{1}{V_{i,j}^2\,\Delta t^2} + \frac{\mu_o\,\sigma_{i,j}}{\Delta t}\right]^{-1} \tag{A.7}$$

$$C_2 = C_1\left[\frac{2}{V_{i,j}^2\,\Delta t^2} + \frac{\mu_o\,\sigma_{i,j}}{\Delta t}\right] \tag{A.8}$$

$$C_3 = C_1\left[\frac{1}{V_{i,j}^2\,\Delta t^2}\right]. \tag{A.9}$$

Before a full solution is possible, a technique for calculating the spatial derivatives in equation A.6 must be chosen. Casper and Kung [53] use a high accuracy pseudospectral method for computing the derivatives. Our solver supports spatial derivative calculations using either the pseudospectral method or finite differences with the choice of 2nd, 4th, 6th, or 8th order central operators. Substituting the 2nd order central difference operator from equation A.3 for the spatial derivatives in equation A.6 yields a simple scheme which is 2nd order accurate in time and space,

$$E_{i,j}^{n+1} = C_1\left[\left(\frac{E_{i+1,j}^n - 2E_{i,j}^n + E_{i-1,j}^n}{\Delta x^2}\right) + \left(\frac{E_{i,j+1}^n - 2E_{i,j}^n + E_{i,j-1}^n}{\Delta z^2}\right)\right] + C_2 E_{i,j}^n - C_3 E_{i,j}^{n-1}. \tag{A.10}$$

In practice, higher order spatial derivatives are desirable. Higher order schemes allow coarser sampling of the wavefield without the introduction of numerical dispersion, greatly reducing computational cost [65]. While pseudospectral methods [98] [144] allow spatial sampling at near the Nyquist frequency ($\sim 2\, s/\lambda$) they also require computation of a large number of $O(n\ \log n)$ FFTs which in practice is more time consuming than the use of high order FD stencils. Using 8th order difference operators, spatial samplings of 3 to 4 grid points per wavelength can be used without greatly reducing waveform quality. The stencils for the 4th, 6th, and 8th order approximations to the second spatial derivative are,

$$\frac{\partial^2 E}{\partial x^2} = \frac{-E_{i+2,j} + 16E_{i+1,j} - 30E_{i,j} + 16E_{i-1,j} - E_{i-2,j}}{12(\Delta x)^2} \tag{A.11}$$

$$\frac{\partial^2 E}{\partial x^2} = \frac{2E_{i+3,j} - 27E_{i+2,j} + 270E_{i+1,j} - 490E_{i,j} + 270E_{i-1,j} - 27E_{i-2,j} + 2E_{i-3,j}}{180(\Delta x)^2} \tag{A.12}$$

$$\frac{\partial^2 E}{\partial x^2} = \frac{1}{(\Delta x)^2}\left[C_0 E_{i,j} + \sum_{m=1}^{4} C_i(E_{i-m,j} + E_{i+m,j})\right], \tag{A.13}$$

where the coefficients for the 8th order form are

$$\begin{aligned} C_0 &= \tfrac{-205}{72} \\ C_1 &= \tfrac{8}{5} \\ C_2 &= \tfrac{-1}{5} \\ C_3 &= \tfrac{8}{315} \\ C_4 &= \tfrac{-1}{560} \end{aligned} \quad . \tag{A.14}$$

Source Function

Several source functions were implemented including a Ricker wavelet, a Gaussian pulse, and a Gaussian tapered *cos* function. We used a so-called “hard” source where the E field is forced to take the value of the source function at the source location for the duration of the recorded wavelet.

Stability Conditions

We use the stability condition derived by Casper and Kung [53] to determine the simulation timestep,

$$\Delta t \; = \; \frac{\sqrt{2}}{\pi}\frac{\Delta x}{max(v)}, \tag{A.15}$$

where v is the velocity field. When $\sigma > 0$ this condition can be somewhat relaxed and the timestep increased but we conservatively use A.15 for all models.

Absorbing Boundary Conditions

We use the sponge absorbing boundary condition suggested by Cerjan et.al. [56] to eliminate spurious reflections from the edges of the computation grid. The sponge condition exponentially attenuates waves passing through a buffer region on the edge of the grid. We use a buffer region with a 10λ width which, in practice, is typically between 30 and 45 points deep for our models. Although weak reflections are still visible at some gain levels, they are much smaller than the primary and significant reflections.

Implementations

Three versions of our 2D radar modeling code were written, a stand-alone C++ code with a GUI front-end to allow model visualization, a MATLAB implementation where the C++ computational kernel was called using a mex gateway function, and a pure MATLAB version suitable for platform-independent distribution. The stand-alone C++ code is relatively fast and allows rapid calculation of full surveys. The C++ FD kernel is modular and exists as a separate class, *gpr2D_FD_engine*. The pure MATLAB code explicitly generates the 8th order laplacian in sparse matrix form and takes advantage of MATLAB's high speed matrix/vector multiplication operation instead of performing an explicit double for-loop over the mesh. While the pure MATLAB version is the slowest and most memory hungry of the three implementations, it is fast enough for most light modeling tasks and is also easy to incorporate into the reverse time-migration and full wavefield inversion codes which we currently developing inside the MATLAB environment.

A.2 Seismic Modeling Method

Our seismic modeling code is almost identical to our radar implementation with the exception of variable names and physical interpretation. We first present a brief derivation of the acoustic wave equation followed by a short outline of differences between the two codes.

A.2.1 Deriving The Acoustic Wave Equation

Following Keiswetter et.al. [139], the acoustic wave equation for variable density/velocity media can be derived from the differential form of Euler's flow equation and the continuity equation,

$$\frac{\partial \hat{v}}{\partial t} = -\frac{1}{\rho}\nabla p \tag{A.16}$$

$$\frac{\partial p}{\partial t} + \rho V^2 \, \nabla \cdot \hat{v} = 0, \tag{A.17}$$

where p is pressure, ρ is fluid density, V is the propagation velocity of sound through the fluid, and $\hat{v}$ is particle velocity. After taking the divergence of Euler's equation and the first derivative of the continuity equation with respect to time, we are left with,

$$\frac{\partial(\nabla \cdot \hat{v})}{\partial t} = -\nabla \cdot \left[\frac{1}{\rho}\nabla p\right] \tag{A.18}$$

$$\frac{\partial^2 p}{\partial t^2} + \rho V^2 \left[\frac{\partial(\nabla \cdot \hat{v})}{\partial t}\right] = 0. \tag{A.19}$$

Substitution of equation (A.18) into equation (A.19) yields a simple scalar wave equation for heterogeneous media,

$$\frac{1}{V^2}\frac{\partial^2 p}{\partial t^2} = \rho \, \nabla \cdot \left[\frac{1}{\rho}\nabla p\right]. \tag{A.20}$$

We will consider equation (A.20) explicitly in 2 dimensions, written as,

$$\frac{1}{V^2}\frac{\partial^2 p}{\partial t^2} = \rho \, \left[\frac{\partial}{\partial x}\left(\frac{1}{\rho}\frac{\partial p}{\partial x}\right) + \frac{\partial}{\partial z}\left(\frac{1}{\rho}\frac{\partial p}{\partial z}\right)\right]. \tag{A.21}$$

Equation A.21 does not include any loss mechanisms. We add a heuristic diffusive loss term which is completely analogous to the conductive loss term in the second order hyperbolic form of the TE mode wave equation. This viscoacoustic wave equation can be written as,

$$\frac{1}{V^2}\frac{\partial^2 p}{\partial t^2} \; + \eta\frac{\partial p}{\partial t} = \rho \, \left[\frac{\partial}{\partial x}\left(\frac{1}{\rho}\frac{\partial p}{\partial x}\right) + \frac{\partial}{\partial z}\left(\frac{1}{\rho}\frac{\partial p}{\partial z}\right)\right], \tag{A.22}$$

where η is a loss coefficient. If we assume that ρ is constant, we are left with an equation identical to A.1 with the exception that E_y is replaced by p and σ by η,

$$\frac{1}{V^2}\frac{\partial^2 p}{\partial t^2} + \eta\frac{\partial p}{\partial t} = \frac{\partial^2 p}{\partial x^2} + \frac{\partial^2 p}{\partial z^2}. \tag{A.23}$$

While σ in the TE-mode wave equation was a loss mechanism with a straight-forward physical interpretation, the η term in equation A.23 is a heuristic viscosity which only has meaning in the case of a wave propagating in a pure fluid. We will use η to introduce losses in a qualitative fashion since representation of the appropriate $Q_p(f)$ models are not possible with our current formulation. In one example we will make η proportional to a map of $1/Q_p$ normalized across the model. This approach provides some intuition as to the effects of different spatial distributions of attenuating materials but is not sufficient for quantitative modeling.

A.3 Notes Concerning Implementation

A.3.1 Shot Parallelization

To allow the rapid simulation of large surveys involving hundreds of shot locations, we developed a version of both modeling codes suitable for use on high-latency distributed memory architectures e.g. clusters and pile-of-pcs (POP) systems. The parallel version is based upon the C++/MEX implementation of both codes; all load balancing and process management is handled within MATLAB. Parallelization is handled on the shot level with a pool-of-tasks resource allocation model. Each node is passed a bundle of input data including the location of the current shot, the positions of all receivers, the velocity model, and any auxiliary information concerning the source wavelet and boundary conditions. After completing a given shot, each node returns a synthetic seismogram and is handed a new shot location if any remain. With this approach, no communication is required between nodes during modeling besides the passing of simulation parameters and the return of results. Message passing between the master process and various slave tasks is handled using temporary files and a shared NFS partition instead of MPI. While this approach is relatively expensive, a disk write and read are required for each message passed, the small number of messages required in shot parallel codes insures that communication time is still a very small percentage of total run-time.

A.3.2 Cache Optimizations

A major modification made to the C++ version of our lossy scalar wave equation solver was the introduction of a cache-coherence optimization in the kernel of the FD algorithm. Instead of looping over columns or rows as is typically done in the interior double for-loop, we loop over small patches of the grid to improve the likelihood of cache data reuse. The reordering of the FD evaluations has no impact on the algorithm's result but yields speedups of 40 % on some architectures. The one free parameter in this type of cache optimization is the size of the small patches used for the inner loop. In general, machines with larger L1 caches should use larger patches, however we calculate the optimum patch size empirically through a search over all reasonable values. For most architectures a patch size of 40x40 was an excellent default choice with speedups ranging from 10 % to 40 % over the previous version of the code.

A.4 Example Wavefields

Figure A.1 shows a set of synthetic results for a relatively simple model with a single attenuating block and a similarly attenuating thin layer. The synthetic model used for our demonstration was a 2D domain, 10 m in height and 5 m in width, similar to the dimensions of many well pairs at Pinellas. The mesh is sampled at 0.05 m in both the X and Z directions. A single source was included at 5 m depth on the left boundary of the model. Seismograms were recorded using 100 receivers located on the right boundary of the model. A 3 KHz Ricker wavelet was generated at the source location. Figure A.1 shows wavefield snapshots on the left column with the two anomalous objects superimposed in black. In all cases V_p is a homogeneous 1500 m/s with only the η value for the block and the layer varying. The η values used are 0.01, 0.002, 0.001, and 0.0005 with the 0.01 model occupying the top row. The right hand column shows the corresponding synthetic seismograms. As can clearly be seen, the high η regions efficiently attenuate the primary arrival. Additionally, the change in loss characteristics is an effective impedance contrast and can generate reflected arrivals as is apparent for the 0.01 and 0.002 η models. Wavefront healing is also visible in the 0.01 and 0.002 models; a first arrival is visible directly behind the attenuating block despite the fact that these receivers are located in a specular shadow zone. A demonstration of our forward modeling codes on a realistic DNAPL spill geometry is included in chapter 7.

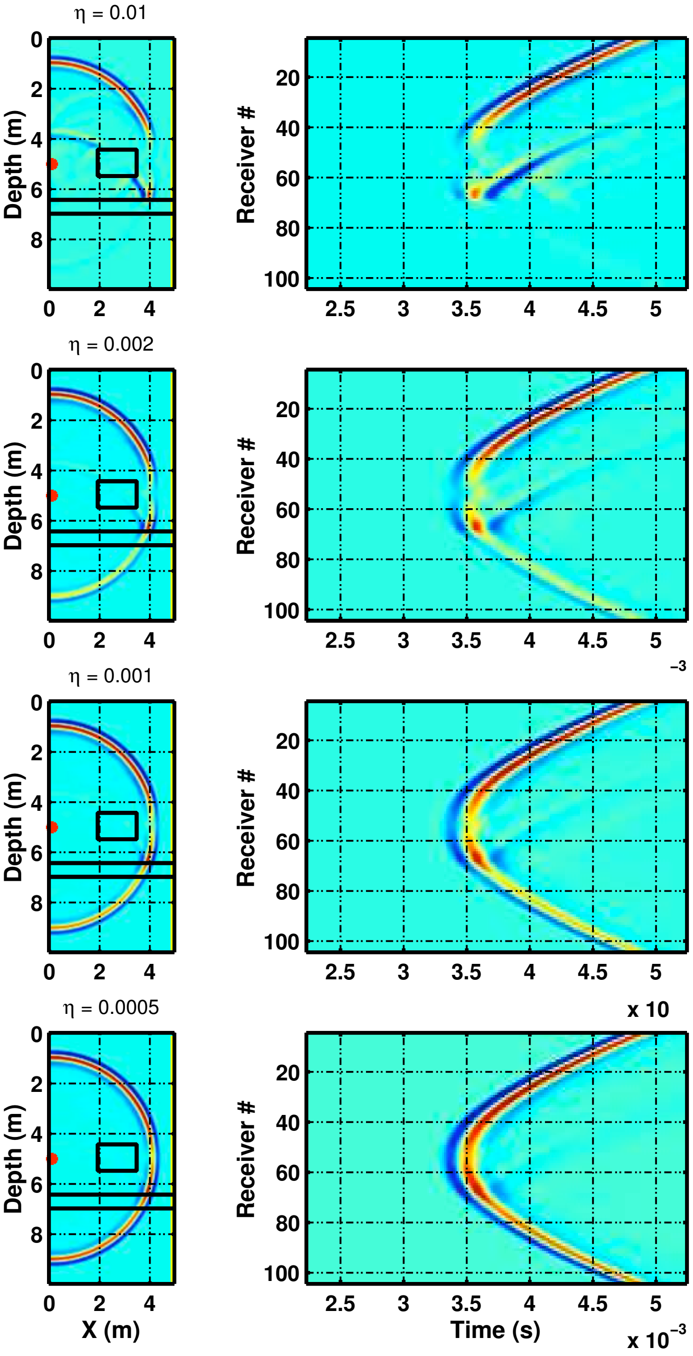

Figure A.1: Example wavefields for viscoacoustic modeling : The left column depicts wavefield snapshots for 4 models with the same geometry but different η values for the central block and thin layer. The source is marked red while 100 receivers are positioned on the opposite side of the model. The right column shows the corresponding synthetic seismograms in true-amplitude form (no clip).

Appendix B

Data Preprocessing, QC, And Picking

Although the preprocessing and picking of seismic and radar datasets is decidedly less glamorous than tomographic inversion, the success of an imaging experiment is probably more dependent upon these steps than the choice of tomography algorithm. Because of very close interwell spacings, near-surface crosswell measurements are exquisitely sensitive to S/R positioning and should be screened for geometry errors. Similarly, errors in the picking of first arrivals , particularly ones with correlated non-Gaussian statistics such as those related to cycle-skipping, can corrupt tomographic images and should be considered within the pre-processing phase.

Since the seismic and radar data collected in the field are simply a collection of unlabeled traces, several steps are required to convert the acquired data into a usable format with the appropriate geometry and header information. Although we will only consider the seismic case the same process with slight modification of file format names is also applied to our radar datasets. A crosswell seismic dataset as collected in the field, is a set of raw shot gathers stored in SEG-2 format with the relevant survey parameters hand-written as observer notes. Before integrating any header information, the SEG-2 gathers are sequentially converted to SEG-Y and then to Seismic Unix (SU) format The observer notes are digitized for later conversion to a survey specification file. The SU files are loaded into MATLAB using a custom script where they are integrated with the survey specification (SS) file and a site geometry (SG) file. The SS file contains all the parameters recorded at the well including Δt, sample counts, vertical stacking rates, and wire-line S/R depths. The SG file contains a complete database of site geometry in absolute state-plane coordinates including well head locations (northing, easting, elevation, and monument stand-up) acquired from EDM surveys and any well deviation data required for conversion from wire-line to absolute positions. The resulting dataset has a fully specified geometry in an absolute coordinate system suitable for integration with surface surveys or logging data. Figure B.1 shows these processing steps in graphical form.

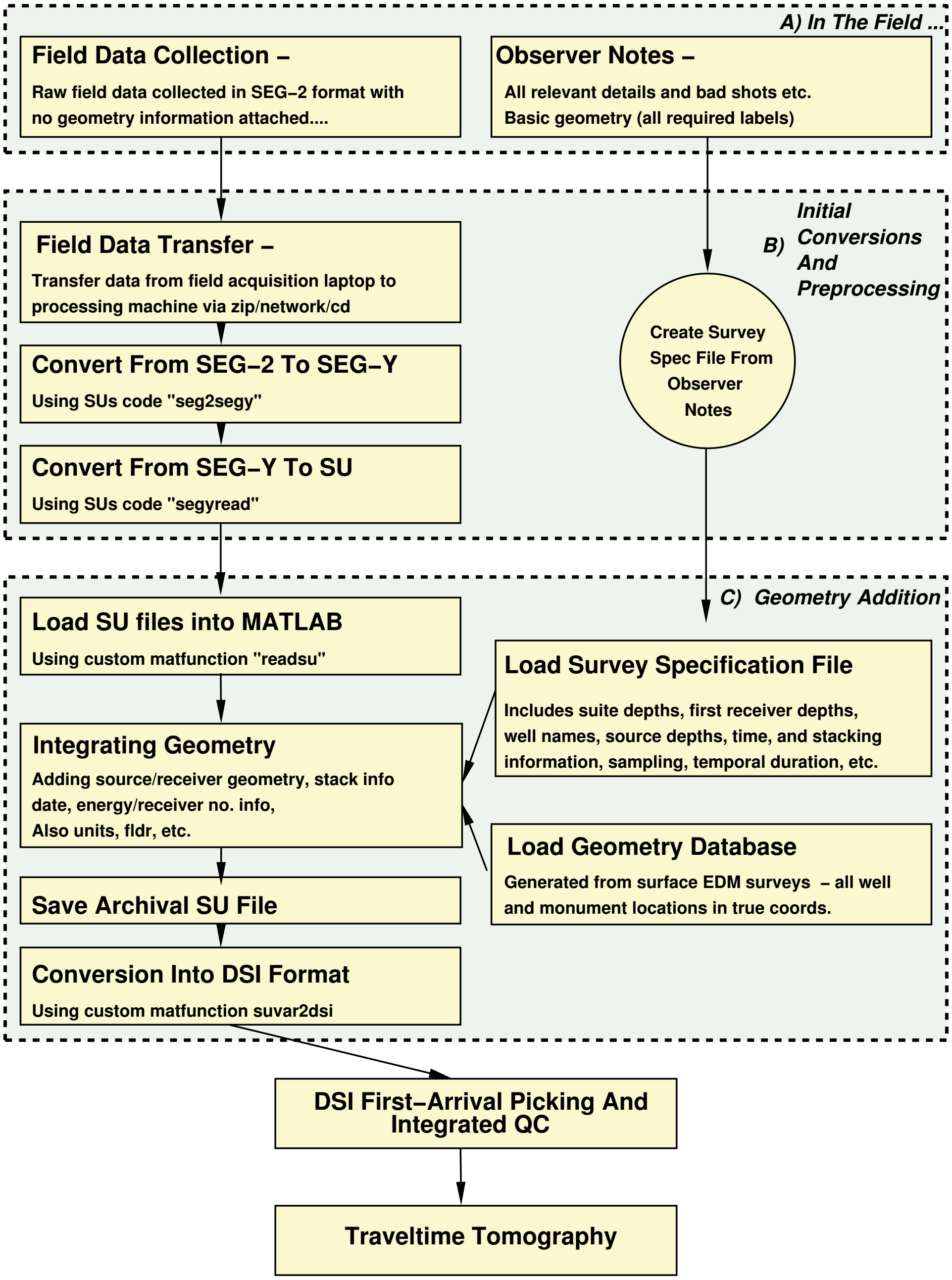

Figure B.1: Seismic data preparation flow

Figure B.2 shows our general approach to picking both seismic and radar traveltimes. We typically begin the process by manually picking first-break arrivals in the shot gather domain. When examining first arrivals we avoid significant filtering or deconvolution, two operations which often modify the phase of the primary wavelet. We do use an interactive combination of trace amplitude equalization and AGC to examine the character of individual traces at a finer scale. During the preliminary picking process we mark traces with low S/N where picking is too uncertain for inclusion in tomographic inversion.

After initially picking the dataset, we generate a set of quality control panels to evaluate geometry and pick consistency errors. We check for geometry errors using the methods described by Peterson [216], the most effective being crossplots of apparent velocity vs. take-off angle. Assuming straight rays, apparent velocities are calculated using the first-arrival pick and the Cartesian length of the ray. These apparent velocities are then cross-plotted with take-off angle as shown on top panel of figure B.3 : asymmetries and inflections of the resulting cross-plots can be used to diagnose mistakes in well-offset or static errors in source or receiver depths. A common source of geometry errors are simple mistakes made in the digital transcription of observer notes. Our first step when geometry errors are detected is a careful examination of observer notes, site EDM data, and geometry files for internal consistency. If no geometry errors are detected we generate several plots of our raw picks in the source/receiver domain.

The bottom left panel of figure B.3 shows a colormap of picked traveltimes as a function of source and receiver number. In this plotting domain columns, correspond to receiver gathers while rows correspond to shot gathers. Discontinuities in this display are indicative of a jump in picked times between gathers, often a sign of a mistake in identification of the true first arrival. In these cases we check for consistency by doing secondary editing in the receiver domain where ambiguity in the first arriving wavelet is sometimes resolved. The lower right panel of figure B.3 shows a similar plot which shows perturbations in apparent velocity as a function of S/R number. In this case a mean velocity is calculated for the entire profile and subtracted from the apparent velocity of each ray. The resulting plot encodes some of the same information as the raw pick grid but is more sensitive to small trace-to-trace variations because times are effectively normalized by ray-length. In practice, tomography can be considered the last step in data QC since tomographic images are sensitive to some of the same errors in geometry and picking.

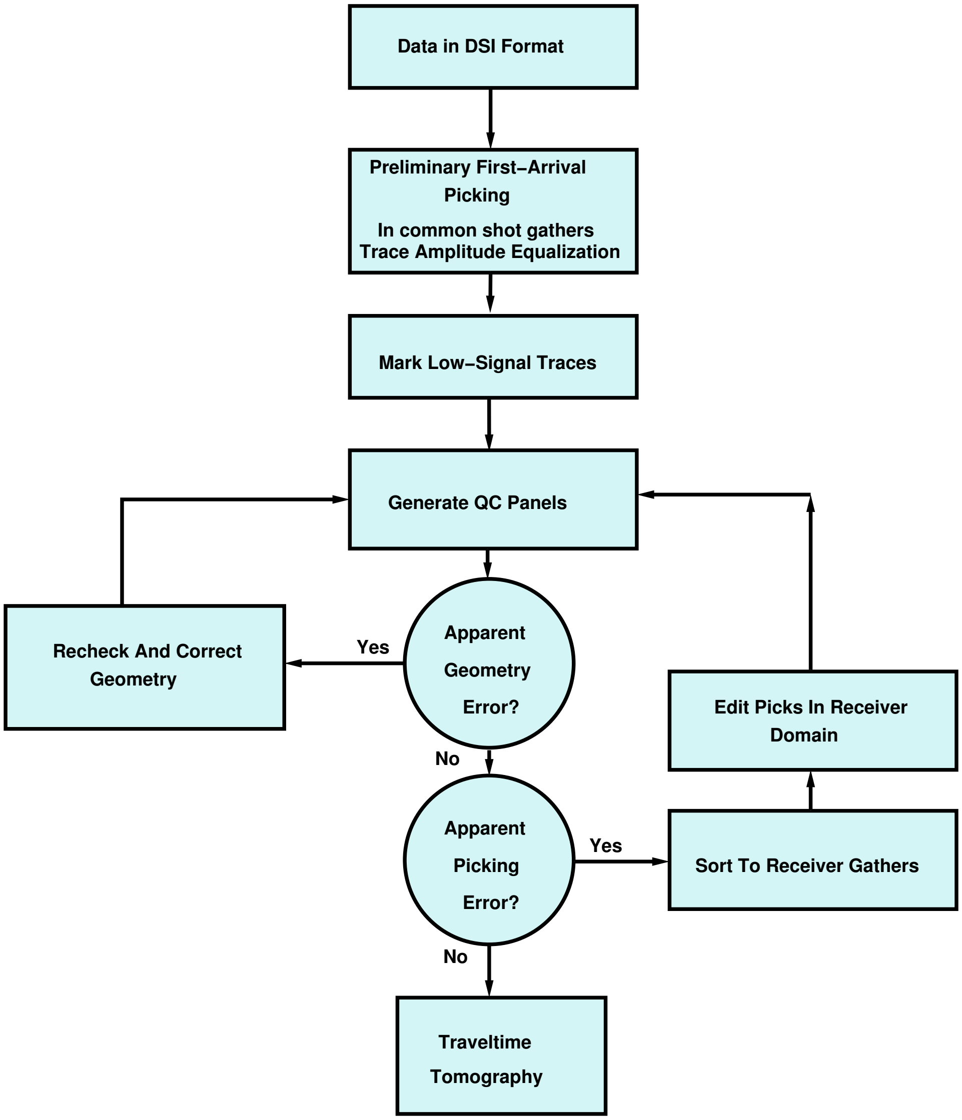

Figure B.2: Standard picking/QC flow

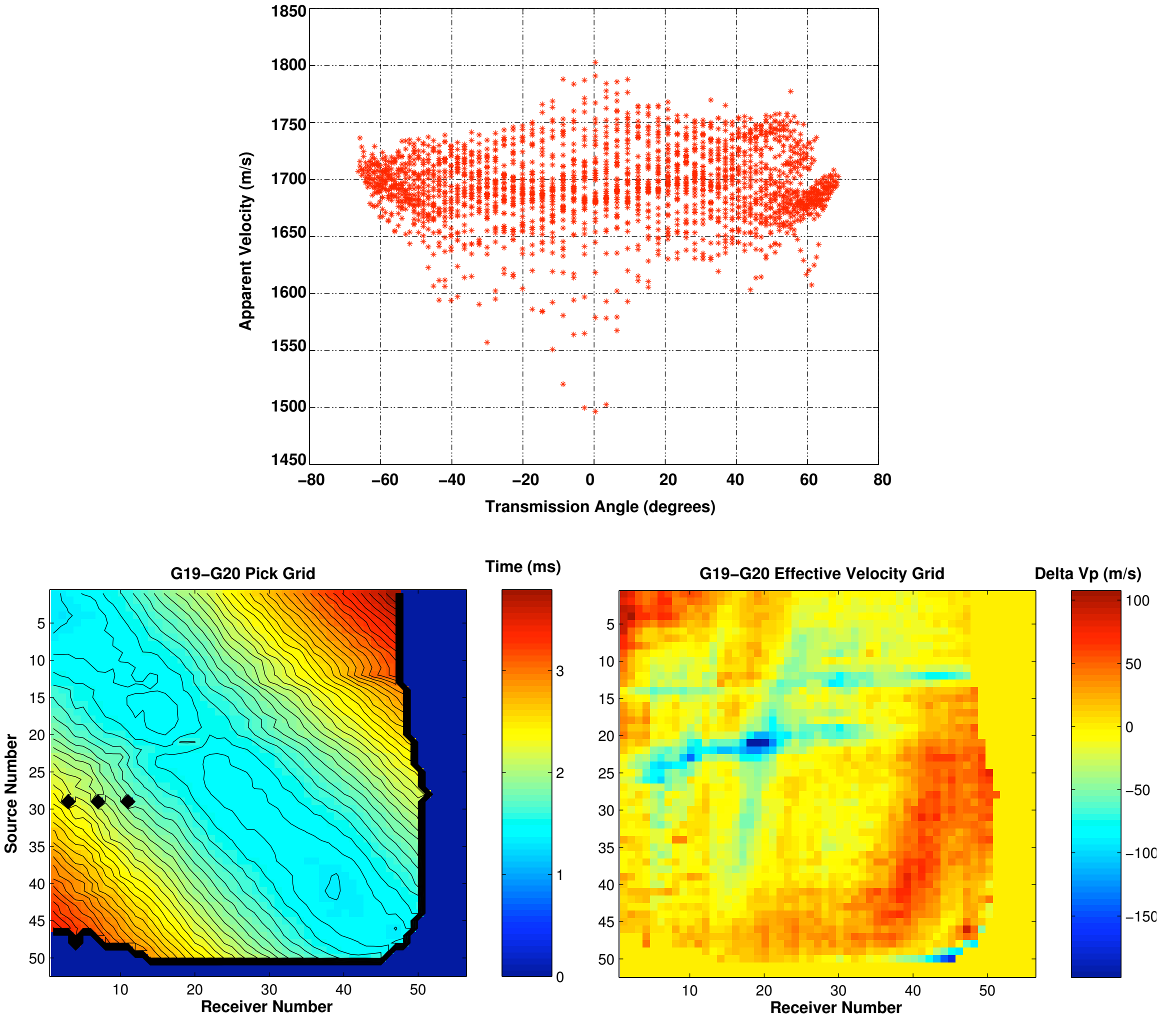

Figure B.3: Three data displays used for quality control on first-break picks and geometry

Appendix C

What Is A Neutron Generator?

Although not directly relevant to the problem of contaminant detection at Pinellas, we were curious about the equipment produced at the plant prior to closure in 1995. Many DOE documents mention that the primary purpose of the Pinellas plant was the fabrication of neutron generators but little hint was given as to precisely what these generators are used for and how they are constructed.

In essence, neutron generators are small linear accelerators used to initiate fission in nuclear warheads after the supercritical mass of fissile material has been assembled. Neutrons are created through the fusion of hydrogen isotopes (deuterium and tritium) by ion acceleration. Within the neutron tube, a deuterium plasma is generated and the resulting ions are accelerated within a high voltage field to impact on a tritium-doped target composed primarily of scandium. The resulting fusion reaction generates a short pulse of 14 MeV neutrons which then initiates fission in the supercritical core. Panels A and B of figure C.1 depict the class of weapons which used GE neutron generators, the Trident II ICBM and the B61 warhead being two examples. Panel C shows a schematic of the physics package, the core component of the warhead, and shows the role of the neutron generator in initiating fission. Panel D shows a simple conceptual diagram of a neutron generator : we were not able to find any designs or photographs of the devices built at Pinellas.

Construction of the generator requires both exotic materials such as molybdenum, scandium, high purity alumina ceramics, and tritium and specialized manufacturing facilities capable of handling metal plating, ceramic-to-metal bonding, and ultrahigh vacuum fabrication. Secondary components manufactured at Pinellas include thermal batteries, specialty capacitors, crystal resonators and other mechanical and electronic components not available through public channels. Such manufacturing tasks could involve the use of chlorinated solvents in a degreasing or cleaning capacity.

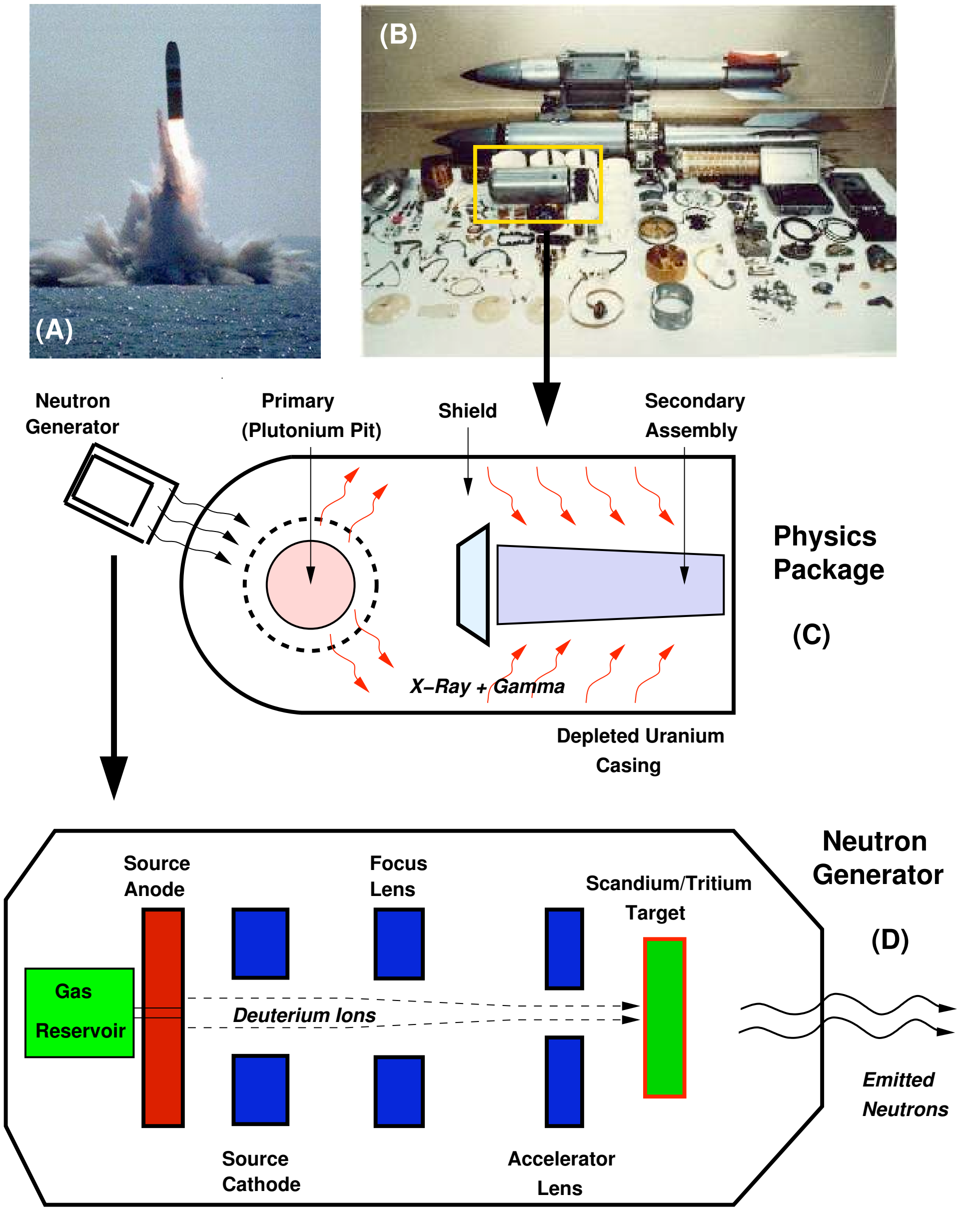

Figure C.1: What is a neutron generator? : Panels (A) and (B) are photos of a Trident II ICBM and a B61 nuclear warhead, both of which use GE neutron generators. Panel (C) is a schematic of the "physics package", the core component of the weapon. Panel (D) is a schematic of a neutron generator of the general type which might be used in such a device. Photographs in panel A and B are from the Federation of American Scientists (FAS) weapons review.

Bibliography

[1] RFA report, Department of Energy (DOE) Pinellas Plant. Tech. Rep. FL6-890-090, US. Environmental Protection Agency (EPA), Region IV, Florida/Georgia Unit, June 1988.

[2] Baseline Environmental Management Report : Pinellas Plant. Tech. rep., U.S. Department Of Energy (DOE) : Office of Environmental Management, 1996.

[3] Geophysical techniques to locate DNAPLs : Profiles of federally funded project. Tech. rep., US Environmental Protection Agency, December 1998.

[4] Northeast site NAPL chacterization report. Tech. Rep. GJO-2000-16S-TAR, U.S. Department Of Energy (DOE), Grand Junction Office, September 2000.

[5] Quarterly progress report for October through December 2000, Sitewide environmental monitoring at the Pinellas STAR center. Tech. Rep. GJO-2001-195-TAR, U.S. Department Of Energy (DOE), Grand Junction Office, January 2001.

[6] Environmental restoration activities at the Young-Rainey STAR center. Tech. Rep. GJ0-2002-334-TAC, U.S. Department Of Energy (DOE), Grand Junction Office, August 2002.

[7] Pinellas environmental restoration project : Sitewide environmental monitoring quarterly progress report for the Young-Rainey STAR center : July through September 2002. Tech. Rep. GJO-2002-378-TAC, U.S. Department Of Energy (DOE), Grand Junction Office, October 2002.

[8] Pinellas environmental restoration project : Biosparaging performance review report. Tech. rep., S.M. Stoller Corporation, June 2003.

[9] Pinellas environmental restoration project : Northeast Site Area A NAPL remediation final report. Tech. Rep. GJO-2003-482-TAC, U.S. Department Of Energy (DOE), Grand Junction Office, September 2003.

[10] Ajo-Franklin, J., Geller, J., and Harris, J. The dielectric properties of granular media saturated with DNAPL/water mixtures. *Geophysical Research Letters 31*, L17501 (2004).

[11] Ajo-Franklin, J., Geller, J., Majer, E., Peterson, J., Williams, K., and Harris, J. Integrated geophysical characterization of a NAPL-contaminated site using borehole and laboratory measurements : T22b-1142. In *EOS Trans. AGU Fall Meet. Suppl.* (2002), vol. 83, American Geophysical Union.

[12] Ajo-Franklin, J., Geller, J., Majer, E., Peterson J., Williams, K., and Harris, J. Integrated geophysical characterization of a DNAPL-contaminated site using borehole techniques. In *Symp.App.Geo.Env.Eng.Prob* (2003), Environmental and Engineering Geophysical Society.

[13] Akhadov, Y. *Dielectric Properties of Binary Solutions - A Data Handbook.* Pergamon Press, 1980.

[14] Aki, K., and Lee, W. Determination of three-dimensional velocity anomalies under a seismic array using first P arrival times from local earthquakes. *Journal of Geophysical Research 1981* (1976), 4381–4399.

[15] Al-Azzawi, S., Awwad, A., Al-Dujaili, A., and Al-Noori, M. Dielectric constants and excess volumes of 2-pyrrolidone + water at several temperatures. *J.Chem.Eng.Data 35* (1990), 463–466.

[16] al Hagrey, S. A. GPR application for mapping toluene infiltration in a heterogeneous sand model. *Journal of Environmental and Engineering Geophysics 9*, 2 (June 2004), 79–85.

[17] Aminabhavi, T., and Banerjee, K. Density, viscosity, refractive index, and speed of sound in binary mixtures of dimethyl carbonate with methanol, chloroform, carbon tetrachloride, cyclohexane, and dichloromethane in the temperature interval (298.15-308.15) K. *J.Chem.Eng.Data 43* (1998), 1096–1101.

[18] Anderson, A., and Hampton, L. Acoustics of gas-bearing sediments. 1. Background. *Journal Of The Acoustical Society of America 67*, 6 (June 1980), 1865–1889.

[19] Anderson, A., and Hampton, L. Acoustics of gas-bearing sediments. 2. Measurements and models. *Journal Of The Acoustical Society of America 67*, 6 (June 1980), 1890–1903.

[20] Anderson, G., Miller, R., and Goodwin, A. Static dielectric constants for liquid water from 300 K to 350 K at pressures to 13 MPa using a new radio frequency resonator. *J.Chem.Eng.Data 45* (2000), 549–554.

[21] Andreae, J. Ultrasonic relaxation in methylene chloride. *Proc.Phys.Soc.B 70*, 1 (1957), 71–76.

[22] Andreae, J., Joyce, P., and Oliver, R. Ultrasonic relaxation in liquid methylene chloride. *Proc.Phys.Soc.B 75* (1960), 82–86.

[23] anf C.J. Eisenmann, Y. S. Toxicological profile for tetrachloroethylene. Tech. rep., U.S. Department Of Health and Human Services, Public Health Service, Agency for Toxic Substances and Disease Registry, 1997.

[24] Arcone, S., and amd P. Peapples, A. D. GPR pulse attenuation in a fine-grained and partially contaminated formation. *Journal Of Environmental And Engineering Geophysics 8*, 2 (2003), 57–66.

[25] Atekwana, E., Sauck, W., and Werkema, D. Investigations of geolectrical signatures at a hydrocarbon contaminated site. *Journal Of Applied Geophysics 44*, 2-3 (2000), 167–180.

[26] Atekwana, E., Werkema, D., Duris, J., S. Rossbach, E. A., Sauck, W., Cassidy, D., Means, J., and Legall, F. In-situ apparent conductivity measurements and microbial population distribution at a hydrocarbon-contaminated site. *Geophysics 69*, 1 (2004).

[27] Atkins, P. *Physical Chemistry.* Freeman And Company, 1978.

[28] Bachrach, R., and Nur, A. High-resolution shallow-seismic experiments in sand, Part I: Water table, fluid flow, and saturation. *Geophysics 63*, 4 (1998), 1225–1233.

[29] Baker, G. Applying AVO analysis to GPR data. *Journal of Geophysical Research 25*, 3 (February 1998), 397–400.

[30] Bergmann, T., Robertsson, J., and Holliger, K. Finite-difference modeling of electromagnetics wave propogation in dispersive and attenuating media. *Geophysics 63*, 3 (1998), 856–867.

[31] Berryman, J. Lecture notes on nonlinear inversion and tomography : Borehole seismic tomography. Tech. Rep. UCRL-LR-105358-Rev. 1, Lawrence Livermore National Laboratory, October 1991.

[32] Berryman, J. Mixture theories for rock properties. In *A Handbook Of Physical Constants*, T. Ahrens, Ed. American Geophysical Union, 1995, pp. 205–228.

[33] Best, A., Tuffin, M., Dix, J., and Bull, J. Tidal height and frequency dependence of acoustic velocity and attenuation in shallow gassy marine sediments. *Journal of Geophysical Research 109* (2004).

[34] Bijwaard, H., Spakman, W., and Engdahl, E. Closing the gap between regional and global traveltime tomography. *Journal of Geophysical Research 103* (December 1998), 30055–30078.

[35] Biot, M. Theory of propagation of elastic waves in fluid saturated porous solids. 1. Low frequency range. *Journal Of The Acoustical Society Of America 28* (1956), 168–191.

[36] Bobik, M. Thermodynamic quantities for liquid benzene : 1. Sound velocities between 283 and 463 K and up to 62 MPa. *J.Chem.Thermodyn. 10* (1978), 1137–1146.

[37] Bohm, G., Galuppo, P., and Vesnaver, A. 3D adaptive tomography using Delaunay triangles and Voronoi polygons. *Geophysical Prospecting 48* (2000), 723–744.

[38] Bohm, G., and Vesnaver, A. In quest of the grid. *Geophysics 64*, 4 (1999), 116–1125.

[39] Born, M., and Wolf, E. *Principles of Optics : Electromagnetic Theory of Propagation, Interference, and Diffraction of Light*. Pergamon Press, 1980.

[40] Bradford, J. GPR offset dependent reflectivity analysis for characterization of a high-conductivity LNAPL plume. In *Symp.App.Geo.Env.Eng.Prob* (2003), Environmental And Engineering Geophysical Society.

[41] Bradford, J. 3D multi-offset, multi-polarization acquisition and processing of GPR data: A controlled DNAPL spill experiment. In *Symp.App.Geo.Env.Eng.Prob* (2004), Environmental And Engineering Geophysical Society.

[42] Brandt, H. A study of the speed of sound in porous granular media. *Journal Of Applied Mechanics 22* (1955), 479–486.

[43] Brewster, M., and Annan, A. Ground-penetrating radar monitoring of a controlled DNAPL release: 200 MHz radar. *Geophysics 59*, 8 (1994), 1211–1221.

[44] Brewster, M., Redman, J., and Annan, A. Monitoring a controlled injection of perchlorethylene in a sandy aquifer with ground penetrating radar and time domain reflectometry. In *Symp.App.Geo.Env.Eng.Prob* (1992), vol. 2, Environmental And Engineering Geophysical Society, pp. 611–618.

[45] Broska, J. C., and Barnette, H. L. Hydrogeology and analysis of aquifer characteristics in West-Central Pinellas County, Florida. Tech. Rep. 99-185, US Geological Survey, 1999.

[46] Brown, M., and Bittner, P. Toxicological profile for vinyl chloride. Tech. rep., U.S. Department Of Health and Human Services, Public Health Service, Agency for Toxic Substances and Disease Registry, 1993.

[47] Carcione, J. Ground-pentrating radar: Wave theory and numerical simulation in lossy anisotropic media. *Geophysics 61*, 6 (1996), 1664–1677.

[48] Carcione, J. Radiation patterns for 2-D GPR forward modeling. *Geophysics 63*, 2 (March-April 1998), 424–430.

[49] Carcione, J., Lenzi, G., and Valle, S. GPR modelling by the fourier method: Improvement of the algorithm. *Geophysical Prospecting 47* (1999), 1015–1029.

[50] Carcione, J., and Seriani, G. An electromagnetic modelling tool for the detection of hydrocarbons in the subsoil. *Geophysical Prospecting 48* (2000), 231–256.

[51] Carcione, J., Seriani, G., and Gei, D. Acoustic and electromagnetic properties of soils saturated with salt water and NAPL. *Journal Of Applied Geophysics 52* (2003), 177–191.

[52] Cartensen, E. Measurement of dispersion of velocity of sound in liquids. *J.Acoust.Soc.Am. 26* (September 1954), 858–861.

[53] Casper, D., and Kung, K. Simulation of ground-penetrating radar waves in a 2-D soil model. *Geophysics 61*, 4 (1996), 1034–1049.

[54] Castagna, J., Batzle, M., and Eastwood, R. Relationships between compressional-wave and shear-wave velocities in clastic silicate rocks. *Geophysics 50* (1985), 571–581.

[55] Causseaux, K. The surficial aquifer in Pinellas County, Florida. Tech. Rep. 84-4289, US Geological Survey, 1984.

[56] Cerjan, C., Kosloff, D., Kosloff, R., and Reshef, M. A nonreflecting boundary condition for discrete acoustic and elastic wave equations. *Geophysics 50*, 4 (April 1985), 705–708.

[57] Cerveny, V. Ray tracing algorithms in three-dimensional laterally varying layered structures. In *Seismic Tomography : With Applications In Global Seismology and Exploration Geophysics*, G. Nolet, Ed. D. Reidel Publishing Company, 1987, pp. 99–133.

[58] Cerveny, V. *Seismic Ray Theory.* Cambridge University Press, 2001.

[59] Chambers, J., Loke, M., Ogilvy, R., and Meldrum, P. Noninvasive monitoring of DNAPL migration through a saturated porous medium using electrical impedance tomography. *Journal Of Contaminant Hydrology 68* (2004), 1–21.

[60] Chan, C., and Knight, R. Laboratory measurements of electromagnetic wave velocity in layered sands. *Water Resources Research 37*, 4 (April 2001), 1099–1105.

[61] Corradini, F., Marchetti, A., Tagliazucchi, M., and Tassi, L. Static dielectric constants of 1,2-dichloroethane + 2-methoxyethanol + 1,2-dimethoxyethane ternary liquid mixtures from -10 to 80 C. *Fluid Phase Equilib. 124* (1996), 209–220.

[62] Cox, B. E. *Tomographic Inversion Of Focusing Operators.* PhD thesis, University Of Delft, 2004.

[63] Cumberland, D., and Crawford, R. *The Packing Of Particles.* Elsevier Press, 1987.

[64] Curtis, A., and Snieder, R. Reconditioning inverse problems using the genetic algorithm and revised parametrization. *Geophysics 62*, 4 (1997), 524–1532.

[65] Dablain, M. High-order finite differences. *Geophysics 58* (1986).

[66] Daley, T., and Cox, D. Orbital vibrator seismic source for simultaneous P- and S-wave crosswell acquisition. *Geophysics 66*, 5 (September-October 2001), 1471–1480.

[67] Daley, T., Majer, E., and Peterson, J. Crosswell seismic imaging in a contaminated basalt aquifer. *Geophysics 69*, 1 (January-February 2004), 16–24. INEEL TAN results.

[68] Dana, D., Levander, A., Danbom, S., and Zelt, C. 3-D, near-surface seismic reflection investigation at a groundwater contamination site. *AGU Fall Meeting Abstracts* (December 2002), A1131+.

[69] Dana, D., Levander, A., Danbom, S., and Zelt, C. High resolution seismic mapping at a groundwater contamination site: 3-D reflection data. *EGS - AGU - EUG Joint Assembly, Abstracts from the meeting held in Nice, France, 6 - 11 April 2003, abstract #12726* (April 2003), 12726–+.

[70] Daniels, J., Roberts, R., and Vendl, M. Ground penetrating radar for the detection of liquid contaminants. *Journal Of Applied Geophysics 33* (1995), 195–207.

[71] D'Arrigo, G., and Paparelli, A. Sound propagation in water-ethanol mixtures at low-temperatures 1. Ultrasonic velocity. *Journal Of Chemical Physics 88*, 1 (1987), 405–415.

[72] Davidson, A., and Zon, L. Love, honor, and protect (your liver). *Science 299* (February 2003).

[73] Davis, J., and Annan, A. Ground-penetrating radar for high-resolution mapping of soil and rock stratigraphy. *Geophysical Propspecting 37* (1989), 531–551.

[74] Day-Lewis, F., Harris, J., and Gorelick, S. Time-lapse inversion of crosswell radar data. *Geophysics 67*, 6 (November-December 2002).

[75] Day-Lewis, F., and Lane, J. Assessing the resolution-dependent utility of tomograms for geostatistics. *Geophysical Research Letters 31* (2004).

[76] D.Dana, Azaria, A., Levander, A., Morozov, I., Zelt, C., and Magani, M. High-resolution seismic survey over a near-surface contamination site. In *71st Ann. Interna. Mtg: Soc. Of Expl. Geophysics* (2001), Society Of Exploration Geophysics, pp. 1337–1340.

[77] de Berg, M., van Kreveld, M., Overmars, M., and Schwarzkopf, O. *Computational Geometry : Algorithms and Applications*. Springer Verlac, 1997.

[78] de Hulst, H. V. *Light-scattering by small particles*. Wiley and Sons, 1975.

[79] Dean, J. A. *Lange's Handbook Of Chemistry*. McGraw Hill, 1992.

[80] Digby, P. The effective elastic moduli of porous granular rocks. *Journal Of Applied Mechanics 48* (1981), 803–808.

[81] Domenico, S. Effect of brine-gas mixture on velocity in an unconsolidated sand reservoir. *Geophysics 41* (1976), 882–894.

[82] Domenico, S. Elastic properties of unconsolidated porous sand reservoirs. *Geophysics 42* (1977), 1339–1368.

[83] Doyle, P., Roman, E., Beral, V., and Brooks, M. Spontaneous abortion in dry cleaning workers potentially exposed to perchloroethylene. *Occupational And Environmental Medicine 54* (1997), 848–853.

[84] Dutta, N., and Ode, H. Attenuation and dispersion of compressional waves in fluid-filled porous rocks with partial gas saturation (White model) - Part 1: Biot theory, Part 2 : Results. *Geophysics 44* (1979), 1777–1805.

[85] Dvorkin, J., Mavko, G., and Nur, A. Squirt flow in fully saturated rocks. *Geophysics 60*, 1 (1995), 97–107.

[86] Dvorkin, J., Nolen-Hoeksema, R., and Nur, A. The squirt-flow mechanisms : Macroscopic description. *Geophysics 59*, 3 (March 1994), 428–438.

[87] Dvorkin, J., and Nur, A. Dynamic poroelasticity : A unified model with the squirt and the Biot mechanisms. *Geophysics 58*, 4 (April 1993), 524–533.

[88] Dwarakanath, V., Deeds, N., and Pope, G. Analysis of partitioning interwell tracer tests. *Environmental Science and Technology 33*, 21 (1999), 3829–3836.

[89] Eggers, F., and Kaatze, U. Broad-band ultrasonic measurement techniques for liquids. *Meas.Sci.Technol. 7* (1996), 1–19.

[90] Elbring, G. Crosswell seismic imaging of an *in-situ* air stripping waste remediation process. In *Proceedings of the Symposium on the Application of Geophysics to Engineering and Environmental Problems* (1993), Environmental and Engineering Geophysical Society, pp. 55–63.

[91] Ellefsen, K., Nelson, P., Horton, R., and Wright, D. Summary of geophysical investigations for DNAPL remediation at Savannah River Site, South Carolina. Tech. rep., U.S. Gelogical Survey, 1997.

[92] Endres, A., and Knight, R. A theoretical treatment of the effect of microscopic fluid distibution on the dielectric properties of partially saturated rocks. *Geophysical Prospecting 40* (1992), 307–324.

[93] Endres, A., and Redman, J. Modeling the electrical properties of porous rocks and soils containing immiscible contaminants. In *Symp.App.Geo.Env.Eng.Prob* (1993), vol. 1, Environmental And Engineering Geophysical Society, pp. 21–38.

[94] Faroon, O., Taylor, J., Roney, N., S. B., and Fransen, M. Draft toxicological profile for carbon tetrachloride. Tech. rep., U.S. Department Of Health and Human Services, Public Health Service, Agency for Toxic Substances and Disease Registry, 2003.

[95] Fellner-Feldegg, J. The measurement of dielectrics in the time domain. *Journal Of Physical Chemistry 73* (1969), 612–623.

[96] Fomel, S., Berryman, J., Clapp, R., and Prucha, M. Iterative resolution estimation in least-squares Kirchoff migration. *Geophysical Prospecting 50* (2002), 577–588.

[97] Fomel, S., and Claerbout, J. Multidimensional recursive filter preconditioning in geophysical estimation problems. *Geophysics 68* (2003), 577.

[98] Fornberg, B. *A Practical Guide to Pseudospectral Methods*. Cambridge University Press, 1996.

[99] Francisca, F., and Rinaldi, V. Complex dielectric permittivity of soil-organic mixtures (20 MHz - 1.3 GHz). *Journal Of Environmental Engineering 129*, 4 (2003), 347–357.

[100] Freedman, R., and Vogiatzis, J. Theory of microwave dielectric constant logging using the electromagnetics wave propagation method. *Geophysics 44*, 5 (May 1979), 969–986.

[101] Freyer, E., Hubbard, J., and Andrews, D. Sonic studies of the physical properties of liquids. I. The sonic interferometer. The velocity of sound in some organic liquids and their compressibilities. *J.Amer.Chem.Soc. 51* (1929), 759–771.

[102] Gandhi, R., Hopkins, G., Goltz, M., S. G., and McCarty, P. Full-scale demonstration of *in-situ* cometabolic biodegredation of trichloroethylene in groundwater, 1, Dynamics of a recirculating well system. *Water Resources Research 38*, 4 (2002).

[103] Gandhi, R., Hopkins, G., Goltz, M., S. G., and McCarty, P. Full-scale demonstration of *in-situ* cometabolic biodegredation of trichloroethylene in groundwater, 2, Comprehensive analysis of field data using reactive transport modeling. *Water Resources Research 38*, 4 (2002).

[104] Gardner, T. An acoustic study of soils that model seabed sediments containing gas bubbles. *Journal Of The Acoustical Society of America 107*, 1 (2000), 163–176.

[105] Gardner, T. Modeling signal loss in surficial marine sediments containing occluded gas. *Journal Of The Acoustical Society of America 113*, 3 (March 2003), 1368–1378.

[106] Gardner, T., and Sills, G. An examination of the parameters that govern the acoustic behavior of sea bed sediments containing gas bubbles. *Journal Of The Acoustical Society of America 110*, 4 (October 2001), 1878–1889.

[107] Geer, R. Neutron generator facility opens, marks a major milestone of new production mission : Remodeled "cookie factory" will manufacture neutron tubes, generators. *Sandia National Laboratory Press Release* (April 1996).

[108] Geller, J., Ajo-Franklin, J., and Majer, E. Effect of immiscible liquids on P-wave transmission through natural aquifer samples. In *Symp.App.Geo.Env.Eng.Prob* (2003), Environmental and Engineering Geophysical Society.

[109] Geller, J., Kowalsky, M., Seifert, P., and Nihei, K. Acoustic detection of immiscible liquids in sand. *Geophyiscal Research Letters 27*, 3 (February 2000), 417–420.

[110] Geller, J., Majer, E., Peterson, J., Williams, . K., and Flexser, S. Mapping DNAPL transport and contamination in sedimentary aquifers with high resolution borehole seismic imaging. Tech. Rep. Project Ni. SF11SS13, Lawrence Berkeley National Laboratory, December 2001.

[111] Geller, J., and Myer, L. Ultrasonic imaging of organic liquid contaminants in unconsolidated porous media. *Contaminant Hydrology 19* (1995), 85–104.

[112] Geller, J., Peterson, J., Williams, K., Ajo-Franklin, J., and Majer, E. First field test of NAPL detection with high resolution borehole seismic imaging. In *9th Biennial International Conference on Nuclear and Hazardous Waste Management* (2002).

[113] Gerhard, J., Kueper, B., and Hecox, G. The influence of waterflood design on the recover of mobile DNAPLs. *Journal Of Ground Water 36*, 2 (1998), 283–292.

[114] Goodman, D. Ground-penetrating radar simulation in engineering and archaeology. *Geophysics 59*, 2 (1994), 224–232.

[115] Goodwin, A., Mehl, J., and Moldover, M. Reentrant radio-frequency resonator for automated phase-equilibria and dielecric measurements in fluids. *Rev. Sci. Instrum. 67* (1996), 4294–4303.

[116] Greenhouse, J., Brewster, M., Schneider, G., Redman, . D., Annan, P., Olhoeft, G., J. L., Sander, K., and Mazella, A. Geophysics and solvents : The Borden experiment. *The Leading Edge* (April 1993), 261–267.

[117] G.Schuster, and Quintus-Bosz, A. Wavepath eikonal traveltime inversion: Theory. *Geophysics 58* (1993), 1314–1323.

[118] Gueguen, Y., and Palciauskas, V. *Introduction To The Physics Of Rocks.* Princeton University Press, 1994.

[119] Hamilton, E. V_p/v_s and poisson's ratios in marine sediments and rocks. *Journal of the Acoustical Society of America 66*, 4 (1979), 1093–1101.

[120] Han, D., Nur, A., and Morgan, D. Effects of porosity and clay content on wave velocities in sandstones. *Geophysics 51* (1986), 2093–2107.

[121] Hansen, P. Analysis of discrete ill-posed problems by means of the L-curve. *SIAM Review 34*, 4 (1992), 561–580.

[122] Heasell, E., and Lamb, J. The absorbtion of ultrasonic waves in a number of pure liquids over the frequency range 100 to 200 Mc/s. *Proc.Phys.Soc.B 69*, 9 (1956), 869–877.

[123] Heimovaara, T. J. Design of triple-wire time domain reflectometry probes in practice and theory. *Soil Sci. Soc. Am. J. 57* (1993), 1410–1417.

[124] Heron, G., Carroll, S., Sowers, H., B. M., Juhlin, R., Daniel, J., and Ingle, D. Steam and ET-DSP combined for DNAPL remediation : full-scale site restoration at the Young-Rainey STAR center. In *Proceedings of the Fourth International Conference on Remediation of Chlorinated and Recalcitrant Compounds*. 2004.

[125] Hightower, M. Cost and performance report : Dual auger rotary steam stripping, Pinellas Northeast Site, Largo, Florida. Tech. rep., U.S. Department Of Energy (DOE), April 1998.

[126] Hightower, M. Cost and performance report : *In situ* anaerobic bioremediation Pinellas Northeast Site, Largo, Florida. Tech. rep., U.S. Department Of Energy (DOE), April 1998.

[127] Hill, R. Elastic properties of reinforced solids : Some theoretical principles. *J. Mech. Phys. Solids 11* (1963), 357–372.

[128] Hubbard, S., Chen, J., Peterson, J., Majer, E., Williams, K., Swift, D., Mailloux, B., and Rubin, Y. Hydrogeological characterization of the South Oyster bacterial transport site using geophysical data. *Water Resources Research 37*, 10, 2431–2456.

[129] Hyndman, D., Harris, J., and Gorelick, S. Inferring the relation between seismic slowness and hydraulic conductivity in heterogeneous aquifers. *Water Resources Research 36*, 8 (August 2000), 2121–2132.

[130] Iloukhani, H., Parsa, J., and Azizian, S. Ultrasonic studies for binary mixtures with trichloroethylene abd alkan-1-ols ($c_3 - c_8$) at 303.15 K. *J.Chem.Eng.Data 44* (1999), 152–154.

[131] Israelachvili, J. *Intermolecular And Surface Forces*. Academic Press, 1992.

[132] Johnson, R., and Poeter, E. Interpreting DNAPL saturations in a laboratory-scale injection with GPR data and direct core measurements. Tech. Rep. Open-File Report 03-349, US Geological Survey, 2003.

[133] Jordan, T., and Baker, G. A conceptual model for the detection of NAPL using amplitude and phase variation with offset (APVO) analysis of ground penetrating radar data. In *Symp.App.Geo.Env.Eng.Prob* (2002), Environmental And Engineering Geophysical Society.

[134] Jordan, T., and Baker, G. Reprocessing GPR data from the CFB Borden experiment using APVO/GPT techniques. In *Symp.App.Geo.Env.Eng.Prob* (2004), Environmental And Engineering Geophysical Society.

[135] Juhlin, R., Butherus, M., Daniel, J., D. I., Heron, G., and McGee, B. Successful field-scale *in situ* thermal NAPL remediation at the Young-Rainey STAR center. In *Proceedings of the Fourth International Conference on Remediation of Chlorinated and Recalcitrant Compounds*. 2004.

[136] Kajfez, D., Reed, M., and Smith, C. Loss tangent of motor oil at 10 GHz. *Microwave and Optical Technology Letters 21*, 1 (April 1999).

[137] Kaya, A., and Fang, H. Identification of contaminated soils by dielectric constant and electrical conductivity. *Journal of Environmental Engineering 132*, 2 (February 1997), 169–177.

[138] Keers, H., Johnson, L., and Vasco, D. Acoustic crosswell imaging using asymptotic waveforms. *Geophysics 65*, 5 (2000), 1569–1582.

[139] Keiswetter, D., Black, R., and Schmeissner, C. A program for seismic wavefield modeling using finite-difference techniques. *Computers in the Geosciences 22*, 3 (1996), 267–286.

[140] Keller, G. Rock and mineral properties. In *Electromagnetic Methods In Applied Geophysics*, M. N. Nabighian, Ed. Society Of Exploration Geophysics, Tulsa, Oklahoma, 1987, pp. 13–51.

[141] Kerndorff, H., Schleyer, R., Milde, G., and Plumb, R. Geochemistry of groundwater pollutants at German waste disposal sites. In *Groundwater Contamination and Analysis at Hazardous Waste Sites*, S. Lesage and R. Jackson, Eds. Marcel Dekker Inc., New York, 1992, pp. 245–271.

[142] Kim, C., Daniels, J., Guy, E., Radzevicius, S., and Holt, J. Residual hydrocarbons in a water-saturating medium : A detection strategy using ground penetrating radar. *Environmental Geosciences 7*, 4 (2000), 169–179.

[143] Knight, R. Ground penetrating radar for envionmental applications. *Annu. Rev. Earth Planet Sci. 29* (2001), 229–255.

[144] Kosloff, D., and Baysal, E. Forward modeling by a Fourier method. *Geophysics 47* (1982), 1402–1412.

[145] Kowalsky, M., Dietrich, P., Teutsch, G., and Rubin, Y. Forward modeling of ground penetrating radar data using digitized outcrop images and multiple scenarios of water saturation. *Water Resources Research 37*, 6 (June 2001), 1615–1625.

[146] Kowalsky, M., Geller, J., Seifert, . P., Nihei, K., and Myer, L. Acoustic visibility of immiscible liquids in poorly consolidated sand. In *Society Of Exploration Geophysics Annual Meeting, 1998* (1998), p. 4.

[147] Kremer, F., and Schonhals, A. *Broadband Dielectric Spectroscopy.* Springer Verlag, 2003.

[148] Krishnaiah, A., and Surendranath, K. Densities, speeds of sound, and viscosities of mixtures of oxolane with chloroethanes and chloroethenes. *J.Chem.Eng.Data 41* (1996), 1012–1014.

[149] Kueper, B., and Frind, E. Two-phase flow in heterogeneous porous media 1. Model development. *Water Resources Research 27*, 6 (1991), 1049–1057.

[150] Kueper, B., and Frind, E. Two-phase flow in heterogeneous porous media 2. Model application. *Water Resources Research 27*, 6 (1991), 1059–1070.

[151] Kueper, B., and Gerhard, J. Variability of point source infiltration rates for two-phase flow in heterogeneous porous media. *Water Resources Research 31*, 12 (December 1995), 2971–2980.

[152] Kueper, B., Redman, D., Starr, R., Reitsma, S., and Mah, M. A field experiment to study the behavior of tetrachloroethylene below the water table : Spatial distribution of residual and pooled DNAPL. *Ground Water 31*, 5 (1993), 756–766.

[153] Kumari, P., Radhamma, M., Sekhar, G., and Rao, M. Excess volumes and speeds of sound of n-methyl-2-pyrrolidone with chloroethanes and chloroethenes at 303.15 K. *J.Chem.Eng.Data 47* (2002), 425–427.

[154] Kutrubes, D. Dielectric permittivity measurements of soils saturated with hazardous fluids. Master's thesis, Colorado School Of Mines, Golden, CO, 1986.

[155] Lagemann, R., Evans, J., and McMillan, D. Ultrasonic Velocity in Some Organic Halides: Constitutive Effects. *J.Amer.Chem.Soc. 70* (1948), 2996–2999.

[156] Landauer, R. The electrical resistance of binary metallic mixtures. *The Journal Of Applied Physics 23* (1952), 779–784.

[157] Lane, J., Buursink, M., Haeni, F., and Versteeg, R. Evaluation of Ground-Penetrating Radar to Detect Free-Phase Hydrocarbons in Fractured Rocks : Results of Numerical Modeling and Physical Experiments. *Groundwater 38*, 6 (2000), 929–938.

[158] Lane, J., Lewis, F., Versteeg, R., and Casey, C. Object-based inversion of crosswell radar tomography data to monitor vegetable oil injection experiments. *Journal Of Environmental And Engineering Geophysics 9*, 2 (June 2004), 63–77.

[159] Lee, M., Odom, J., and Jr., R. B. New perspectives on microbial dehalogenation of chlorinated solvents : Insights from the field. *Annual Reviews Of Microbiology 52* (1998), 423–452.

[160] Lemke, L., Abriola, L., and Goovaerts, P. Dense nonaqueous phase liquid (DNAPL) source zone characterization: Influence of hydraulic property correlation on predictions of dnapl infiltration and entrapment. *Water Resources Research 40* (2004).

[161] Li, C., and Nowack, R. Application of autoregressive extrapolation to seismic tomography. *Bulletin of the Seismological Society Of America 94*, 4 (August 2004), 1456–1466.

[162] Loon, R. V., Fuks, S., and Bellemans, A. Dielectric constant of carbon tetrachloride and 1,1,1-trichloroethane mixtures. *Bulletin des Societes Chimiques Belges 76* (1967), 202–210.

[163] Lorah, M., and Olsen, L. Natural attenuation of chlorinated volatile organic compounds in a freshwater tidal wetland: Field evidence of anaerobic biodegredation. *Water Resources Research 35*, 12 (1999), 3811–3827.

[164] Lorenzi, L., Fermeglia, M., and Torriano, G. Density and viscosity of 1-methoxy-2-propanol, 2-methyltetrahydrofuran, trifluorotoluene, and their binary mixtures with 1,1,1-trichloroethane at different temperatures. *J.Chem.Eng.Data 41* (1996), 1121–1125.

[165] Lucius, J., Olhoeft, G., Hill, P., and Duke, S. *Properties And Hazards Of 108 Selected Substances.* USGS Open-File Report 92-527, 1992.

[166] Lunn, S., and Kueper, B. Removal of pooled dense, nonaqueous phase liquid from saturated porous media using upward gradient alcohol floods. *Water Resources Research 33*, 10 (1997), 2207–2219.

[167] MacDonald, J. Cleaning up the nuclear weapons. *Environmental Science and Technology 33*, 15 (1999), 314–319.

[168] Mackay, D., and Cherry, J. Groundwater contamination : Pump-and-treat remediation. *Environmental Science and Technology 23*, 6 (1989), 630–637.

[169] Mackay, D., Roberts, P., and Cherry, J. Transport of organic contaminants in groundwater. *Environmental Science and Technology 19*, 5 (1985), 384–392.

[170] Majer, E., Peterson, J., Williams, K., Daley, T., and Gee, G. High resolution imaging of vadose zone transport using crosswell radar and seismic methods. Tech. Rep. PNNL-13791, Pacific Northwest National Laboratory, Richland, Washington 99352, September 2000.

[171] Manahan, S. *Environmental Chemistry.* CRC Press, 1994.

[172] Mario Fernandez, J. Reconnaissance of water quality at a U.S. Department of Energy site, Pinellas county, Florida. Tech. Rep. 85-4062, US Geological Survey, 1985.

[173] Mavko, G., Mukerji, T., and Dvorkin, J. *The Rock Physics Handbook: Tools For Seismic Analysis In Porous Media*. Cambridge University Press, 1998.

[174] Mavko, G., and Nur, A. Wave attenuation in partially saturated rocks. *Geophysics 44* (1979), 161–178.

[175] Mavko, G., and Nur, A. The effect of a percolation threshold in the Kozeny-Carman relation. *Geophysics 62*, 5 (September 1997), 1480–1482.

[176] Maymo-Gatell, X., Chien, Y., Gosset, J., and Zinder, S. Isolation of a bacterium that reductively dechlorinates tetrachloroethene to ethene. *Science 276* (1997), 1568–1571.

[177] Mazella, A. Electrical resistivity variations associated with controlled gasoline spills. In *70th Ann. Interna. Mtg: Soc. Of Expl. Geophysics* (2000), Society Of Exploration Geophysics.

[178] McCarty, P. Breathing with chlorinated solvents. *Science 276* (1997), 1521–1522.

[179] Menke, W. *Geophysical Data Analysis : Discrete Inverse Theory.* Academic Press, 1984.

[180] Mercer, J., and Cohen, R. A review of immiscible fluids in the subsurface: properties, models, characterization, and remediation. *Contaminant Hydrology 6* (1990), 107–163.

[181] Michelini, A. Velocity model inversion using parametric curves. *Geophysical Journal International 115* (1993), 337–343.

[182] Michelini, A. An adaptive-grid formalism for traveltime tomography. *Geophys. J. Int. 121* (1995), 489–510.

[183] Milligan, P., Rector, J., and Bainer, R. Hydrophone VSP imaging at a shallow site. *Geophysics 62*, 3 (May-June 1997), 842–852.

[184] Mindlin, R. Compliance of elastic bodies in contact. *Journal Of Applied Mechanics 16* (1949), 259,268.

[185] Montgomery, J. *Groundwater Chemicals Field Guide.* Lewis Publishers, 1991.

[186] Mopsik, F. Dielectric properties of slightly polar organic liquids as a function of pressure, volume, and temperature. *J.Chem.Phys. 50*, 6 (March 1969), 2559–2569.

[187] Mora, P. Elastic wave-field inversion of reflection and transmission data. *Geophysics 53*, 6 (1988), 750–759.

[188] Morgan, S., and Lowry, H. Dielectric polarization of some pure organic compounds in the dissolved, liquid, and solid states. *J.Phys.Chem. 34* (1930), 2385–2432.

[189] Moser, T., Nolet, G., and Snieder, R. Ray bending revisited. *Bulletin of the Seismological Society of America 82*, 1 (February 1982), 259–288.

[190] Moser, T. J. Shortest path calculation of seismic rays. *Geophysics 56* (1991), 59 – 67.

[191] Moumouzias, G., and Ritzoulis, G. Relative permittivities and refractive indices of propylene carbonate and toluene mixtures from 283.15 K to 313.15 K. *J.Chem.Eng.Data 42* (1997), 710–713.

[192] Moysey, S., and Knight, R. Full-inverse statistical calibration : A monte carlo approach to determining field-scale relationships between hydrologic and geophysical variables. vol. 84, American Geophysical Union.

[193] Murphy, W. *Effects of Microstructure and Pore Fluids on the Acoustic Properties of Granular Sedimentary Materials.* PhD thesis, Stanford University, 1982.

[194] Mussari, L., Postigo, M., Lafuente, C., Royo, F., and Urieta, J. Viscosity measurements for the binary mixtures of 1-2-dichloroethane or 1-2-dibromomethane with isomeric butanols. *J.Chem.Eng.Data 45* (2000), 86–91.

[195] Nath, J. Ultrasonic velocities, relative permittivities, and refractive indices for binary liquid mixtures of trichloroethylene with pyridine amd quinoline. *Fluid Phase Equilib. 109* (1995), 39–51.

[196] Nath, J., and Dixit, A. Ultrasonic velocities in, and adiabatic compressibilities and excess volumes for, binary liquid mixtures of acetone with tetrachloroethylene, trichloroethylene, methylene chloridem 1,2-dichloroethane, and cyclohexane. *J.Chem.Eng.Data 29* (1984), 313–316.

[197] Nath, J., and Dubey, S. N. Binary systems of trichloroethylene with benzene, toluene, p-xylene, carbon tetrachloride, and chloroform. ultrasonic velocities and adiabatic compressibilities at 303.15 and 313.15 K, and dielectric properties and refractive indexes at 303.15 K. *J.Phys.Chem. 84* (1980), 2166–2170.

[198] Nath, J., and Narain, B. Binary systems of tetrachlorethylene with benzene, toluence, p-xylene, carbon tetrachloride, and cyclohexane. 1. Ultrasonic velocities and adiabatic compressibilities at 293.15 and 303.15 K, dielectric constants at 298.15 and 308.15 K, and refractive indexes at 298.15 K. *J.Chem.Eng.Data 27* (1982), 308–312.

[199] Nath, J., and Saini, R. Ultrasonic and dielectric behavior of binary systems of methyl ethyl ketone with 1,2-dichloroethane, methylene chloride, trichloroethene, tetrachloroethene, and cyclohexane. *J. Chem. Soc. Faraday Trans. 86*, 4 (1990), 645–650.

[200] Nath, J., and Singh, G. Ultrasonic velocities in and adiabatic compressibilities for, binary liquid mixtures of 1,2-dichloroethane with benzene, toluene, p-xylene, quinoline, and cyclohexane. *J.Chem.Eng.Data 31* (1986), 327–329.

[201] Nath, J., and Tevari, M. Ultrasonic and dielectric behavior of binary systems of quinoline with methylene chloride, chloroform, carbon tetrachloride, benzene, and cyclohexane. *J. Chem. Soc. Faraday Trans. 88*, 18 (1992), 2197–2202.

[202] Nelson, S., Lindroth, D., and Blake, R. Dielectric properties of selected minerals at 1 to 22 GHz. *Geophyiscs 54*, 4 (October 1989), 1334–1349.

[203] Nemeth, T., Normark, E., and Qin, F. Dynamic smoothing in crosswell traveltime tomography. *Geophysics 62*, 1 (1997), 168–176.

[204] Newmark, R., amd K.R. Kyle, W. D., and Ramirez, A. Monitoring DNAPL pumping using integrated geophysical techniques. Tech. rep., Lawrence Livermore National Laboratory : DOE, 1997.

[205] Norris, R., and Arkin, W. Nuclear notebook. *Bulletin of the Atomic Scientists 47*, 1 (January/February 1991).

[206] Oakley, B., Barber, G., Worden, T., and Hanna, D. Ultrasonic parameters as a function of absolute hydrostatic pressure 1. A review of the data for organic liquids. *J.Phys.Chem.Ref.Data 32*, 4 (2003), 1501–1533.

[207] Oakley, B., Hanna, D., Shillor, M., and Barber, G. Ultrasonic parameters as a function of absolute hydrostatic pressure 2. Mathematical models of the speed of sound in organic liquids. *J.Phys.Chem.Ref.Data 32*, 4 (2003), 1535–1544.

[208] Olhoeft, G. Geophysical dectection of hydrocarbon and organic chemical contamination. In *Symp.App.Geo.Env.Eng.Prob* (1992), vol. 2, Environmental And Engineering Geophysical Society, pp. 587–595.

[209] Orlando, L. Detection and analysis of LNAPL using the instantaneous amplitude and frequency of ground-penetrating radar. *Geophysical Prospecting 50* (2002), 27–41.

[210] Page, G. Comparison of groundwater and surface water for patterns and levels of contamination by toxic substances. *Environmental Science and Technology 15*, 12 (December 1981), 1475–1481.

[211] Paige, C., and Saunders, M. An algorithm for sparse linear equations and sparse least squares. *ACM Transactions in Mathematical Software 8* (1982), 43–71.

[212] Pankow, J., and Cherry, J. *Dense Chlorinated Solvents and other DNAPLs in Groundwater*. Waterloo Press, 1996.

[213] Parker, B., Cherry, J., Chapman, S., and Guilbeault, M. Review and analysis of chlorinated solvent dense nonaqueous phase liquid distributions in five sandy aquifers. *Vadose Zone Journal 2* (2003), 117–137.

[214] Pellam, J., and Galt, J. Ultrasonic propagation in liquids: I. Application of pulse technique to velocity and absorption measurements at 15 megacycles. *J.Chem.Phys. 14*, 10 (1946).

[215] Persson, M., and Berndtsson, R. Measuring nonaqueous phase liquid saturation in soil using time domain reflectometry. *Water Resources Research 38*, 5 (2002).

[216] Peterson, J. Pre-inversion corrections and analysis of radar tomographic data. *Journal Of Environmental And Engineering Geophysics 6* (March 2001), 1–18.

[217] Porokhovoi, S., du Mouza, J., and Reiter, M. Dielectric properties of polluted soils as a potential tool to detect low level organic pollution in unsaturated soils. In *Symp.App.Geo.Env.Eng.Prob* (1996), vol. 2, Environmenal and Engineering Geophysical Society, pp. 1237–1246.

[218] Prasad, M. *Experimental and theoretical considerations of velocity and attenuation interactions with physical parameters in sands.* PhD thesis, Kiel University, 1988.

[219] Prasad, M. Acoustic measurements in unconsolidated sands at low effective pressure and overpressure detection. *Geophysics 67*, 2 (March-April 2002), 405–412.

[220] Prasad, M., and Meissner, R. Attenuation mechanisms in sands : Laboratory versus theoretical (Biot) data. *Geophysics 57*, 5 (May 1992), 710–719.

[221] Prasad, T., Mythili, R., Nirmala, G., and Prasad, D. Densities and viscosities of the binary mixtures of chloroethylenes with some aliphatic alcohols. *J.Chem.Eng.Data 47* (2002), 68–71.

[222] Pratt, R., and Worthington, M. Inverse theory applied to multi-source cross-hole tomography. Part 1: Acoustic wave-equation method. *Geophysical Prospecting 38* (1990), 287–310.

[223] Pratt, R., and Worthington, M. Inverse theory applied to multi-source cross-hole tomography. Part 2: Elastic wave-equation method. *Geophysical Prospecting 38* (1990), 311–330.

[224] Redman, J. Geophysics and the solvents-in-groundwater program. In *Symp.App.Geo.Env.Eng.Prob* (1992), Environmental And Engineering Geophysical Society, pp. 375–382.

[225] Ritzoulis, G., Papadopoulos, N., and Jannakoudakis, D. Densities, viscosities, and dielectric constants of acetonitrile + toluene at 15, 25, and 35 C. *J.Chem.Eng.Data 31* (1986), 148–152.

[226] Romig, P., Ed. *Seeing into the Earth : Noninvasive Characterization of the Shallow Subsurface for Environmental and Engineering Application.* National Academy Press, 2000.

[227] Roth, K., Schulin, R., Fluhler, H., and Attinger, W. Calibration of time domain reflectometry for water content measurement using a composite dielectric approach. *Water Resources Research 26*, 10 (October 1990), 2267–2273.

[228] Ruiz, D. *Intrinsic And Stress-Induced Velocity Anistropy In Unconsolidated Sands.* PhD thesis, Stanford University, Stanford, CA, December 2003.

[229] Sallmen, M., Lindbohm, M., Anttila, A., Kyyronen, P., Taskinen, H., Nykyri, E., and Hemminki, K. Time to pregnancy among the wives of men exposed to organic solvents. *Occupational And Environmental Medicine 55* (1998), 24–30.

[230] Sander, K., Olhoeft, G., and Lucius, J. Surface and borehole radar monitoring of a DNAPL spill in 3D versus frequency, look angle, and time. In *Symp.App.Geo.Env.Eng.Prob* (1992), vol. 2, Environmental And Engineering Geophysical Society, pp. 455–469.

[231] Santamarina, J., and Fam, M. Dielectric permittivity of soils mixed with organic amd inorganic fluids. *Journal Of Environmental And Engineering Geophysics 2* (1997), 37–51.

[232] Sastry, N., George, A., Jain, N., and Bahadur, P. Densities, relative permittivities, excess volumes, and excess molar polarizations for alkyl ester (methyl propanoate, methyl butanoate, ethyl propanoate, and ethyl butanoate) + hydrocarbons (n-heptane, benzene, chlorobenzene, and 1,1,2,2-tetrachloroethane) at 308.15 K and 318.15 K. *J.Chem.Eng.Data 44* (1999), 456–464.

[233] Schon, J. *Physical Properties Of Rocks : Fundamentals And Principles Of Petrophysics.* Pergamon Press, 1996.

[234] Seifert, P. *Effects of Pore Fluids in the Subsurface on Ultrasonic Wave Propagation.* PhD thesis, University Of California, Berkeley, Berkeley, CA, 1998.

[235] Seifert, P., Geller, J., and Johnson, L. Effect of P-wave scattering on velocity and attenuation in unconsolidated sand saturated with immiscible liquids. *Geophysics 63*, 1 (1998), 161–170.

[236] Seifert, P., Kaelin, B., and Johnson, L. Effect on ultrasonic signals of viscous pore fluids in unconsolidated sand. *J.Acoust.Soc.Am. 106*, 6 (December 1999).

[237] Sekhar, G., Venkatesu, P., and Rao, M. Excess molar volumes and speeds of sound of n,n-dimethylacetamide with chloroethanes and chloroethenes at 303.15 K. *J.Chem.Eng.Data 46* (2001), 377–380.

[238] Semprini, L., Kitanidis, P., Kampbell, D., and Wilson, J. Anaerobic transformation of chlorinated aliphatic hydrocarbons in a sand aquifer based on spatial chemical distributions. *Water Resources Research 31*, 4 (April 1995), 1051–1062.

[239] Sen, P., Scala, C., and Cohen, M. A self-similar model for sedimentary rocks with application to the dielectric constant of fused glass beads. *Geophysics 46*, 5 (May 1981), 781–795.

[240] Sethian, J., and Popovici, A. M. 3-D traveltime computation using the fast marching method. *Geophysics 64*, 2 (1999), 516–523.

[241] Shewchuk, J. Triangle : Engineering a 2D quality mesh generator and delaunay triangulator. Tech. rep., Carnegie Mellon University, 1996.

[242] Singha, K., Binley, A., Lane, J., and Gorelick, S. Electrical imaging of tracer migration at the Massachusets Military Reservation, Cape Cod. In *Symposium on the Application of Geophysics to Environmental and Engineering Problems* (April 2004), Environmental and Engineering Geophysical Society.

[243] Sneddon, K., Olhoeft, G., and Powers, M. Determining and mapping DNAPL saturation values from noninvasive GPR measurments. In *Symp.App.Geo.Env.Eng.Prob* (2000), Environmental And Engineering Geophysical Society, pp. 293–302.

[244] Steeples, D. Shallow seismic reflection section : Introduction. *Geophysics 63*, 4 (1998), 1210–1212.

[245] Steeples, D. A review of shallow seismic methods. *Annali di Geofisica 43*, 6 (2000), 1021–1044.

[246] Stephenson, J. Good workers may get bad breaks on health. *Journal Of The American Medical Association 273*, 21 (1995), 1645–1646.

[247] Swanson, J. Pressure coefficients of acoustic velocity for nine organic liquids. *J.Chem.Phys. 2* (1934), 689–693.

[248] Tabor, C., Juhlin, R., Darr, P., Cabellero, J., Daniel, . J., and Ingle, D. Non aqueous-phase liquid characterization and post remediation sampling. In *Proceedings of the Fourth International Conference on Remediation of Chlorinated and Recalcitrant Compounds.* 2004.

[249] Tarantola, A. Inversion of travel times and seismic waveforms. In *Seismic Tomography : With Applications In Global Seismology and Exploration Geophysics*, G. Nolet, Ed. D. Reidel Publishing Company, 1987, pp. 135–158.

[250] Temples, T., Waddel, M., Domoracki, W., and Eyer, J. Noninvasive determination of the location and distribution of DNAPLs using advanced seismic reflection techniques. *Groundwater 39* (May-June 2001), 465–474.

[251] Thomas, J. *Numerical Partial Differential Equations: Finite Difference Methods.* Springer-Verlag, 1995.

[252] Timmermans, J., and Hennaut-Roland, M. Travaux du bureau international d'etalons physico-chimiques : 9. Etude des constantes physiques de vingt composes organiques. *Journal de Chimie Physique 52* (1955), 223–244.

[253] Timmermans, J., Piete, A., and Philippe, R. Methodes et appareils utilises au bureau des etalons physico-chimiques : 14. Measure de la constante dieletrique des composes organiques a 20 c. *Bulletin des Societe Chimiques Belges 64* (1955), 5–23.

[254] Tokida, T., Miyazaki, T., and Seki, K. *In situ* accumulation if methane bubbles in a natural wetland soil. *European Journal Of Soil Science* (2004).

[255] Topp, G., Davis, J., and Annan, A. Electromagnetics determination of soil water content: measurements in coaxial transmission lines. *Water Resources Research 16* (1980), 574–582.

[256] Topp, G., Yanuka, M., Zebchuk, W., and Zegelin, S. Determination of electrical conductivity using time domain reflectometry : Soil and water experiments in coaxial lines. *Water Resources Research 24*, 7 (July 1988), 945–952.

[257] Tutuncu, A., and Sharma, M. The influence of fluids on grain contact stiffness and frame moduli in sedimentary rocks. *Geophysics 57*, 12 (1992), 1571–1582.

[258] van Trier, J., and Symes, W. Upwind finite-difference calculation of traveltimes. *Geophysics 56* (1991).

[259] Vasco, D., Peterson, J., and Lee, K. Ground-penetrating radar velocity tomography in heterogeneous and anisotropic media. *Geophysics 62*, 6 (November-December 1997), 1758–1773. radar tomography - applied to INEEL TAN data.

[260] Vega-Ruiz, D. *Intrinsic And Stress-Induced Velocity Anisotropy In Unconsolidated Sands.* PhD thesis, Stanford University, Stanford, CA, December 2003.

[261] Venkatesulu, D., Venkatesu, P., and Rao, M. Viscosities and densities of trichloroethylene or tetrachloroethylene with 2-alkoxyethanols at 303.15 K and 313.15 K. *J.Chem.Eng.Data 42* (1997), 365–367.

[262] Vidale, J. Finite-difference calculation of travel times. *Bull. Seis. Soc. Of America 78* (1988), 2062–2076.

[263] Vinje, V., Iverson, E., and Gjoystdal, H. Traveltime and amplitude estimation using wavefront construction. *Geophysics 58* (1993), 1157–1166.

[264] von Hippel, A. *Dielectric Materials and Applications.* Artech House, 1954.

[265] Wahba, G. *Spline Models for Observational Data*, vol. 59 of *CBMS-NSF Regional Conference Series in Applied Mathematics.* Society For Industrial And Applied Mathematics, 1990.

[266] Walden, P., and Werner, O. Uber die dielektrizitatskonstanten (ϵ-konstanten) gechlorter paraffine und olefine. *Zeitschrift fur Physikalische Chemie 111* (1924), 465–471.

[267] Walton, K. The effective elastic moduli of a random packing of spheres. *Journal Of Mechanics And Physics: Solids 35*, 2 (1987), 213–226.

[268] Wang, T., and Tripp, A. Simulation of EM wave propogation in three-dimensional structures by a finite-difference method. *Symposium on the Application of Geophysics to Engineering and Environmental Engineering 2* (1994), 737–755.

[269] Wang, Z., and Nur, A. Ultrasonic velocities in pure hydrocarbons and mixtures. *J. Acoust. Soc. Am. 89* (1991), 2725–2730.

[270] Ward, C., Kavanaugh, M., and Hornberger, G., Eds. *Groundwater & Soil Cleanup : Improving Management Of Persistent Contaminants.* National Academy Press, Washington D.C., 1999.

[271] Weissler, A. Ultrasonic investigation of molecular properties of liquids : IV. Cyclic Compounds. *J.Amer.Chem.Soc. 71* (1949), 419–421.

[272] Werkema, D., Atekwana, E., Endres, A., Sauck, W., and Cassidy, D. Investigating the geoelectrical response of hydrocarbon contamination undergoing biodegredation. *Geophysical Research Letters 30*, 12.

[273] White, D. Two-dimensional seismic refraction tomography. *Geophysical Journal International 97* (1989), 223–245.

[274] White, J. Computed seismic speeds and attenuation in rocks with partial gas saturation. *Geophysics 40* (1975), 224–232.

[275] Wilkens, R., and Richardson, M. The influence of gas bubbles on sediment acoustic properties: *in-situ*, laboratory, and theoretical results from the Ecernforde Bay, Baltic Sea. *Continental Shelf Research 18* (1998), 1859–1892.

[276] Williams, K. Monitoring microbe-induced physical property changes using high-frequency acoustic waveform data : Toward the development of a microbial megascope. Master's thesis, 2002.

[277] Williams, K., Hubbard, S., Ntarlagiannis, D., and Banfield, J. Monitoring microbe-induced sulfide precipitation under dynamic flow conditions using multiple geophysical techniques. *Eos Trans. AGU, Jt. Assem Suppl, Abstract NS13A-01 85*, 17 (2004).

[278] Williamson, P., and Worthington, M. Resolution limits in ray tomography due to wave behavior: Numerical experiments. *Geophysics 58*, 5 (May 1993), 727–735.

[279] Wilson, R., and Mackay, D. Direct detection of residual nonaqueous phase liquid in the saturated zone using sf_6 as a partitioning tracer. *Environmental Science and Technology 29* (1995), 1255–1258.

[280] Winkler, K. Contact stiffness in granular porous materials: Comparison between theory and experiment. *Geophysical Research Letters 10*, 11 (1983), 1073–1076.

[281] Yi, M., Kim, J., and Chung, S. Enhancing the resolving power of least-squares with active constraint balancing. *Geophysics 68* (2003), 931.

[282] Zimmer, M. *Seismic Velocities In Unconsolidated Sands : Measurements Of Pressure, Sorting, And Compaction Effects*. PhD thesis, Stanford University, Stanford, CA, November 2003.

[283] Zimmer, M., Prasad, M., and Mavko, G. Pressure and porosity influences on V_p - V_s ratios in unconsolidated sands. *The Leading Edge 21* (2002), 178–183.

Index